COMPETING FATIGUE MECHANISMS IN

Ni-BASE SUPERALLOY René 88DT

by

Paul N. Chang

A dissertation submitted to the faculty of
The University of Utah
in partial fulfillment of the requirements for the degree of

Doctor of Philosophy

Department of Metallurgical Engineering

University of Utah

May 2011

The University of Utah Graduate School

STATEMENT OF DISSERTATION APPROVAL

The dissertation of **Paul N. Chang**

has been approved by the following supervisory committee members:

Ravi Chandran	, Chair	**12/2/2010** Date Approved
Gerald T. Cashman	, Member	**12/2/2010** Date Approved
Sivaraman Guruswamy	, Member	**12/2/2010** Date Approved
Dinesh K. Shetty	, Member	**12/2/2010** Date Approved
Daniel O. Adams	, Member	**12/2/2010** Date Approved

and by **Jan D. Miller** , Chair of the Department of **Metallurgical Engineering**

and by Charles A. Wight, Dean of The Graduate School.

ABSTRACT

Nickel base superalloys exhibit superior high temperature mechanical properties required for aircraft engine components. It has been known that the processing of these alloys by the powder metallurgy route introduces inclusions inside the material. The presence of such inclusions often leads to competing failure modes in fatigue that is described by a step-wise or two distinct S-N curves involving both the surface and internally-initiated cracks, resulting in large uncertainties of fatigue life. A clear understanding of such behavior is yet to be established.

The principal objective of this research is to examine the effect of inclusions on the extent of fatigue failure competition from surface and internal initiators at two different specimen test volumes. Experimental fatigue testing has been performed to explore how the presence of inclusions affects the competing fatigue failure modes. In addition, how the competing failure modes will behave with changes in the specimen size was also studied.

Two groups of material each with two different specimen sizes were used in this study. It has been shown that the two crack initiation mechanisms occurred in the small unseeded René 88DT specimens tested at 650ºC over the stress range tested. Additionally, the fatigue lives were reduced with increase in specimen volume.

All fatigue failures in seeded material occurred due to crack initiations from the seeded inclusions. In the fatigue life of seeded material, two competing and separate S-N

curves were found in small test volume, whereas, in the large test volume, the regions were separated by a “step” in S-N curve.

It has been found that the largest inclusion size observed in metallographic surfaces was smaller than the size determined from the fatigue failure origin. An analysis method based on extreme value statistics developed by Murakami was used to predict the largest size of inclusion in the test volume.

The results of this study clearly show that competition for fatigue failure between surface and internal initiations is affected by inclusion content and specimen volume. Extreme value statistics is capable of predicting the largest inclusion that can start fatigue failure, even if the inclusion is not seen in microscopy.

Dedicated to my Parents and Sister

TABLE OF CONTENTS

LIST OF TABLES

LIST OF FIGURES

Figure **Page**

Figure **Page**

Figure **Page**

Figure **Page**

Figure **Page**

Figure **Page**

Figure **Page**

Figure **Page**

Figure **Page**

Figure **Page**

ACKNOWLEDGEMENTS

First and foremost I want to thank my advisor Dr. K.S. Ravi Chandran for his guidance during my research and study at University of Utah. I appreciate all his contributions of time and ideas to make my Ph.D. experience productive and stimulating. The joy and enthusiasm he has for his research was contagious and motivational for me, even during tough times in the Ph.D. pursuit.

I gratefully acknowledge one of my supervisory committee members Dr. Jerry Cashman for his advice, and crucial contribution, which make him a backbone of this research. Jerry, I am grateful in every possible way and hope to keep up our collaboration in the future. For this dissertation I would like to thank my supervisory committee members: Dr. Daniel Adams, Dr. Sivaraman Guruswamy and Dr. Dinesh K.Shetty, for their time, interest and helpful comments. My special thanks go to Dr. Zhigang Z. Fang for letting me use their equipment.

I also recognize the support and help from the GE Aviation and National Science Foundation. I would like to acknowledge my lab mates Biplab Sarma and Madhu Jagannathan for their constant help in my work.

Lastly, I would like to thank my family for all their love and encouragement.

CHAPTER 1

INTRODUCTION

Fatigue is the progressive and localized structural damage that occurs when a material is subjected to cyclic loading. Many failures of engineering structures such as bridges, rails, gears, turbine blades, rotating shafts and bearings are caused by fatigue. It is therefore important to be able to understand the factors that lead to material fatigue. In fatigue analysis, the material performance is commonly characterized by an S-N curve, where the cyclic stress amplitude (S) is plotted against the number of cycles to the time of failure (N) in semilogarithmic scale. The typical S-N curve has been thought of as a single curve, that is, as the stress range increases, the fatigue life decreases. At a limiting value of stress amplitude, the S-N curve asymptotically approaches that value. This stress is referred to as the "endurance limit" in fatigue.

It has generally been found that fatigue cracks normally initiate at the surface of a material. This observation has generally been consistent with the notion of a single S-N curve showing the asymptotic nature of the endurance limit. However, recently a number of researchers [1-5] have reported some unusual shapes of the S-N curve in the experimental results obtained from fatigue tests using specimens from commercial titanium alloys, high strength steels and nickel-base superalloys. The researchers suggest, on the basis of these tests, that there are step-wise S-N curves or two distinct S-N curves, one corresponding to surface and the other to internal initiation. The internal failure mode

is predominant at low stress ranges and is evidenced by a “fish-eye” facet on the fracture surface. Failures from the surface occurred at high stresses only. Similar behavior has been observed for materials even at elevated temperatures [3]. This dual failure mode seems to challenge or contradict the traditional representation of the fatigue behavior through the S-N curve paradigm.

Nickel-base superalloys are the primary material choice for high temperature applications such as a gas turbine disk because of their exceptional strength and oxidation resistance at the service temperatures. Their capabilities are limited to about 650-700˚C of operating temperature, and include commercially used alloys such as René 88DT. Superalloy turbine disks are commonly manufactured using powder metallurgy processing, to achieve the strength and high temperature resistance requirements but this process leads to inclusions and variability in the microstructure. Inclusions serve as stress concentration points, providing starting points for fatigue cracks. Over the years, there has been a substantial effort by industry to reduce inclusions in specialty alloys used for aerospace applications. These alloys include aerospace titanium, nickel-base superalloys, and high-strength steel alloys. The major concern with these inclusions is that they cause chemical and/or microstructural discontinuities that are harder or softer than the base alloy or have an interface, all of which may act as crack-initiation sites for fatigue failure. Since the early 1980s, a number of aircraft disasters have occurred, primarily caused by engine problems traceable to the presence of inclusions. For example, on 19 July 1989, United Airlines Flight 232, a wide-bodied DC-10, crashed at Sioux City, Iowa. This crash was determined by the FAA to be a direct consequence of a fatigue failure initiated by the presence of a ‘hard-alpha’ inclusion in a titanium alloy compressor disk. Ensuring the

safe performance of turbine components is therefore of paramount importance for aircraft safety. An understanding of the fatigue crack initiation characteristics of these inclusions can help to improve the material and/or allow a more accurate life prediction for the components.

The effects of inclusions introduced during the powder atomization and handling processes may be present in very small volume fractions within the microstructure, but they may have a large influence on fatigue life. For fixed fatigue test conditions, surface-initiated fatigue produce significantly lower fatigue lives than internally-initiated failures. Therefore, the effects on fatigue life of inclusions residing at or near the surface of a material could be quite substantial. However, the volume fraction of inclusions in the microstructure is very small and therefore, the probability of the presence of a critically sized inclusion or inclusion cluster within a critical area of the microstructure is low. It is therefore exceedingly difficult to assess the full effects of inclusions on life with a statistically significant manner. Testing of intentionally seeded material offers significant advantages. The impact of inclusion sizes may be assessed. Seeding distributions may be statistically described, and competition with grain initiated failures may be observed. Yet, the specimen sizes will have influence the occurrence probabilities of the inclusions. Larger specimen size has a greater volume of material, and thus a larger population of material-related initial inclusions. Statistically, a larger population contains more extreme inclusion sizes, both large and small. The presence of larger inclusions leads to crack initiation and growth and failures at lower stress levels, hence a lower endurance limit.

This study was conducted in collaboration with General Electric (GE) Aircraft Engines, Cincinnati, OH. Two groups (seeded and unseeded) with two different test

volumes in the gauge sections, following the GE specifications, were prepared for fatigue testing at 650˚C. Stress-controlled fatigue tests were done to map the S-N curves. Analyses were performed to compare the fatigue lives and failure initiation sites, the causes of competing failure modes and how to control them, and characterizing fatigue life in René 88 DT.

CHAPTER 2

LITERATURE REVIEW

2.1 Competing Failure Modes

It is known that fatigue cracks are normally initiated at the surface of a material. This is often explained by several factors, e.g., weaker constraints for slip deformation at the surface compared to the interior; surface roughness resulting from local strain concentrations; and environmental effects assisting the growth of small cracks. However, a number of researchers [1-15] investigating the fatigue behavior of some commercial titanium alloys, high strength steels and nickel-base superalloys reported some unusual S-N fatigue behavior where cracks initiating at surface and subsurface locations compete to produce fatigue failure. The researchers have learned from these tests that there are two distinct stress-life curves or a step-wise S-N curve at stresses below the conventional fatigue limit. Subsurface crack initiation is dominant at low stress amplitudes and high numbers of cycles, whereas surface fatigue crack initiation occurs at high stress amplitudes and low cycles. Thus there is a definite stress range where the crack initiation site changes from the surface to the subsurface inclusion, giving a step-wise S-N curve or two distinct separate S-N curves. There is little information about this phenomenon and the mechanisms of competing failure modes. The main issues to be discussed in this review are the shape of the S–N curve and clarifying how the competing failure modes result in varied S-N curves that are quite different from traditional ones. As these

examples will indicate, different mechanisms of fatigue failure can be activated based on the stress level, loading conditions, material and testing environment.

2.1.1 Traditional S-N Curves

Fatigue is the progressive, localized, permanent structural change that occurs in materials subjected to fluctuating stresses and strains leading to crack nucleation and fracture after a sufficient number of fluctuations. The most common way to obtain fatigue test data is to test a number of different specimens at different stress levels and determining the cycles to failure. Fatigue test data exhibit wide scatter because of inherent microstructural inhomogeneity, microstructure differences in the surface and test conditions, and other factors including environment and temperature. In general, the scatter in fatigue life increases as the stress level decreases. The results of fatigue test data are plotted in the form of an S-N curve. The S-N curve is the graphical representation of stress amplitude (S) versus the number of stress cycles (N) to failure on a semilog scale. Schematic representations of the traditional notions/expectations of S-N curves for ferrous and nonferrous materials are shown in Figure 2.1. Some metallic materials have an apparent fatigue limit or endurance limit which represents a stress level below which the material does not fail and can be cycled indefinitely. Thus, if the applied stress level is below the endurance limit of the material, the structure is said to have an infinite life. This is characteristic of materials such as steel and titanium corresponding to the top curve in Figure 2.1.

Many nonferrous metals and alloys, such as aluminum, magnesium, and copper alloys, do not exhibit well-defined endurance limits. These materials instead display a

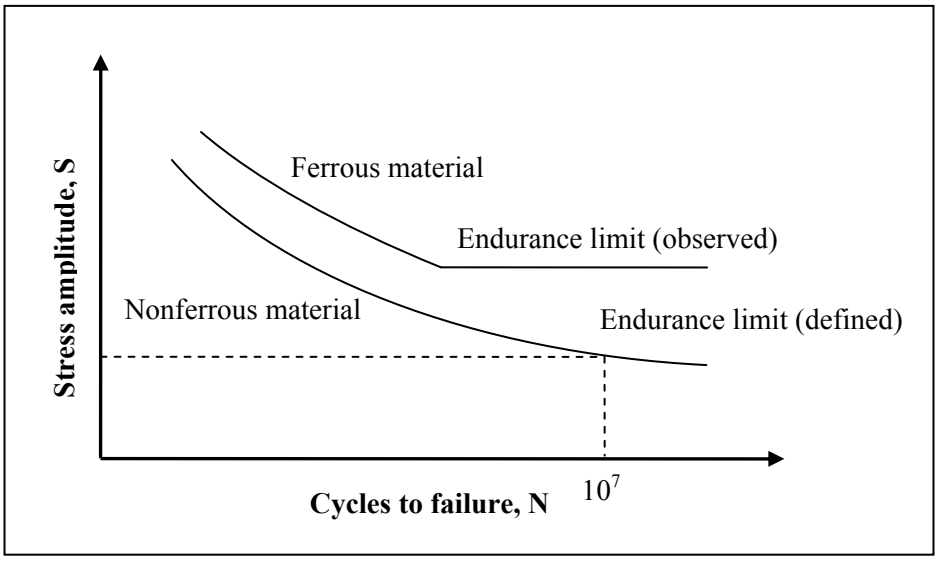

Figure 2.1 Schematic representations of traditional notions of S-N curves for ferrous and nonferrous materials.

continuously decreasing S-N response, similar to the lower curve in Figure 2.1. In such cases, the fatigue strength for a given number of cycles must be specified. An effective endurance limit (fatigue limit) for these materials is sometimes defined as the stress that causes failure at some large number of cycles, for example, at 10^7. However, other definitions are also sometimes reported, for example 10^6 or $5x10^6$ cycles.

2.1.2 Duality of S-N Curves

Some recent research [9] shows that S-N curve for many alloys are not smooth and continuous functions of stress range versus number of cycles to failure, but consist of two stages separated by a "discontinuous region." The discontinuous region runs as a horizontal line running parallel to the cycle axis. For stresses above this line, failures are almost always from cracks initiating from surface inclusions or persistent slip bands (PSBs) whereas for stresses below this line, failures are mostly from internally initiated

cracks. The failure lives of internal cracks can be one or more orders of magnitude larger than the failure lives of cracks initiating from surface regions.

Research on titanium alloys [2-4] and steels [5-7] have documented this behavior. Such a behavior was also observed in aluminum alloys four decades ago [8] but it seems that it has not been widely recognized. A common practice when reporting S-N data is to present the failure cycles of multiple specimens tested at a given stress range as averaged or extensively extrapolated data, leading to "artificially" smoothed S-N curves. Such a practice would smooth or dampen-out any small discontinuous region in the S-N curve and might make the two-stage S-N curve appear to show no discontinuity region.

In the recent past researchers in our group [9] showed that some materials containing "inclusions" or some peculiar microstructural elements acting as inclusions can trigger an interesting phenomenon that is not only perplexing to conventional wisdom but also is very relevant to applications where fatigue is critical. The phenomenon is the existence of two distinct separated S-N curves over a range of stress levels (Figure 2.2) in some engineering materials. This raises questions about the common notion that fatigue life is described by a unique S-N curve. This research showed that in the beta-titanium alloy Ti-10V-2Fe-3Al, having a "nominally-uniform" microstructure, two separate S-N curves, one for cracks initiating from surface regions and the other for cracks initiating in interior or subsurface locations exist. The data were obtained from a group of random samples where almost half failed by surface-initiated cracks and the other half failed by interior-initiated cracks with the fatigue lives of surface failures being more than an order of magnitude smaller than that of the interior-initiated failures. This phenomenon is an expanded version of the two-stage behavior where a discontinuity or step in the S-N

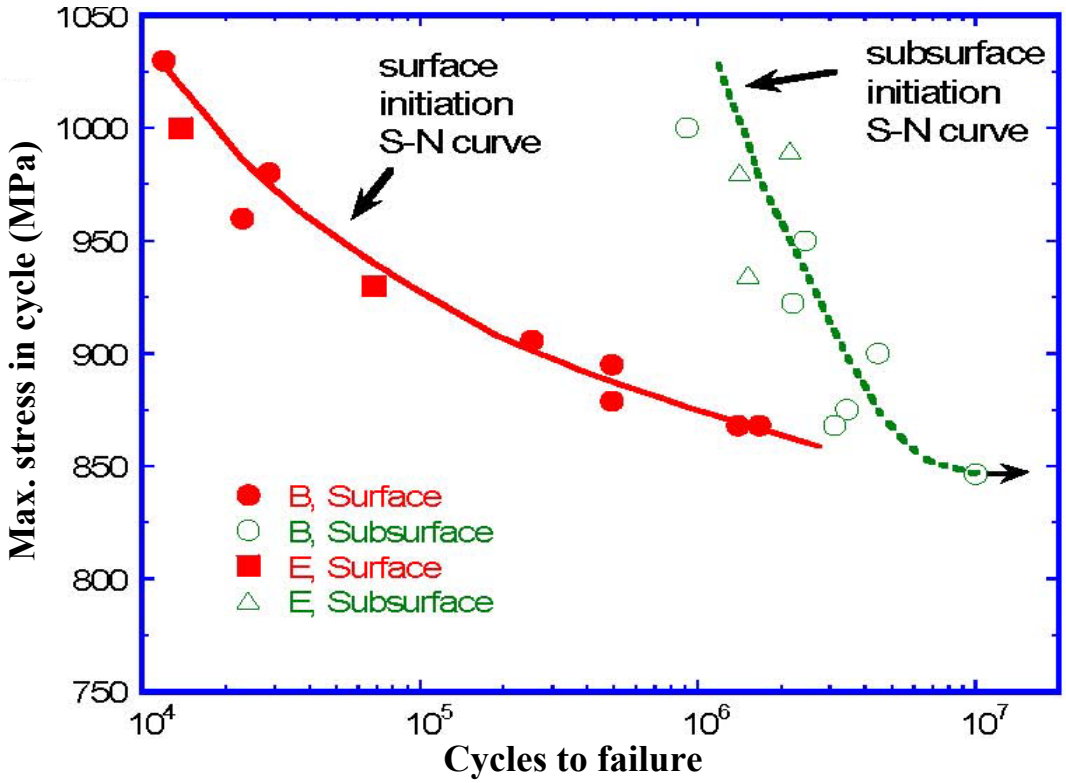

Figure 2.2 Duality of the S-N curve in Ti-10V-2Fe-3Al beta-titanium alloy. Adapted from Ref. [9]

curve is seen. It has also been shown that this behavior is caused by sparsely populated microstructural inclusions that are distributed following a Poisson inclusion pattern in the material [10].

Cashman [13] has observed a bimodal nature in the fatigue lifetime curves representing the low-cycle fatigue (LCF) of a nickel-base superalloy, René 95. The bimodal distribution of lifetimes was attributed to the distribution of surface and subsurface fatigue crack initiation sites, in which the initiation sites were mostly found to be nonmetallic particles. In that work, fatigue lifetime was determined only by the location of the fatigue crack initiation site with respect to the specimen surface with the

shorter lifetimes resulting from surface crack initiation (Figure 2.3). It was also established that the life differences observed between the surface and internal initiated failures were due to an environmental effect. Note that the ordinate in Figure 2.3 is identified as pseudostress amplitude. Pseudostress amplitude is defined as:

$$\sigma_p = \Delta\varepsilon_t E / 2 \tag{2.1}$$

where $\Delta\varepsilon_t$ is the total strain range and E is the modulus of elasticity.

The behavior shown in the two examples discussed above was termed as "duality," because a material can fail by two separate but competing mechanisms. This can result in two levels of fatigue life at a given stress range, which is recognized as

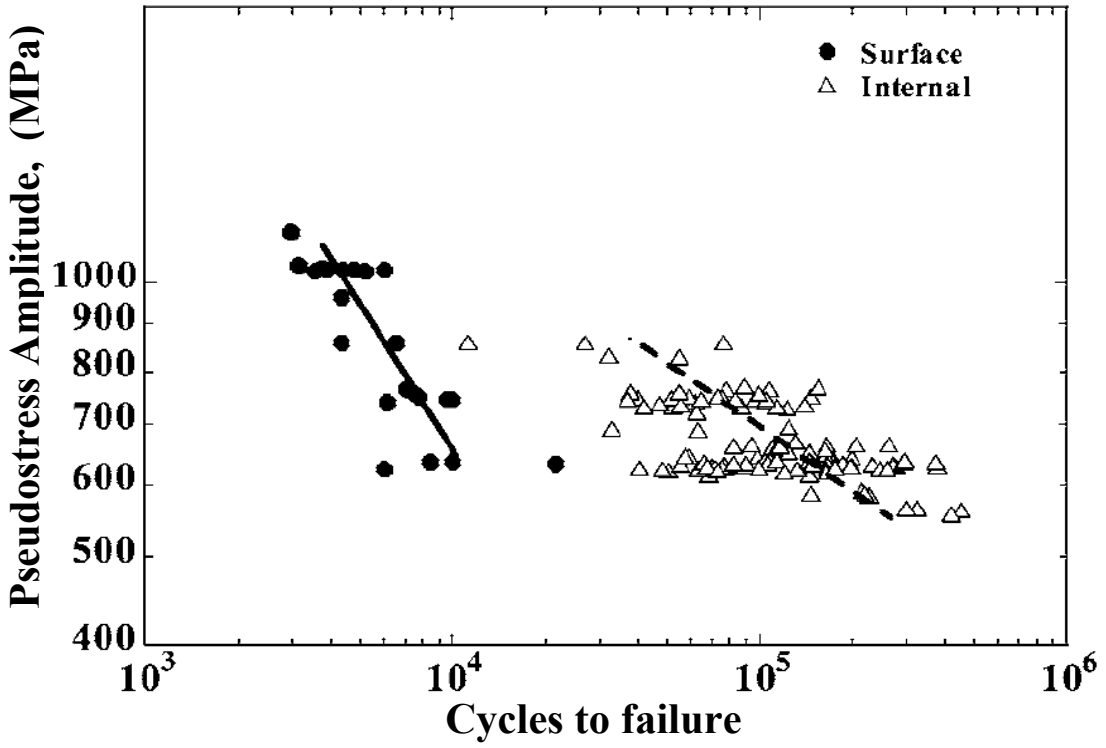

Figure 2.3 Duality of the S-N curve in strain controlled low-cycle fatigue data (R = 0.0) for René 95 powder metallurgy Ni-base superalloy at 538˚C. Adapted from Ref. [13]

something different from the traditional "variability" in fatigue life. Thus, duality is a special case of fatigue life-variability. It is possible that it can exist in any material, under conditions that make the two competing fatigue failure mechanisms possible. Such conditions may include some combination of microstructural features, specimen size, environment and/or loading mode.

2.1.3 Partial Duality in S-N Curves

Research in Japan [5-6, 11-12] has also revealed a partial manifestation of the duality phenomenon in high-C and high-Cr high strength steels tested in high cycle fatigue (Figure 2.4). In these studies, fatigue tests done in rotating bending and the high strength steels that typically had a quenched and tempered martensitic microstructure along with some nonmetallic inclusions of Al_2O_3/SiO_2 type. Shamblen and Chang [14] in USA as well as Pineau [15] in France, have observed the partial occurrence of duality in fatigue life in Ni-base superalloys, low-cycle fatigue tested at aircraft engine operating conditions. The superalloys, mostly made by powder metallurgical technique, contained a small number of Al_2O_3 inclusions that formed and were entrapped in the alloy due to powder atomization from the liquid metal and the subsequent handling/processing steps. At Wright Patterson Air Force Base, OH, USA, Jha et al. [16, 17] also found that similar effects are seen in γ-TiAl intermetallics and α+β titanium alloys (Figure 2.5) that do not contain inclusion, the origin of duality in these materials seems to be entirely microstructural.

In most of the studies discussed above, environment is likely to have played a significant role in distinguishing the two fatigue life distributions that are surface and internal. It is known that surface cracks, being exposed to ambient environment can lead

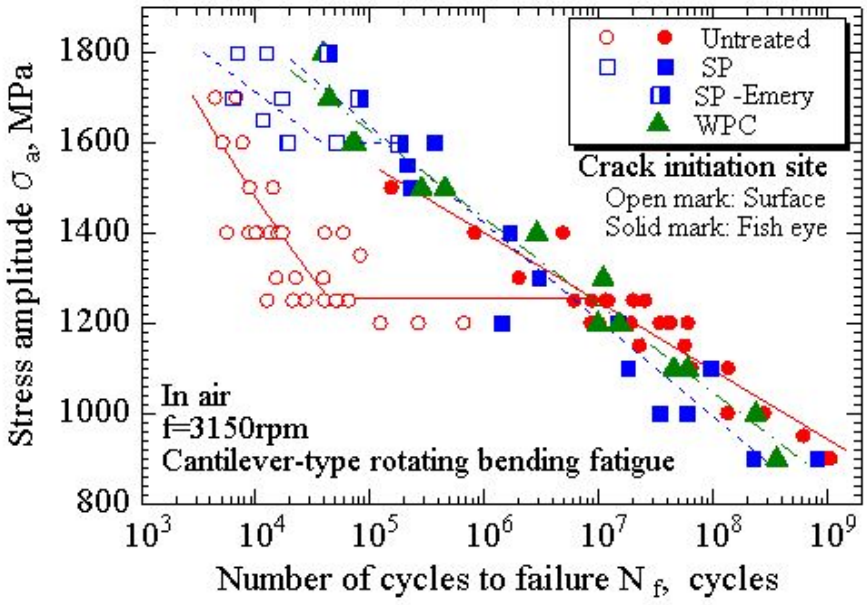

Figure 2.4 Duality of the S-N curve in a high-C and high-Cr steel. Adapted from Ref. [5]

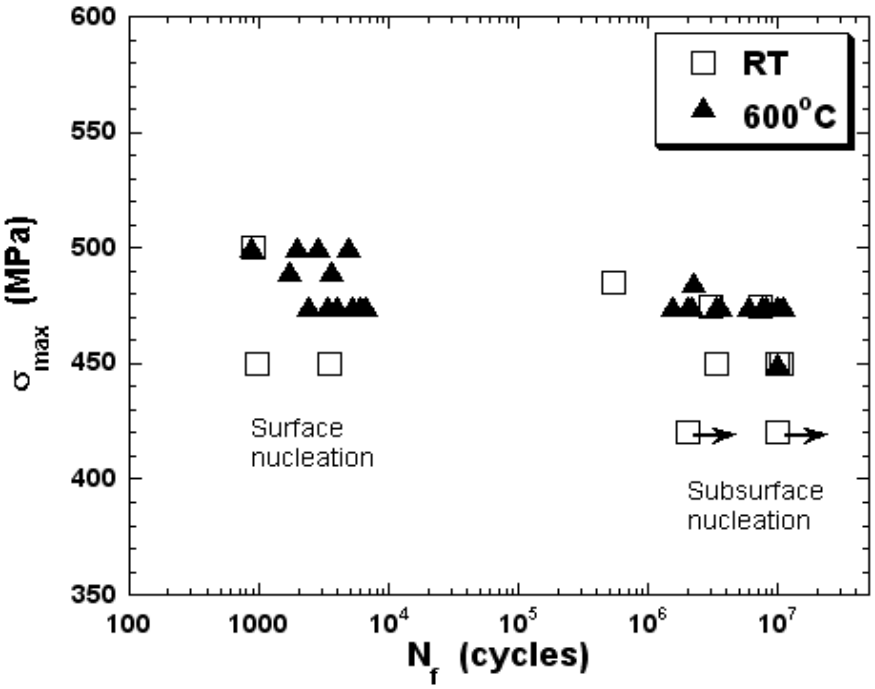

Figure 2.5 Duality of the S-N curve in stress-controlled room and high temperature tests of γ-TiAl intermetallic alloy. Adapted from Ref. [16]

to shorter fatigue life, as opposed to a relatively longer fatigue life for internal cracks growing in a quasi-vacuum. Tokaji et al. [18] varied the level of humidity in the environment and explored how the fatigue crack initiations occurred in rotating bending fatigue of JIS SNCM439 steel (equivalent to AISI 4340 steel). With the increased humidity starting from dry laboratory air to distilled water, the crack initiations in fatigue specimens increasingly shifted to surface locations. Fatigue crack initiations in tests with distilled water environment occurred entirely at surface locations, resulting in the shortest fatigue lives, relative to the interior crack initiations. Despite these observations, the precise mechanism that caused the switching of crack initiation between surface and interior locations was not clear. Additionally, the question of whether such competing crack initiations were exclusively limited to inclusions or PSBs or whether other microstructural or surface factors are also involved, is yet to be resolved.

The change in the nature of the competing fatigue failure mechanism can also be illustrated from the work of Tokaji et al. [19], performed on a beta-titanium alloy, Ti-22V-4V. This alloy is a high strength material, with the values of tensile properties reported as ultimate tensile strength = 1279 MPa, elongation = 1%, reduction of area = 13% and Vickers hardness = 380 Kg/mm2. In the standard solution treated and aged condition, the alloy exhibits an S-N curve with a step of about 600 MPa of cyclic stress amplitude, separating the short-life fatigue failures due to surface-initiated cracks from the long-life failures associated with subsurface/interior-initiated cracks (Figure 2.6a). Fatigue lives of the interior-initiated cracks are at least about 10 times higher than those of surface-initiated cracks. This situation dramatically changes when the surface is shot-peened before being age treated. The shot-peened surface resulted in a rapidly aged

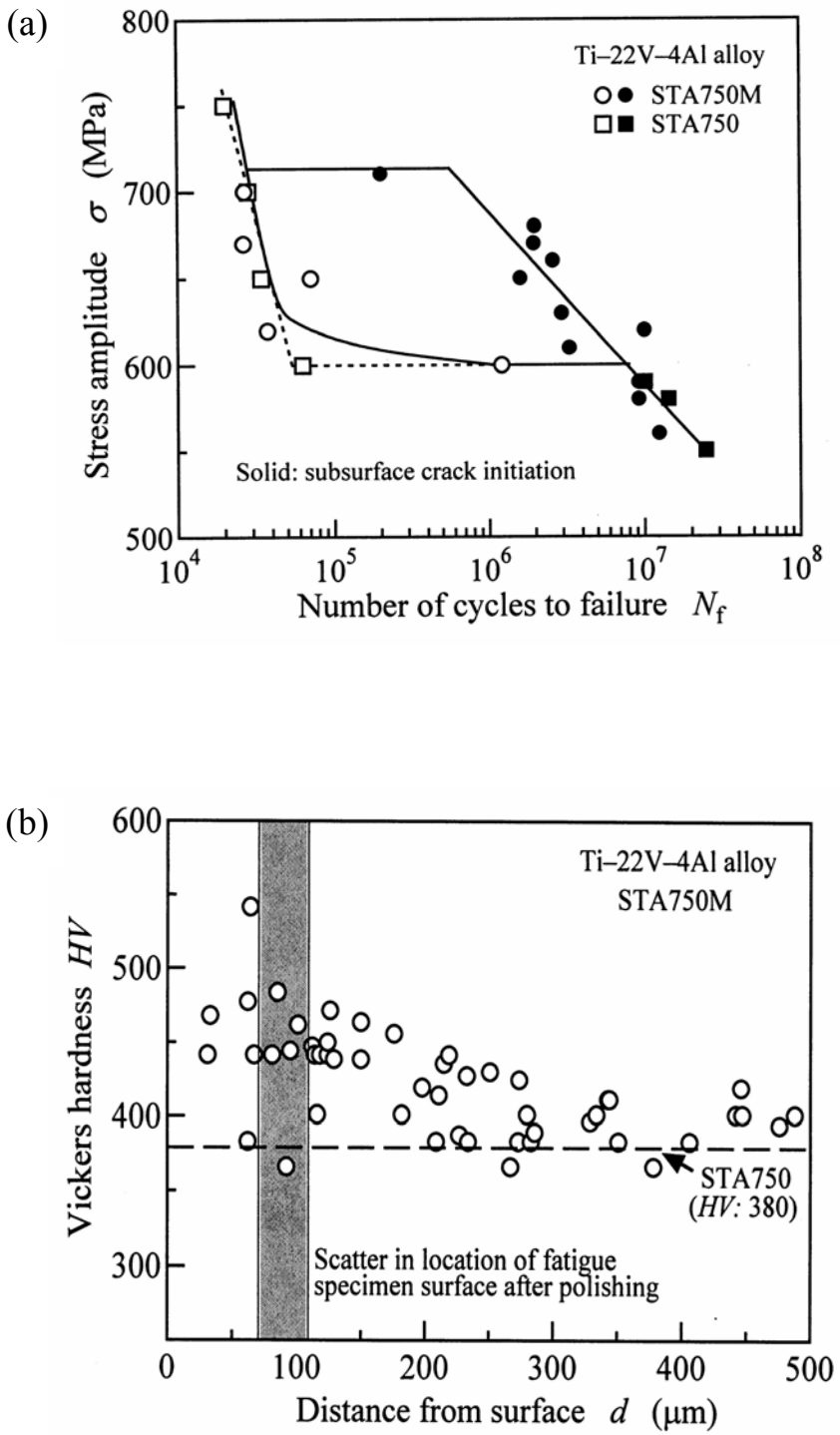

Figure 2.6 S-N curve and hardness profile for Ti-22V-4Al beta titanium alloy (a) Solution treated (750˚C/1hr) and aged (450˚C/8hr) condition (STA750) compared against the same material with the same heat treatment, but with an intermediate shot-peening process before aging (STA750M). (b) Hardness profile from surface to interior of the material in the as-heat-treated material (horizontal line) and in the material heat treated and shot-peened before aging. Adapted from Ref. [19]

surface relative to the unaffected interior region, producing a surface-hardened layer having a Vicker's hardness in excess of 100 Hv relative to the interior region. Figure 2.6b illustrates the hardness profile from the surface to the interior of the shot-peened and polished (to remove the roughness produced by shot-peened) specimen. The hardened layer shifted the fatigue failures to interior-initiated cracks.

Interestingly in the shot peened condition, there is about equal chance for failure from the surface-initiated and the interior-initiated cracks at stress amplitudes in the range of 600-720 MPa, suggesting the existence of duality of fatigue and competing failure mechanisms at a given stress level. This appears to have largely been caused by the increased resistance of surface layers for crack initiation after shot-peening treatment. Thus, when surface and interior conditions of materials are made to compete equally for failure, the "duality" phenomenon appears in the fatigue behavior, similar to the behavior shown in Figure 2.2.

2.1.4 Step or Discontinuity of S-N Curves

Recently, the presence of "step" or "discontinuity" in the S-N curves of various metals and alloys, when plotted in terms of stress amplitude versus number of cycles to failure, has been reported in several studies [20-23]. This interesting feature of the S-N curve is associated with a corresponding change in the fatigue crack initiation mechanism. At cyclic stress levels above the "step" or "discontinuity," fatigue failures mostly occurred from cracks that had initiated at the surface, whereas at lower stress levels, fatigue failures were almost always from internally initiated cracks. The "step" arises due to the fact that the environmentally-affected fatigue lives of surface-initiated cracks are shorter than the fatigue lives of internal cracks that grow in a quasi-vacuum

condition for almost their entire lives. It is not necessary, however, for the "step" or "discontinuity" to occur when crack initiation in fatigue switches from surface to interior. For example, Hyzak and Bernstein [24] noted S-N curves without "step," even though there was a critical stress above and below which surface and interior fatigue crack initiations were seen, respectively.

In the study by Jha and Chandran [21], the beta-titanium alloy, Ti-10V-2Fe3Al, microstructures with varied yield strength levels. Electro-polished fatigue samples, made of these microstructures, were tested in tension-tension fatigue at R=0.1 and at 35 Hz. The S-N curves (Figure 2.7) show presence of a two-stage S-N behavior with a transition

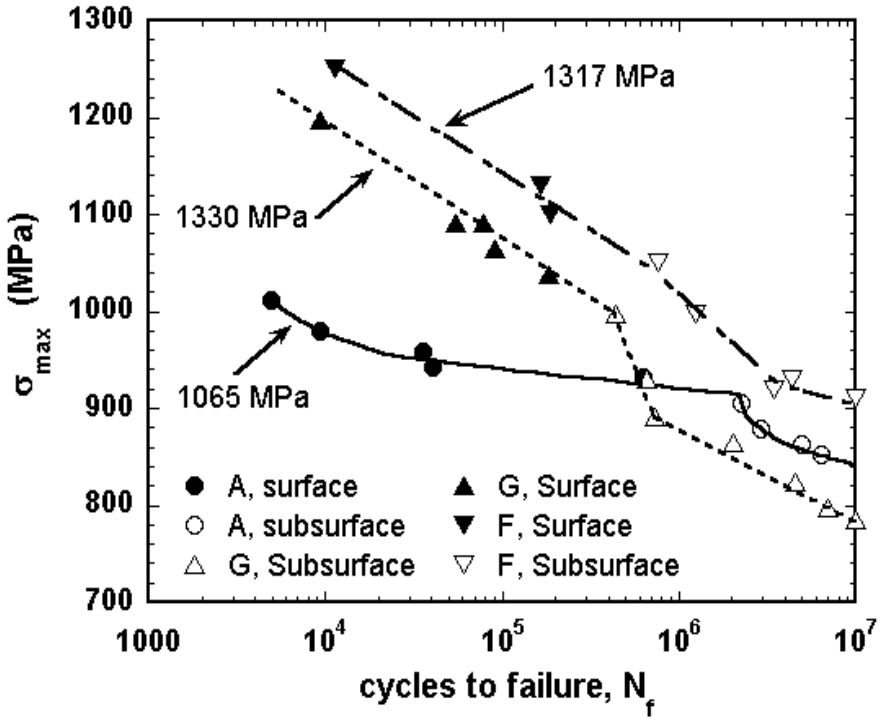

Figure 2.7 Illustration of the "step" or "discontinuity," marked by a change in the fatigue crack-initiation mechanism, in the S-N curves of heat treated Ti-10V-2Fe-3Al beta-titanium alloy. Adapted from Ref. [21]

cyclic stress level above and below which all specimens failed by surface nucleation and subsurface nucleation, respectively. The shape of the "step" seems to depend on the strength level in this material.

In fatigue studies of Finney [8], the 2024-T4 aluminum alloy showed a "step" in the S-N curve even when tested in a notched (Kt=1.5) condition in rotating bending at a frequency of 200 Hz in air environment (Figure 2.8a). It may be expected that a preexisting notch might "bias" failure initiation to the surface and that all failures, regardless of the stress level, would occur due to cracks starting from the notch. However, this was not the case. At stresses above the step (indicated by the arrow in the figure) failures occurred by cup-and-cone type failures, presumably from the notch root. However, the failures below the step originated from the interior of the samples, away from the tip of the notch root which was present all around the sample. The final fracture surface was mostly flat and normal to the applied stress direction and was connected with the notch root all around the specimen. The intensity of the "step" was relatively more pronounced at high test frequencies, but diminished at test frequency of 1.67 Hz, in the same material. This may be surprising because, if the change in failure mechanism is caused by environment-microstructure interaction, one would expect the "step" to be more pronounced at low test frequencies.

The "steps" in the S-N fatigue curve for different heat treated microstructures ofTi-22V-4Al alloy are illustrated in Figure 2.9, taken from the work of Tokaji et al. [25]. The legends STA750, STA800, STA850 and STA950 refer to solution treating above the beta transus (720ºC) at temperatures of 750, 800, 850 and 950ºC for 60 min., respectively, followed by aging treatment at 450ºC for 480 min. The respective beta grain

(a)

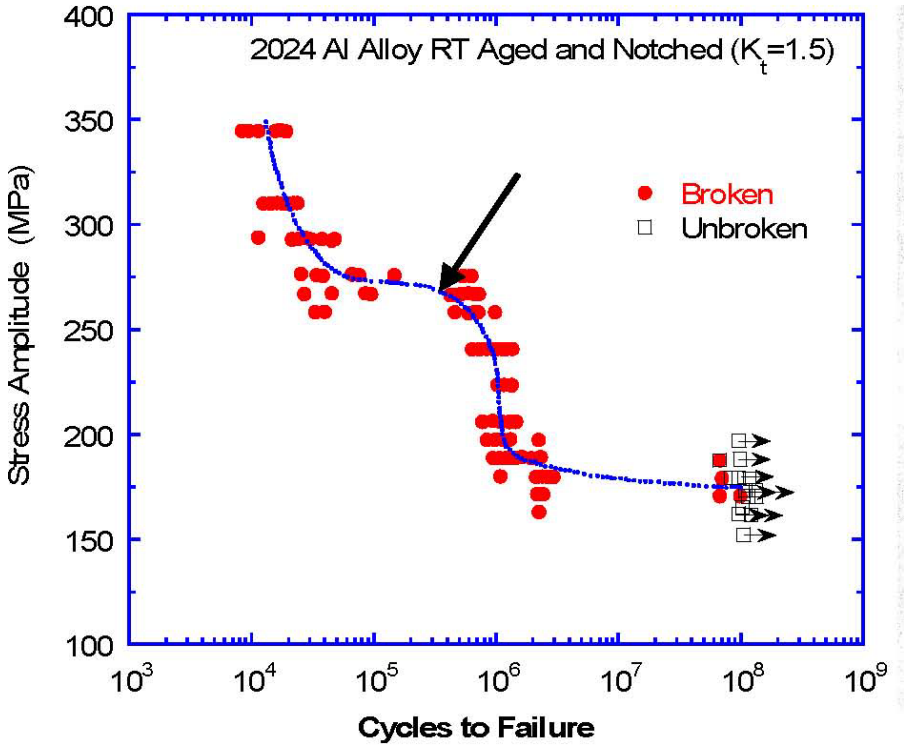

(b)

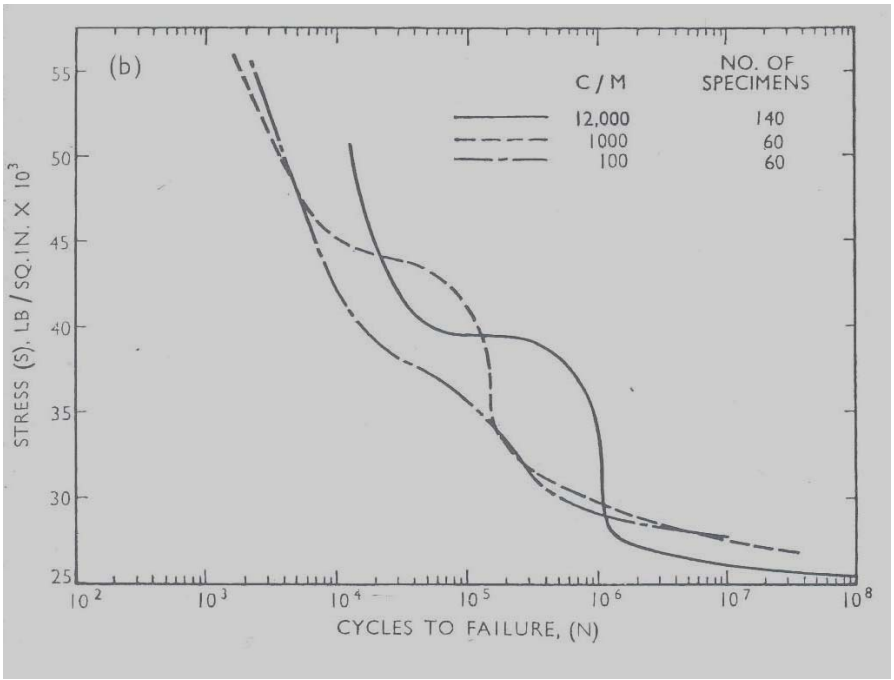

Figure 2.8 The S-N fatigue curve for 2024-T4 aluminum alloy (a) Tested in notched condition (Kt=1.5), showing a clear "step" in the curve (different failure mechanisms existed above and below the step marked by arrow) (b) The shape of the S-N curve changes with frequency. Adapted from Ref. [8]

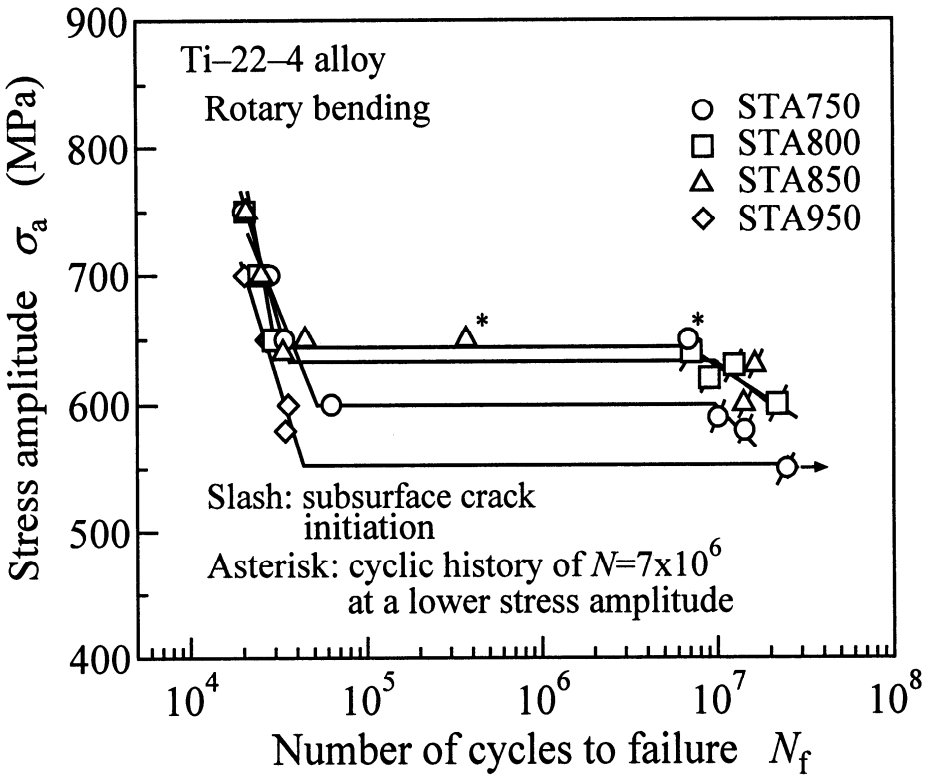

Figure 2.9 S–N diagrams for the Ti–22V–4Al alloy in the solution-treated and aged condition. Adapted from Ref. [25]

sizes were 31, 32, 58, and 165 μm. In Figure 2.9, the subsurface crack initiations are marked by slashes through the symbols. It can be seen there are about three orders of magnitude difference in fatigue lives between surface initiated cracks and the interior initiated crack, indicating a strong effect of environment on fatigue. It is clear that the "step' is observed regardless of the grain size or strength levels, suggesting that other microstructural characteristics may determine the switching of crack initiation from surface to interior locations, as the fatigue stress amplitude is lowered.

The change in crack initiation mechanism at low cyclic stresses and its effect on the shape of the S-N curve are illustrated in Figure 2.10 based on the data of Kobayashi

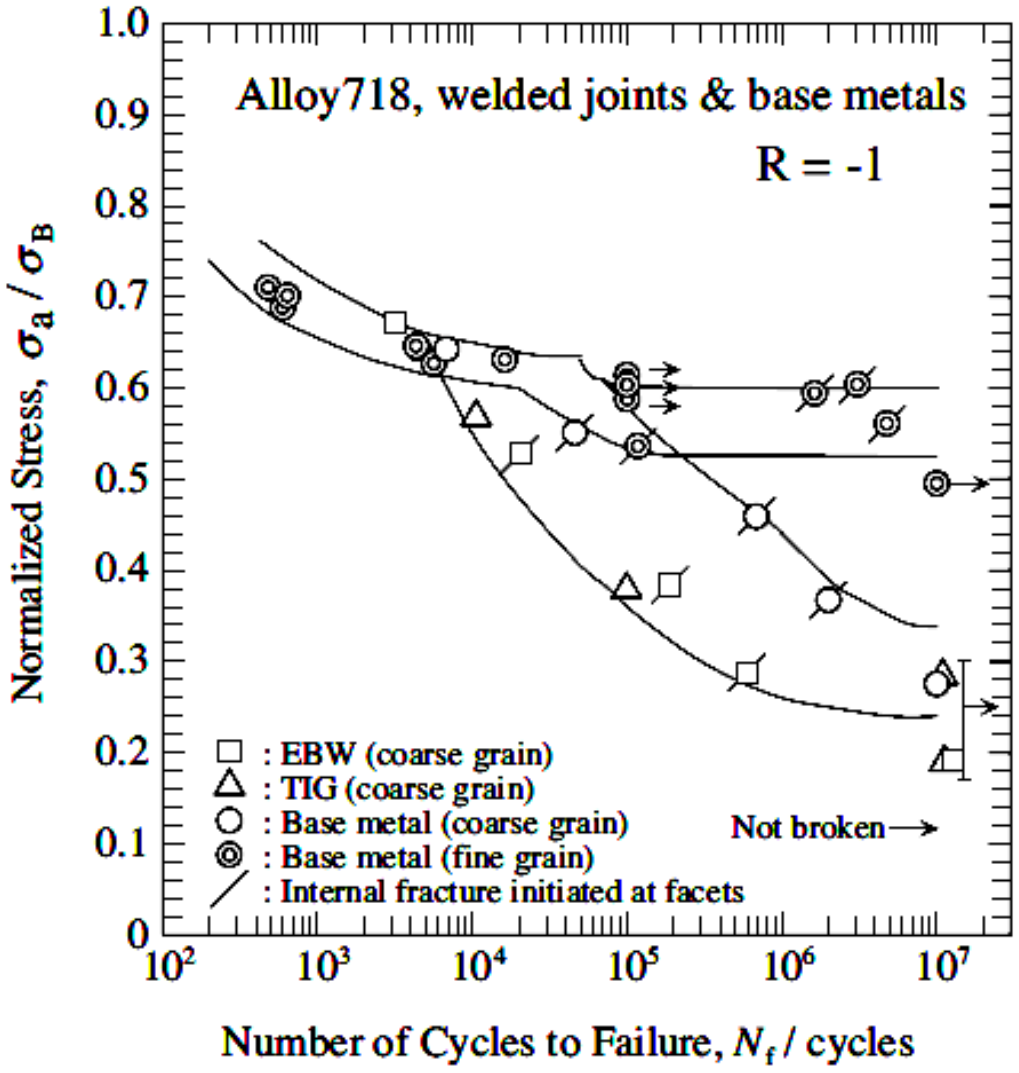

Figure 2.10 S-N fatigue curves for IN718 alloy with two grain sizes, before and after welding with different methods. Adapted from Ref. [26]

and Yamaguchi [26]. For both the coarse and fine grain sizes, the base metal showed surface crack initiations at high stress levels and internal crack initiation at low stress levels. The consequent "step" in the S-N curve is only vaguely evident for the coarse-grained material. The fine grained material did not show a clearly evident "step." The coarse-grained electron beam welded (EBW) material has lower fatigue resistance than the unwelded coarse-grain material, with most of the low-stress failures occurring from

internal crack initiations. However, the coarse-grained tungsten inert gas (TIG) welded material did not show any internal crack initiations at any stress level. These results suggest that both the grain size, inclusion distribution and the microstructural changes accompanying welding can have substantial effect on the shape of the S-N curves and the associated crack initiation mechanisms.

2.2 Fatigue Life Variability

The term "variability" is often used in fatigue to refer to the scatter in fatigue data. A variety of factors contribute to fatigue life variability. These include inherent material variability (i.e., variation in chemical composition, impurity levels, and discontinuities), variations in heat treatment and manufacturing (i.e., differences in notch radii and weld geometry), and variability from differences in testing conditions (i.e., environment and deviation from pure tension). In addition, there are sources of uncertainty arising from the load history. These variations and uncertainties can result in significant fatigue life variations in the specimen, component, or machine.

2.2.1 Scatter in S-N Fatigue Data

Scatter is common in the fatigue data of materials and structures. The fatigue lives of similar specimens under a given fatigue load can be significantly different. In one of the earliest studies, Shabalin [27] reported the S-N fatigue curve for D16T duralumin aluminum alloy (equivalent to 2024 aluminum alloy) that showed a very large variability of fatigue life, especially at low stress levels (Figure 2.11). The tests were done on 2.5 mm thick, 10 mm wide and 65 mm long (test section) sheet samples after stripping the aluminum clad layer. A constant minimum stress of 2 kg/mm^2 and varying maximum

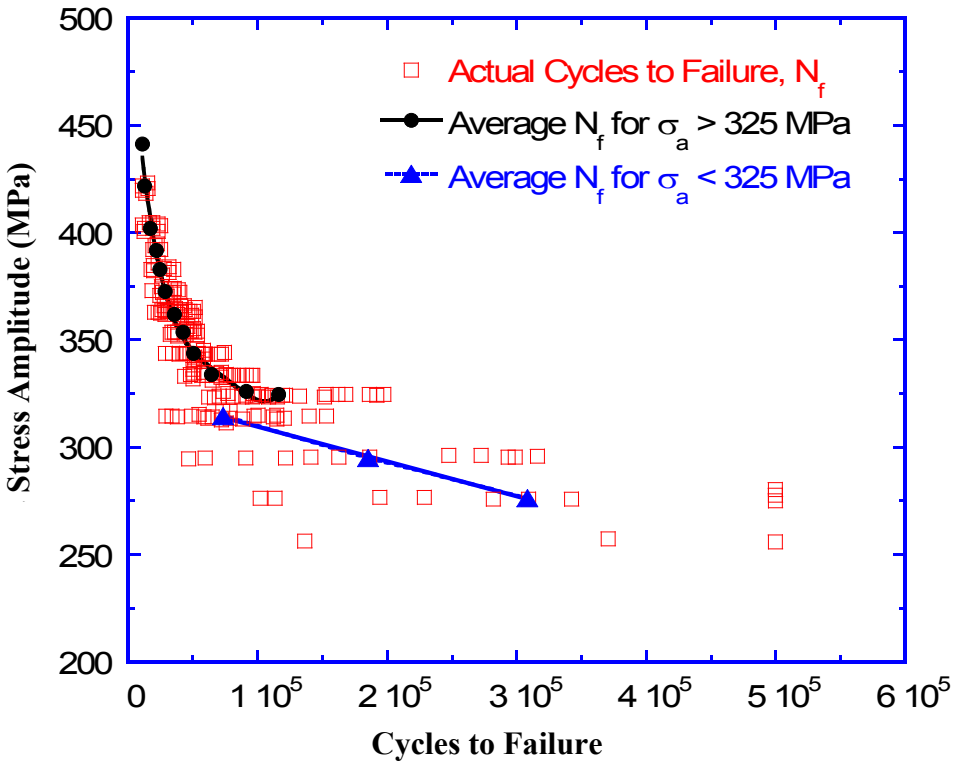

Figure 2.11 S-N fatigue curves for D16T duralumin aluminum alloy. Adapted from Ref. [27]

stress were employed in fatigue tests conducted in laboratory air environment. The data also showed the discontinuous nature of the S-N curve at about 33 Kg/mm^2. In Figure 2.11, the mean lives at each stress range are connected with a solid line. Two different mechanisms of cyclic deformation and fatigue crack initiation were suggested to be separated by the discontinuity. Laz and Hillberry [28] recently reported S-N fatigue data for 2024-T3 alloy, presented in Figure 2.12. The fatigue life variability between the data of Shabalin and that of Laz and Hillberry is difficult to compare, as there are no data at a large enough range of stress levels in the latter study, and the specimen/testing conditions were different between the two studies. Both these studies, however, make one aspect very clear—that the fatigue life variability increases at low stresses approaching the

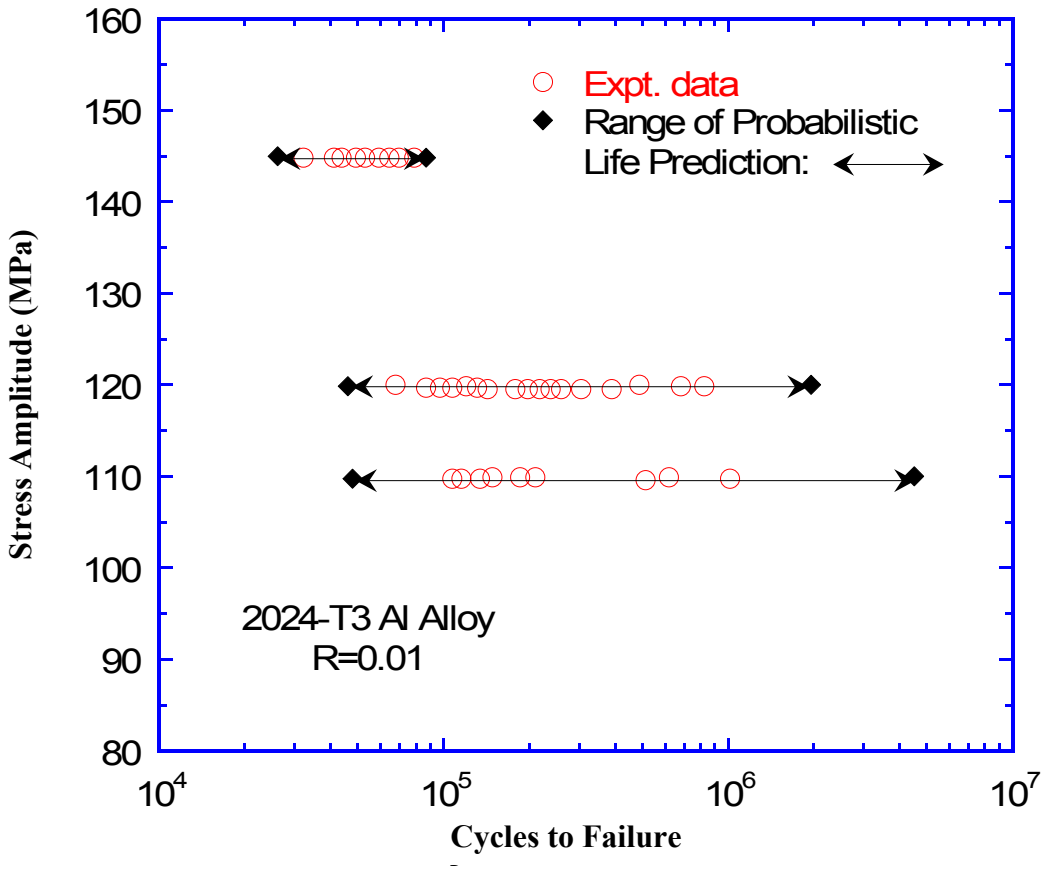

Figure 2.12 S-N fatigue curves for 2024-T3 aluminum alloy. Adapted from Ref. [28]

endurance limit and that it is an open question whether there is exists a unique endurance limit or not. This question may not be settled until a large number of tests are done that locate or rule out the existence of a unique endurance limit.

It appears that a large part of the variability in the fatigue lives of 2024-T3 aluminum alloy arises from Fe/Si-rich inclusions. The alloy contains several types of Fe/Si rich inclusions that are distributed as intermetallic constituent particles, varying in sizes from about 1 to 100 μm. Mareti [29] determined the distribution of crack-initiating Fe-rich particles on the actual fatigue fracture surfaces of 2024-T3 alloy fatigue tested at low and high humidity conditions. These data, when plotted along with the total particle

size distribution in the polished surface of the material (Figure 2.13), reveal that only large sized particles, of the order of 68 μm^2 or above are involved in fatigue crack initiation. Interestingly, the total fatigue life of the specimens did not show correlation with the size the inclusion, as shown in Figure 2.14. Higher humidity levels in the test environment led to shorter fatigue lives, but this was evident from the results of thin samples (1.6 mm)—thicker samples (4 mm) did not show any discernible difference in fatigue lives between low and high humidity test conditions. Another interesting result was that whereas fatigue cracks almost always initiated from large-sized inclusions in the bare 2024-T3, crack initiation occurred in multiple surface sites of the clad material in the case of cladded 2024-T3 alloy. Cladded 2024-T3 material was actually a used material, the fatigue specimens were made from a 1.6 mm thick sheet of 2024-T3 with both sides clad, and had been removed from a C-130 fuselage. Whether the change in crack initiation mechanism from inclusions to the clad material regions is due to the presence of cladding or due to the fact that this material is an "aged" material due to its prior use in C-130 aircraft, is to be explored further. It is possible that the difference in strength levels between the clad layer and the core 2024-T3 alloy caused the change in the nature of fatigue crack nucleation behavior.

The fact that the reporting of average fatigue lives, instead of actual individual fatigue lives, obscures a great deal of information associated with the nature of fatigue variability, can be best understood from Figure 2.15. Jha et al. [17] studied the fatigue life variability in room temperature fatigue tests of Ti–6Al–2Sn–4Zr–6Mo titanium alloy, using electro-polished specimens tested at R=0.05 in axial fatigue. When the results were plotted on the basis of mean fatigue lives of several specimens tested at each stress level,

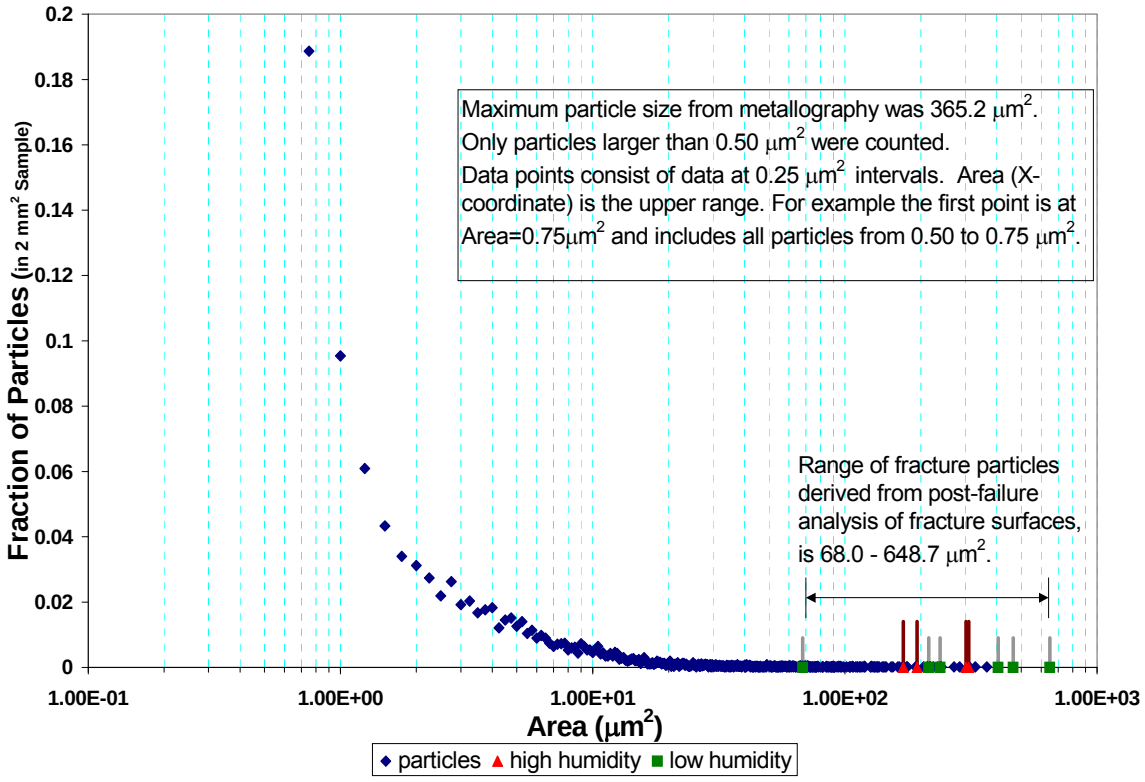

Figure 2.13 Distribution of particle sizes in 4 mm thick 2024-T3 aluminum alloy, as measured on the polished ST plane of the plate material. The longer vertical lines and smaller vertical lines along the X-axis highlight the nucleating particles at fracture origins, measured on the actual fracture surfaces, in the high and low humidity fatigue tests, respectively. Adapted from Ref. [29]

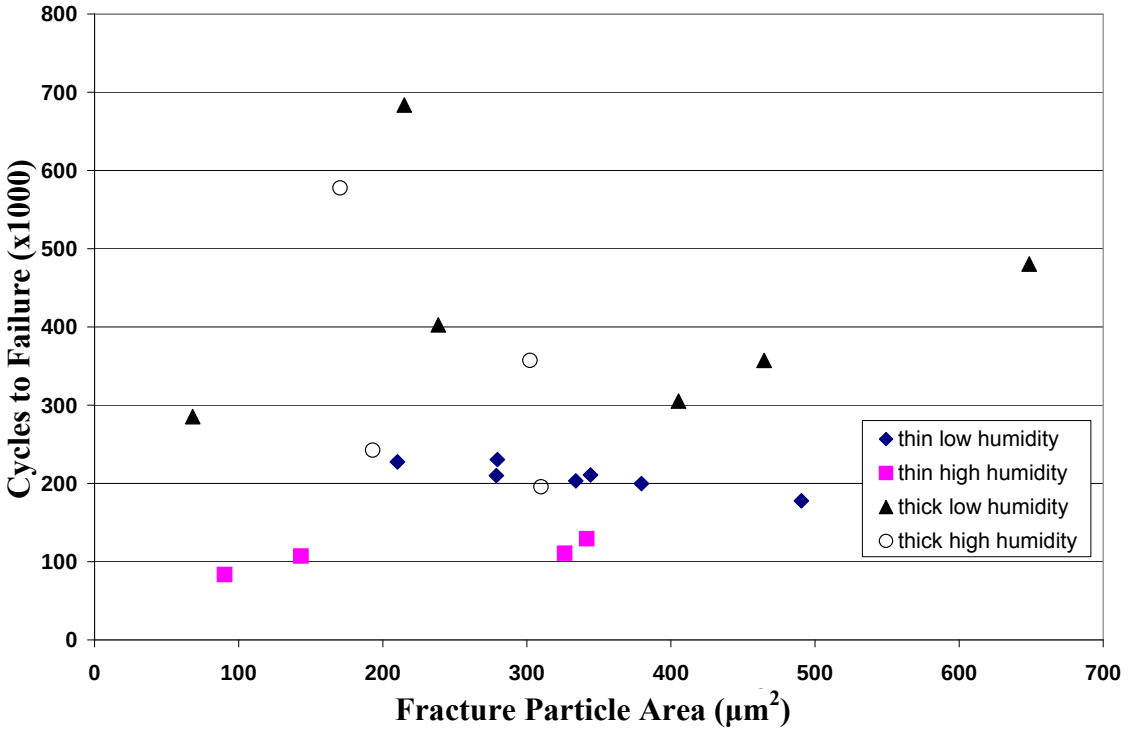

Figure 2.14 Fatigue life and the sizes of the crack-initiating particles in 2024-T3 alloy. Adapted from Ref. [29]

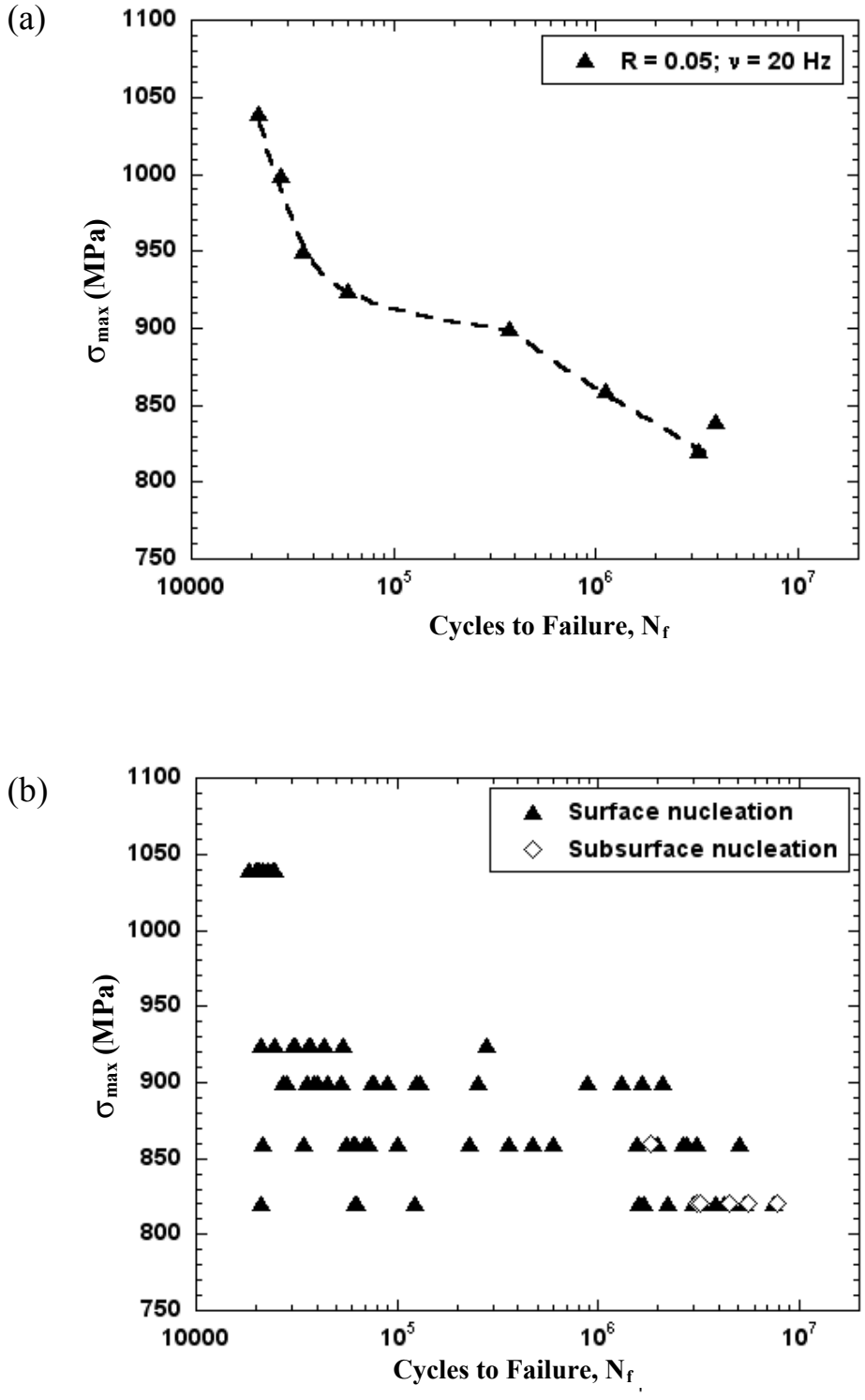

Figure 2.15 S-N curves for the titanium alloy, Ti–6Al–2Sn–4Zr–6Mo: (a) based on mean lives at each stress level and (b) showing actual fatigue lives of each sample tested. The samples were electrolytically polished prior to testing—the variability in lives seems to arise from the microstructure. Adapted from Ref. [17]

a nearly smooth S-N curve resulted (Figure 2.15a), whereas the fatigue curve exhibited a large variability in fatigue failure lives when the actual specimen lives were plotted (Figure 2.15b). Since all the samples have been consistently electro-polished, it seems that the variability arises almost entirely from the microstructural inhomogeneity. However, the titanium alloy investigated is a commercially made material having no inclusions. Therefore stress concentration issues associated with distributions of inclusions of varied sizes and shapes are not relevant here. There may be a spatial inhomogeneity of deformation characteristic in the microstructure, arising from a particular crystallographic slip process, which triggers this kind of variability in fatigue lives.

2.2.2 Fatigue Variability Due to Inclusions

In fatigue of materials containing defects such as pores and cavities or some unknown defects, statistical treatment of fatigue lives by parameterization has become a standard approach. Statistical analysis can be used to describe fatigue properties, as well as to estimate the probability associated with fatigue failure or product life. Such analysis allows us to evaluate component or product reliability quantitatively and to predict service performance for a given margin of safety. Statistical analysis can also be used for the design of experiments such that confounding of sources of variability is avoided and the number of specimen or component tests required for a given reliability and confidence level can be determined.

Aluminum alloy castings are employed in large numbers in many applications because they can be easily processed for manufacturing objects with complex shapes. The shrinkage of aluminum alloys during solidification and the release of dissolved

gases, such as hydrogen, lead to a certain amount of porosity. This porosity has a detrimental effect on the mechanical properties of the material. For instance, in the case of AS7G03 aluminum alloy, it has been shown by Odegard and Pedersen [30] that 1% volume fraction porosity can lead to a reduction of 50% of the fatigue life and 20% of the endurance limit compared with the same alloy with a similar microstructure but with no pores. Therefore, a significant amount of research has been performed on the fatigue crack initiation from pores or inclusions and the subsequent crack growth in cast aluminum alloys.

The nature of variability of fatigue life in cast Sr-modified A356-T6 aluminum alloy under two stress ratios (R= 0.l and -1) are illustrated in Figure 2.16. Figure 2.16 (a) shows the fatigue lives of the alloy with varying amounts of porosity and oxide films, tested at the stress ratio, R=0.1. Fig. 2.16b shows the data obtained for the stress ratio of R=-1. Figure 2.17 illustrates the morphologies of the crack initiation sites in specimens where the fatigue cracks apparently nucleated from pores and oxide films. Fatigue failure from pores results in large, often clearly recognizable, outlines of pores at the crack initiation site (Figure 2.17a) where as failure from oxide films leads to only a scanty evidence of the initiation site on the fracture surface (Figure 2.17b), which can, however, be located with some difficulty.

2.2.3 Statistical Analysis of Two Mode Fatigue Failures

Weibull's early study [32] on the statistical aspects of fatigue has established the fact that fatigue data are inherently stochastic and the degree of variability is influenced by the material test volume, surface condition and the presence of inclusions. The manifestation of variability in fatigue lives due to inclusions of various sizes and shapes

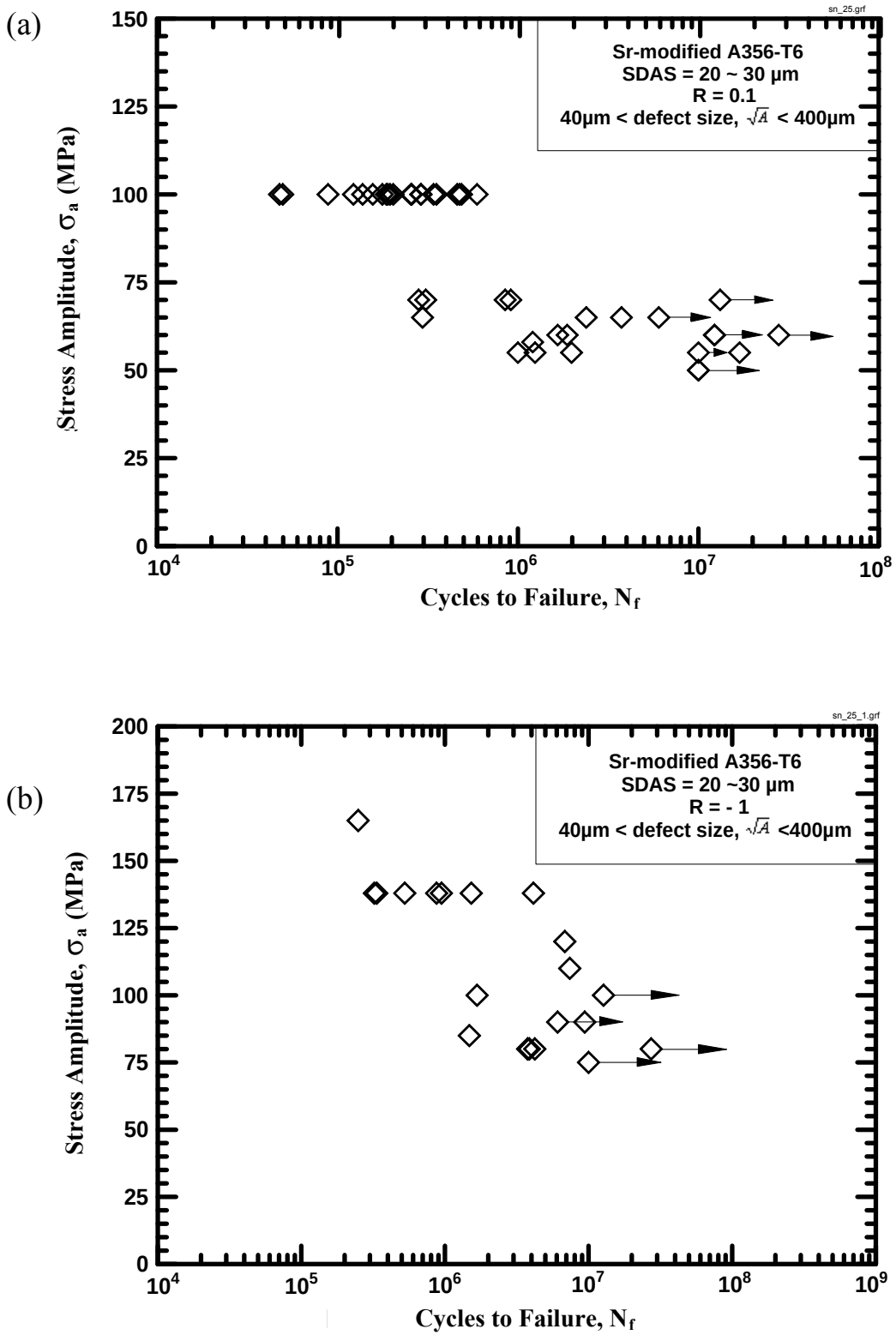

Figure 2.16 S-N fatigue data of Sr-modified A356-T6 alloy with various inclusion sizes (a) Tested at stress ratios R = 0.1 (b) Tested at stress ratios R = -1. Adapted from Ref. [31]

(a)

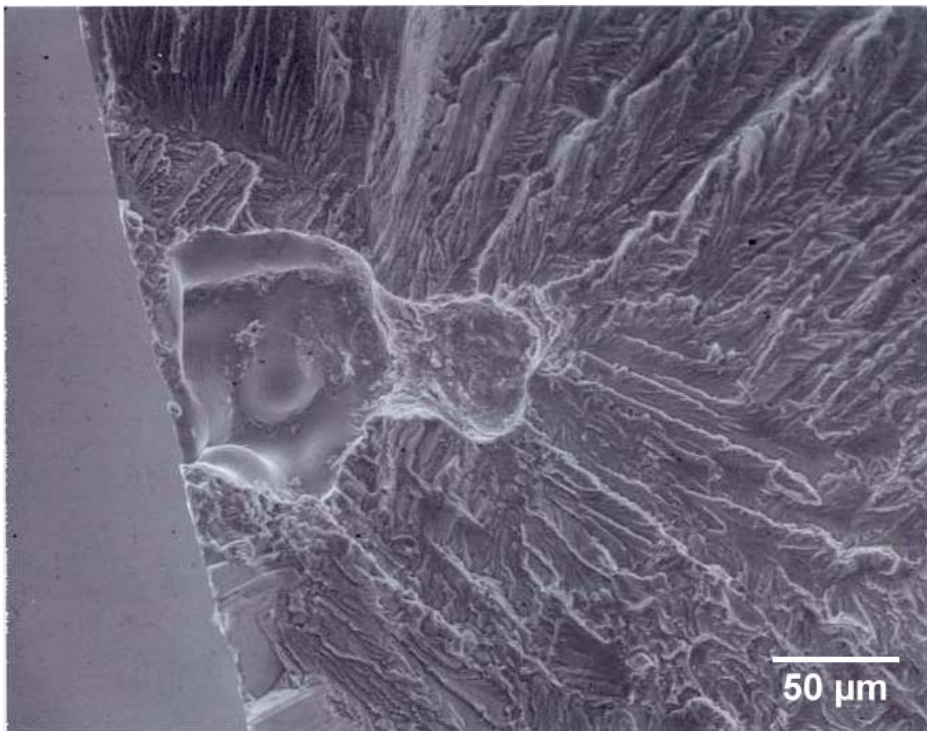

(b)

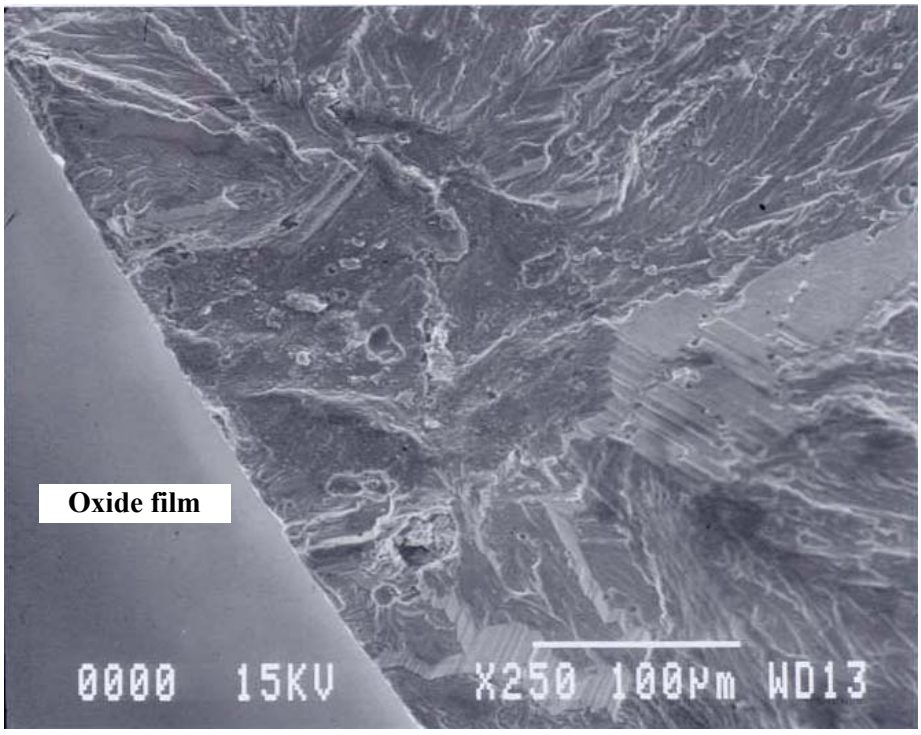

Figure 2.17 SEM images showing different inclusions originating fatigue cracks in the Sr-modified A356-T6 aluminum alloy castings: (a) pores; (b) oxide films. Adapted from Ref. [31]

leading to scatter in the S-N data is now well known [33-35]. One would expect that the largest-sized inclusions would control fatigue failures, which has not always been entirely supported by experimental findings. For example, fatigue life distributions due to pores in castings were investigated and it was found that only large pores close to surface were responsible for crack initiation. It is not clear why interior pores did not initiate cracks, because the largest pore, in a given distribution of pore sizes, is more likely to occur at interior regions than at surface. Ting et al. [36] found that the distribution functions of crack-initiating pores, determined by fractography, were different from the size-distribution of actual pores present in the material. Laz and Hillberry [28] found that fatigue crack initiation occurred in the large inclusions from the overall inclusion-size distribution. Fatigue life variability could only be linked to crack-initiating particle sizes, and not to the entire distribution. Additional fatigue life variability can arise if test conditions (aggravating temperature or corrosive environment) and specimen size change even in laboratory testing.

Characterization of fatigue life variability, in terms of Weibull approach [37], serves as a very useful parameterization procedure. It provides a mathematical description of the variability in terms of Weibull parameters. Very little, however, is known about what microstructural aspects govern such variability and what should be done to control them in material manufacturing and design. However, by characterizing variability on the basis of tests with known inclusion types and sizes often can help to calibrate the variability. This can serve as a reference for cases where the variability is complex, arising from multiple inclusion types and sizes.

It is quite remarkable that the competing failure modes actually existed even in fatigue tests conducted about 40 years ago, but remained hidden inside laboratory reports.

Cicci [38] conducted a large number of (R. R. Moore type) rotating bending tests to explore the scatter in fatigue life during the fatigue of 18NiCoMo maraging steel. The material was produced by then Bethlehem Steel Corporation in USA by air melting and vacuum stream degassing during pouring. The material had a martensitic structure produced by air cooling after solution treatment. Microstructure contained some small inclusions distributed throughout the volume, but the details of the distribution were not reported. Tensile and fatigue specimens, oriented in the transverse direction of the plate were machined and then aged for 3 hrs at 900^{o}C. The tensile properties were determined as 197 GPa elastic modulus, 1814 MPa yield strength, 1893 MPa ultimate tensile strength, 7.9% elongation, 37% reduction in area. The Rockwell hardness was 51.2. Fatigue tests were conducted on rotating bending specimens that had a test section of length 12.5 mm with a uniform minimum diameter of 6.1 mm. At each stress level, 48 samples machined from random locations of 10 plates, obtained from different heat treatment batches, were tested.

Figure 2.18 illustrates the distributions of fatigue lives for the 18NiCoMo maraging steel for stress amplitude levels in the range of 703-824 MPa. Although fatigue lives at each stress amplitude spanned over two orders of magnitude, an examination of the raw test data revealed that there were two points in fatigue lives where data were crowded. This suggested that what may appear as random scatter in fatigue life might actually consist of two overlapping life distributions, one being the short term life and the other being the long term life. In order to separate the two regimes, all the fatigue lives at a given stress amplitude were characterized in terms of the three-parameter Weibull distribution.

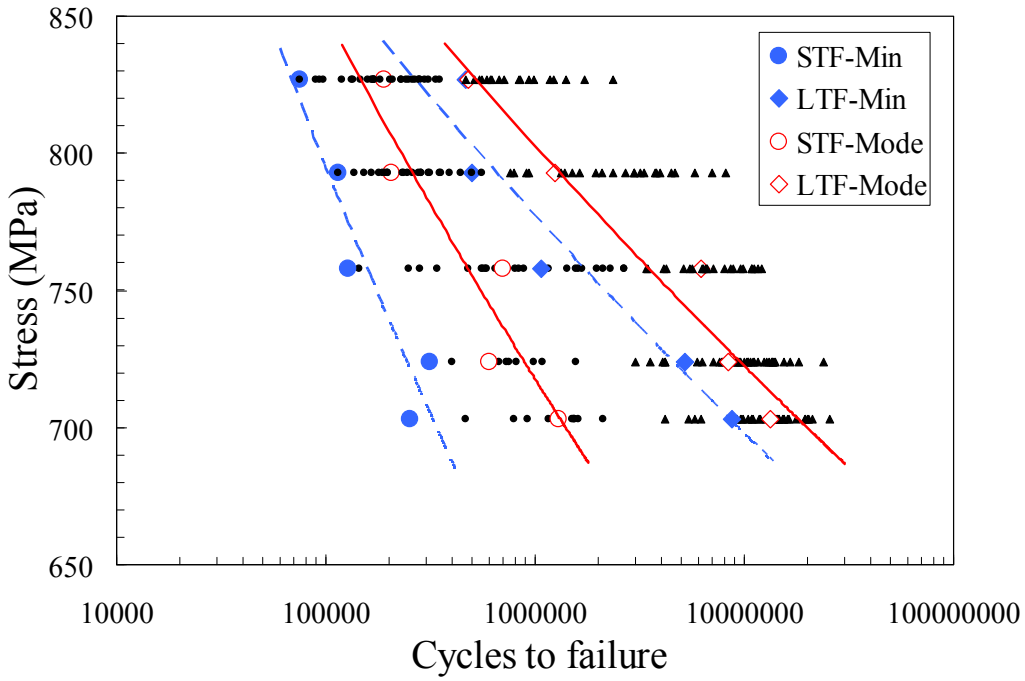

Figure 2.18 Distributions of fatigue live in 18NiCoMo maraging steel in rotating bending. At each stress level, the distribution can actually be split into two separate distributions, based in short term failure life (STF) and long term failure life (LTF). The minimum and modal lives for the STF and LTF distributions were obtained from three-parameter Weibull characterizations of the two distributions as discussed in the text.

$$F(N) = 1 - e^{-\left(\frac{N - N_{\min}}{N_{\max} - N_{\min}}\right)^{\beta}} \tag{2.2}$$

where *F(N)* is the probability of failure at N cycles and Nmin, Nmax and β are the tree parameters that characterized the Weibull distribution. Nmin, Nmax are the minimum and maximum lives, respectively, and β is a constant. The values of the three parameters can be obtained by finding the best fit to the fatigue life distribution.

Figure 2.19a and 2.19b illustrate the three parameter Weibull characterizations for fatigue life data at the stress amplitudes of 703 and 824 MPa, respectively. Even though

both the life distributions are within 95% confidence limits when characterized as single distributions, the presence of a “gap” or “discontinuity” in distribution (as marked by vertical dashed lines in Figure 2.19a and 2.19b) can be clearly noticed. It is plausible to take this “gap” as evidence for the presence of actually two separate distributions based on two different fatigue failure mechanisms. However, this may be ascertained by splitting data across the gap and plotting two separate three-parameter Weibull distributions, one for the data on the left side, and the other for the data on the right side of the gap. These distributions are called here the short term failure life (STF) and long term failure life (LTF) distributions, respectively. Figure 2.20a and 2.20b illustrate the two separate distributions, for the cyclic stress amplitudes of 703 and 824 MPa, respectively.

The increase in the quality of fitting in the two separate distributions, over the single distributions in Figure 2.19a and 2.19b is evident. Using the parameters of fit, namely, Nmin, Nmax and β for each of the distributions, the corresponding frequency distribution of failures were obtained and plotted in Figure 2.21 and 2.22, respectively, along with the experimental density distributions of fatigue life data. The “grouping” of multiple fatigue failures at some modal values for STF and LTF distributions is clearly evident. This indeed may suggest that there are actually two separate fatigue failure mechanisms corresponding to STF and LTF producing different distributions of fatigue lives. While the STF and LTF are clearly separated at 703 MPa, the separation is not very distinct for the high stress amplitude (824MPa). Nevertheless, there is some indication of the presence of two failure distributions in Figure 2.22. When the two failure mechanisms are not separated, they can indeed appear as a single distribution as well, as shown by the

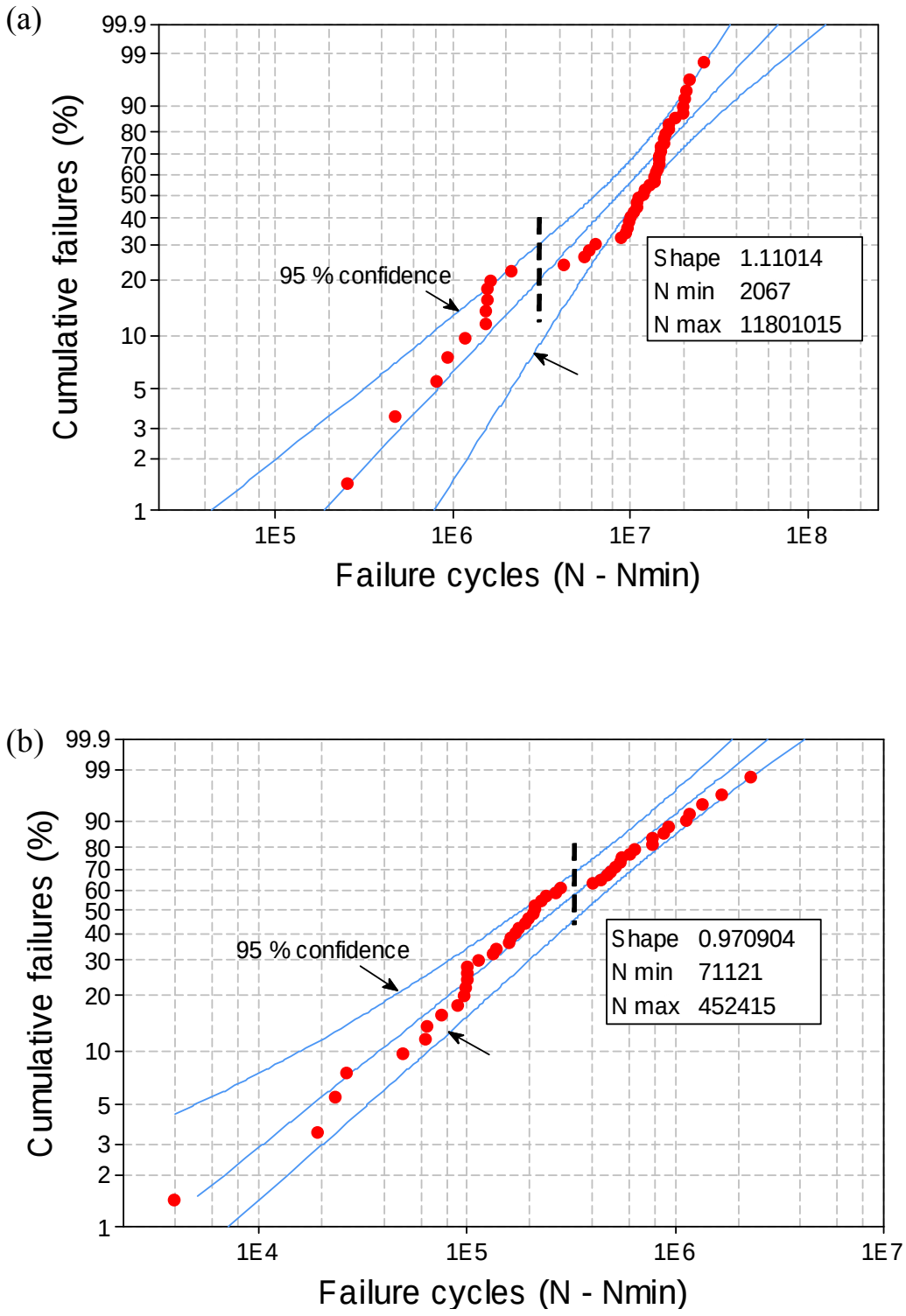

Figure 2.19 Characterization of fatigue life variability on the basis of three-parameter Weibull distribution (a) at the stress amplitude of 703 MPa (b) at the stress amplitude of 824 MPa

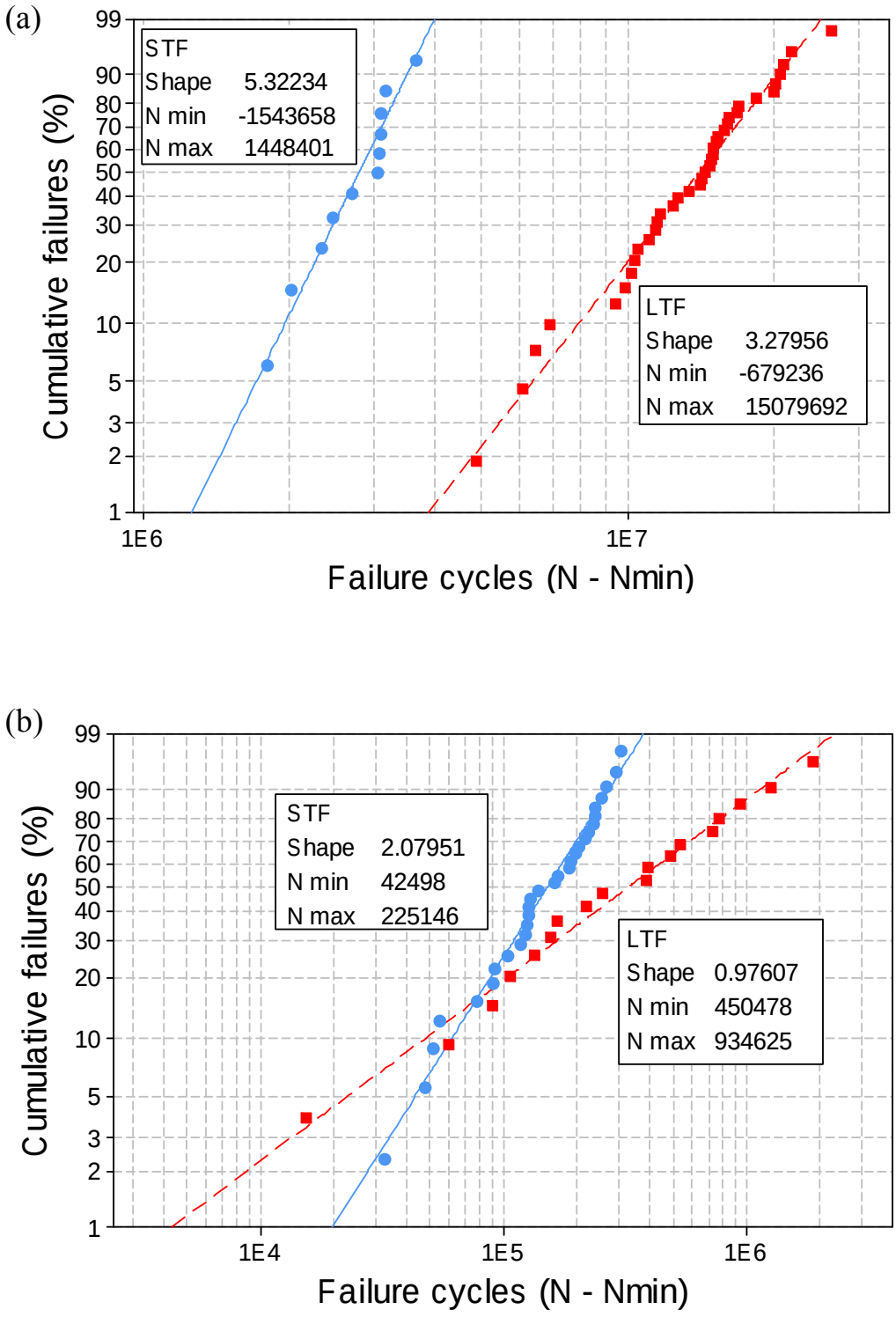

Figure 2.20 Characterization of fatigue life variability separation into two distributions on the basis of three-parameter Weibull distribution (a) at the stress amplitude of 703 MPa (b) at the stress amplitude of 824 MPa

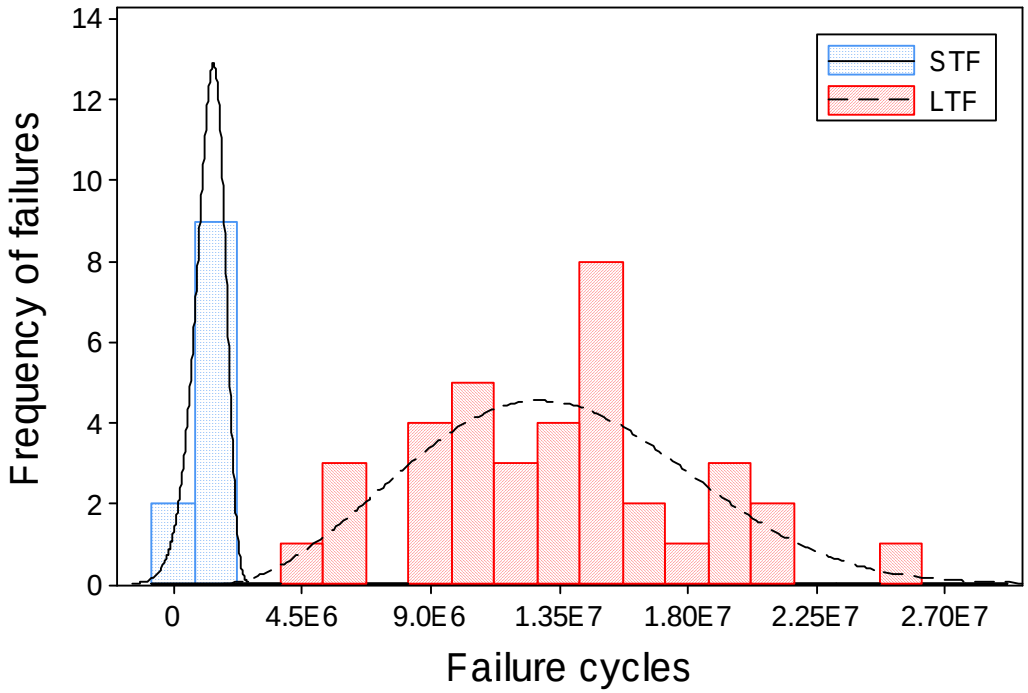

Figure 2.21 Characterization of fatigue life variability at the stress amplitude of 703 MPa on the basis of frequency distribution of failures based on two separate distributions

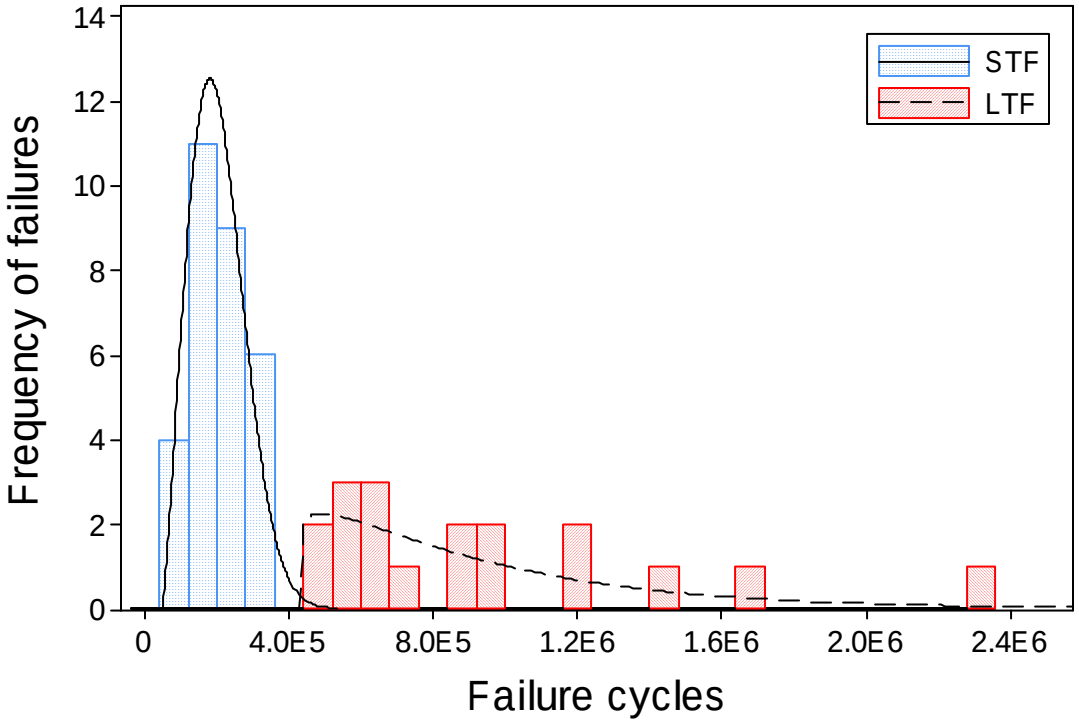

Figure 2.22 Characterization of fatigue life variability at the stress amplitude of 824 MPa on the basis of frequency distribution of failures based on two separate distributions.

data in Figure 2.19a and 2.19b. The two separate distributions existed possibly because of the presence of two different crack initiation mechanisms in the material. Sometimes examination of crack initiation sites of each fatigue sample after failure may be required in order to fully corroborate the two modes of failures.

The minimum and modal lives for the STF and LTF distributions are plotted as lines in Figure 2.18. The line can be considered as the two separate S-N curves, one for the STF and LTF, based on the respective failure mechanisms. Thus, the dual fatigue failure mechanisms, each with its own distribution of fatigue lives, appear to have existed in the 18NiCoMo maraging steel.

2.3 Microstructure of Superalloys

Superalloys are materials with superior mechanical strength and creep resistance at high temperatures, good surface stability, corrosion and oxidation resistance. Nickel-base superalloys structure consists of a face-centered cubic (FCC), austenitic solid-solution matrix with a precipitated nickel-aluminum-titanium compound (γ') as the principal strengthening phase. Various carbides, depending on the alloy composition and heat treatment, exist as second precipitated phases. These alloys are used in the most demanding applications relative to stress and temperature in gas turbine engines.

Figure 2.23 provides a perspective for the alloy and process development. The history of Ni-base superalloys began in 1940s with the development of Nimonic alloys, a fairly simple Ni-Cr materials that contained small amounts of Ti and Al which formed the Ni_3(Ti,Al) precipitates, known as γ'. Since then, a wide range of other alloying elements have been added to alloy compositions in order to enhance creep and oxidation properties. Modern superalloy compositions contain 8 or more elements, creating a very complex system to describe thermodynamically [39].

The microstructure of nickel-base superalloys basically consists of an austenite FCC matrix, the γ phase; an ordered L12 precipitate, γ'; and various carbides ($M_{23}C_6$, MC, and M_6C, where M represents a metal atom) and borides distributed throughout. Chemical additions such as aluminum and titanium promote the creation of the gamma prime phase. The FCC gamma prime phase Ni_3(Al,Ti) present in nickel-base superalloys presents a barrier to dislocations hence slowing their speed, this significantly contributes to creep resistance. The gamma prime phase size can be finally controlled by annealing. Typical nickel-base superalloy microstructures are shown in Fig. 2.24.

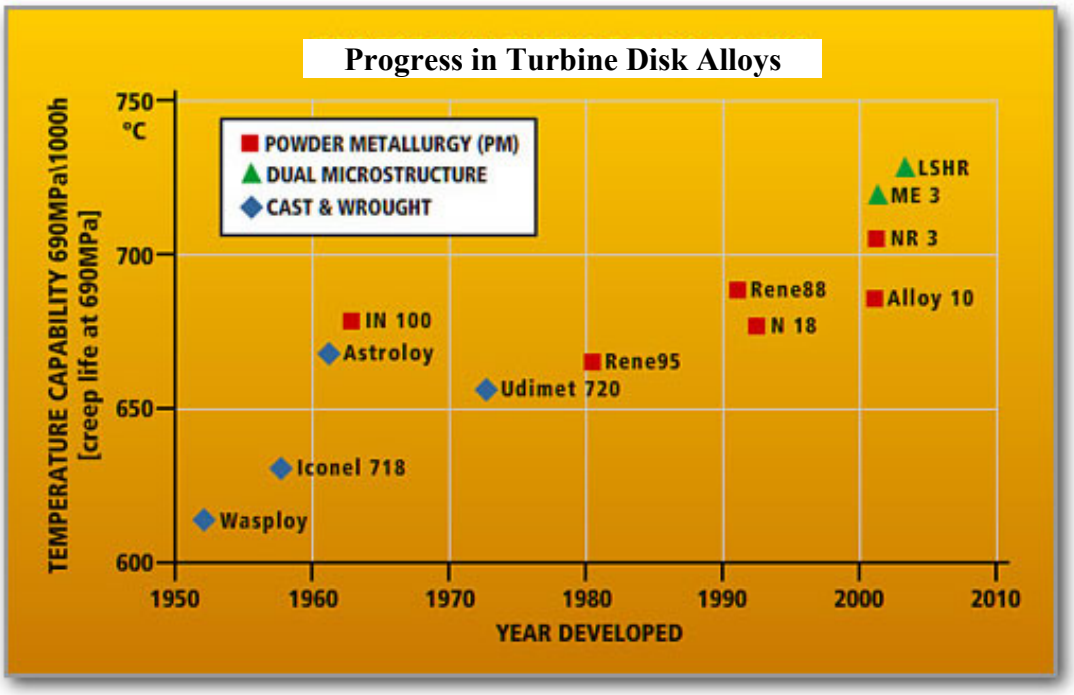

Figure 2.23 Evolution of the temperature capability of superalloys with approximate year of introduction. Adapted from Ref. [39]

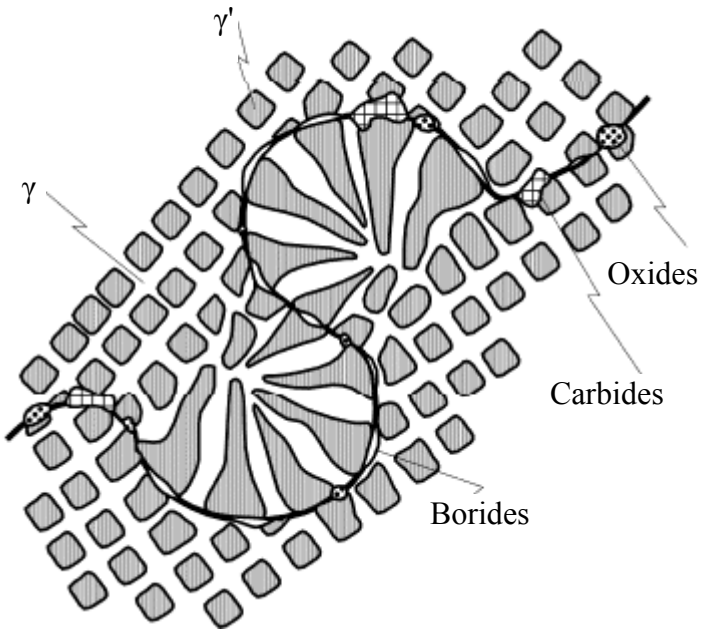

Figure 2.24 Microstructure of nickel-base superalloys. Adapted from Ref. [40]

Many of the industrial nickel-base superalloys contain alloying elements, including chromium, aluminum, and titanium, also molybdenum, tungsten, niobium, zirconium, boron and cobalt. The addition of chromium is done primarily to protect the alloy from oxidation and other forms of corrosion. Optimum corrosion properties are expected with the addition of 15-30 wt. % chromium, which also forms chromium carbides when carbon is present, leading to precipitation hardening. Unfortunately, the Cr_2O_3 layer is only effective around 900°C [41].

Another major element used to environmentally protect nickel-based superalloys is aluminum. Aluminum, like chromium, forms a protective layer on the surface, but is more stable than Cr_2O_3 at higher temperatures. However, Al_2O_3 does not protect well in corrosive environments, such as sulfur intensive hot corrosion [42], so both aluminum and chromium are needed in relatively high quantities to protect the part. While being a solid-solution strengthener, Cobalt enhances the high temperature strength, and reduces the solubility of aluminum and titanium in the nickel-chromium matrix. Cobalt also reduces the stacking fault energy (SFE), improves creep resistance and makes dislocation cross slip around γ' particles more difficult [43, 44].

Titanium, niobium, tungsten, and molybdenum are all used as solid-solution strengtheners. Titanium and niobium strengthen the γ' precipitates by enhancing the anti-phase boundary (APB) energy, while tungsten and molybdenum strengthen the γ matrix. These elements, along with chromium, also react with carbon to form the various carbides present in superalloys. Carbon, boron, and zirconium are added to strengthen and stabilize grain boundaries. Carbon reacts with zirconium to form MC carbides, which slow down grain boundary sliding. Boron forms borides that also strengthen the grain

boundaries. Table 2.1 summarizes the alloying additions in nickel-base superalloys and their principal functions.

The high strength and creep rupture properties of nickel-base superalloys result from a number of strengthening mechanisms. The strength of the alloy depends on the grains and the grain boundary. At less than 0.6Tm (melting point), the strength is mainly determined by the deformation of the grains. The main strengthening mechanisms that come into play are solid solution strengthening and precipitation hardening. At temperatures above 0.6Tm the alloys are affected by relative grain movement and rotation, coupled with grain boundary sliding. The formation of carbides at the grain boundaries contributes to the strength at these temperatures [43].

Table 2.1: Alloying additions in nickel-base superalloys and their principal functions

Addition	Function
Nickel	FCC matrix; forms γ’
Chromium	oxidation resistance; solution strengthening; $M_{23}C_6$
Cobalt	increases hardener phase stability and maximum temperature limit
Molybdenum	increases high temperature strength and stiffness
Tungsten	solution strengthening; affects γ’; affects carbides
Titanium	form γ’; forms MC
Aluminum	form γ’; oxidation resistance
Niobium	form γ”; form MC
Carbon	carbide former
Boron	form boride; improves grain boundary strength
Zirconium	form MC; improves grain boundary strength

2.4 Crack Initiation Mechanisms in Ni-base Superalloys

The life of a superalloy part may be controlled by the number of cycles required to initiate a crack in the part, the cycles required to propagate an existing crack, or a combination of both fatigue stages. Thus, a thorough understanding of the mechanisms governing both the crack initiation and growth processes is necessary to determine the contribution of each to the total fatigue life. Crack initiation in nickel-base superalloys is controlled by three main factors: microstructure, temperature, and environment. Furthermore, the microstructural effects are the result of the alloy's powder and processing history because inclusions and pores in the microstructure are often the sites of crack initiation. Grains oriented favorably for slip are prone to slip band cracking and are especially detrimental on the surface. The formation of a dominant crack is primarily a competition between initiation from slip band cracking and initiation from inclusions.

2.4.1 Role of Inclusions

According to Shamblen and Chang [45], there are five major types of inclusions that are found at fatigue failure initiation sites: 1) nonmetallic inclusions, 2) minor reactive nonmetallic inclusions, 3) reactive material inclusions, 4) pores, and 5) reactive metallic inclusions. Contamination from the melting crucible, pouring tundish, or atomizing nozzle causes the formation of the first two types of inclusions. These type 1-2 inclusions accounted for about 85% of the LCF fracture initiation site observation. Type 1 inclusions are chunky particles while type 2 inclusions are agglomerates of several smaller particles. Inclusions type 3 were recognized to be caused by reactive material inclusions such as organics and rust. These inclusions are generally much larger than type 1 and 2 inclusions because they are not limited by the mesh size. Type 4 inclusions are

pores formed by entrapped argon from the atomization process. They are smaller in size than types 1 through 3 inclusions but can become larger when particle size increases. Copper containing alloys are the only recognized inclusions for Type 5. Possible sources include brass valves or copper piping for the argon supply, brass or wiring in the production/handling facilities. When these inclusions are present at the surface of a part, interaction with the environment makes them even more detrimental.

Surface inclusions are more likely sites for crack initiation than subsurface inclusions in fatigue experiments, but the applied stress range influences the location of crack initiation and the subsequent small crack propagation. Hyzak and Bernstein [46] identified three mechanisms of crack initiation at strain ranges above 0.7% that were frequency and temperature dependent: transgranular initiation normal to the loading direction, transgranular initiation 45 degrees to the loading direction, and intergranular cracking. The most common of the three was transgranular initiation normal to the loading direction, but there was no obvious inclusion associated with these initiation sites though serial sectioning through the specimen cross section revealed cracking in nonmetallic inclusions and carbides near the specimen surface; smaller pores also contributed to initiation. Transgranular cracking at a 45 degree angle to the loading axis occurred on the same fracture surfaces as the transgranular initiation normal to the surface. Intergranular cracking only occurred at 760ºC (1400ºF) and a frequency lower than 0.2 cycles per minute. Below 0.7% strain range, cracks usually initiated at nonmetallic inclusions. They conjectured that a high temperature oxide layer on the surface of a specimen could crack at large applied strain ranges, which could be one reason the initiation mechanism varies with applied strain range. The work of Gell and

Leverant [47] is cited, which suggests that at low strain ranges surface oxides could fill surface cracks, preventing crack closure and crack tip resharpening, and thus, increasing the number of cycles to failure; experiments by Hyzak and Bernstein failed to prove the hypothesis. They found that the percentage of life spent initiating a crack increases as strain range decreases. They also report the low cycle fatigue failures originated from the specimen surface or near surface sites above a certain transition strain range in LCF experiments, while below the transition strain range, the failure initiated at an internal inclusion. At larger strain ranges, cracks initiate quickly and are able to propagate more easily on the surface because of the large stress intensity associated with a surface flaw; at lower strain ranges, cracks only initiate at the inclusions with the highest stress intensities. The surface-subsurface transition strain range is dependent on the alloy's composition and the size and volume fraction of inclusions.

Chang et al. [48] showed that extruded and forged René 95 has far fewer and more dispersed inclusions than HIPed René 95; the result is an improvement in ductility and LCF properties. They also found that most of the inclusions at the initiation sites of LCF fracture surfaces of the extruded and forged materials were of metallic, reactive nonmetallic or pores; no nonreactive metallic type inclusions were found. The sizes of the metallic and reactive nonmetallic inclusions were between 0.0026 mm^2 and 0.0065 mm^2 on average. The pores were less than 0.00065 mm^2 on average.

Jablonski [49] intentionally doped a low carbon Astroloy powder with Al_2O_3 or SiO_2 particles at concentrations ranging from 2 to 40 ppm and compared their LCF properties to a clean Astroloy material. The particles simulate reactive and nonreactive inclusions in a powder, where reactive inclusions are reduced by elements in the alloy to

form a complex nonmetallic inclusion and a reaction zone around the inclusion; for example, the silicon reacts with aluminum to form an aluminum rich inclusion with a 15 μm layer of ZrO_2 and TiO_2 surrounding it. A residual tensile stress is found around the inclusions because their coefficient of thermal expansion (CTE) is less than the CTE of the alloy; also, they have a higher modulus of elasticity than the surrounding alloy resulting in an additional stress concentration around the inclusions. He showed through surface replication of specimens performed throughout the LCF experiments that cracks can initiate from persistent slip bands. At 500ºC (932ºF), the highest testing temperature, cracks initiated when subsurface inclusions cracked in half. Cracks initiated at 25ºC (77ºF) when the matrix material debonded from the inclusions. Ceramics did not initiate fracture in the clean material or the material doped with 2 ppm SiO_2. Ceramics initiated fracture at least 50% of the time in the materials doped with 4 ppm Al_2O_3, 40 ppm Al_2O_3, and 20 ppm SiO_2. Cracks in the SiO_2 doped material originated at granular inclusions that had been enriched by aluminum.

Miner and Dreshfield [50] examined the effect of pores on crack initiation and growth. They cited two possible mechanisms for producing pores in the microstructure: atomization producing hollow particles filled with argon and lack of complete evacuation of argon gas from a powder container before consolidation. Leaks in the powder container can also allow penetration of argon gas and result in pores in the material. They produced an excess of pores in Astroloy for their research, roughly 15 times manufacturer's specifications. They discovered that cracks in the porous material initiated at single sites in the area of closely spaced pores; initiation at small pores (< 5μm) did not significantly reduce life, but a single 25 μm pore did.

Huron and Roth [51] summarized the influence of seeded inclusions on the low cycle fatigue response of René 88DT at elevated temperature. At low temperature test condition, majority of the test bars failed at grain facet and the seeds had very little impact on life. At 650ºC, most test bars failed at inclusions, with life strongly correlated to inclusion size. They also found shot peening was very effective in suppressing surface initiation in their study.

2.4.2 Effects of Microstructure

Microstructure plays an important role in determining the fatigue and fracture properties of superalloys. Aging accompanied by the precipitation of γ' precipitates leads to enhanced fatigue properties. A study done by Bartosiewicz et al. [52] on Incoloy 825 showed the effect of aging on fatigue properties. It was found that the crack-growth rates were lower for materials that had been aged to peak hardness as compared to specimens that were underaged and specimens that were as-received. Higher ΔK_{th} and lower crack-growth rates in the threshold region for the underaged and aged samples can be explained on the basis of the crack closure phenomenon. The underaged and aged samples exhibit crack closure, which reduces the effective stress intensity factor range. Hence, the driving force for the crack propagation decreases, which results in lower crack-growth rates relative to the as-received samples.

A similar study was conducted by Singh et al. [53] on Nimonic alloy PE16, where the low-cycle fatigue properties were studied by varying the aging time. The maximum stress generally increases with increasing the γ' particle size up to the peak-aged condition and decreases thereafter in the overaged condition. The cumulative plastic strain at which the maximum stress is achieved increases with increasing particle size.

This study revealed that the cyclic-stress response curve is determined by the operating dislocation-precipitate interaction mechanism. When precipitate shearing is the dominant mechanism (underaged and peak-aged conditions), the initial hardening is generally followed by a period of softening. For the overaged condition where both Orowan looping and precipitate shearing are operating, the extent of hardening and softening is relatively small. At low strain amplitudes, the number of cycles to achieve the maximum stress in underaged and peak-aged materials is attained within a narrow range of cycles. The number of cycles for the maximum stress continuously decreases with an increase in the strain amplitude for the overaged state.

2.4.3 Effects of Grain Size

Grain size has been shown to influence fatigue properties. Significant effort in both research and production of alloys is directed at control of grain growth and grain size distributions. Fine grain size contributes to high strength and increased ductility in superalloys, driving the development of the powder metallurgy process that is unique in its ability to achieve a homogenous fine grain size. In a study conducted by Kobayashi et al. [54] on Inconel 718, it was observed that the coarse-grained material exhibits lower fatigue strength than the fine-grained material. Similar results have been observed by Denda et al. [55] and Krueger et al. [56]. Miner and Gayda [57] studied the effect of grain size on the low cycle fatigue behavior in Nickel-base superalloy René 95 produced by different processing methods with same heat treatment. The extruded-and-forged form had average grain sizes of 5 μm showed superior fatigue life in low strain range tests at 540ºC. The cast-and wrought René 95, however, had lower fatigue life but higher fatigue crack propagation resistance because of larger grain size (150 μm). The difference in low

cycle fatigue lives between the three processing conditions is largely due to differences in strength and ductility based on the grain size produced during processing.

A similar study to understand the effect of grain size on fatigue properties was done by Alexandre et al. [58] on Inconel 718 showed how grain size affects crack initiation mechanisms in different heat treatments. The grain size in the materials tested ranged from 5 to 150 μm, and the tests were conducted at 600°C. In the small grain size material, the initiation sites were systematically related to the presence of a second phase particle; nevertheless, in larger grain size material, conventional Stage I crack initiation along intense slip bands is observed. The initiation mechanism in the 40 μm grain size material was found to be dependent on the grain size. A large reduction of the fatigue life can be accounted for in his model when the crack initiation mechanism switches from Stage I at large grain sizes to particle induced initiation observed at smaller grain sizes.

2.4.4 Effects of Precipitates

The morphology and volume fraction of the γ' and/or the γ'' precipitates affect the crack-growth behavior and fatigue life. A study conducted on Inconel 718 showed that finer precipitates result in a slower long-crack growth rate and longer low-cycle fatigue life in many cases. The short-crack-growth behavior is not significantly affected by changes occurring in the precipitate morphology. It has been estimated that the finer precipitates can result in an extension of the short-crack propagation regime. Floreen and Kane [59] speculated that the homogenization of slip and, consequently, the minimization of localized stress concentrations at the grain boundaries through changes in the precipitate morphology are a way in which the overaging heat treatment could increase resistance to high-temperature crack growth. Smith and Michel [60] suggested that the

improvement in the crack growth resistance produced by a modified heat treatment is likely to be a result of the alteration of mechanisms of dislocation interactions with the γ' particles and grain boundaries. The works of Smith and Michel [60] and Zheng and Ghonem [61] have shown that by coarsening the γ" precipitate particles, the mechanism of dislocation motion will be altered from a mechanism involving the shearing of precipitate particles to that of bypassing by the Orowan process.

Wlodek et al. [62] found several different types of carbides and borides in a René 88DT forging that had undergone a typical heat treatment. An MC precipitate was identified that had a significant amount of titanium and a lower amount of niobium. Also, $M_{23}B_3$ carbides formed on grain boundaries after service. They observed a tetragonal M_3B_2 phase that contained a large amount of chromium along with molybdenum and tungsten. A rare tetragonal M_5B_3 precipitate was observed that contained large amounts of Mo and W plus Cr. The borides and carbides were all equiaxed, 0.1 to 0.5 μm in diameter, and located at grain boundaries.

Menon and Reimann [63] studied LCF crack initiation in René 95. They observed the number of load cycles to produce crack initiation can be strongly affected by brittle constituents of the microstructure. The present of the fracture MC carbides probably accelerates or aids the initiation of fatigue cracks.

Most of the studies described in this section on crack initiation in superalloys imply there are two main crack initiation mechanisms and they attempt to determine the conditions where each mechanism becomes dominant. The divergence of crack initiation mechanisms in René 88DT was recently studied by Caton et al. [64]. They performed fatigue tests at 593ºC and at various stress levels. Testing was conducted under load

control at 10 Hz with a stress ratio of 0.05. Analysis of the fracture surfaces indicated that the critical cracks initiated in the subsurface of the specimens except for one test with stress equal to 1400 MPa. A possible explanation for this is that the tests were all conducted below the transition strain range defined by Hyzak and Bernstein [46]. It was discovered that the variability in fatigue life increased as the applied stress level decreased. This study has shown that the true fatigue behavior of René 88DT may be composed of superimposed mechanisms that diverge with decreasing stress level. The description in terms of divergent mechanisms has the potential for more accurate life prediction and a reliable methodology for life extension. The probability of failure for tests conducted at various stress levels is plotted in Figure 2.25a. The slope of the function decreases as stress level decreases indicating greater variability at lower stress levels; also, there is seemingly a step function for stress equal to 940 MPa which may imply a divergence of initiation mechanisms at this stress level. Analysis of the fracture surfaces showed that the crack initiation occurred from either a subsurface inclusion or more likely, from a crystallographic facet. An S-N plot is shown in Figure 2.25b that distinguishes between initiation from an inclusion and initiation from a crystallographic facet. It shows that the number of cycles to failure diverges to a greater extent at low stress levels for the two different initiation mechanisms.

2.4.5 Environmental Effects

Numerous studies have been conducted to examine the effect of environment on fatigue growth, e.g., [65-67]. Similarly, there have been various investigations into the effect of the environment, particularly at high temperatures, on the fatigue life of smooth specimens, e.g. [68-70]. In these investigations, a comparison is generally made of the

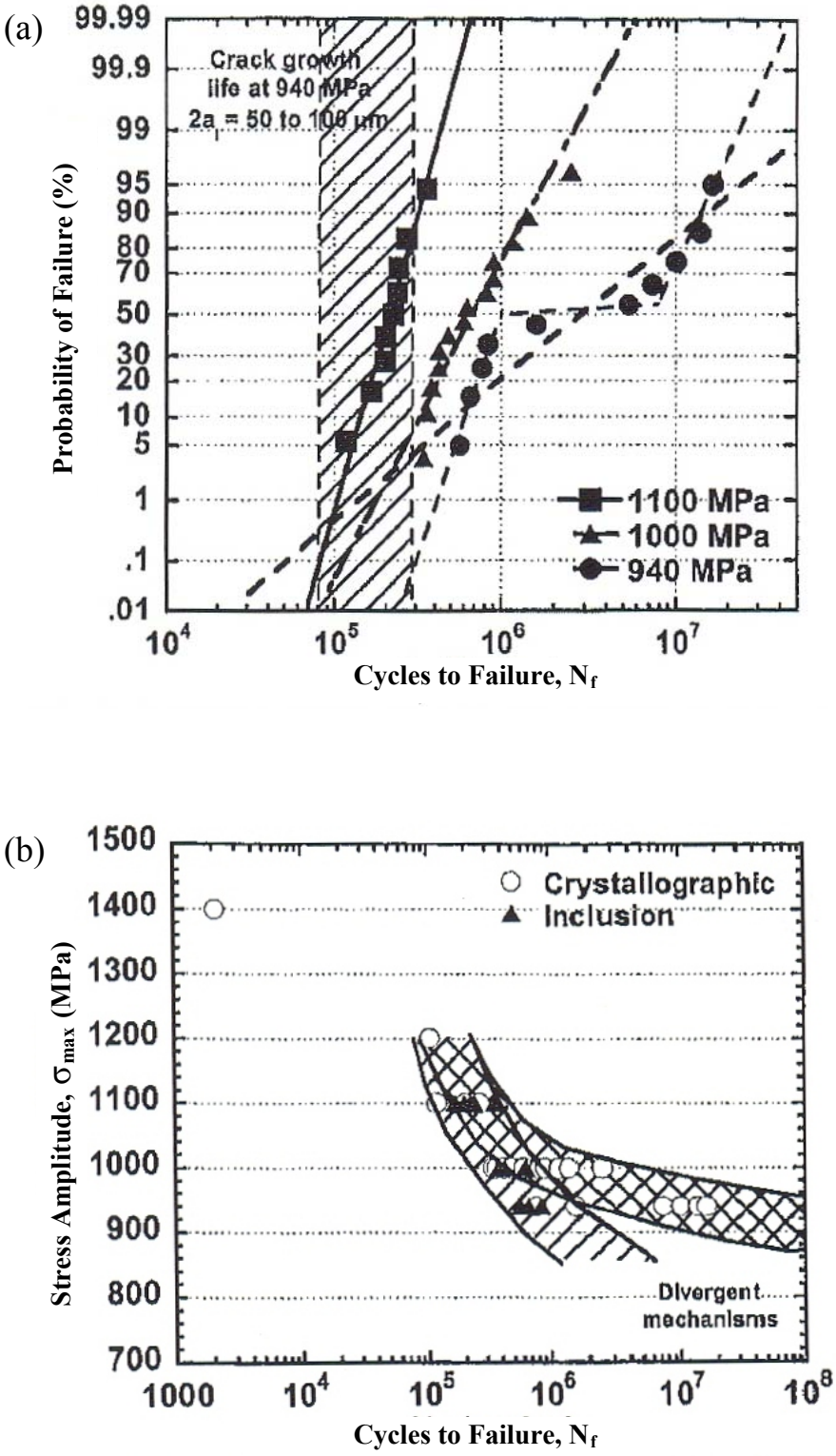

Figure 2.25 Crack initiation mechanisms in René 88D (a) Probability of failure on LCF results at various stress levels at 593°C (b) Divergence of crack initiation mechanisms. Adapted from Ref. [65]

fatigue behavior in a vacuum and air to show the effect of environment. Metallurgical evidence has suggested the environment plays a crucial role in assisted crack initiation, as environmental attack precedes crack initiation through the formation of both oxide layers and a detrimental γ'-depleted zone [71, 72]. The observance of intergranular crack formation and propagation serves as further evidence of sustained environmental damage ahead of the crack tip. This behavior is often due to preferential oxidation of the grain boundaries, which can change the fatigue fracture mode from transgranular to intergranular. Oxidation plays a crucial role in the crack initiation behavior of Ni-base superalloys at high operating temperatures. Oxygen is the primary environmental effect which reacts with, and incidentally, changes the compositional makeup of the exposed alloy.

The effect of a harsh environment on fatigue life was demonstrated on Figure 2.26 [73] shows the existence of competing failure modes in the low-cycle fatigue (LCF) test data of Rene'95 Ni-base superalloy. The strain-controlled LCF fatigue data compiled in Figure 2.26 also include three vacuum fatigue test data (two points are superimposed at the stress amplitude of about 1000 MPa) generated at a vacuum level of about 10^{-7} torr. All the 3 specimens failed by surface-crack-initiations even though there was no environmental factor. However, fatigue life cycles for these failures are in agreement with the life trend for internal crack initiations. This clearly suggests that the fatigue life differences between the surface and internal fatigue crack initiations were due to the high temperature air environment. Fatigue crack growth rates in René 95 at 650ºC in air are significantly faster than that in vacuum [74] corroborating this behavior.

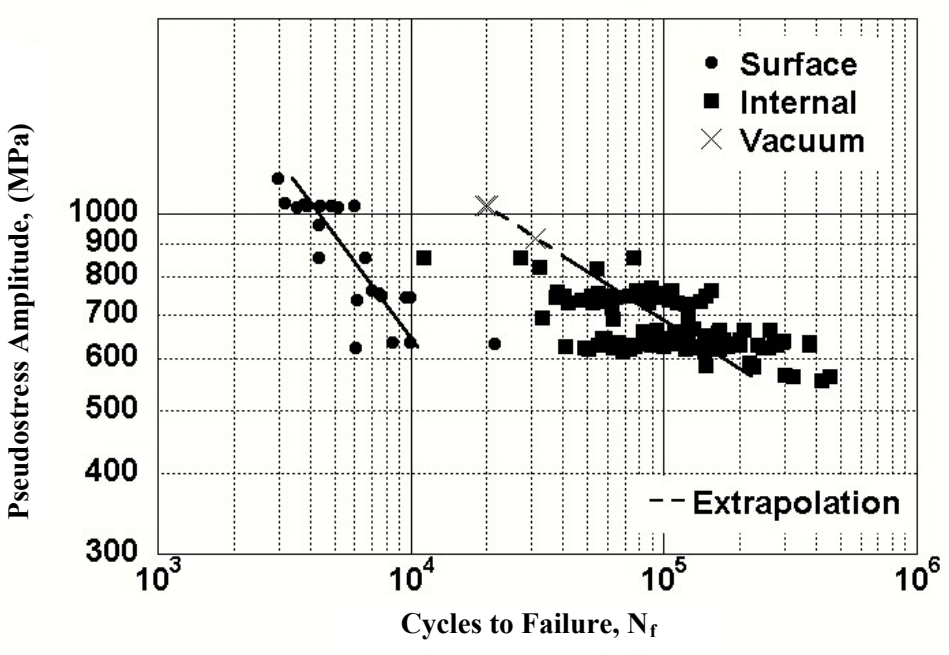

Figure 2.26 Duality of the S-N curve in strain-controlled low-cycle fatigue data (R=0) of René 95 nickel-base superalloy at 583ºC, in air environment. The line through internal initiation fatigue failures extrapolates to the surface-crack-initiated failure of vacuum tests. The data are plotted in terms of pseudo-stress amplitudes that were determined from the strain amplitudes. Adapted from Ref. [74]

2.5 Fatigue Crack Growth in Ni-base Superalloys

Early compositions of the superalloys were based on the Fe-Ni system—the compositions of Nimonic and Inconel alloys were progressively optimized and later became known as alloys that are primarily strengthened by γ' precipitates. The demand for more efficient engines with higher disk temperatures and operating stresses lead to the development of Waspaloy and Astroloy classes of superalloys that contain carbides and intermetallic compounds, in addition to the γ' precipitates. In recent years, the successful implementations of powder atomization and consolidation techniques led to the evolution of commercial powder-metallurgy superalloys such as IN100, René 95 and René 88DT.

2.5.1 Temperature Effects on Fatigue Crack Growth Behavior

In the past, much of the material design and qualification for the engine disks were based on low-cycle fatigue (LCF) performance at around 650˚C. However, the engine component management at that time was a conservative approach, since the components are retired after the design life based on predicted LCF life. An improvement to this approach is the "retirement-for-cause" methodology that relies on nondestructive testing and accurate prediction of fatigue crack growth lives of component containing cracks, using fracture mechanics based fatigue crack growth data. In this section, high temperature fatigue crack growth behavior of nickel base superalloys are reviewed, with a particular emphasis on the effects of grain size, stress ratio, test frequency and dwell periods on the fatigue behavior.

Hoffelner [75] presented a compilation of fatigue crack growth data of several nickel base superalloys at room temperature (Figure 2.27a) and at 850˚C (Figure 2.27b). The fatigue crack growth tests were conducted using double-cantilever bend (DCB) samples. According to the author, the fatigue crack growth curves reveal the well known crack growth regimes: the threshold region associated with the low-ΔK levels and the intermediate ΔK regime where fatigue crack growth rates largely follow the Paris' law for crack growth. At room temperature, where the effects of oxidation and creep are not present, all the alloys fall into a narrow scatter band in the Paris law regime. However, some sensitivity to alloy type is seen in the near threshold region, similar to that seen in other metallic materials. At 850˚C, there seems to be a little bit more variability in the crack growth data in the Paris regime. At low ΔK levels, the spread in the data is similar to that seen in room temperature tests—this variability at high temperature could be due

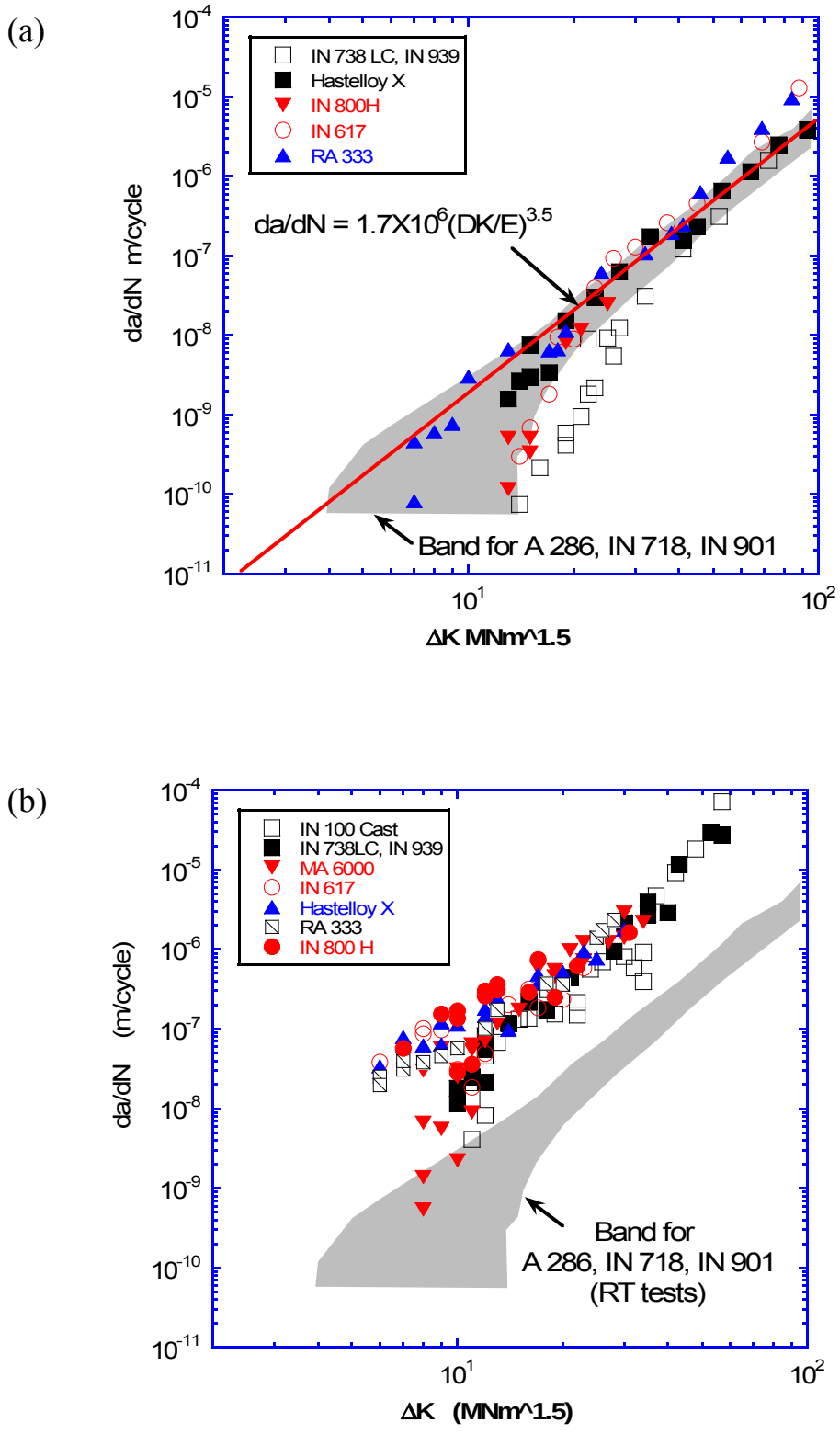

Figure 2.27 Fatigue crack growth rates of several Ni-base superalloys in air and at R=0.1 (a) at room temperature (b) at 850°C. Adapted from Ref. [75]

to the differences in the microstructure and the strength levels of these materials—a more thorough study is required to make a firm conclusion in this respect.

King [76] and King et al. [77] studied the fatigue crack growth behavior of Astroloy at room temperature at different grain sizes and stress ratios—the data are shown in Figure 2.28. Tests were done at stress ratios of R=0.1, 0.5 and 0.8. The "fine-grain" material had a grain size range of 11-13 μm and the "coarse-grain" material had an average grain size of 50 μm. It can be seen that at room temperature, a strong effect of stress ratio on fatigue crack growth is present in the coarse-grained material. This indicates that most of the stress-ratio effect comes from roughness-induced crack closure, due to the interference of crack surfaces in the wake of the crack. This is also evident from the fact that both at the near threshold and in the low end of the intermediate

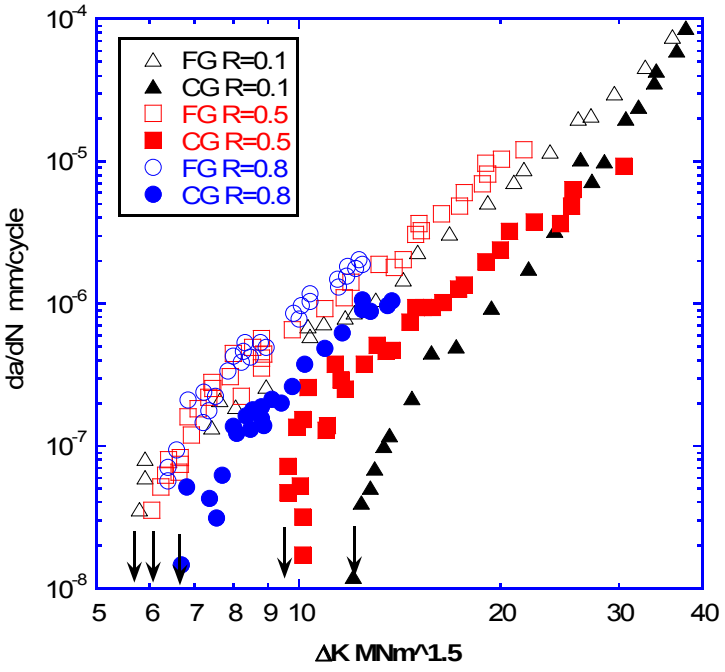

Figure 2.28 The effect of grain size and stress ratio on the room temperature fatigue crack growth response of Astroloy. Adapted from Ref. [76]

ΔK regimes, the growth data for different stress ratios are separated by approximately a constant amount of ΔK. The separation vanishes at ΔK levels above 20 MPa√m, indicating that the crack wake interference, to cause crack closure, is small. The partial closure of cracks is known to be caused by the formation of large fatigue fracture facets (because of a larger grain size) due to slip along crystallographic planes, when the crack propagates through the grains, producing a relatively rough fracture surface. The fracture surface faceting and the associated roughness also exist in fine grained material, but the scale of these features, with respect to the cyclic crack opening displacement, is much smaller than that in the coarse grained material. Therefore, the effect of stress ratio on fatigue crack growth is relatively small, even in the near threshold region, for the fine-grained material. The foregoing results indicate that the grain size of nickel base alloys is a major variable affecting the threshold for fatigue crack growth.

2.5.2 Grain Size Effects on Fatigue Crack Growth

Albrecht [78] performed LCF experiments on Udimet 720 LI with varying grain sizes at 600°C and with σ_{max} values well above the material's yield stress. Because of the large applied stress range, the grain size had little influence on the microcrack propagation rate possibly because the stress concentration in front of the crack tip was very large; thus, grain boundaries were relatively weak barriers because there were a large number of slip systems available to help propagate the microcrack due to the large stress concentration. Variation of the γ' size distribution between the different microstructures tested had little influence on LCF lives.

Alexandre et al. [44] also studied how grain size affects crack initiation mechanisms in different heat treatments of Inconel 718. The grain size in the materials

tested ranged from 5 to 150 μm, and the tests were conducted at 600°C with applied strain ranges between 0.7% and 1.7%. In the small grain size material, the initiation sites were consistently associated with second phase particle cracking; however, in the largest grain size material, crack initiation was purely from intense slip bands. The initiation mechanism in the 40 μm grain size material was found to be dependent on the grain size; for small grains, particle cracking is more likely to cause crack initiation while slip band cracking is more likely for large grain materials. Fatigue initiation life can then be predicted by using a proportionality law that predicts cycles to initiate a crack based on grain size or by predicting the crack growth rate for small particle cracks less than the grain size.

2.5.3 Effects of Frequency and Environment on Fatigue Crack Growth

Pineau [79] summarized observations of the influence of metallurgical factors and oxidation on fracture mechanisms of superalloys in fatigue crack growth. The frequency of fatigue crack growth tests conducted on Inconel 718 was varied and it was discovered that a transition from intergranular fracture to transgranular fracture occurred as test frequency increased. It was found that at low testing frequencies in alloy 718, the fatigue crack growth rate is inversely proportional to frequency, which implies time-dependent behavior. At high frequencies, the crack growth rates are independent of frequency. Microstructure and environment have a much larger effect at low frequencies at 650ºC (1200ºF) when time dependent behavior is dominant; for example, lower rates of crack growth correspond to larger grain sizes.

Kang et al. [80] researched how oxide formation relates to the crack propagation process in IN718. They found a niobium oxide grain boundary film on fracture surfaces

of creep crack growth tests performed at 650ºC (1200ºF) and speculated that the film may have derived from the formation of niobium oxides from NbC particles at the grain boundaries. Also, the δ phase (Ni_3Nb) precipitates at the grain boundaries, which may also form oxide particles. They suggested that the high stresses around the crack tip accelerate the driving forces for diffusion of oxygen and niobium along the grain boundaries, which then react with each other to form brittle niobium oxides and oxide layers on the grain boundaries.

2.6 Statistical Aspects of Fatigue

2.6.1 Weibull Statistics of Fatigue

Weibull proposed functions that keep to describe fatigue life variability. One of the common Weibull distribution functions [37] is:

$$\textit{Probability of failure at } N_f = F(N_f) = 1 - e^{-\left(\frac{N_f}{\alpha}\right)^{\beta}} \tag{2.3}$$

This equation is referred to as two parameter Weibull distribution function where α and β are the two parameters that characterize the probability of failure at a given fatigue life. The survival probability is

$$1 - F(N_f) = e^{-\left(\frac{N_f}{\alpha}\right)^{\beta}} \tag{2.4}$$

The equation can rewrite as:

$$\ln\left[\left(\frac{1}{1-F(N_f)}\right)\right] = \beta \ln N_f - \beta \ln \alpha \tag{2.5}$$

This is now a linear equation, with a slope of β and an intercept $\beta \ln(\alpha)$. The distribution of N_o at a given cyclic stress is often fitted with this equation. However, this equation does not consider the fact that the minimum fatigue life in a distribution cannot be zero. There, a three-parameter equation was proposed to characterize the life variability in a better way. The three-parameter Weibull distribution function is

$$F(N) = 1 - e^{-\left(\frac{N - N_{\min}}{N_{\max} - N_{\min}}\right)^{\beta}} \tag{2.6}$$

The use of the three-parameter equation in characterizing fatigue is described in section 2.2.3.

2.6.2 Poisson Spatial Statistics

For a material where fatigue crack growth is sensitive to environmental effects, the two dominant failure modes may be surface crack initiation and interior crack initiation, because surface cracks are exposed to the environment next to the surface.

The difference in fatigue lives between to the two crack initiation modes, namely surface-initiated and interior-initiated failures is enhanced largely by the presence of crack-initiating inclusions. Occurrence of an inclusion or a particle either at the surface or at the interior of a fatigue specimen can facilitate a given initiation mechanism. When inclusions are involved, the spatial distribution of inclusions influences the relative dominance of either of the crack initiators (surface or interior). When considering spatial distribution of inclusions, the parameters that become important are the average inclusion density, specimen test volume and the number of samples tested. This is because, when the inclusion density is low (as often is the case with the current structural materials with

improved cleanliness and microstructure), some fatigue samples may contain inclusions only at surface, some will contain inclusions only in the interior and some may not contain any inclusion at all. The Poisson distribution of the probability of occurrence of a number (n) of random cluster-inclusions in an arbitrary area A is:

$$P(n) = \frac{e^{-\lambda A}(\lambda A)^n}{n!} \tag{2.7}$$

where λ is the average inclusion density. Thus the important question is how many specimens one needs to test at each stress level to see the true fatigue variability of a material that may contain sparsely populated inclusions. Previous research in our group [9] shows that there are equal proportions of surface-initiated and interior-initiated failures (Figure 2.2), giving each a failure probability of 0.5, in agreement with the prediction in Figure 2.29. However, as often practiced, one may choose to test samples that were located adjacent to each other in the parent bulk material. In this scenario, one may not be able to judge beforehand as to the number of samples to be tested to see the true and complete variability in fatigue life.

By using Monte Carlo simulation, the effect of number of samples tested on the proportions of surface- and interior-initiated failures can be illustrated. The simulations were done using the Lewis-Shedler algorithm [81] as described in the following. According to Poisson spatial statistics, the probability for "n" inclusions to occur in a specimen cross-sectional area having sides as X_o and Y_o is

$$P(n) = \frac{e^{-\lambda X_o Y_o}(\lambda X_o Y_o)^n}{n!} \tag{2.8}$$

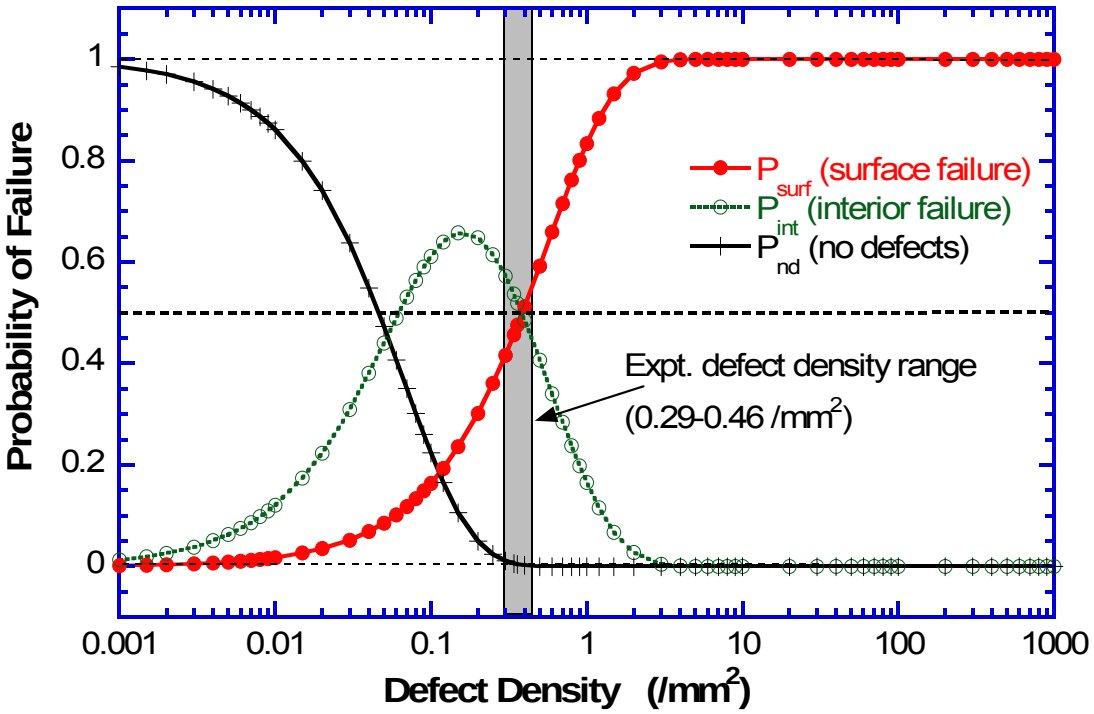

Figure 2.29 Calculated probabilities for fatigue failure from surface and interior regions as a function of inclusion density, for the Ti-10V-2Fe-3Al titanium alloy. The experimental inclusion density is also shown. Adapted from Ref. [9]

$$P(n) = \frac{e^{-\lambda X_o Y_o} (\lambda X_o Y_o)^n}{n!} \tag{2.8}$$

where λ is the average inclusion density.

The probability for at least one or more inclusions to occur in area $X_o Y_o$ is given by

$$1 - e^{-\lambda X_o Y_o} \tag{2.9}$$

The cumulative probability distribution function (PDF) for distances between successive inclusions in one direction is then given by

$$F(x) = 1 - e^{-(\lambda Y_o)x} \tag{2.10}$$

The PDF for distances between successive inclusions in the X-direction is then given by

$$f(x) = \frac{dF(x)}{dx} = \lambda Y_o e^{-(\lambda Y_o)x} \tag{2.11}$$

The interinclusion distances in X-direction is then

$$x_i = -\frac{1}{\lambda Y_o} \ln\left[\frac{f(x)}{\lambda Y_o}\right] \tag{2.12}$$

The Poisson-distributed spatial co-ordinates $\{x_i, y_i\}$ of *n* inclusions are then given by

$$X_n = \sum_{1}^{n} x_i \tag{2.13}$$

and

$$y_i = rand\{0,1\} Y_o \tag{2.14}$$

where the function rand {0,1} generates random numbers in the interval between 0 and 1.

In order to illustrate the effect of number of specimens tested in a batch on the preponderance for surface or interior failures, specimens with a minimum area ($X_o Y_o$) of 7.5 mm^2 containing Poisson distributed inclusions with $\lambda = 0.34/mm^2$ were assumed in the simulations. The spatial occurrence of inclusions in the minimum cross-sectional

area of a large number of specimens was then statistically simulated using the method discussed above. If one or more inclusions occurred within a surface rim of 0.1 mm in width in the minimum cross-sectional area of the specimen, then the failure from these inclusions was classified as surface-initiated failure. All other failures were classified as internal crack initiated failures.

Figure 2.30 illustrates the cumulative failure probabilities of "theoretical" fatigue specimens, depending on whether a crack-initiating inclusion occurred at the surface or at the interior, when random samples were simulated. In the X-axis, the number of specimen simulations mimics the sequence of adjacent fatigue samples cut from one plate. One trial in the simulation mimics one material plate in practice. In trial one (Figure 2.30a), it can be seen that the first specimen failed from surface-initiated crack, since an inclusion occurred in the surface rim in the simulation. The second specimen also failed from surface, because a surface inclusion occurred again. However, in the third specimen, the crack-initiating inclusion occurred in the interior, thus bringing the cumulative probability for interior failure to 0.33 (1 out of 3) and the cumulative probability for surface failure to 0.66 (2 out of 3). With further sample testing, both the probabilities tend to converge to about 0.5, which represents the equal probabilities for surface- initiated and interior-initiated failures, consistent with the actual experimental data in Figure 2.2.

An important point to be emphasized from Figure 2.30 is that in the present example, about 30 adjacent specimens are to be tested in order to faithfully reproduce the true and the nearly equal propensity for surface-initiated and interior-initiated failures and thus produce the dual fatigue behavior of the material. When a second trial was run for

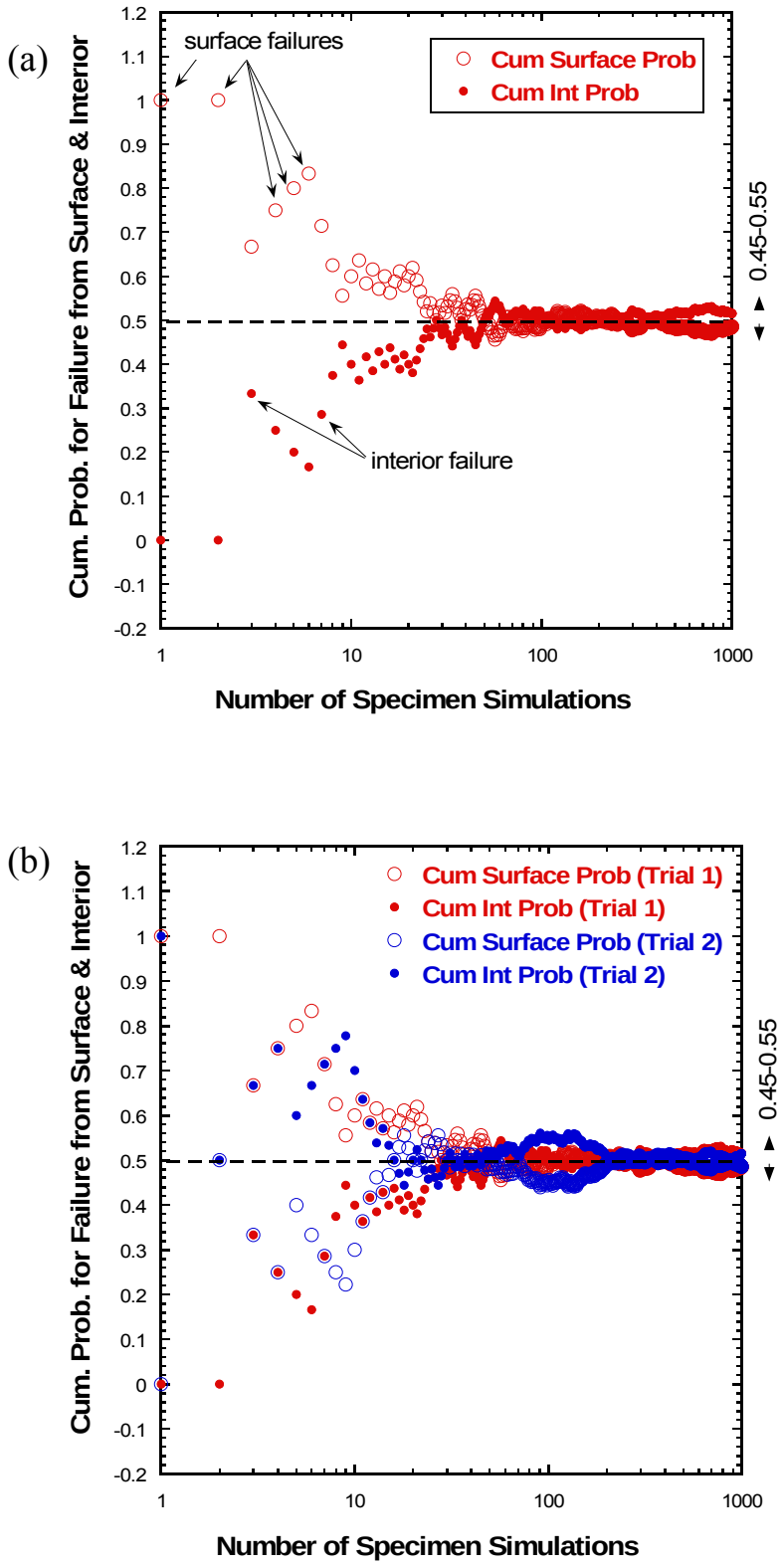

Figure 2.30 Illustration of cumulative failure probabilities for failure from surface-initiated and interior-initiated cracks (a) for trial 1 and (b) for trials 1 and 2. Adapted from Ref. [9]

the same simulation, the convergence to the probability of 0.5 occurred at about 20 sample simulations (Figure 2.30b). In combination with trial 1, it appears that at least 20-30 samples are to be tested to reveal the true fatigue behavior of the material in each stress level, if samples are located adjacent to each other in a material plate having a certain density of inclusion distribution.

2.6.3 Binary Logistic Regression for Failures of Initiation Site

The relationship of stress amplitude to fatigue failure sites was analyzed using a logistic regression. Specimens were considered either surface-initiated failure or not, which is a binary response. Binary logistic regressions (BLR) employ three scales: logits, odds, and probability. Here, surface-initiated failure is assigned a value of one and internal-initiated failure is assigned a value of zero. To create a BLR for this type of response, a line is fitted so that all responses are between 0 and 1. The advantage of logistic regressions is that, unlike linear regression which predicts the actual values of the response variables, they predict the probability associated with each level of the variable by finding a linear relationship between predictor variables and a link function.

Cashman [82] has proposed a methodology for the development of a fatigue design model for the case when there is significant demonstration of Competing Modes behavior. A BLR plot of the probability of surface initiation as a function of applied stress or strain was develop first (Figure 2.31). The simple linear regression had the following form:

$$\log_{10}\left(N_f\right) = b_0 + b_1 \log_{10}\left(\sigma_p\right) \tag{2.15}$$

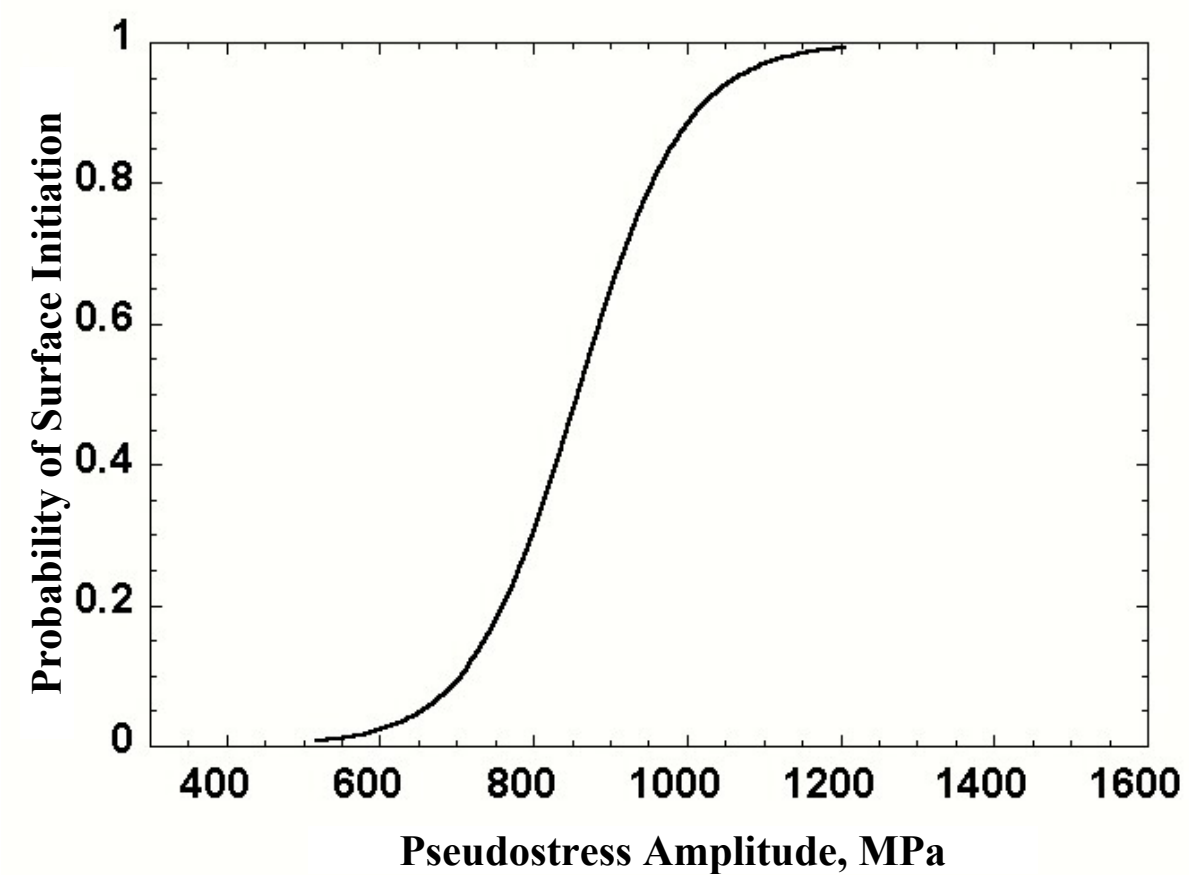

Figure 2.31 Probability of surface crack initiation as a function of pseudo-stress amplitude. Adapted from Ref. [82]

where N_f is the cycles to failure; b_0 and b_1 are referred to the regression fit parametersand σ_p is pseudostress amplitude.

The model, as depicted by the author, helps in the evolution of a statistically consistent S-N type of curve capturing the true physical behavior of the material. Further, because there are three sources of uncertainty, namely the analyses of the surface data, the internal data, and the logistic regression, 100 observations are necessary to adequately characterize S-N response by Mote Carlo simulation results.

2.6.4 Extreme Value Statistics

When one wants to analyze some rare or extreme events, such as flood levels or peak day-to-day temperature, ordinary statistical methods fail to properly describe their distribution. This is because most standard statistics deal with the "normal events" but not those at the ends or the tail of the distribution. Many of these methods tend to lower the influence of precisely those rare events we are interested in. Extreme value statistics deal with those events that are at far ends of the measurements which might be considered outliers under normal statistical analysis. Extreme value statistics can be employed to estimate the largest inclusion size that may then be used to calculate the risk of failure during fatigue tests or in products in real use.

An example of extreme value statistics that is of great interest when discussing the mechanical properties is the size of the largest inclusion found in a stressed volume. There, the probability of the maximum size being over a given distribution z can be described by a mode of Generalized Extreme Value (GEV) distribution [83].

$$G(z) = \exp\left\{-\left[1+\xi\left(\frac{z-\lambda}{\alpha}\right)\right]^{-1/\xi}\right\} \tag{2.16}$$

with three parameters for location, scale and shape, λ, α and ξ, When ξ is greater than 0 the distribution approaches Fréchet distribution with α = 1/ξ, and when ξ < 0 it approaches the Weibull distribution with α = -1/ξ. As ξ → 0 the distribution goes towards a Gumbel distribution,

$$G_1(z) = \exp\left\{-\exp\left[-\frac{z-\lambda}{\alpha}\right]\right\} \tag{2.17}$$

In Figure 2.32, the cumulative distribution for the GEV has been plotted for three values of ξ, using constant values for λ and α.

The expected largest extreme value is largely dependent on the shape parameter ξ, with a finite maximum for ξ < 0. In Figure 2.32 this can be seen as –log(-log[G(z)]) tends to infinity at z = 80. For non-negative values of ξ, the distribution function decreases steadily; however, larger values of ξ lead to slower declines. The Gumble distribution has a exponentially decaying density with a rate that depends on the scale parameter λ.

Another method based on a different branch of the extreme value theory, termed as the As opposed to the Statistics Extreme Value method, GPD method makes use of all inclusions which are over a certain threshold size. Another difference between these two methods is that under certain conditions, the predictions with the GPD method are directed to an upper limit of the maximum inclusion size, which is more in accord with the expectations.

Murakami and co-workers [89] were the first to apply the statistics of extreme to steel predict the maximum inclusion size in a selected volume. The main premise of extreme value theory is that the distribution of inclusions in metals is expected to be nearly exponential. If the cumulative probability of a given population is exponentially decreasing then the distribution of largest inclusion of each surface can be described by a largest extreme value distribution (also called Gumbel distribution). Then the distribution of extremes has the following probability density function:

$$f(x) = \frac{1}{\alpha} \cdot \exp\left[-\frac{(x-\lambda)}{\alpha} \right] \cdot \exp\left\{ -\exp\left[-\frac{(x-\lambda)}{\alpha} \right] \right\} \tag{2.18}$$

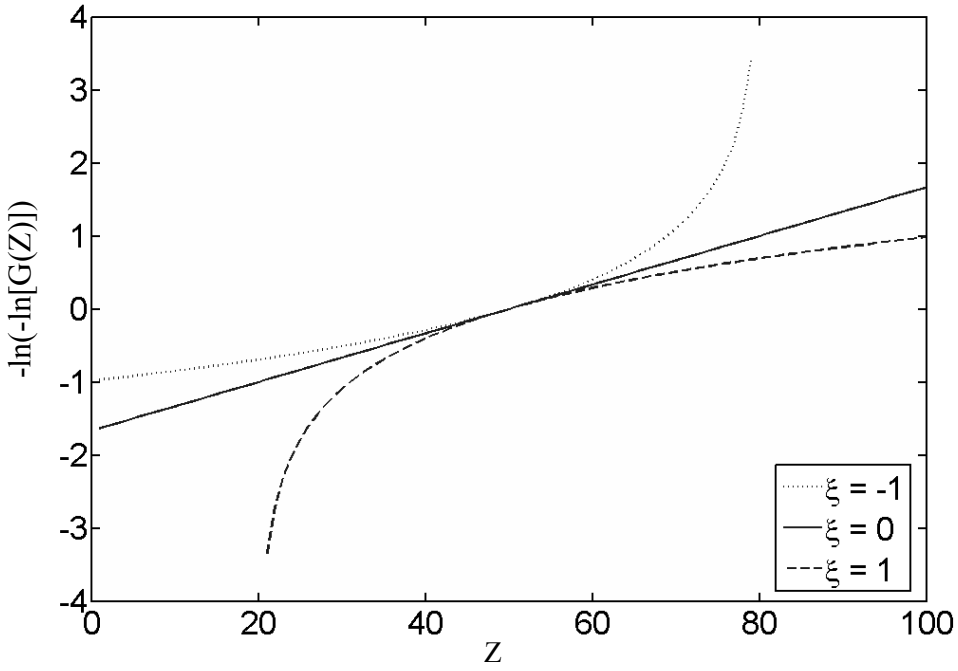

Figure 2.32 The three different appearances of the GEV distributions. λ = 30, α = 50 and ξ as indicated. Adapted from Ref. [83]

and cumulative probability function is

$$F(x) = \exp\left\{-\exp\left[-\frac{x-\lambda}{\alpha}\right]\right\} \tag{2.19}$$

where λ and α are referred to as the location and scale parameter, see Figure 2.33.

By define a reduced variable y, $y = \frac{x-\lambda}{\alpha}$ (2.20)

the transformed variable y then replaces F on such plots is called the reduced variate,

Hence $F(x) = \exp[-\exp(-y)]$ (2.21)

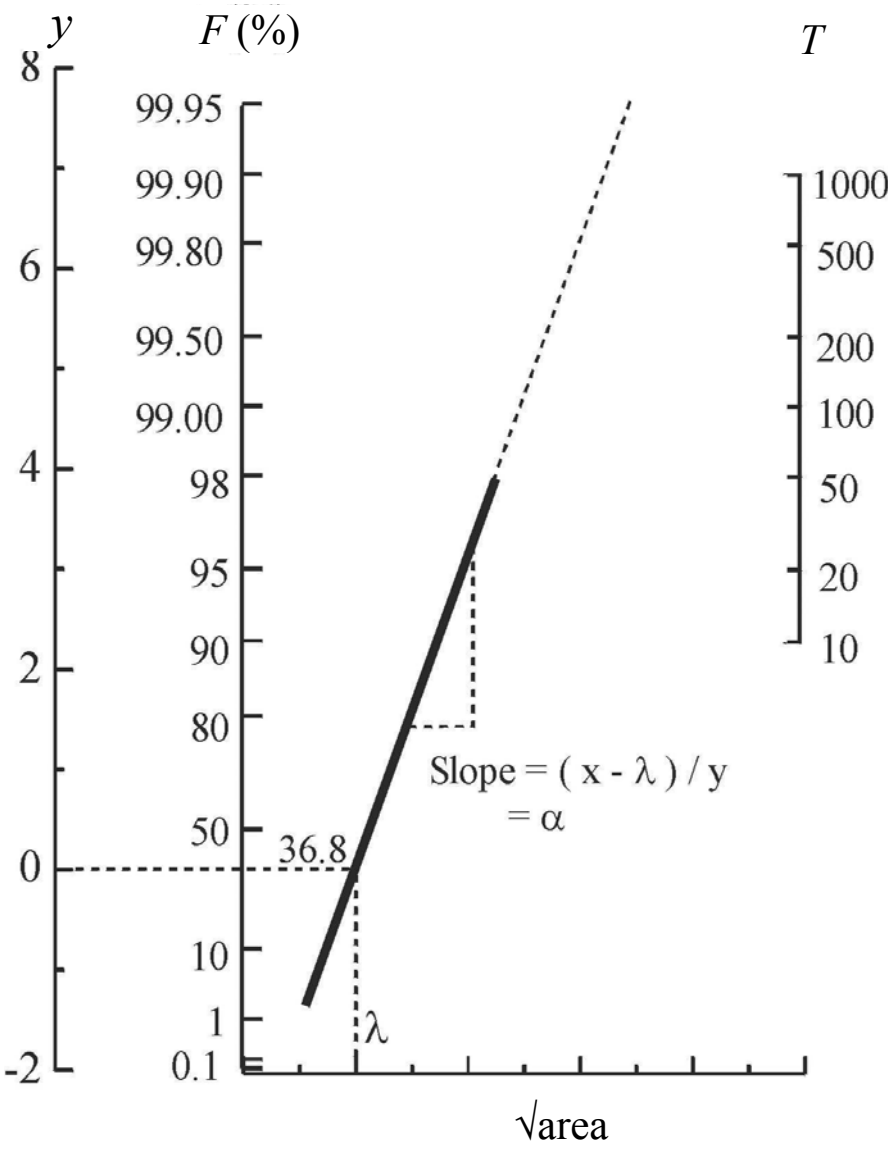

Figure 2.33 Probability plot of extreme distribution. Adapted from Ref. [89]

Reduced variate becomes

$$y = -\ln[-\ln(F(x))] \tag{2.22}$$

The application of extreme value statistics to characterize inclusions in material can be described as follows. The first step is collecting the largest inclusion size that is observed in a given area, A_{scan} of the metallographic image and repeating this for each metallographic imaging area, until some large numbers of inclusion sizes have been collected. The result can be roughly transformed to volume distribution by assuming a "scanning depth" comparable to the linear size of inclusions, that is,

$$V_{scan} = A_{scan} \times h \tag{2.23}$$

where h is the average size of inclusions. If V_{scan} is the inspection volume and V is the volume of the component under fatigue test, the maximum inclusion occurring once in the component has a return period (the number of times that the component volume, relative to the metallographic inspection volume) $T = V/V_{scan}$ then the cumulative probability $F(x) = (1 - 1/T)$, the reduced variated is then

$$y_T = -\ln\left[-\ln\left(1-\frac{1}{T}\right)\right] \tag{2.24}$$

If one knows T, the dimension of the inclusion that expected in that volume would be

$$x_T = \lambda + \alpha \times y_T \tag{2.25}$$

Some times the extreme size distribution can be bilinear (Figure 2.34), due to the population of inclusions consisting of a mixture of two distinct inclusions types. The cumulative probability function constituted by the two inclusion types can then be expressed as

$$F_{mix}(x) = \left(1 - \overline{P}\right) \cdot F_1\left(x, \lambda_1, \alpha_1\right) + \overline{p} \cdot F_2\left(x, \lambda_2, \alpha_2\right) \tag{2.26}$$

where $\overline{p}$ is the fraction of type-2 inclusions and F_1 is the largest extreme value distribution cumulative function for type-1 particles with parameters of λ_1 and α_1. The

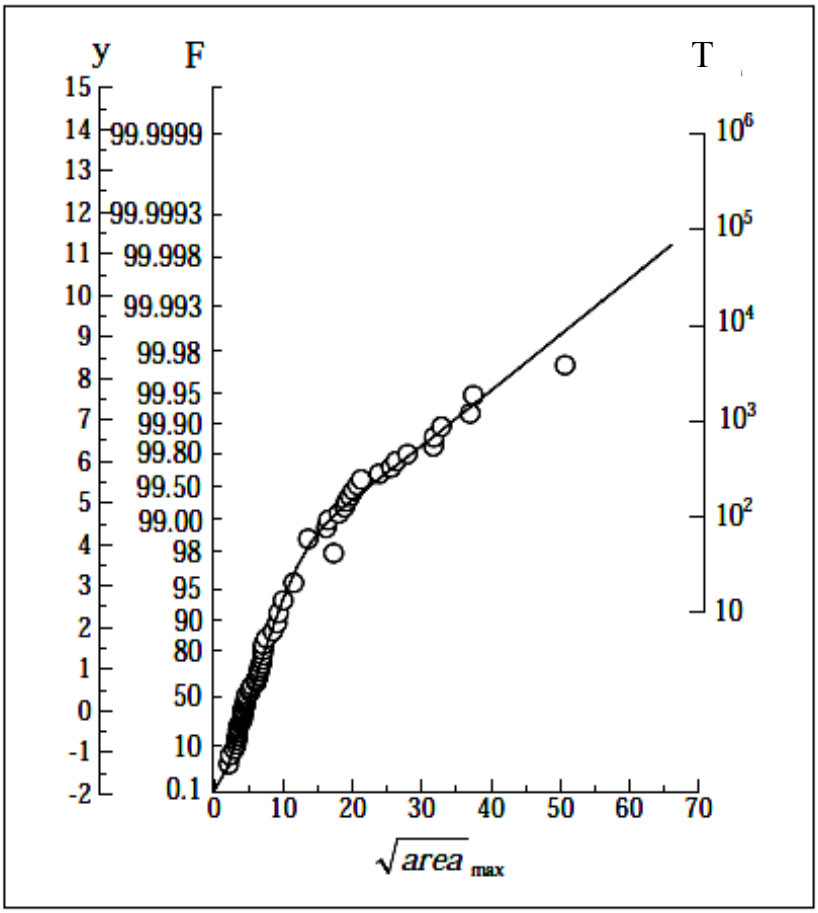

Figure 2.34 Bilinear extreme distributions. Adapted from Ref. [89]

subscript 2 refers to the type-2 inclusions. Similarly, the probability density function is

$$f_{mix}(x) = \left(1 - \overline{P}\right) \cdot f_1\left(x, \lambda_1, \alpha_1\right) + \overline{p} \cdot f_2\left(x, \lambda_2, \alpha_2\right) \text{.....(2.27)}$$

Figure 2.34 illustrates the example of the bilinear extreme value statistics for SCM 435 steel [89].

2.7 Literature Review Summary

The extensive literature survey reveals that different mechanisms of fatigue failure can be activated based on the stress level, loading conditions, material and testing environment. Evidence of varied S-N curves, one for each surface and interior crack initiation mechanism, were seen for many materials. Researchers have investigated mechanisms of competing failure and studied environmental, microstructural, and grain size effects. There is also a definite stress range where the crack initiation site changes from the surface to the subsurface, giving a step-wise S-N curve. Inclusions, such as oxide inclusions, are often found in superalloys that have undergone powder metallurgy processing; these inclusions have a deleterious effect on fatigue life because they are natural sites for crack nucleation. Persistent slip band cracking has also been observed as another dominant crack initiation mechanism.

Despite these studies there are some unanswered questions that need to be resolved.

1. Why do the dual or two separate S-N curves occur in some microstructure and not in others?
2. How many tests are needed to run to clearly see the competing modes behavior?

3. What is the role of inclusion size in affecting the transition from surface to interior failure?
4. Is it possible to predict failures from inclusions, based on the extreme value statistics?

The present thesis research focuses on considering these questions as much as possible.

CHAPTER 3

RESEARCH SCOPE AND OBJECTIVES

Fatigue failure of turbine engine components during service is a serious problem. Among the most demanding structural applications, the requirements for the aircraft engine materials are the most demanding, due to the combination of high operating temperature, corrosive environment, high monotonic and cyclic stresses, long expected component lifetimes and the consequences of structure failure. The general scope of the present research is to investigate the nature of fatigue failures in a high temperature Ni-base superalloy. The principal objective of this research is to determine the microstructure and test conditions that lead to competing fatigue failure modes and the duality of fatigue. A representative superalloy, René 88DT, was selected for this purpose. The specific aims of this project are:

- Determine the proportion of surface-initiated and interior initiated failure modes during high temperature fatigue tests of René 88DT.
- Investigate how the inclusion densities (seeded inclusions) alter the failure mode competition, using a model René 88 alloy containing a known distribution of seeded inclusions.
- Use two different test volumes or sizes in the fatigue tests and determine how test volume affects the competition for failure modes.

- Perform detected fractography of fatigue failure sites and determine the sizes of inclusions/microstructural features causing crack initiation.
- Develop an analysis to predict fatigue failure from inclusions

CHAPTER 4

MATERIAL AND EXPERIMENTAL PROCEDURE

4.1 Material

The material used in this study is the nickel-base superalloy, René 88DT. René 88DT was developed by GE Aircraft Engines in 1988 and is currently in use in some aircraft engines. This alloy was specially designed for gas turbine disks, with the objective of achieving improved strength, creep resistance, as well as creep-fatigue and low-cycle fatigue properties at higher temperatures, compared to other superalloys.

The unseeded René 88 disk was provided by General Electric Company in the heat treated condition. The disk is 47 cm (18.5 inches) in diameter with an approximate thickness of 3.1 cm (1.2 inches). This alloy is commonly known as René 88DT (DT: damage tolerance). The seeded René 88 was prepared by GE Aircraft Engines by Powder Metallurgy (P/M) processing where alumina (Al_2O_3) seeds were added to the powders. Fine powders of René 88 alloy and Al_2O_3 particles were mixed and isostatic pressed into compacts. The seeded and pressed compact was then sent to Wyman-Gordon forgings Inc. in Houston, TX for forging and heat treatment to produce a particular grain size. The final geometry of the seeded and forged material is about 30 cm (13 inches) in diameter and 8.6 cm (3.4 inches) in thickness.

The nominal composition of René 88 DT is provided in Table 4.1. The weight and the sizes of the seeds were added in the powder are given in Table 4.2. Two seed sizes were used. Small mesh seeds were intended to represent the upper end of the distribution that would normally be present in -140 mesh powder. Large -80/+100 mesh seeds were intended to represent inclusions arising from contamination.

4.2 Specimen

4.2.1 Specimen Geometry

The fatigue specimens were machined according to the procedures followed by GE. Primary considerations in the design of a fatigue specimen beyond the geometry of the specimen/grip interface are the elimination of stress raisers in the gage section and proper amounts of effective volume and effective surface area appropriate for the study. The groups of material (unseeded René 88DT and seeded René 88) each with two different specimen sizes were used in this study. The dimensions of the specimens are given in Figure 4.1.

Table 4.1: The nominal composition of René 88 DT [85]

Element	Cr	Co	Mo	W	Ti	Al	Nb	C	Zr	B	Ni
% weight	16	13	4.0	4.0	3.7	2.1	0.7	0.03	0.03	0.015	Balance

Table 4.2: The seeds weight, size and density [86]

Seed type	Times through screen	Mesh size	Avg. seed wt. (mg)	Seed size (cc)	Seed density (mg/cc)
Feepa 100	3	-80+100	0.007835	3.00E-6	2612
ANSI 150	1	-140+70	0.002050	4.39E-07	4670

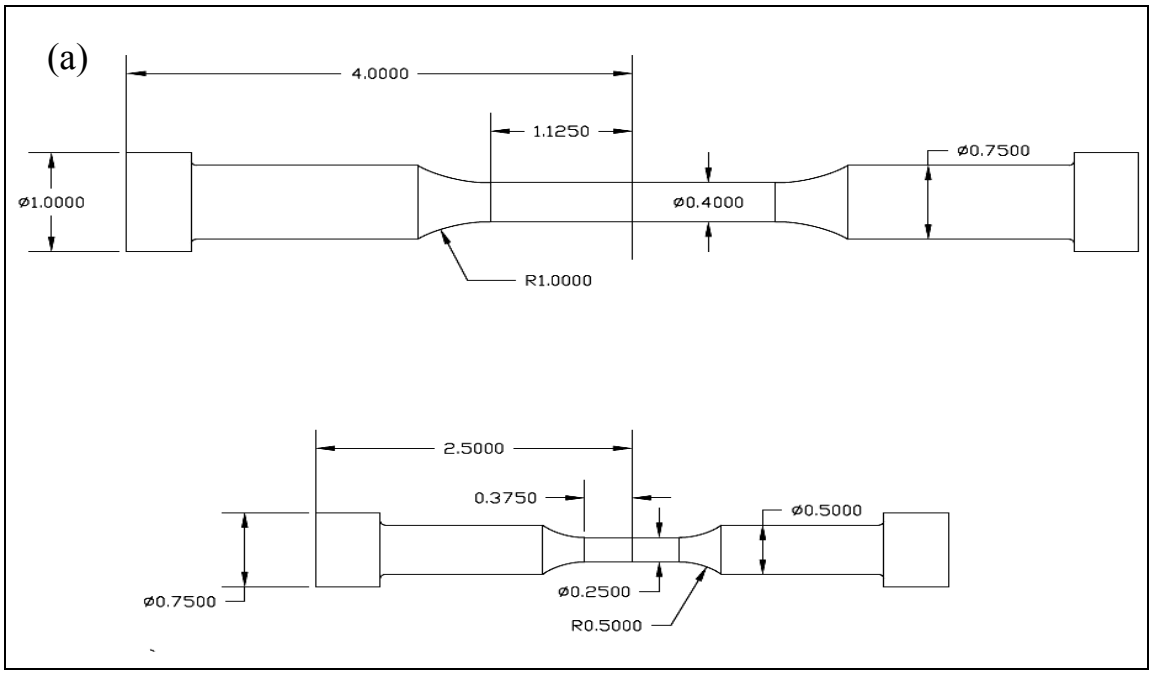

Figure 4.1 The button head specimen used in this study (a) Specimen geometry. All dimensions are in inches (b) Photograph showing a large and a small specimen

The larger specimen had a 10.16 mm diameter reduced cross section in a 57.15 mm gage length. The smaller specimen had 6.35 mm diameter reduced cross section in a 19.05 mm gage length. The specimen sizes were designed to influence the occurrence probabilities of the inclusions (Table 4.3).

4.2.2 Specimen Fabrication Process

Specimen blanks were cut from the disk using a band saw. Figure 4.2 illustrates the small and large René 88 blanks that were used to make the specimens. Figure 4.3 and 4.4 illustrates the two billets (seeded and unseeded) along with a lay out of how the specimen blanks were oriented in space. The large blanks were about 25.4 mm square section and by 114.3 mm in length. The smaller blanks were 19.05 mm square section and 63.5 mm in length. The final specimen preparation was done by Metcut Research Inc., Cincinnati. This included friction welding of Inconel 718 end pieces to each René 88 alloy blank and machining according to GE drawing. Final finishing was done by low stress grinding and mechanically polishing to an average surface roughness of 8 Ra.

Table 4.3: Specimen dimensions

	Gage section properties			
	Small specimen		Large specimen	
	Unseeded	Seeded	Unseeded	Seeded
Length, mm	19.05	19.05	57.15	57.15
Diameter, mm	6.35	6.35	10.16	10.16
Cross section area, mm^2	31.67	31.67	81.07	81.07
Volume, mm^3	603.30	603.30	4633.33	4633.33

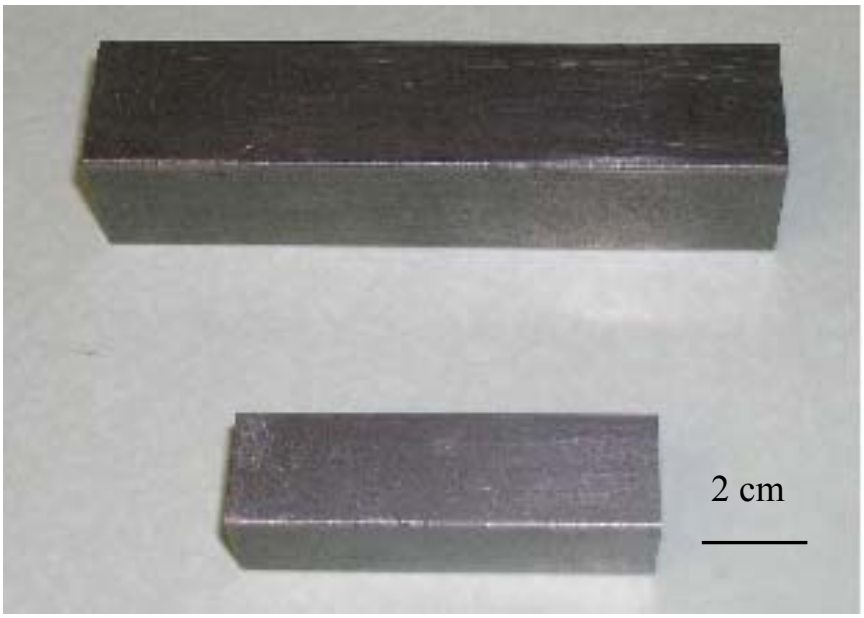

Figure 4.2 Photograph of a small and a large billet.

4.2.3 Microstructure

Samples for metallography were prepared by grinding with silicon carbide papers and then polishing with Al_2O_3 slurries to a fine finish of 1 μm. The final polishing was performed using 0.05μm colloidal silica. The samples were etched using a solution of composition:

100 cc CH_3OH + 100 cc HCL + 5 gm $CuCl_2$.

Grain size measurements were made using an Olympus GX51 optical microscope equipped with a PAXCAM digital camera. Microstructures of the seeded and unseeded materials are shown in Figure 4.5 and Figure 4.6, respectively. The grain size was determined by the linear intercept method (Figure 4.7) over an inspection area of about 75 cm^2. Table 4.4 shows the grain size data for the seeded and unseeded materials.

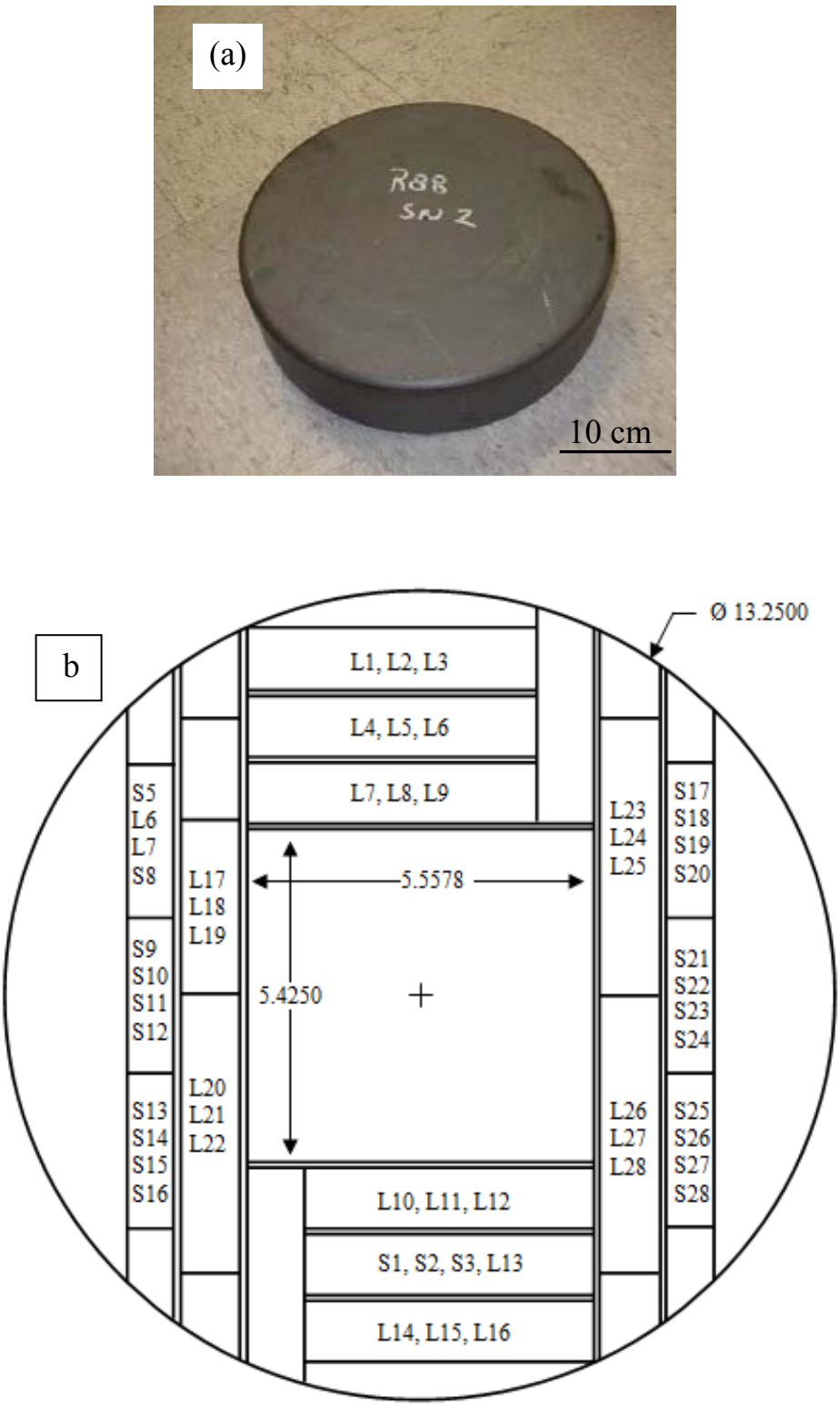

Figure 4.3 René 88 disk and the specimen blanks lay out (a) Photograph of seeded René 88 disk after forging. (b) Top view of the disk showing how specimen blanks were oriented.

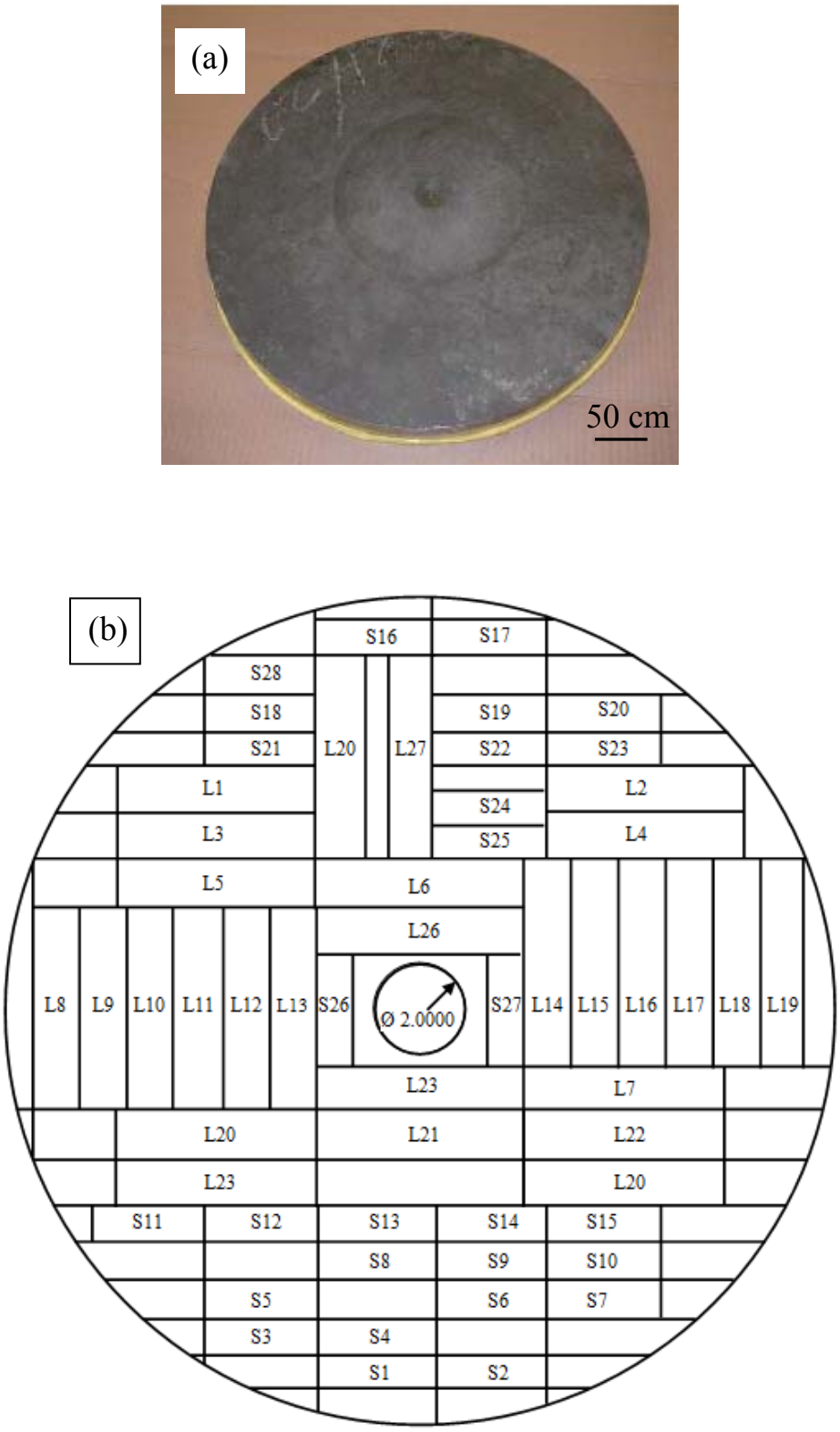

Figure 4.4 René 88DT disk and specimen blanks lay out (a) Photograph of unseeded René 88DT disk after forging. (b) Top view of the disk showing how specimen blanks were oriented.

Figure 4.5 Optical micrograph of unseeded René 88DT grain structure. 200X

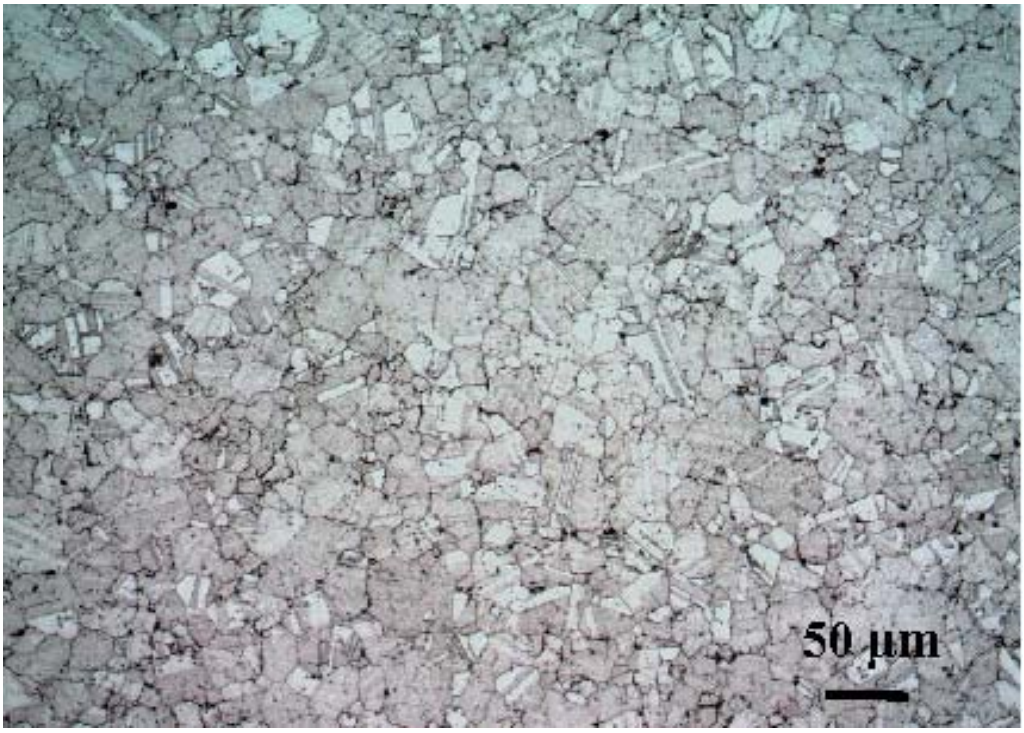

Figure 4.6 Optical micrograph of seeded René 88 grain structure. 200X

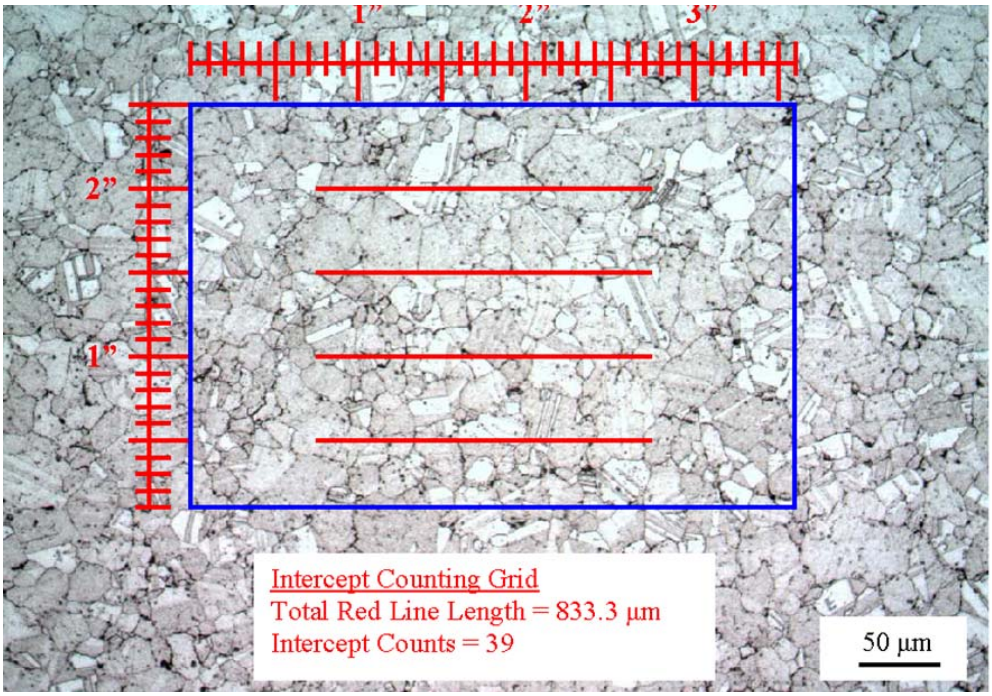

Figure 4.7 Example of grain size measurement by the intercept method. 200X

Table 4.4: Grain size measurement data for the materials

	Unseeded René 88DT	Seeded René 88
Photo Mag.	200	200
Count Length (µm)	833.3	833.3
Intercept Count 1	43.5	39
Intercept Count 2	39.5	40.5
Intercept Count 3	35	39
Intercept Count 4	43	46
Intercept Count 5	45	35.5
Intercept Count 6	46	44
Avg. of Counts	42	40.7
Avg. Intercept Distance (µm)	19.84	20.47

The size distributions of inclusions in both unseeded René 88DT and seeded René 88 were determined using image analysis software, **Image J**. For each material, a large set of images of contiguous regions was captured over an inspection area of 1726 mm^2. Figure 4.8a, 4.8b and 4.9a, 4.9b illustrate examples of images for the seeded René 88 and unseeded René 88DT, respectively. Figure 4.8c and 4.9c show the inclusion size distribution for both the materials.

4.3 Testing Equipment

4.3.1 Fatigue Testing

Fatigue testing was performed using a MTS 810 servohydraulic test system equipped with TESTSTAR II digital controller. A Pentium PC with the fatigue test software enabled the control, execution and analysis of tests. The fatigue tests were performed in tension-tension mode at the stress ratio R of 0.005 and at the frequency of 5 Hz. The test was stopped if the test specimen endured more than 10^7 cycles. Fatigue tests were conducted in laboratory air and at 650^{o}C. The details of induction heating of the specimens, temperature control and grip system design are provided in the following sections.

4.3.2 Induction Heating of Fatigue Specimens

In order to perform sustained fatigue testing at 650^{o}C for sustained periods of time, the specimens were heated by Ameritherm solid-state induction heating system. (HOTSHOT 5 kW and 250 kHz). The most efficient coil design was found by trial and error in order to maintain the specimen gage section temperature at 650^{o}C. Two thermocouples were used to control the induction heater power output. The specimen

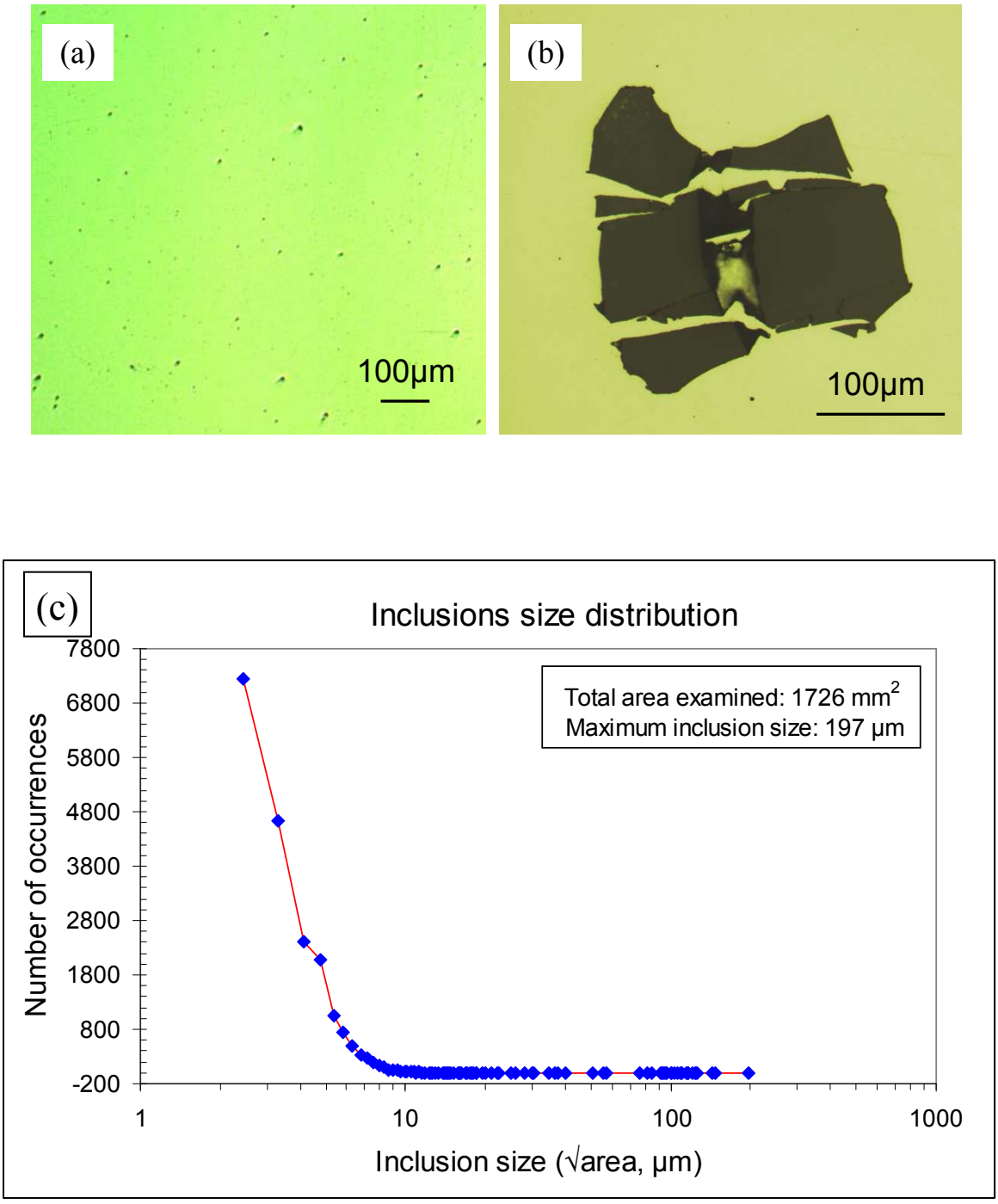

Figure 4.8 Optical micrographs of (a) small size and (b) big size inclusions and (c) the plot of number of occurrences versus the inclusion size in seeded René 88 alloy.

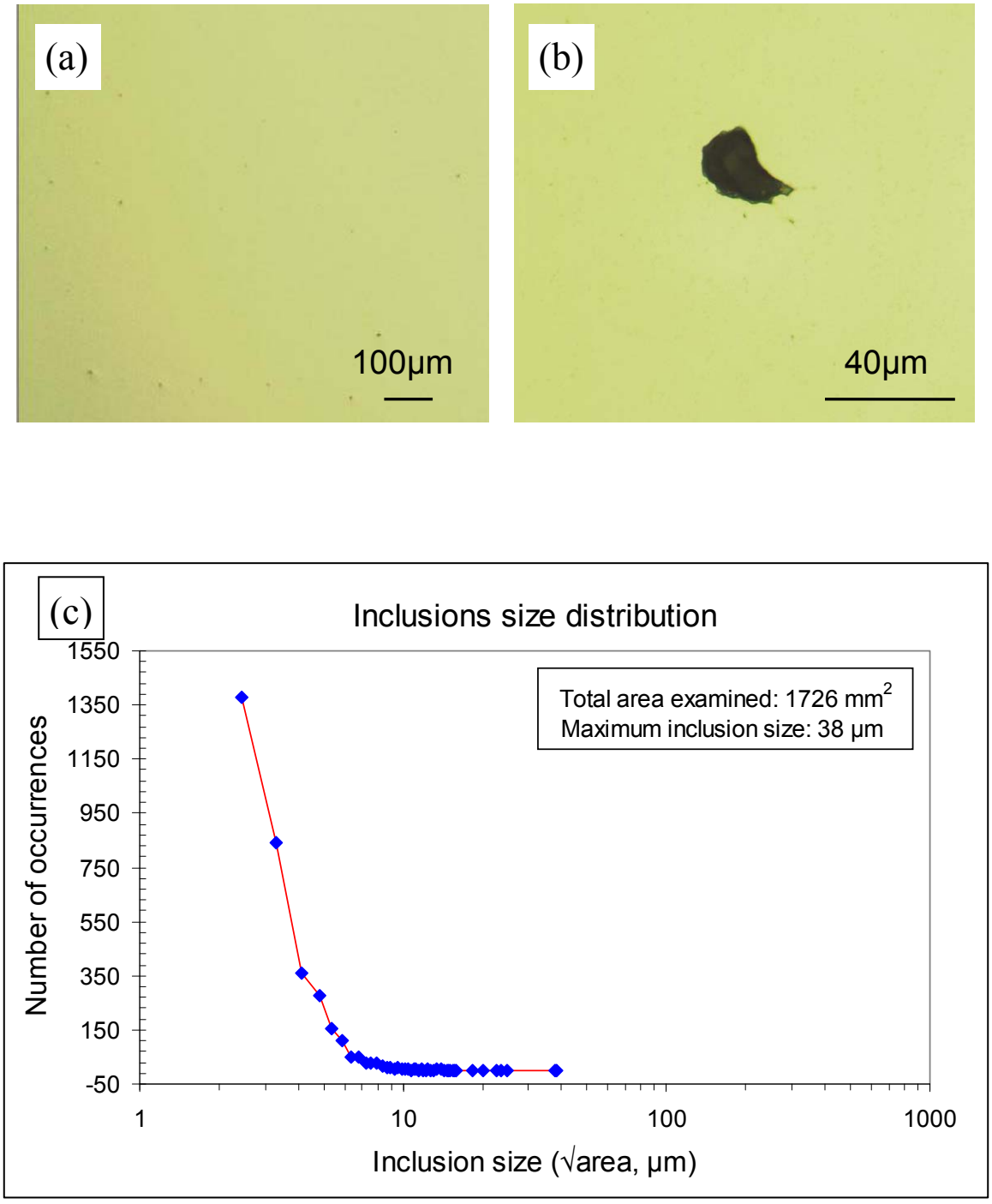

Figure 4.9 Optical micrographs of (a) small size and (b) big size inclusions and (c) the plot of number of occurrences versus the inclusion size in unseeded René 88DT alloy.

temperature was controlled by a Yokokawa controller using the thermocouple spot welded to the edge of the shoulder section of the specimen. Another controller with relay switch acted as the shut-down device with the thermocouple spot welded to the edge of the bottom shoulder. The first controller was used to maintain the desired temperature across the gage section. The second controller mostly acted as the back-up and also served to shut off the induction heating system after the specimen fracture. The actual temperature distribution in the specimen test or gage section was verified by spot welding a total of five thermocouples onto the specimen, two at the shoulder edges and three in the gage section. The induction coil was adjusted sufficiently to make the two shoulders edge temperatures the same while getting the gage section temperature uniformly to 650^{o}C. The temperature variation in the gage section was controlled to ± 2^{o}C.

4.3.3 Fatigue Test Fixture Design

A special test fixture was designed and constructed to perform the fatigue tests in this study. This is because of the high loads encountered and the requirement of precise specimen alignment. The fixtures consisted of two major parts: the test specimen grip system holding the actual test specimen and the component attachments that connect the grip system to the test machine. The grip was designed to reduce any eccentricity in loading and to maintain a uniaxial stress state.

A drawing of the test fixture and photograph including the gripping system and components is shown in Figure 4.10 and 4.11. The upper and lower connecting rods are threaded into the load cell and actuator of the MTS machine. Threaded coupling in between two connecting rods is used to adjust the height of the grid and allow the collet-

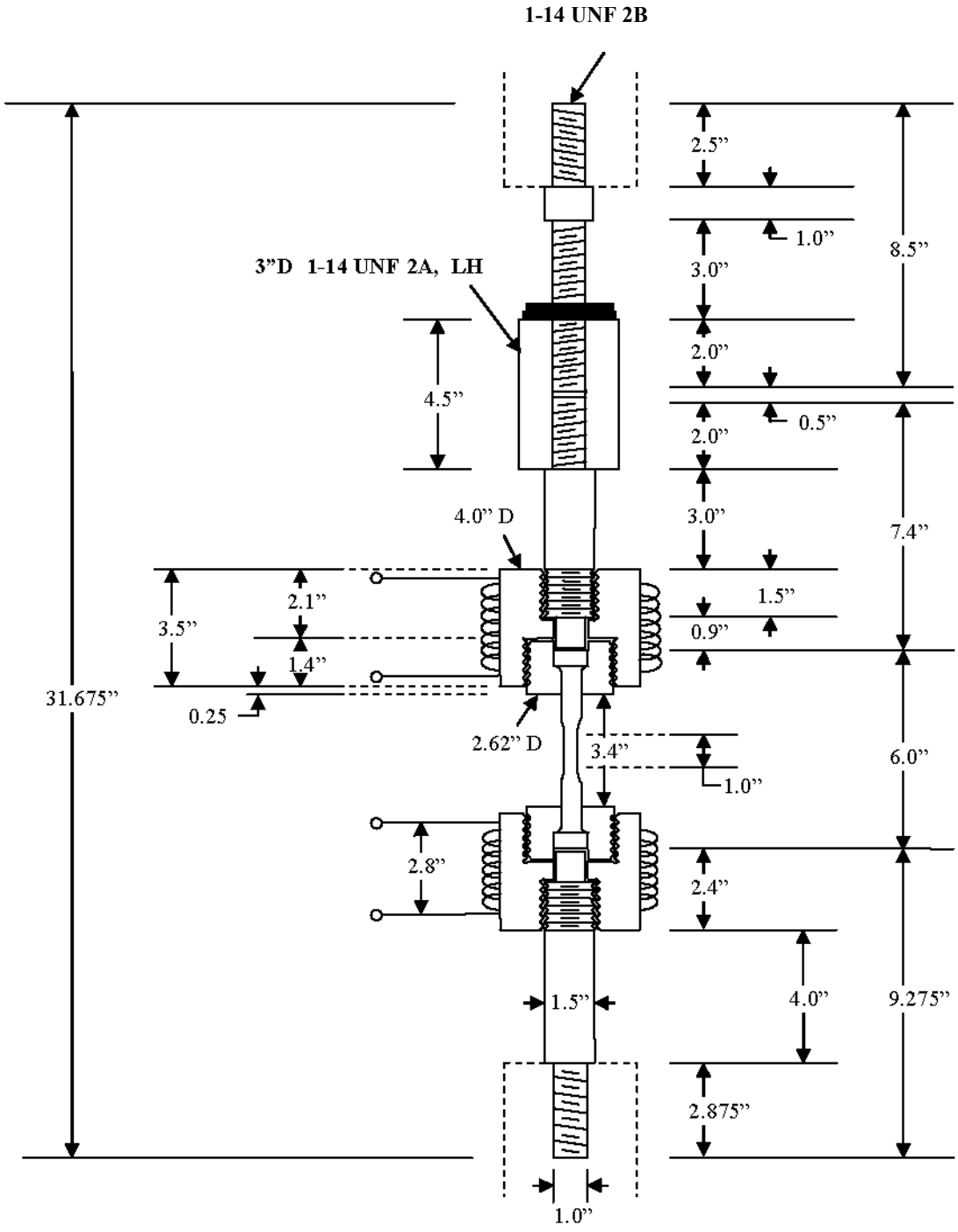

Figure 4.10 Drawing of grip system.

Figure 4.11 Photograph of assembled grip system.

housing to be completely unscrewed and removed. A split-collet arrangement acts as the grip interface holding the button-head of the specimen. The upper and lower split-collets secure the specimen into test position. The split-collets are threaded inserts in the collet housings. Surrounding the housings are copper tube coils to cool the housing by circulating a cooling fluid.

The material used for making this grip system and components was Inconel 718. Inconel 718 is a precipitation hardenable Ni-base superalloy and it is well suited for applications requiring high strength at temperatures up to 1300°F. The following heat treatment was used to obtain the best combination of tensile and stress rupture properties to ensure long term structural integrity under test conditions. After rough machining IN718 to approximate sizes, the pieces were heat treated following AMS 5663 specifications: Solution treatment at 954°C (1750°F) for one hour and water quenched to room temperature follow by age hardening at 718°C (1325°F) for 8 hours and furnace cool 38°C (100°F) /hr to 621°C (1150°F) and hold at 621°C (1150°F) for 8 hours and then air cool. Final machining to the exact dimensions was done after the heat treatment.

4.3.4 Specimen Alignment

Precise specimen alignment to achieve a pure tension loading is very important for the fatigue tests of this research. Any misalignment can introduce bending on the sample and can cause crack initiation on the high tension side. For the purpose of the present study, the crack initiation side section should be random and should be influenced by the actual crack initiation defects in the material. Repeated failures on one particular side of the specimen usually indicate that the machine is out of alignment. The fatigue testing was performed in a MTS 810 system. The load frame was equipped with a ±100

KN force transducer. To produce valid test results, it was necessary to ensure that there were no bending stresses arising out of misalignment of the load train. The misalignment was forced to be largely due to the angular and concentric components arising either at the machine crosshead attachment or at the individual components of the grip system.

A fatigue specimen, with a strain gage attached to the mid-section was used to adjust the alignment for the range of test loads. The strain signal was acquired using a 2200 signal conditioning amplifier manufactured by the Measurement Group (Vishy). Figure 4.12 shows an example of a strain gage attached to the specimen under test. Strains measurement was taken 0, 90, 180 and 270 degree location by rotating the specimen. Several preliminary tests showed that fixture misalignment predisposes crack initiation to one side. Figure 4.13, 4.14 illustrate a couple of examples where the specimens were severely misaligned. Several adjustments including angular and concentric were made in order to achieve the perfect alignment. Figure 4.15 and 4.16 show the load strain plots prior to and after fully aligning the grip system.

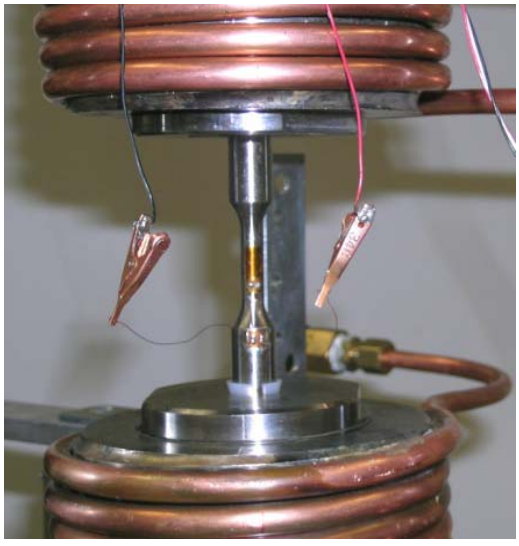

Figure 4.12 The strain gage attached specimen that was used to adjust the loading train.

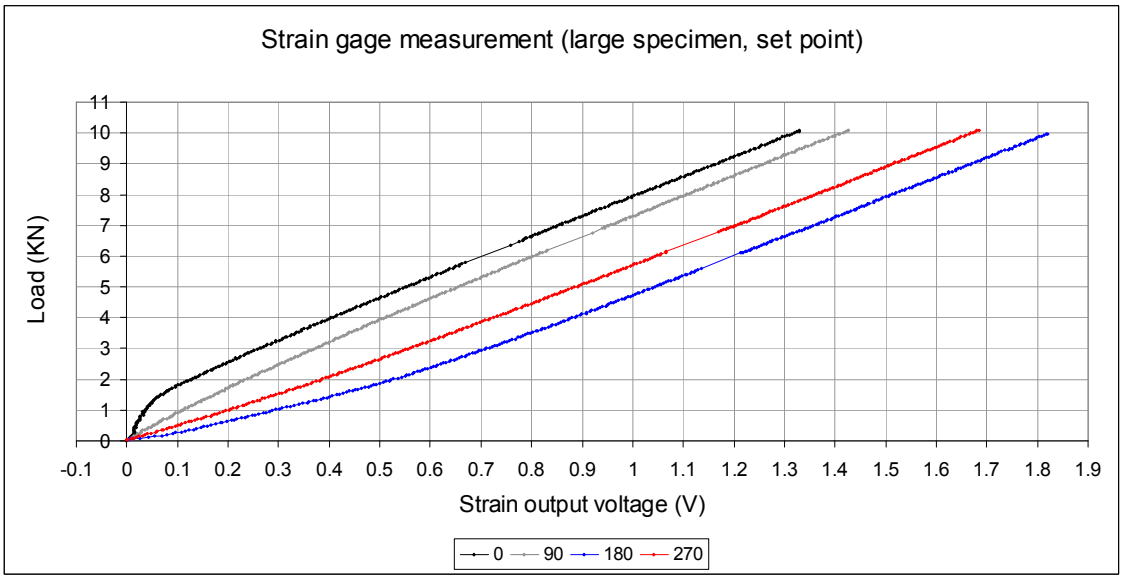

Figure 4.13 Strain as a function of load with the strain gage positioned at 0, 90, 180 and 270 orientations. The measurements correspond to misaligned load train.

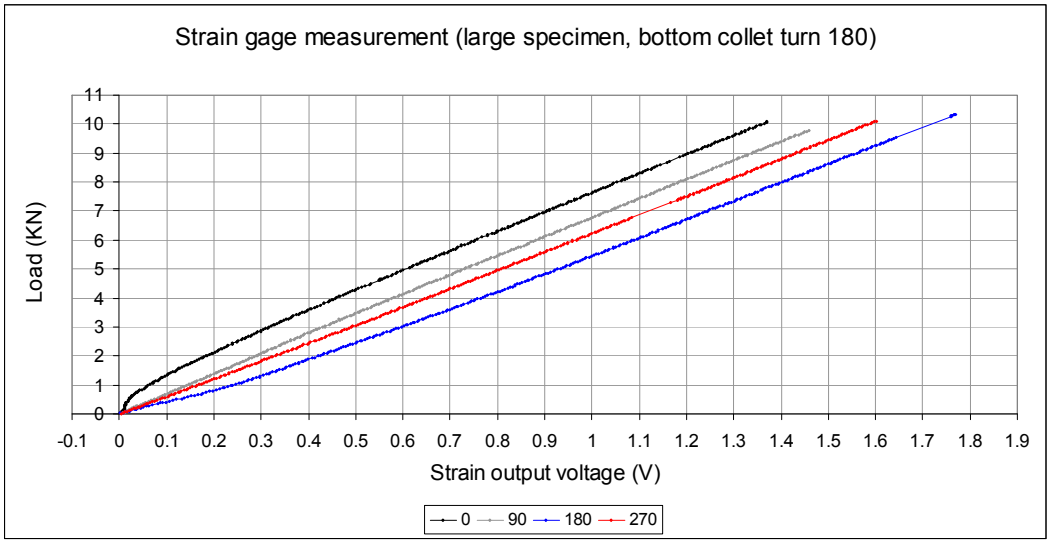

Figure 4.14 An illustration of strain output due to misalignment strain reading from 0, 90, 180, 270 positions after rotating the bottom collet by 180^{o}, with respect to the position in Figure 4.13.

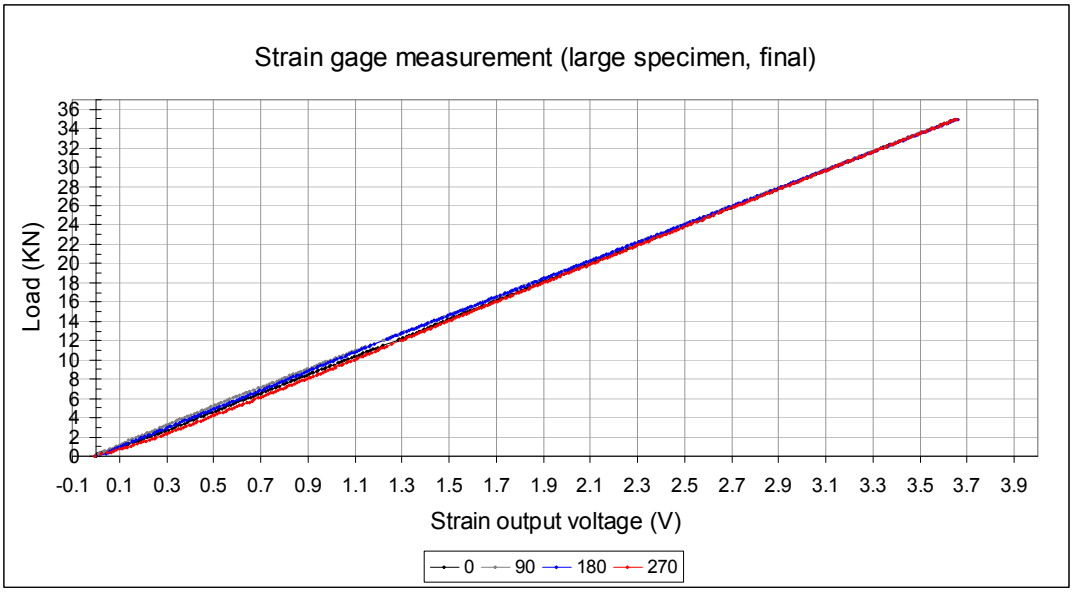

Figure 4.15 Strain output at 0, 90, 180 and 270 orientations after near-perfect alignment of the large fatigue specimen.

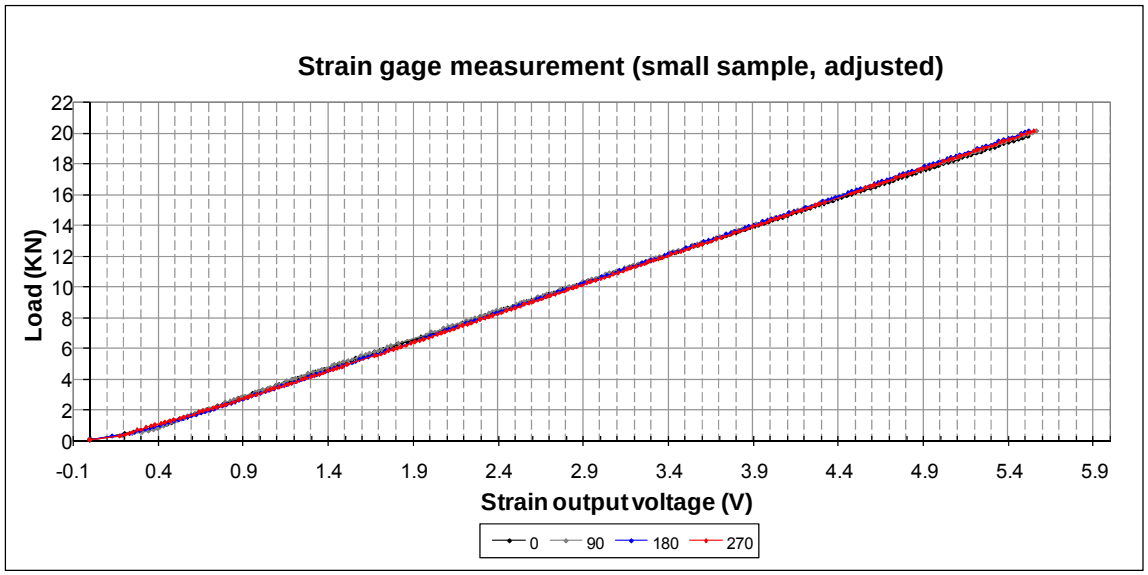

Figure 4.16 Strain output at 0, 90, 180 and 270 orientations after near-perfect alignment of the small fatigue specimen.

CHAPTER 5

RESULTS AND DISCUSSION

5.1 Materials Characterization

One objective of the research was to relate the microstructural parameters such as inclusion size and density to fatigue properties specifically crack initiation mechanisms. So, it was necessary to check that the matrix microstructural conditions excluding the inclusions did not change after the tests. To examine the effect of exposure to test temperature, on the γ - γ' matrix microstructure, a specimen was subjected to 650^{o}C for 95 hours. Figure 5.1 shows the microstructures with no exposure and 650^{o}C exposure, taken at low as well as higher magnifications. There was no discernable difference in the microstructures of both specimens.

The microstructural states of the specimens after 650^{o}C/95 hours of no load exposure and then fatigue tested were also compared to determine if the high temperature fatigue loading altered the matrix microstructure. Figures 5.2, 5.3 and 5.4 show the SEM images of the no load 650^{o}C/95 hours specimens as well as the specimens in which surface failure and subsurface failure occurred, at three different magnifications. The test conditions for surface failure were 1150 MPa load and 650^{o}C/0.2 hours exposure. For the subsurface failure sample, 1000 MPa was the applied load and 650^{o}C/159 hours exposure.

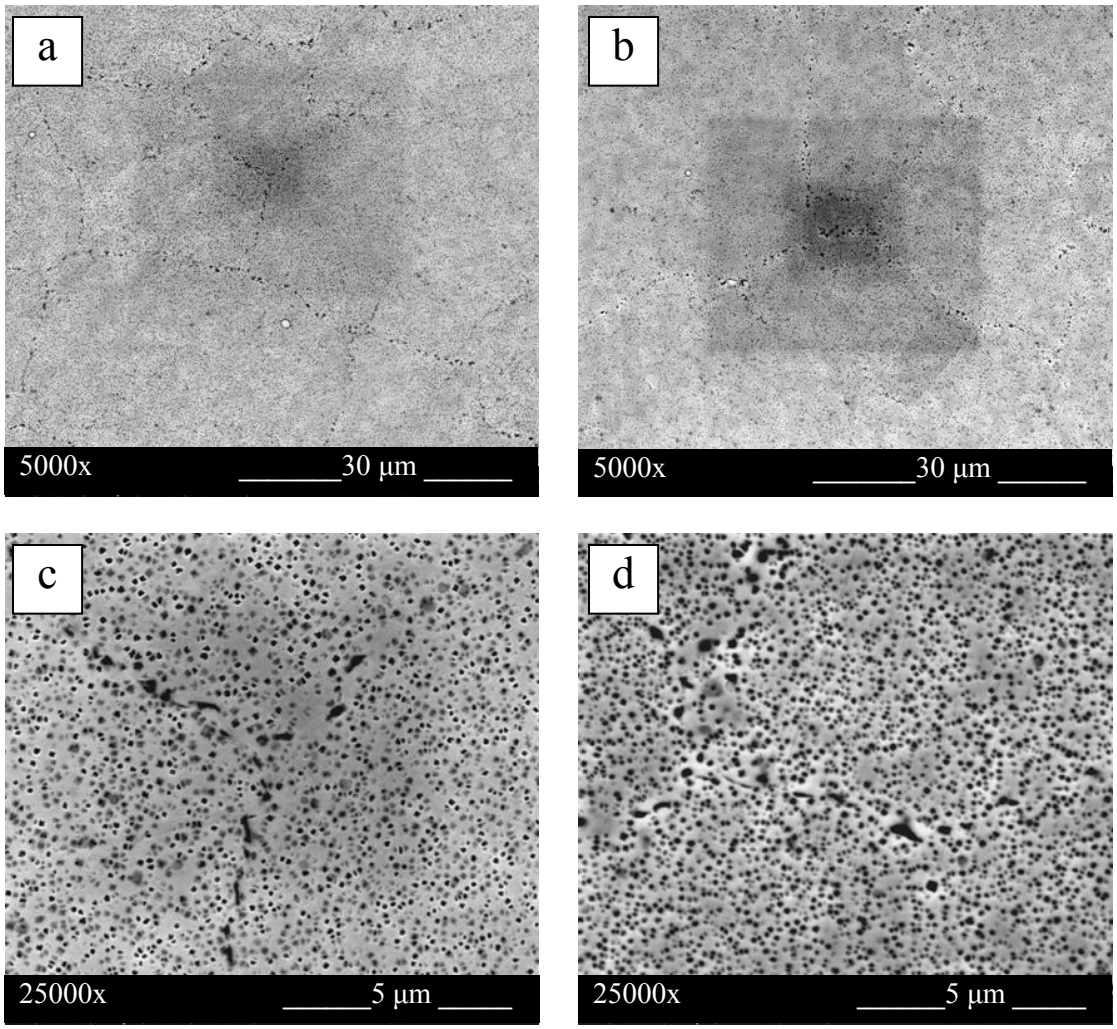

Figure 5.1 SEM micrographs of microstructure (a, c) with no exposure and (b, d) after exposure to 650^{o}C for 95 hours

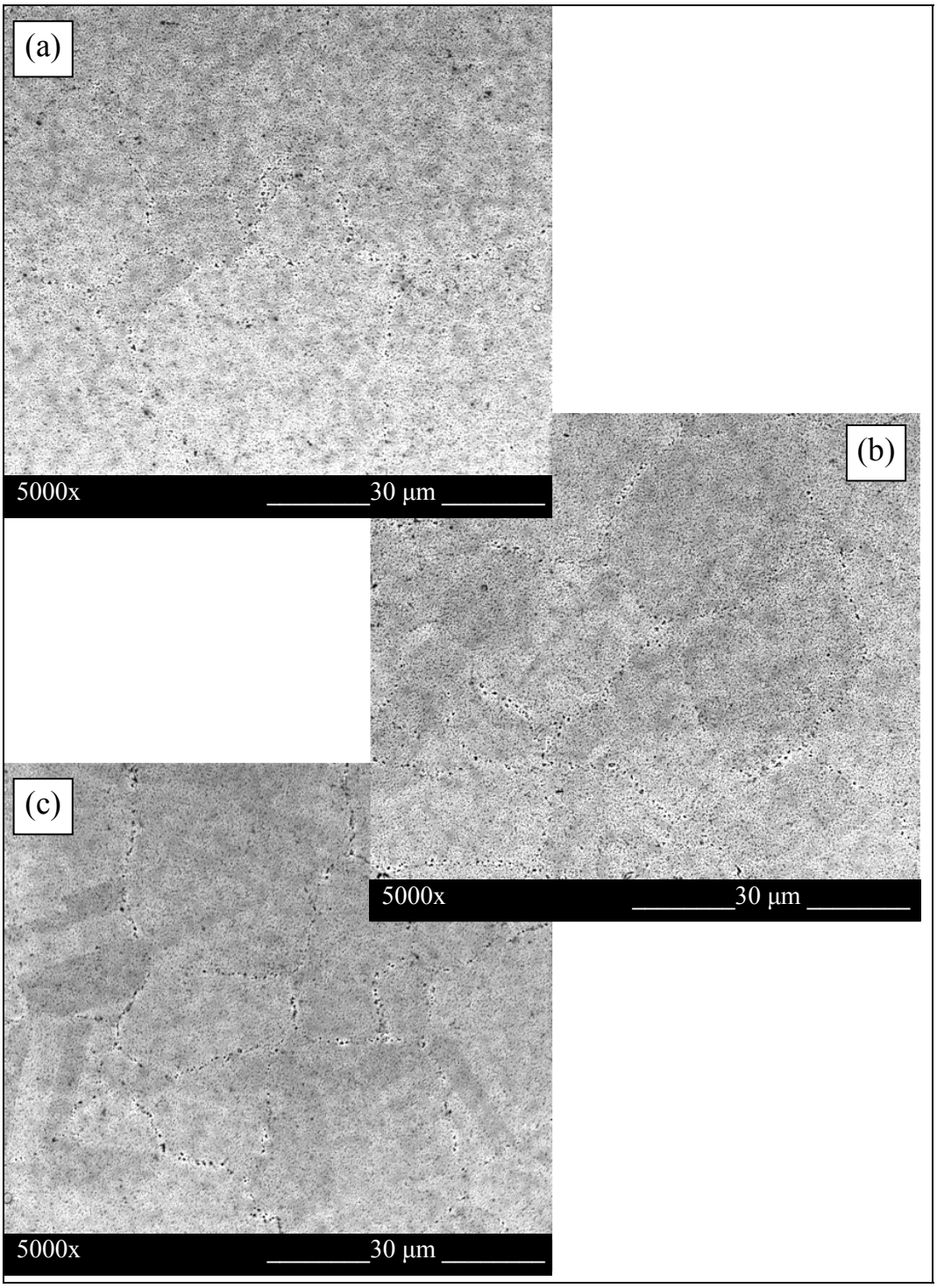

Figure 5.2 SEM microstructures of the baseline material and fatigue tested specimens at 5000X (a) Baseline material after 650^{o}C/95 hours exposure and no load (b) Surface initiated failure specimen (c) Internal initiated failure specimen.

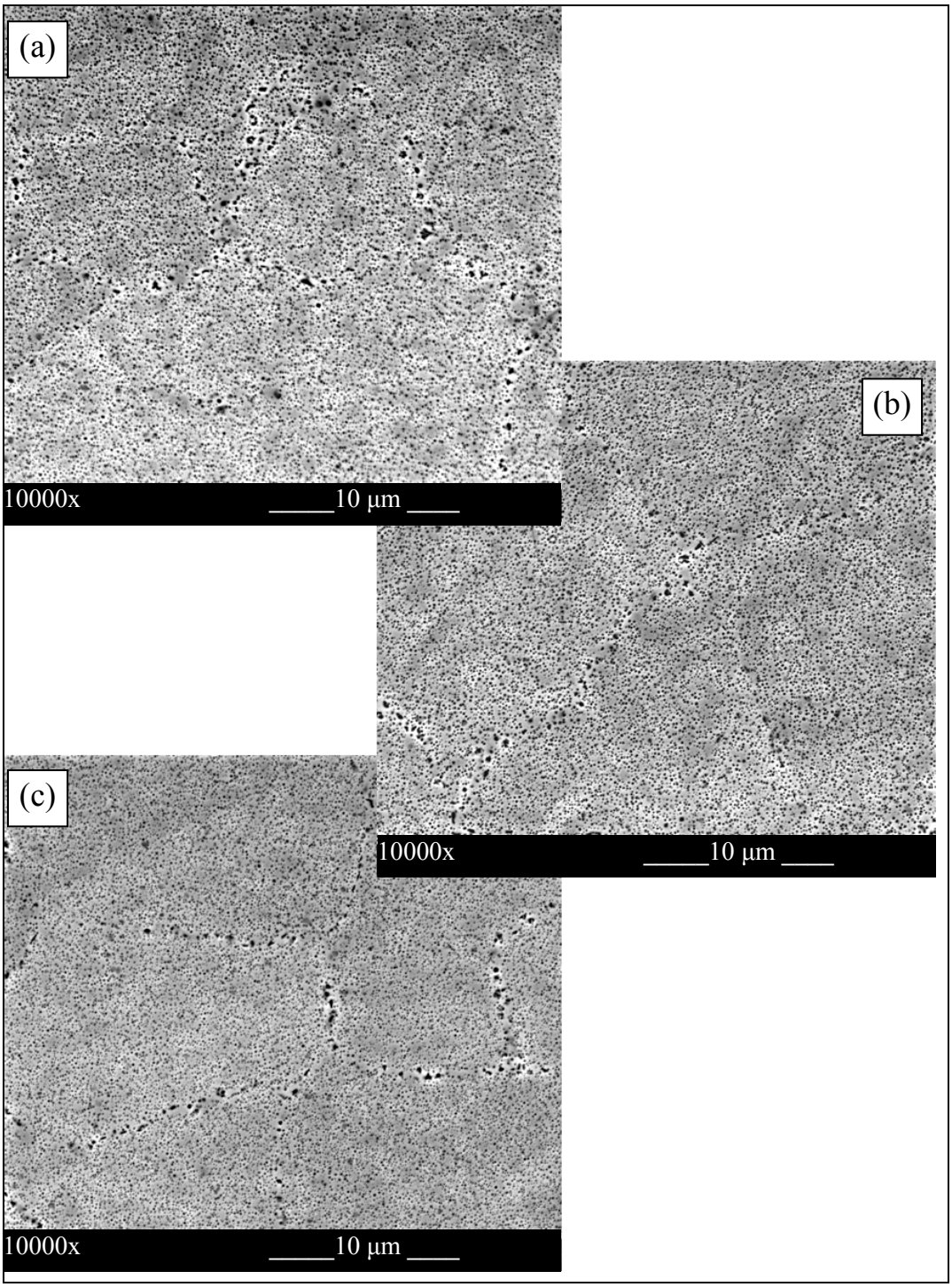

Figure 5.3 SEM microstructures of the baseline material and fatigue tested specimens at 10000X (a) Baseline material after 650^{o}C/95 hours exposure and no load (b) Surface initiated failure specimen (c) Internal initiated failure specimen.

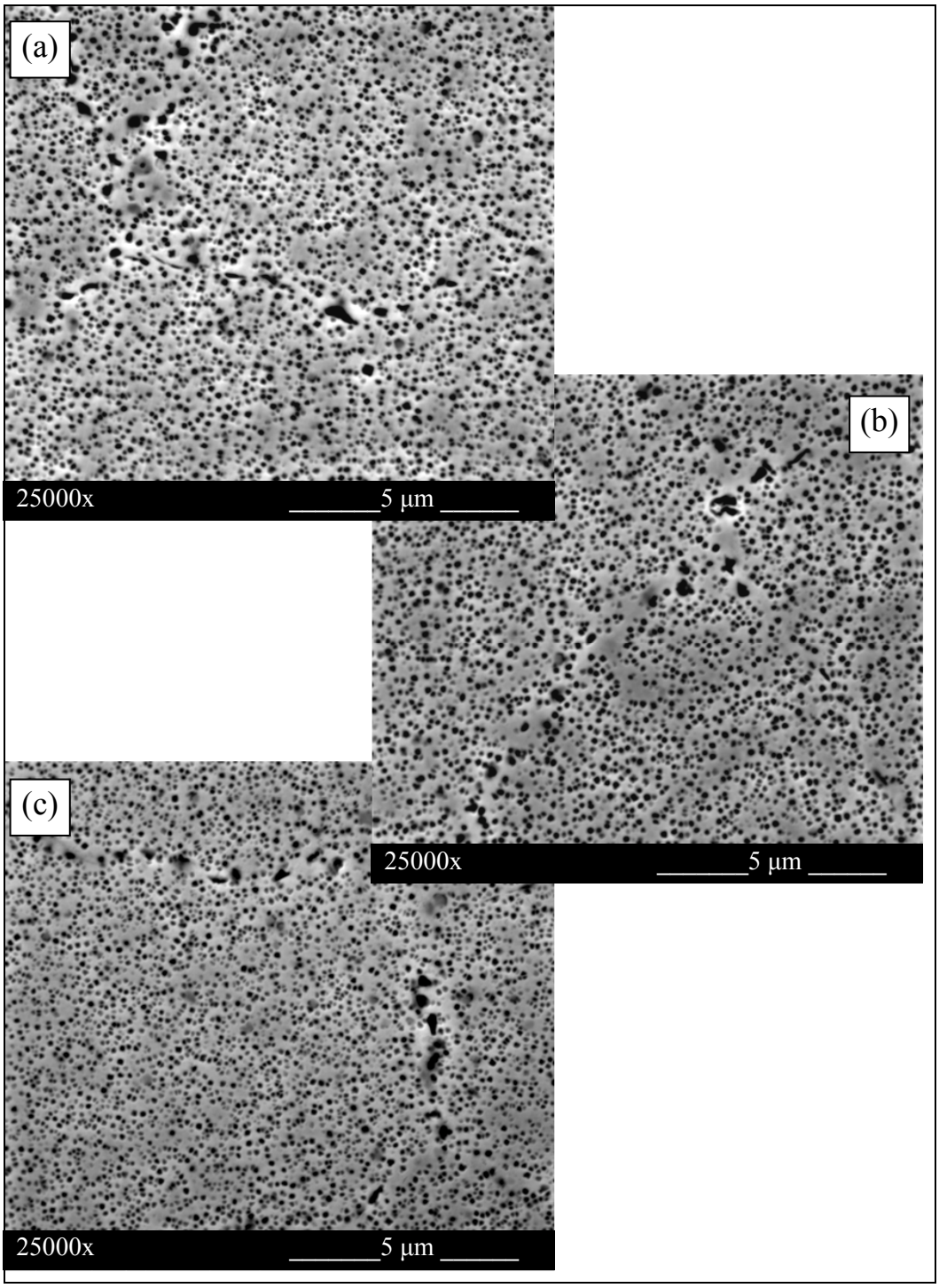

Figure 5.4 SEM microstructures of the baseline material and fatigue tested specimens at 5000X (a) Baseline material after 650^{o}C/95 hours exposure and no load (b) Surface initiated failure specimen (c) Internal initiated failure specimen.

X-ray diffraction (XRD) analyses of the grip sections and material volume in the test sections and near the fracture surfaces were also performed to see if there were any microstructure change due to fatigue. Figure 5.5 shows the resulting XRD scans from the three samples. The XRD scans indicate that there was no significant difference between the three specimens in term of γ - γ' crystallography or carbide/boride phase content.

5.2 Fatigue Test Results

Fatigue tests were performed at 650^{o}C in a closed-loop servohydraulic testing machine with induction heating to maintain the temperature. Fatigue tests were conducted in load control conditions using a sine waveform loading at a frequency of 5 Hz. The ratio of minimum to maximum load was R=0.005. Two different test specimen sizes of René 88DT unseeded material and seeded René 88 material were tested. The general goal was to completely map the stress-life curves in an attempt to capture the multiple/competing failure modes over a wide range of stress–life domain. Theoretically, larger specimens should fail at lower stress than smaller specimens. This is mainly due to the higher probability of flaws being present in larger volume. Tables 5.1 and 5.2 summarize the fatigue test data for small unseeded and seeded René 88 specimens, respectively, including stress range, cycles to failure and the characteristics of the crack initiation site.

The fatigue test data for large unseeded and seeded specimens are summarized in Tables 5.3 and 5.4, respectively. The data demonstrate the substantial differences between the numbers of cycles to failure for specimens corresponding to the surface initiation and that corresponding to internal crack initiation.

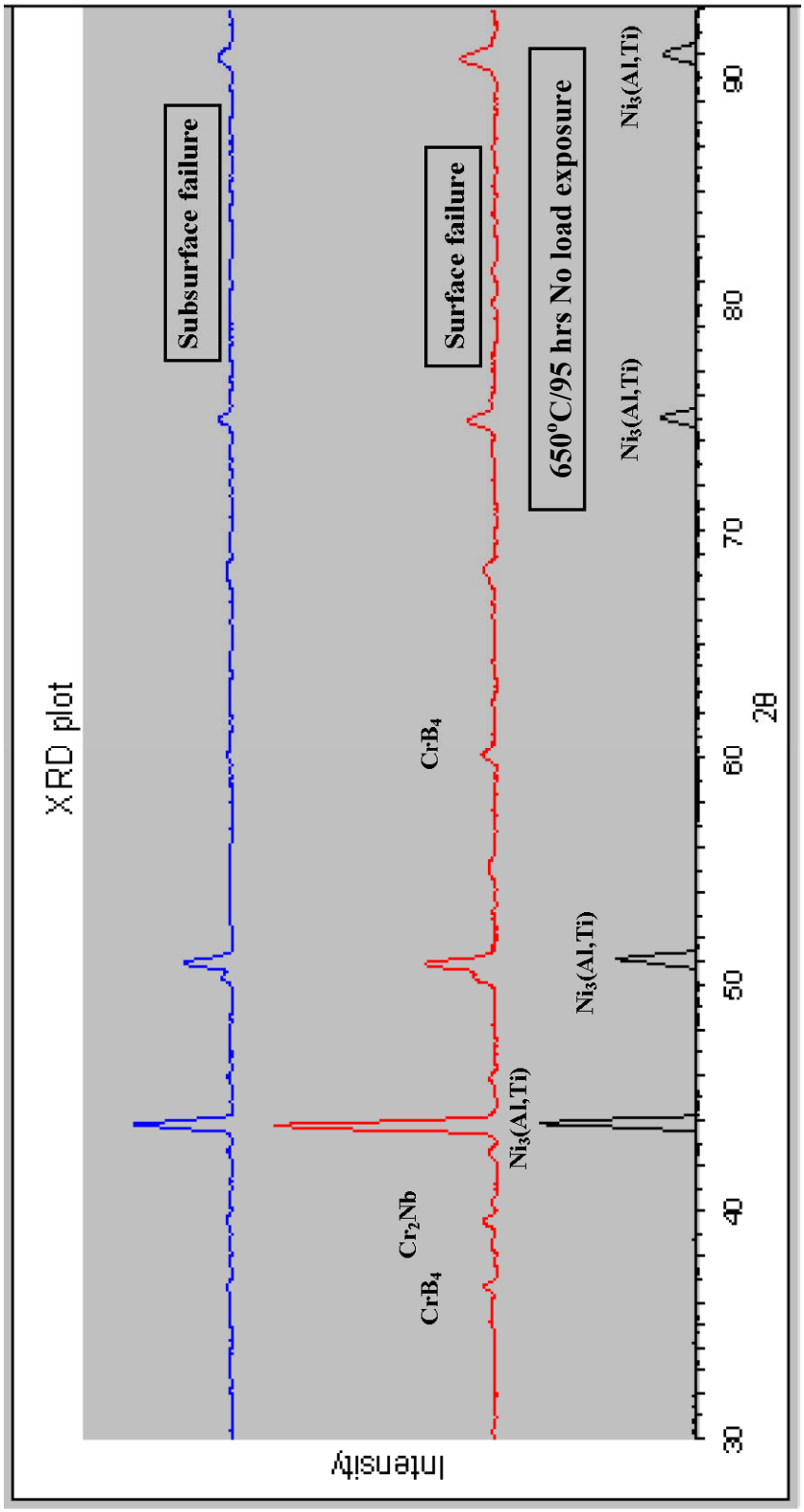

Figure 5.5 Comparison of X-ray diffraction patterns for baseline material, surface failure and internal failure samples

Table 5.1: Summary of fatigue test results from small unseeded specimens of René 88DT

Specimen ID	Max. Stress (MPa)	Cycles to Failure	Fatigue crack initiation site	Fracture mechanism at facture origin	Effective size of the inclusion at initiation site √area (μm)	Distance from surface* (mm)
UD1-S17	1150	2,997	Surface	Faceted intergranular	-	-
UD1-S18	1125	2,576	Surface	Faceted intergranular	-	-
UD1-S13	1100	10,575	Surface	Faceted intergranular	-	-
UD1-S19	1090	9,397	Surface	Faceted intergranular	-	-
UD1-S15	1075	34,796	Surface	Faceted intergranular	-	-
UD1-S12	1050	74,762	Surface	Faceted intergranular	-	-
UD1-S28	1040	423,320	Surface	Tungsten particle	-	-
UD1-S14	1050	2,643,501	Internal	Inclusion	31.2	0.068
UD1-S16	1025	2,735,308	Internal	Inclusion	19.7	1.481
UD1-S11	1000	2,864,473	Internal	Inclusion	25.7	1.635
UD1-S21	980	4,725,134	Internal	Grain facet	111.0	0.078
UD1-S22	970	801,380	Internal	Inclusion	35.9	1.762
UD1-S23	970	2,000,946	Internal	Grain facet	68.9	0.059
UD1-S24	960	187,815	Internal	Inclusion	50.9	0.829
UD1-S25	960	1,707,944	Internal	Inclusion	44.8	2.404
UD1-S26	940	1,236,583	Internal	Grain facet	155.0	0.572

* The distance from specimen edge to center of the fracture origin.

Table 5.2: Summary of fatigue test results from small seeded specimens of René 88

Specimen ID	Max. stress (MPa)	Cycles to failure	Fatigue crack initiation site	Fatigue mechanism at facture origin	Effective size of the inclusion at initiation site √area (μm)	Distance from surface* (mm)
SD1-S5	960	5,715	Surface	Seeded inclusions	166	-
SD1-S22	880	6,553	Surface	Seeded inclusions	166	-
SD1-S2	1000	7,269	Surface	Seeded inclusions	156	-
SD1-S19	880	7,501	Surface	Seeded inclusions	156	-
SD1-S12	640	10,789	Surface	Seeded inclusions	173	-
SD1-S1	900	10,921	Surface	Seeded inclusions	149	-
SD1-S24	800	11,162	Surface	Seeded inclusions	148	-
SD1-S8	720	12,551	Surface	Seeded inclusions	152	-
SD1-S16	700	38,818	Surface	Seeded inclusions	178	-
SD1-S9	840	69,989	Internal	Seeded inclusions	156	0.164
SD1-S15	820	105,277	Internal	Seeded inclusions	164	0.111
SD1-S20	860	107,446	Internal	Seeded inclusions	141	0.848
SD1-S10	720	241,320	Internal	Seeded inclusions	243	1.193
SD1-S6	800	283,304	Internal	Seeded inclusions	186	0.934
SD1-S25	680	335,557	Internal	Seeded inclusions	204	1.403
SD1-S7	760	370,468	Internal	Seeded inclusions	152	0.486
SD1-S18	700	383,225	Internal	Seeded Inclusions	219	0.465
SD1-S27	660	587,750	Internal	Seeded inclusions	196	1.182
SD1-S11	680	1,153,570	Internal	Seeded inclusions	191	0.200
SD1-S13	640	1,771,691	Internal	Seeded inclusions	142	0.167
SD1-S26	620	Run-out at 10^7 cycle				
SD1-S14	600	Run-out at 10^7 cycle				

* The distance from specimen edge to center of the fracture origin.

Table 5.3: Summary of fatigue test results from large unseeded specimens of René 88DT

Specimen ID	Max. Stress (MPa)	Cycles to Failure	Fatigue crack initiation Site	Fracture mechanism at facture origin	Effective size of the inclusion at initiation site √area (μm)	Distance from surface* (mm)
UD1-L16	1120	1,505	Surface	Faceted intergranular	-	-
UD1-L15	1100	3,215	Surface	Faceted intergranular	-	-
UD1-L14	1080	9,312	Surface	Faceted intergranular	-	-
UD1-L18	1060	5,588	Surface	Faceted intergranular	-	-
UD1-L6	1050	53,222	Surface	Faceted intergranular	-	-
UD1-L19	1030	9,804	Surface	Faceted intergranular	-	-
UD1-L20	1020	14,623	Surface	Faceted intergranular	-	-
UD1-L8	1000	58,751	Surface	Faceted intergranular	-	-
UD1-L11	960	179,325	Surface	Faceted intergranular	-	-
UD1-L10	940	9,063	Surface	Faceted intergranular	-	-
UD1-L22	940	130,893	Surface	Faceted intergranular	-	-
UD1-L26	920	100,217	Surface	Faceted intergranular	-	-

* The distance from specimen edge to center of the fracture origin.

Table 5.4: Summary of fatigue test results from large seeded specimens of René 88

Specimen ID	Max. stress (MPa)	Cycles to failure	Fatigue crack initiation site	Fatigue mechanism at facture origin	Effective size of the inclusion at initiation site √area (μm)	Distance from surface* (mm)
SD1-L1	1000	3,630	Surface	Seeded inclusions	165	-
SD1-L3	950	3,560	Surface	Seeded inclusions	197	-
SD1-L2	900	9,217	Surface	Seeded inclusions	163	-
SD1-L14	800	5,853	Surface	Seeded inclusions	160	-
SD1-L7	800	7,685	Surface	Seeded inclusions	175	-
SD1-L6	760	11,170	Surface	Seeded inclusions	144	-
SD1-L17	740	16,362	Surface	Seeded inclusions	206	-
SD1-L8	720	31,992	Surface	Seeded inclusions	145	-
SD1-L9	680	12,222	Surface	Seeded inclusions	182	-
SD1L19	680	13,899	Surface	Seeded inclusions	139	-
SD1-L10	660	17,016	Surface	Seeded inclusions	139	-
SD1-L5	700	206,911	Internal	Seeded inclusions	192	2.593
SD1-L16	660	427,949	Internal	Seeded inclusions	222	1.703
SD1-L18	640	453,361	Internal	Seeded Inclusions	224	1.869
SD1-L11	620	443,568	Internal	Seeded inclusions	210	0.278
SD1-L12	600	815,993	Internal	Seeded inclusions	217	2.356
SD1-L13	580	7,717,338	Internal	Seeded inclusions	231	4.349
SD1-L15	560	1,091,527	Internal	Seeded inclusions	225	2.310
SD1-L27	540	2,483,622	Internal	Seeded inclusions	225	1.828

* The distance from specimen edge to center of the fracture origin.

Figure 5.6 illustrates the S-N curve for the seeded and unseeded materials; these are the results obtained using a small specimen. Fatigue lives of the seeded specimen were significantly lower than unseeded specimens. Surface and internal crack initiations were seen both in seeded and unseeded specimens. Internal crack initiation is dominant at low stress amplitudes and high numbers of cycles, whereas surface fatigue crack initiation occurs at high stress amplitudes and low cycles. In the case of small unseeded René 88DT, there seems to be in a plateau region at 1050 MPa, which was close to the yield strength of the alloy (1040 MPa at room temperature, 990 MPa at 650^{o}C). The two regions are separated at about 10^5 cycles. However, in the case of seeded René 88, two separate S-N curves are seen – this is quite similar to the duality of the S-N curve [9, 13].

High-cycle fatigue testing S-N curves of the large seeded and unseeded specimens are presented in Figure 5.7. It is to be noted that the large specimen has a test volume of 7.7 times that of the small specimen. Similar to that observed with small test specimens, lives of seeded specimens were invariably lower than unseeded specimen. Surface and internal crack initiations were seen in the seeded specimens. We can observe the formation of two regions, the first corresponding to short fatigue life at a high stress level, separated by a "step". In the case of large unseeded René 88DT, the trend of the S-N data was that the fatigue life increased with decreasing the maximum stress level. All surface initiations were seen between 920 MPa to 1120 MPa. Further tests are necessary to find results for stresses of less than 920 MPa. These tests have not been successful due to several button head failures, possibly due to stress concentration effects in the long-life regime.

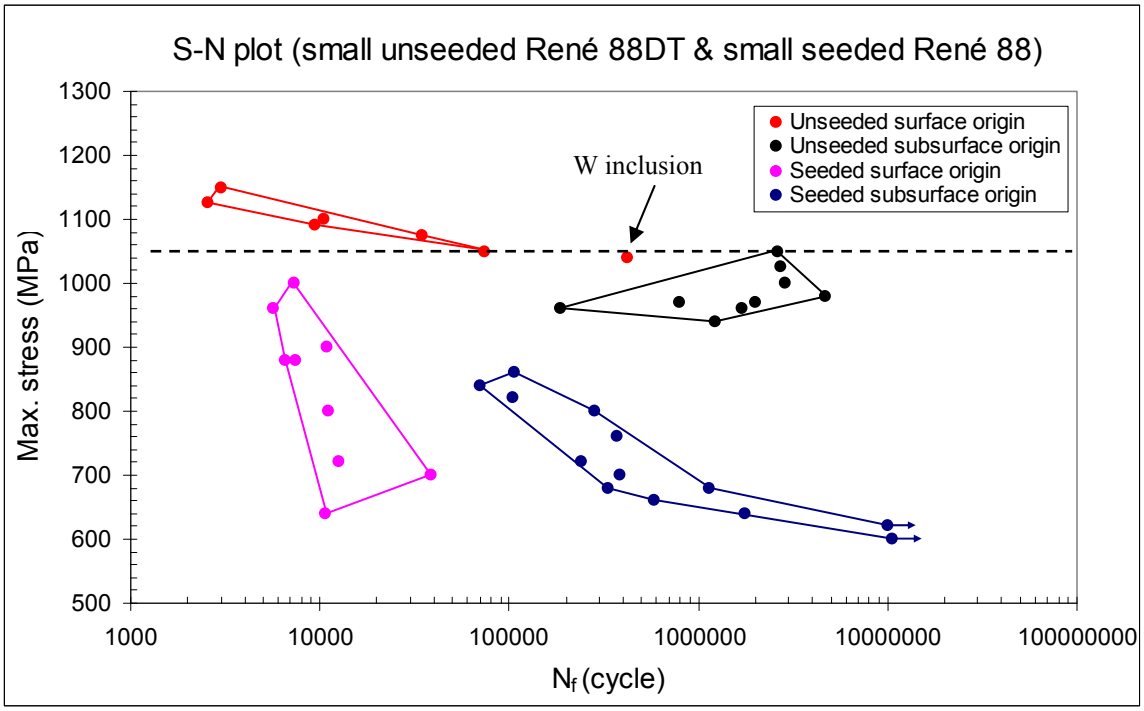

Figure 5.6 S-N fatigue curves of unseeded René 88DT and seeded René 88 obtained using small size test specimens.

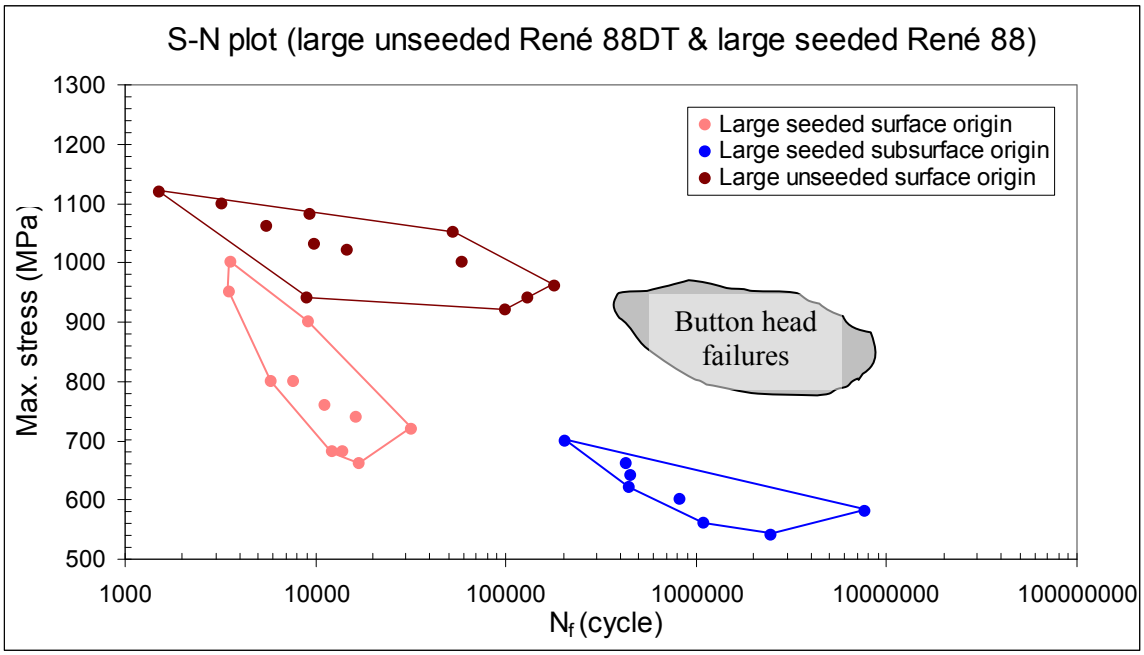

Figure 5.7 S-N fatigue curves of unseeded René 88DT and seeded René 88 obtained using large size test specimens.

As described in the chapter on Experimental Procedure, there is a difference in the geometries of the small specimens compared to the large specimens. The test volume of the large specimen was 7.7 times more than that of the small specimen. Since there is no difference in the microstructures of the specimens, then one can expect longer fatigue lives for the smaller diameter specimens. The larger diameter specimens have a larger volume which increases the probability of the presence of crack-initiating inclusions within the gage section.

5.3 Fatigue Crack Initiation Sites

Fracture surface analysis was performed on the fatigue specimens using low magnification (~10x-60x) stereo microscopes and high magnification Scanning Electron Microscopes (SEM). The objective was to identify the fatigue crack initiator and classify the fatigue failure mechanism. Stereo microscope was used to observe macroscopic features such as oxidation patterns and striation markings that accompany crack initiation and growth on the fracture surface. SEM was used predominantly to determine the inclusions and microstructural details at the crack initiation sites. The objective was to determine the mechanisms associated with fatigue crack initiation in each specimen. It was found that the initiation occurred by either of the two different mechanisms: cracks initiating due to plastic damage accumulation in slip bands at the surface of the specimens and cracks initiating around inclusions in the surface or subsurface regions of the specimen. All the fracture surface images taken in this work are given in Appendix A, B, C and D.

5.3.1 Fatigue Fracture in Small Unseeded René 88DT Specimens

All of the small specimens tested exhibited clear oxidation patterns outlining the shape of the crack and the direction of crack growth; this helped in identifying crack initiation and crack growth regimes on the fracture surfaces. Figure 5.8 shows a low magnification image of specimen UD1-S12, tested at 1050 MPa. A similar fracture surface image of UD1-S14, also tested with 1050 MPa, shows the dominant crack initiated in the subsurface of the specimen (Figure 5.9, 5.10); the oxidation pattern this time forms a circular pattern around the crack initiation site. Figure 5.10 is an SEM image of the subsurface crack initiation site. The dark region is the cluster of hard inclusions that was present in the material.

Whether crack initiation occurs on the surface or subsurface of the fatigue specimens appears to be indicative of the two different operating initiation mechanisms. In general, cracks initiating from the surface of the fatigue specimens seemed to originate as a crack formed along grain boundaries of a few grains, while cracks initiating in the subsurface of the fatigue specimens seemed to have started at an inclusion particle or cluster of inclusion particles. The region around the initiation site of specimen UD1-S12 is shown in Figure 5.11, an intermediate magnification SEM image. There is a larger region defining a short “thumbnail” crack and exhibiting facetted characteristics fracture along the grain boundaries. Outside of this region, the fracture exhibits more crystallographic in nature, that is crack following transgranular regions.

The other crack initiation mechanism involved internal cracks initiating from inclusion particles in the material. These inclusion particles were entrapped in the material during the powder processing stages. Cracks are likely to nucleate around hard

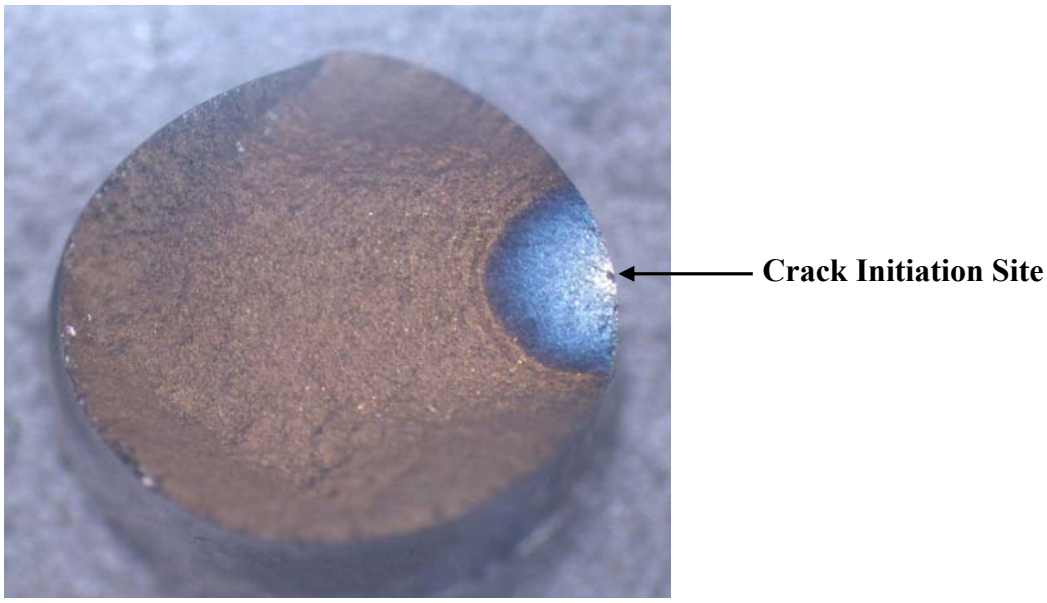

Figure 5.8 Low magnification image of the fracture surface of specimen UD1-S12 tested at 1050 MPa and 650ºC.

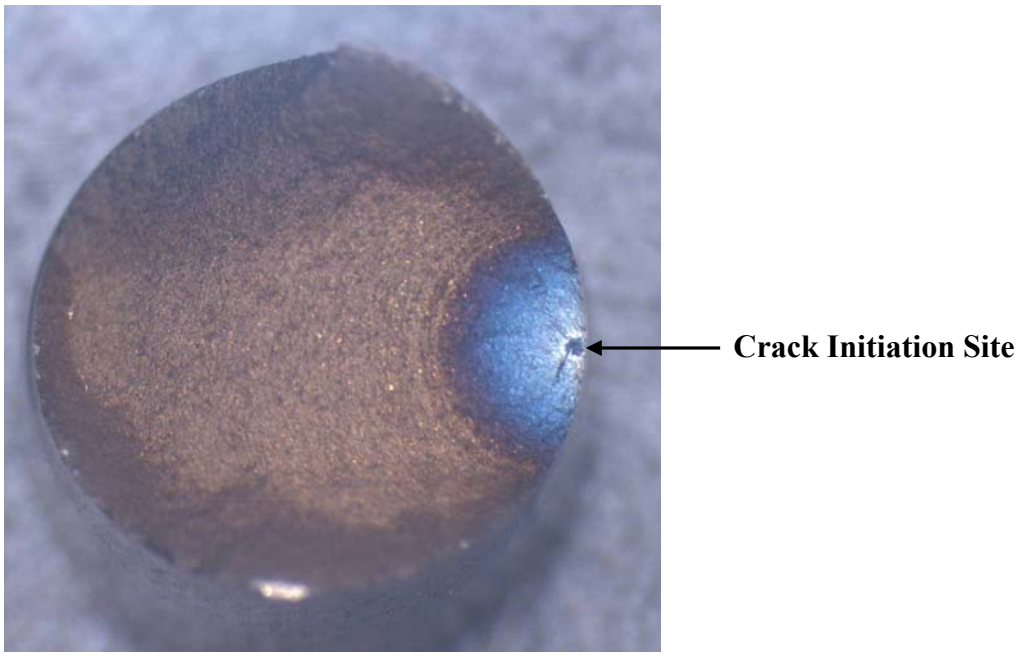

Figure 5.9 Low magnification image of the fracture surface of specimen UD1-S14 tested at 1050 MPa and 650ºC.

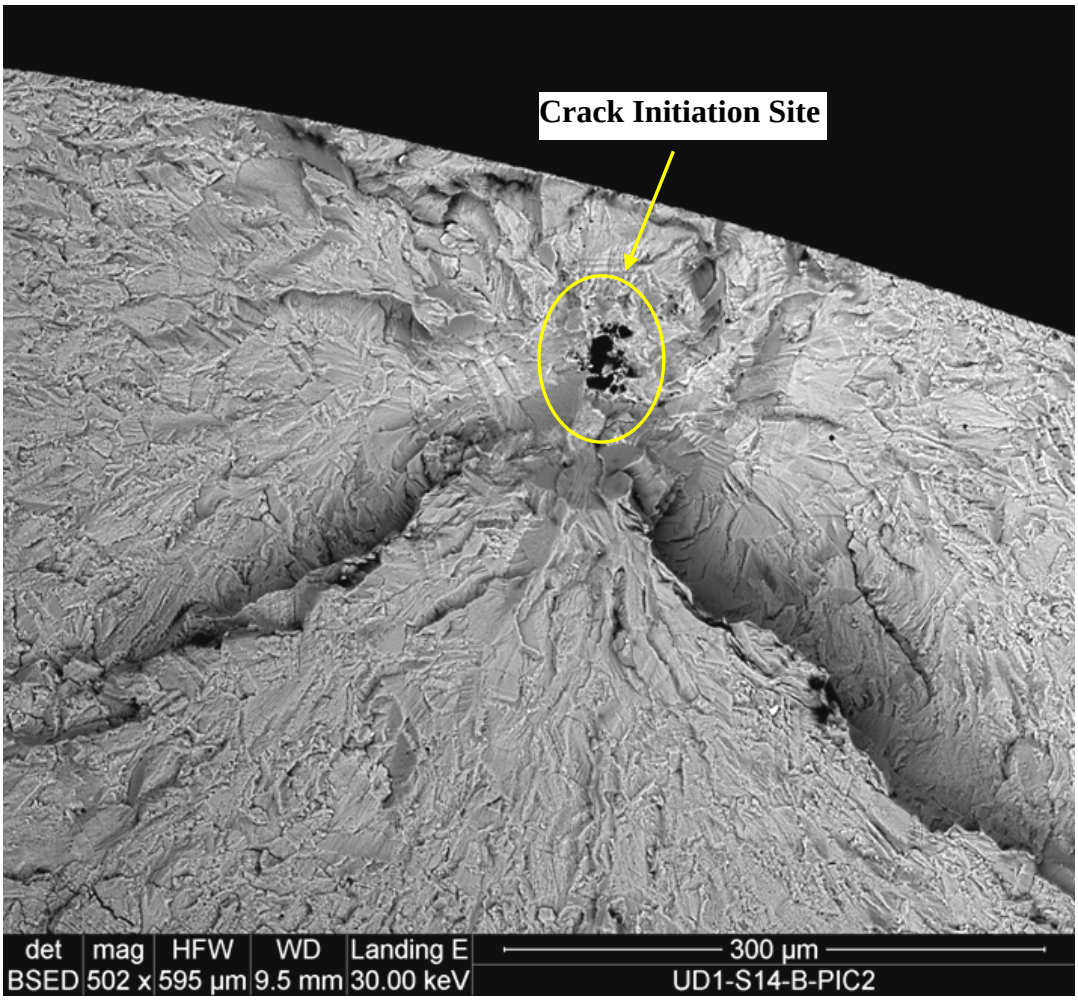

Figure 5.10 SEM image of the subsurface crack initiation region in specimen UD1-S14 tested at 1050 MPa and 650ºC.

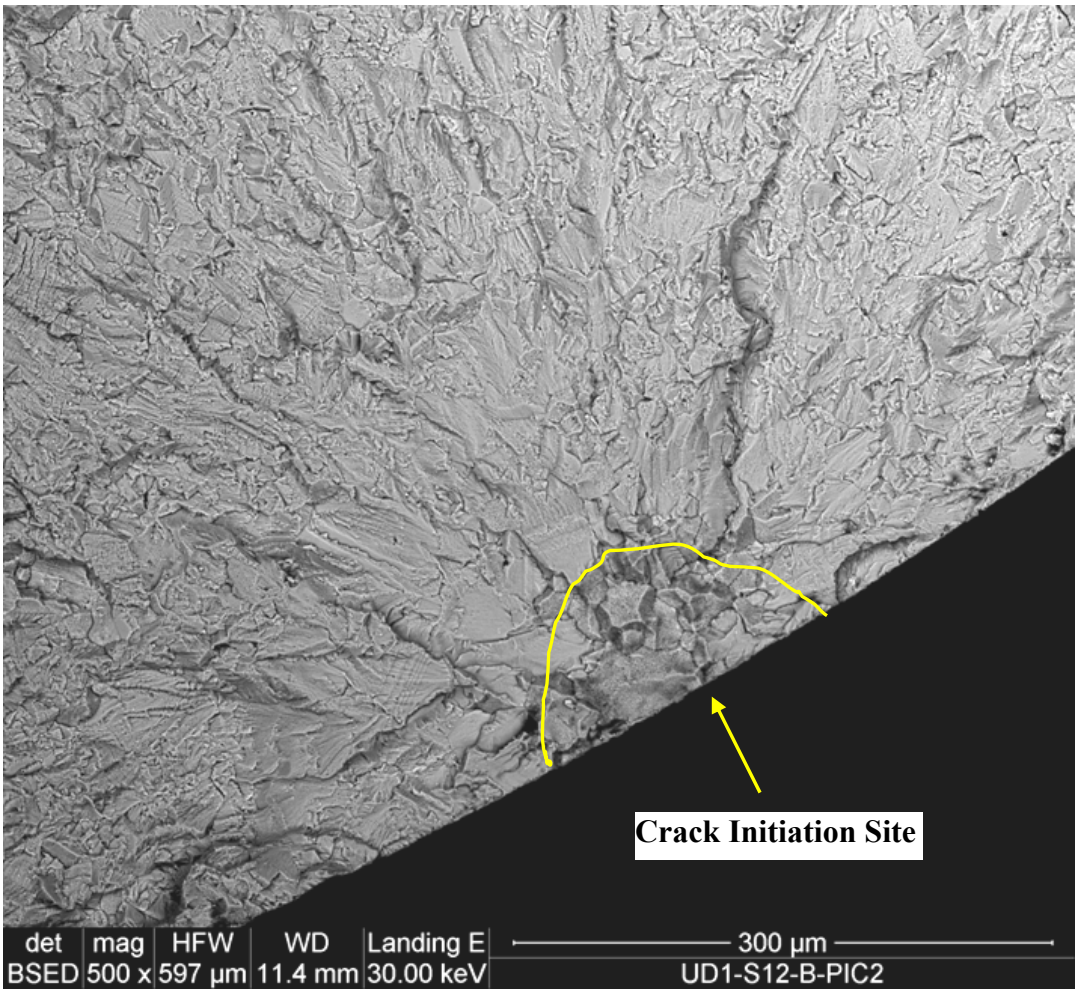

Figure 5.11 SEM image of the surface crack initiation region in specimen UD1-S12 tested at 1050 MPa and 650ºC.

inclusion particles because they generally have a different hardness, elastic modulus and thermal expansion compared to the René 88 material. The difference is elastic modulus and coefficients of thermal expansion can generate differential stresses between the particles and the surrounding matrix. The superposition of an external stress and the stress concentrating effect of the particles can yield a higher local stress than that is applied. A total of 16 small unseeded specimens were tested.

Seven of the tested specimens that showed surface initiations, had dominant cracks that initiated in slip bands, with the exception of one, where the crack initiation started at surface Tungsten particles (Appendix A.7). Crack initiated from inclusions or particles was observed in six of the nine subsurface initiation tested specimens. Remaining three tested specimens were faceted intergranular at fracture origin (Appendix A).

Figure 5.12 shows a low magnification optical image of a small unseeded specimen fracture surface tested at σ = 960 MPa where the dominant internal crack initiated from a cluster of inclusions. A bright area forms a circular pattern around the initiation site. An intermediate magnification SEM image reveals that the initiation site is a cluster of particles (Figure 5.13). A river or radial pattern on the fracture surface points back to the particle cluster, indicating that the dominant crack did indeed start there. A higher magnification image of the particle cluster (Figure 5.14) shows the cluster is made up of several individual particles or grains of inclusion material.

Energy dispersive X-ray spectroscopy (EDS) analysis was performed on the particles to determine there identity. EDS can only provide semiquantitative results because the penetration depth into the specimen of the sampling beam is unknown. The

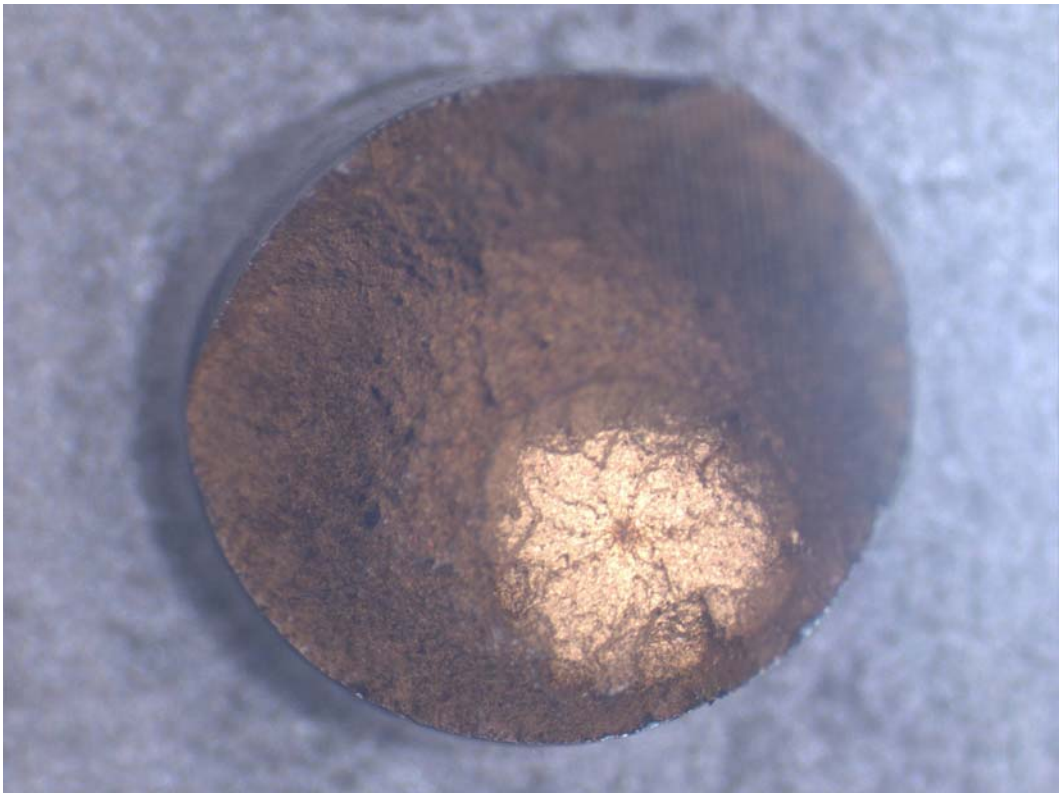

Figure 5.12 Low magnification image of fatigue fracture surface from UD1- S22 small unseeded specimen tested at σ = 1000 MPa and 650^{o}C. The bright pattern outlines an internal crack initiation site.

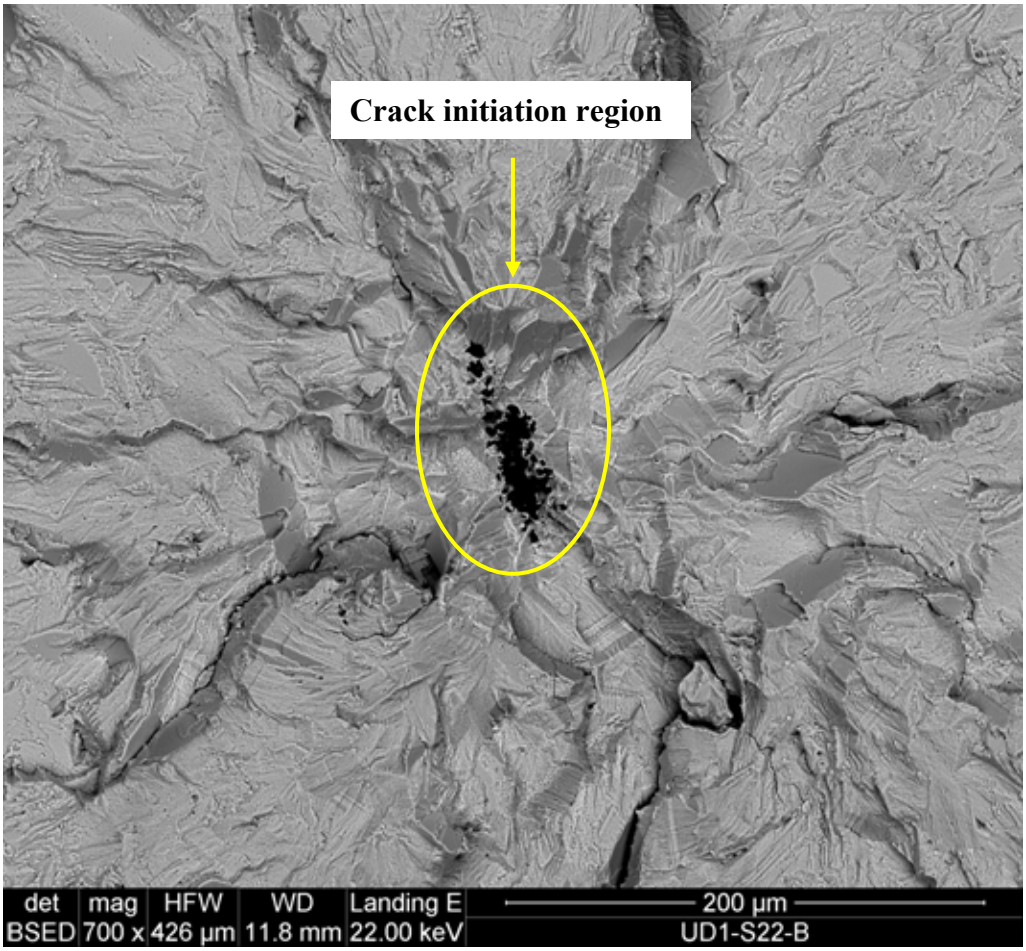

Figure 5.13 SEM image of a cluster particles at the internal initiation site in an unseeded small specimen tested at σ = 960 MPa and at 650^{o}C.

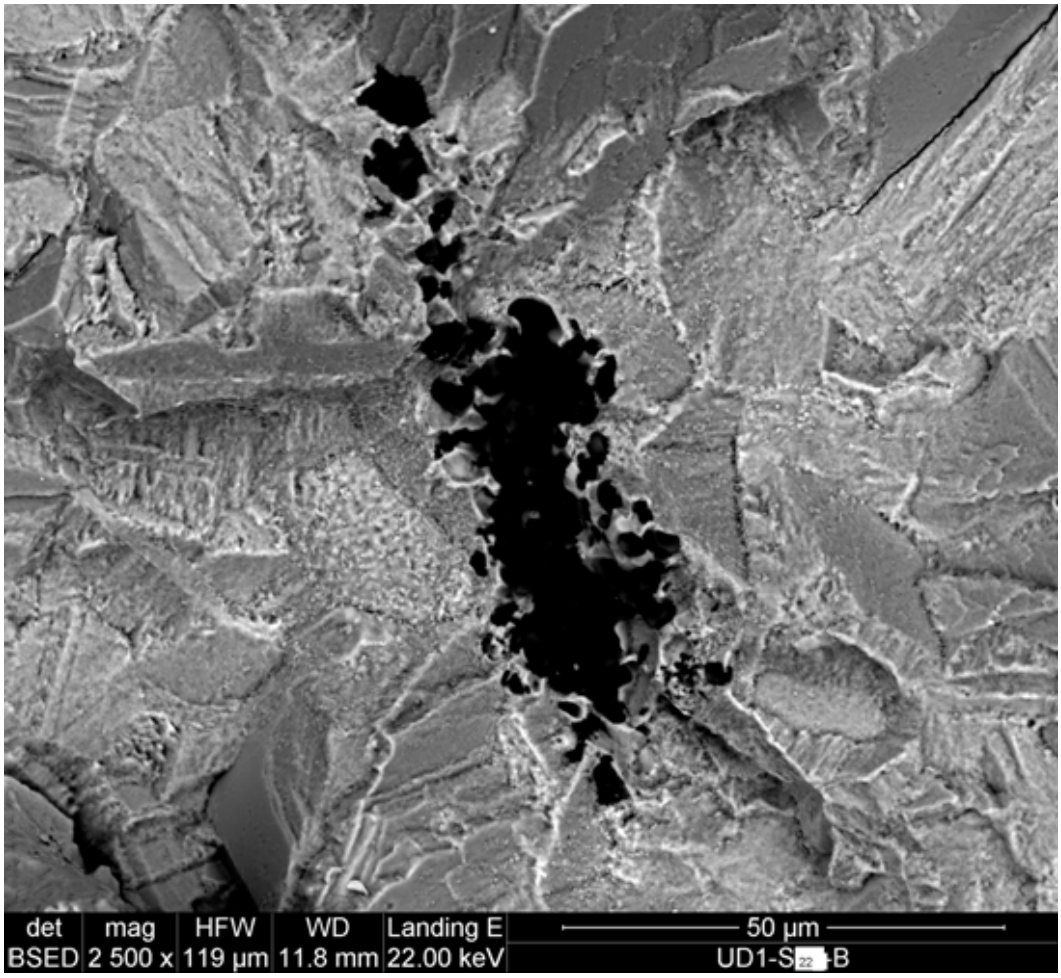

Figure 5.14 Higher magnification SEM image of the particle cluster shown in Figure 5.13.

EDS analysis showed the presence of strong aluminum and oxygen peaks compared to an EDS spectrum from the matrix material (Figure 5.15). Past research identified that the presence of aluminum oxide (Al_2O_3) particles in the material is due to entrapment of ceramic crucible lining fragments during powder manufacturing [87, 88]. The EDS analysis indeed confirms that the particles present on the UD1-S22 fracture surfaces are Al_2O_3 particles. These particles, though present in extremely low volume fractions, can be very detrimental to fatigue life because they have a different hardness, coefficient of thermal expansion and elastic modulus than the matrix. They are also quite brittle easily fracturing under fatigue loading. The fracture region around the cluster was facetted, and extended in the form of a circular ring around the crack initiation site as seen in Figure 5.12. Outside of this region, the fracture surface displayed more of a ductile, crystallographic mechanism, associated with fatigue crack growth.

5.3.2 Fatigue Fracture in Small Seeded René 88 Specimens

Typical fatigue crack initiation sites of small seeded specimens are shown in Figure 5.16 and 5.17, illustrating the surface and internal initiations. All failures in small specimens of seeded material occurred due to cracks initiating from the seeded inclusions. Half of tested specimens failed from cracks initiated at seeded inclusions located at the surface. Specimens tested at lower stress ranges invariably failed from a single crack initiation at an inclusion intersecting the surface or located at a depth less than the inclusion size in from the surface. The smaller inclusions initiating cracks appeared to be more granulated and broken up than the larger inclusions. However, the larger inclusions also were at least partially cracked. Cracks sometimes seem to have initiated from several of the seeded inclusions at high stress range (Figure 5.18). The

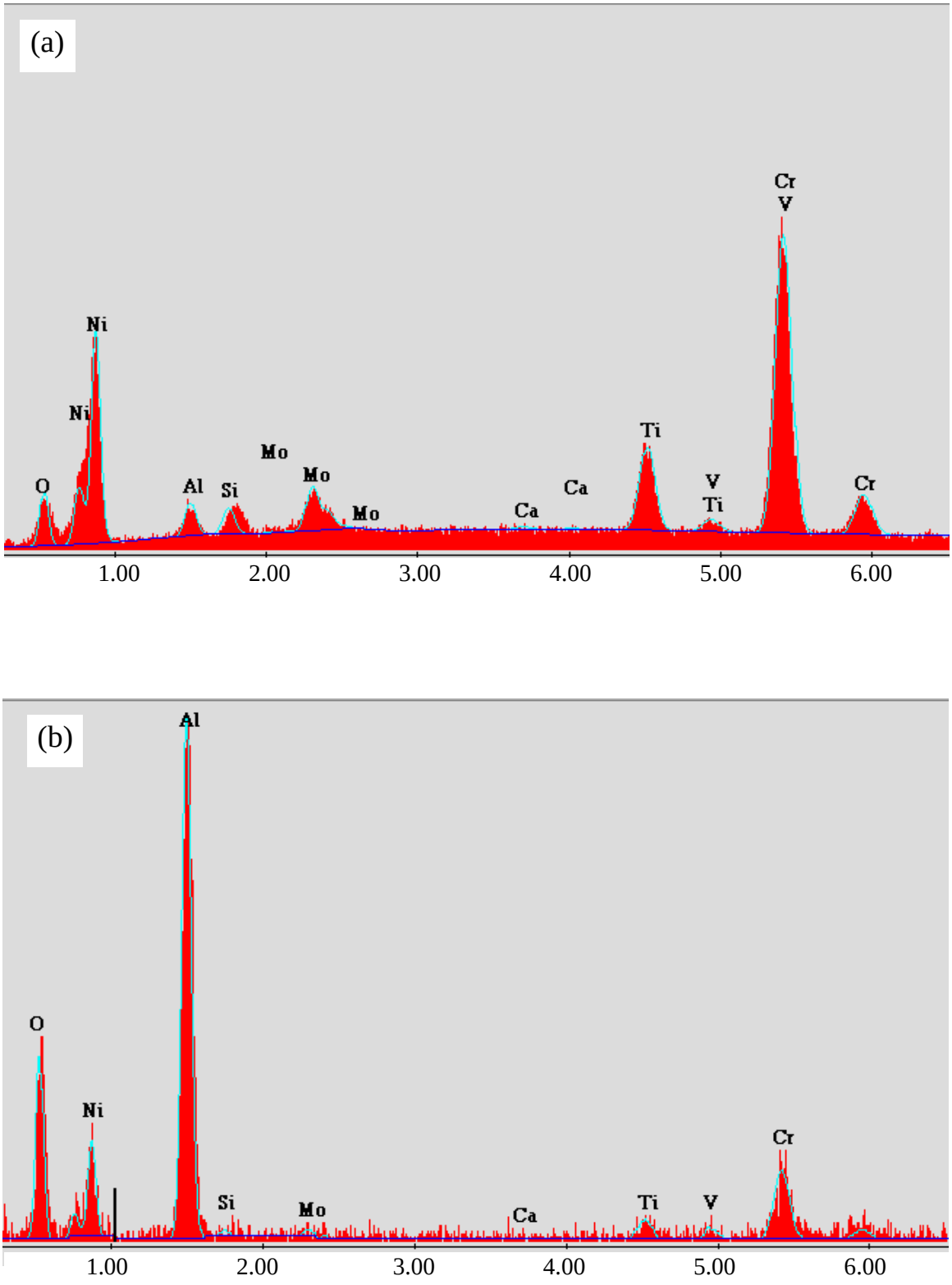

Figure 5.15 EDS spectrum **(**a) Baseline EDS spectrum from the matrix of UD1-S22 small unseeded specimen. (b) Spectrum obtained from internal particle cluster of UD1-S22.

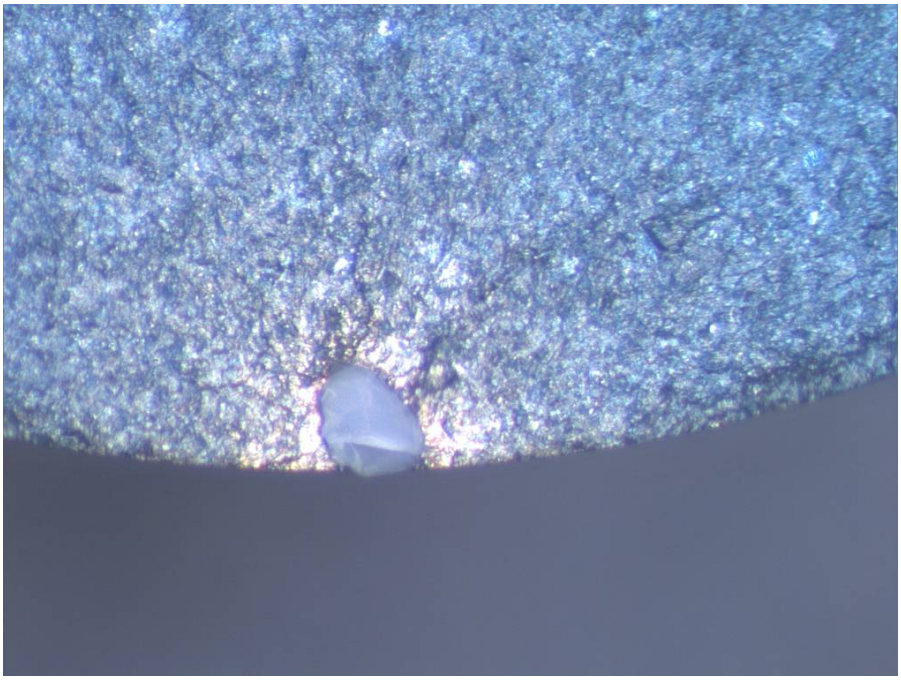

Figure 5.16 Surface initiation in seeded specimen SD1-S19 tested at 880 MPa.

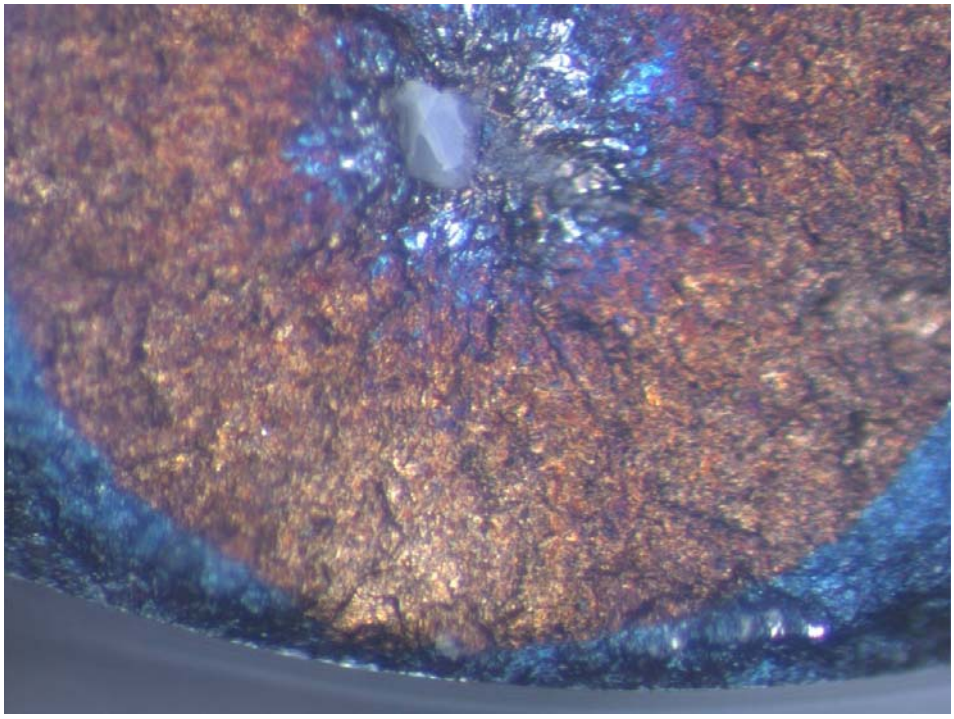

Figure 5.17 Internal crack initiation in seeded specimen SD1-S20 tested at 860 MPa with a life of 107446 cycles.

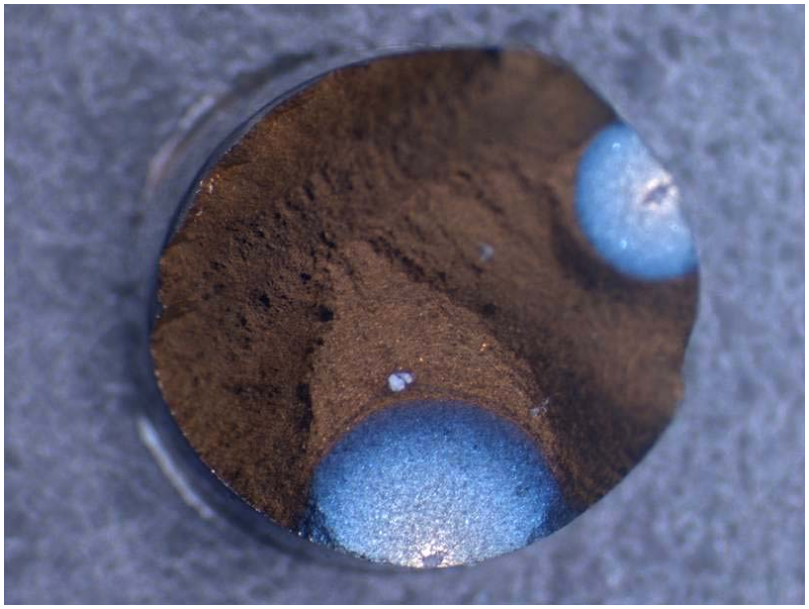

Figure 5.18 Surface initiation in seeded specimen SD1-S22 tested at 880 MPa.

EDS analysis (Figure 5.19) indicated all seeded inclusions had the same composition, that is, Al_2O_3 inclusion type and could be assumed to be the seeds.

5.3.3 Fatigue Fracture in Large Unseeded René 88DT Specimens

All the fractures appeared generally similar. Fracture originated along outer circumference of the specimen and progressed across the inner section until the applied tensile stress caused the remaining section to fail by ductile fracture. Many of the specimens appeared to have multiple fracture initiation sites (Figure 5.20, 5.21). So far, all tests have resulted in failure due to fracture originating from a collection of grain boundary fractures (Figure 5.22). No nonmetallic inclusions were observed for the surface fracture origins for any of the test specimens. There is a possibility that internal failure will be seen at stresses below a certain level, like in the tests for small unseeded specimens.

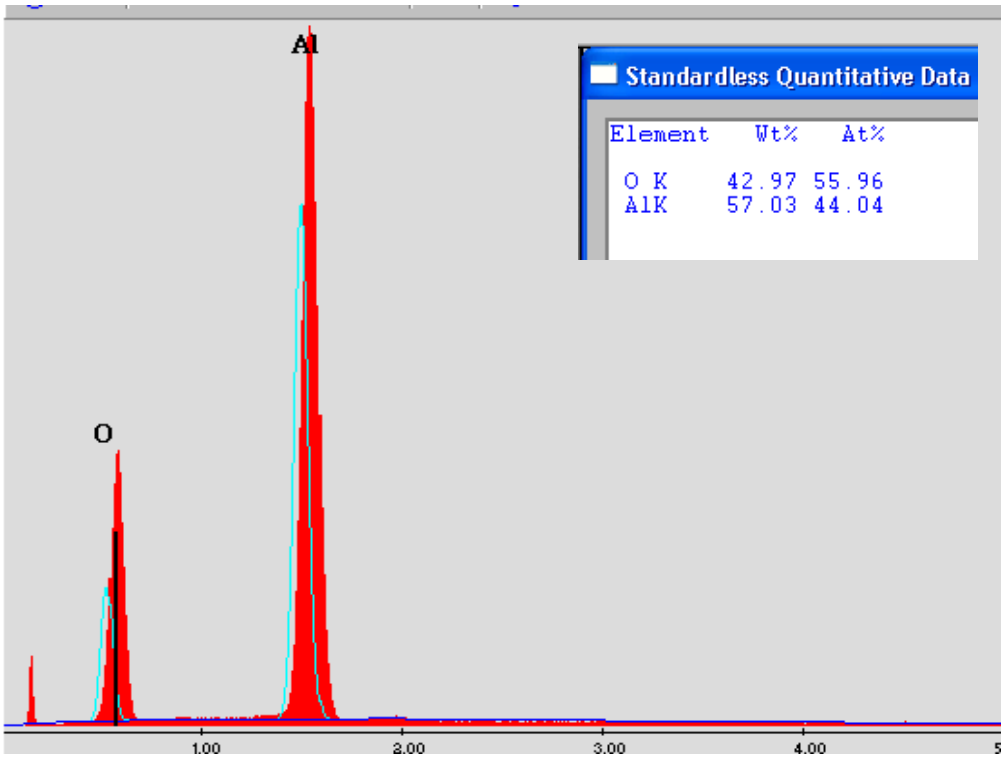

Figure 5.19 EDS spectrum obtained from SD1-S6 seeded inclusion.

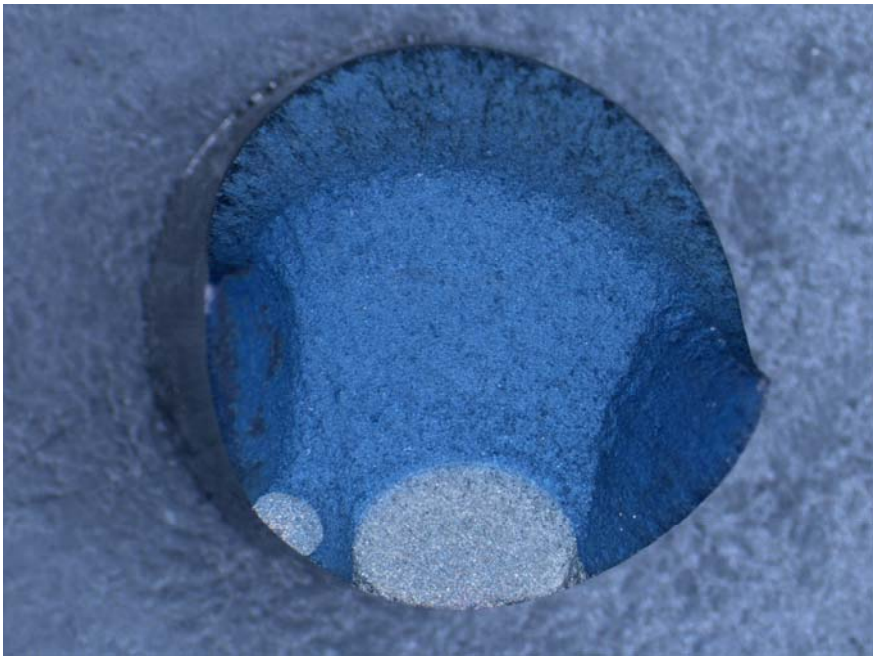

Figure 5.20 Surface initiation in unseeded specimen UD1-L10 tested at 940 MPa. Multiple fracture initiation sites were observed

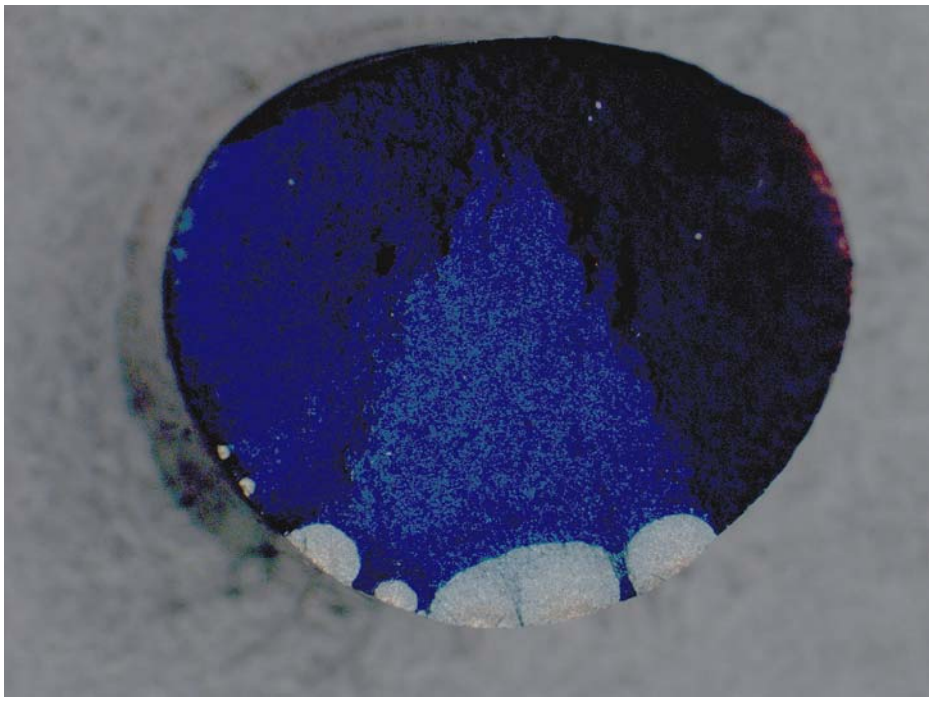

Figure 5.21 Surface initiations in unseeded specimen UD1-L18 tested at 1060 MPa. Multiple fracture initiation sites were observed

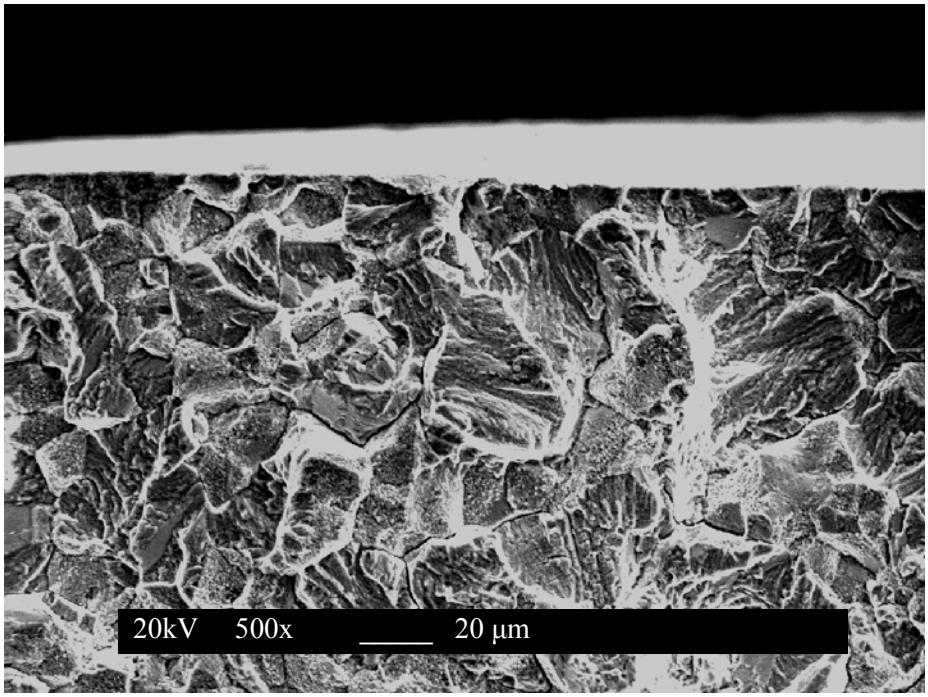

Figure 5.22 SEM image of the surface crack initiation region in specimen UD1-L16 tested at 1120 MPa.

5.3.4 Fatigue Fracture in Large Seeded René 88 Specimens

Results for crack-initiation mechanism in large seeded specimens appeared similar to the results for small seeded specimens: both surface and subsurface fractures initiating from seeded inclusions. EDS analysis of all the inclusions at the fracture origins detected primarily Aluminum and Oxygen. It is important to note that the inclusion sizes are larger than those discovered during the initial seeds distribution analysis (Figure 5.23a). Specimen SD1-L13 (Figure 5.23b) had an unusually long life, possibly due to the inclusion being perfectly centered within the specimen's cross-section.

5.4 Inclusion Size at Crack Initiation Site

The size of crack initiating a fatigue crack was defined as the square root of the projection area of the inclusion at the fatigue crack initiation site in this study. Figure 5.24 shows the relationship between the $\sqrt{area}$ of nonmetallic inclusions which initiated the surface and internal failure mode and the number of cycles to failure for small and large seeded specimens. The area of the crack initiation site was determined from SEM photographs by image processing software. The sizes of inclusions varied from 140 to 240 μm. There appears to be no correlation between $\sqrt{area}$ of inclusion size and the fatigue life. Furthermore, a comparison of the effects of different inclusion morphology at the same size would be necessary to separate any possible additional effects on life associated with the granulated versus singular nature of the seeds.

5.5 Fatigue Life Correlation Based on Stress-intensity Factor

An attempt to explain the fatigue test results, by calculating the stress intensity factor (K) for the crack initiating particles observed on the fracture surfaces was made.

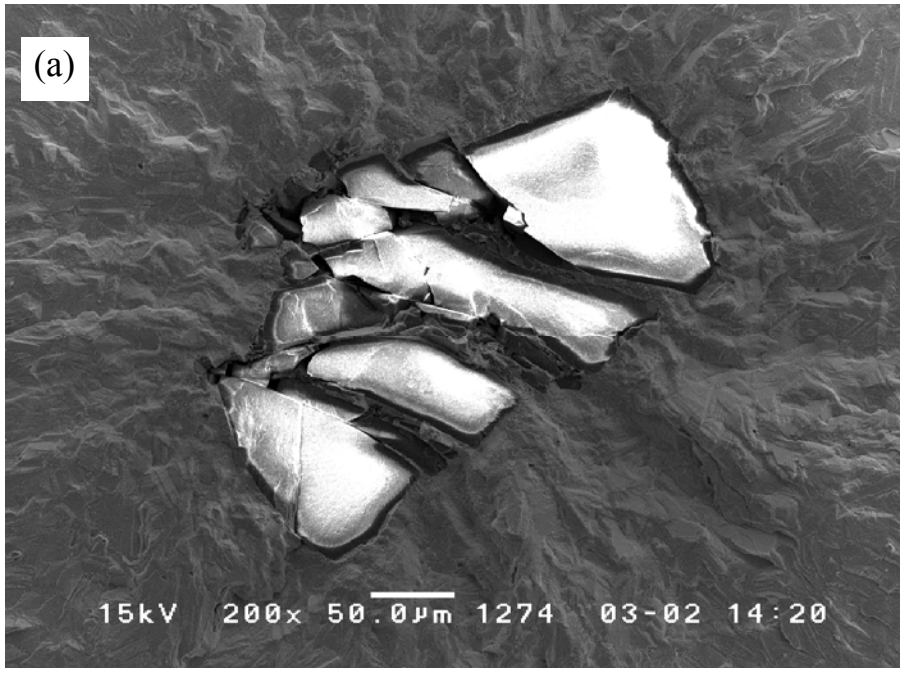

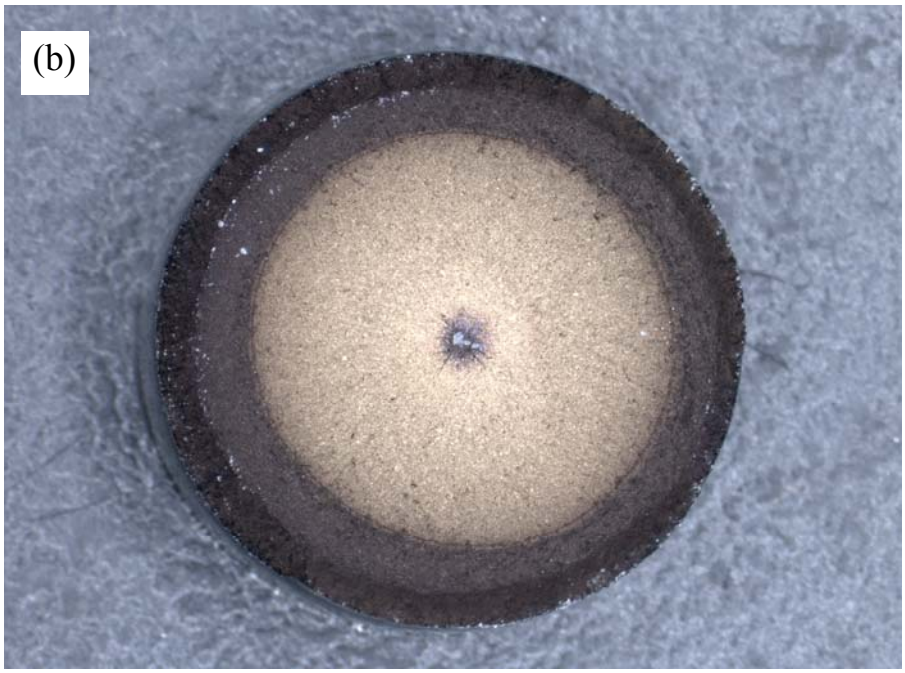

Figure 5.23 Fatigue fracture surface (a) SEM image of the surface crack initiation region in specimen SD1-L27 tested at 540 MPa. Inclusion size based on $\sqrt{area}$ is 225 µm. (b) Internal initiation in seeded specimen SD1-L13 tested at 580 MPa giving a life of 7717338 cycles.

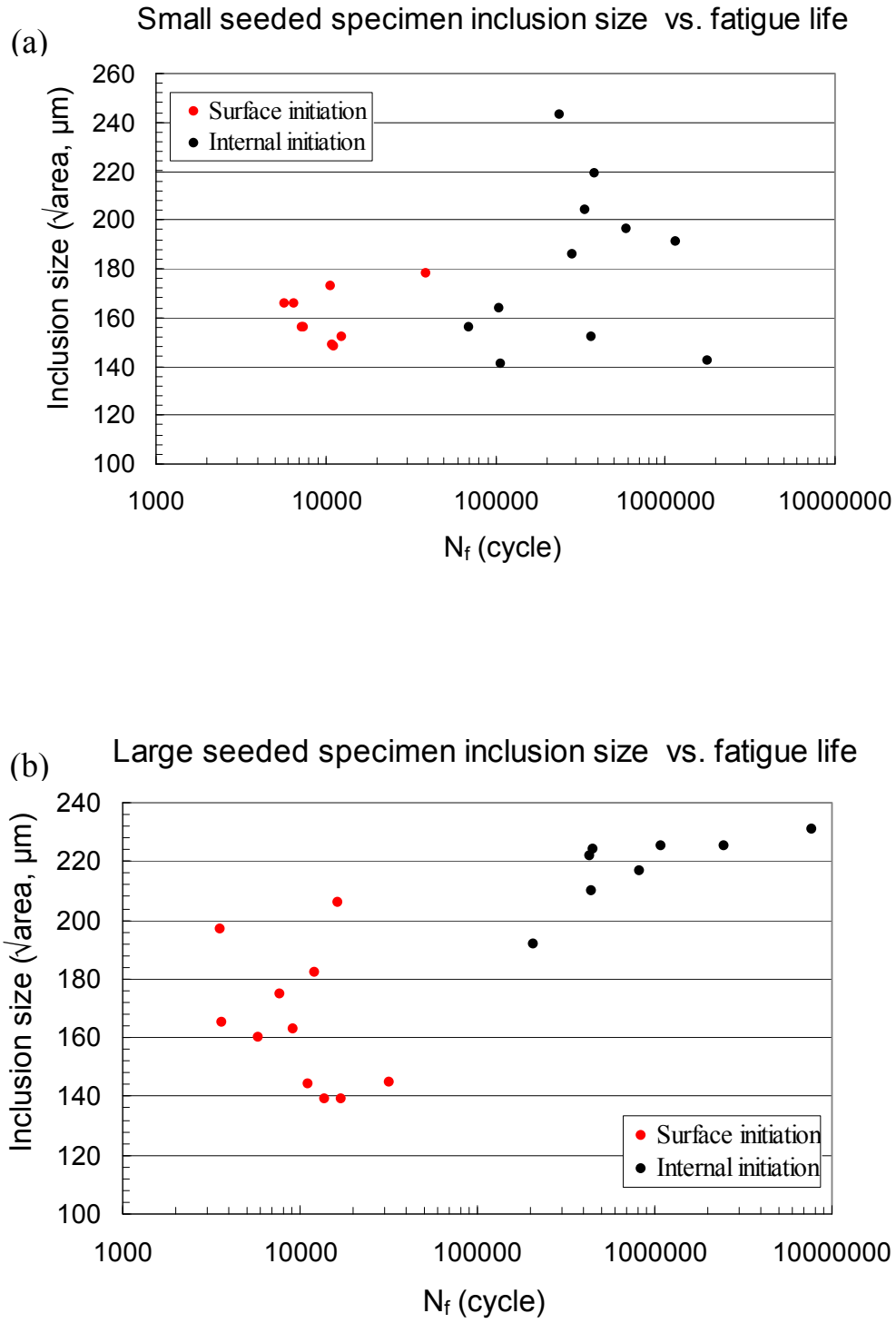

Figure 5.24 Experimental relationship between the sizes of the inclusion at crack initiation site and the number of cycles to failure N_f: (a) Small seeded specimen and (b) Large seeded specimen

The stress intensity factor proposed by Murakami [89] is:

For a surface crack, *K* along its crack front is given approximately by:

$$K = 0.65\sigma_0\sqrt{\pi\sqrt{area}} \tag{5.1}$$

Similarly, for an internal crack, *K* is given approximately by:

$$K = 0.5\sigma_0\sqrt{\pi\sqrt{area}} \tag{5.2}$$

where $\sqrt{area}$ is the equivalent inclusion size and σ_0 the nominal stress.

Figure 5.25a and 5.25b illustrate the revised S-N curve with fatigue life plotted against the stress intensity factor (*K*) determined for all the crack initiating inclusions found fracture surfaces. It can be seen that *K* values lie in the range of 9-15 MPa$\sqrt{m}$ for surface crack and 7-10 MPa$\sqrt{m}$ for internal crack. It can be seen that the fatigue life curves based on Murakami's *K* solution also show separated internal versus surface failure domains. However, there are considerable changes in the form of these curves when compared to that in Figure 5.6 and 5.7. In particular, the extent of duality in the curves or the existence of a domain where two competing failure modes were possible, at a given cycle stress failure amplitude, has significantly reduced. The failure domains seem to follow one single curve, with surface failures above a critical *K* and internal failures below that *K*. The transition seem to occur at about K_{max} = 8.5 – 9 MPa √m. The absence of "duality" in these curves suggests that inclusion sizes determine the probability for surface crack initiation leading to duplex curves (Figure 5.6, 5.7).

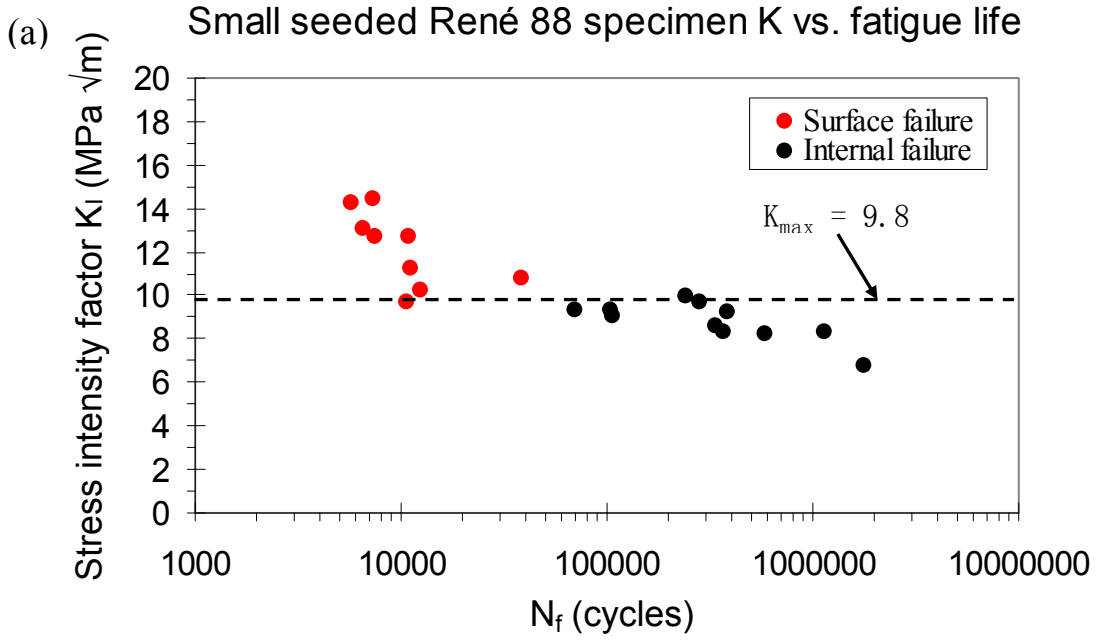

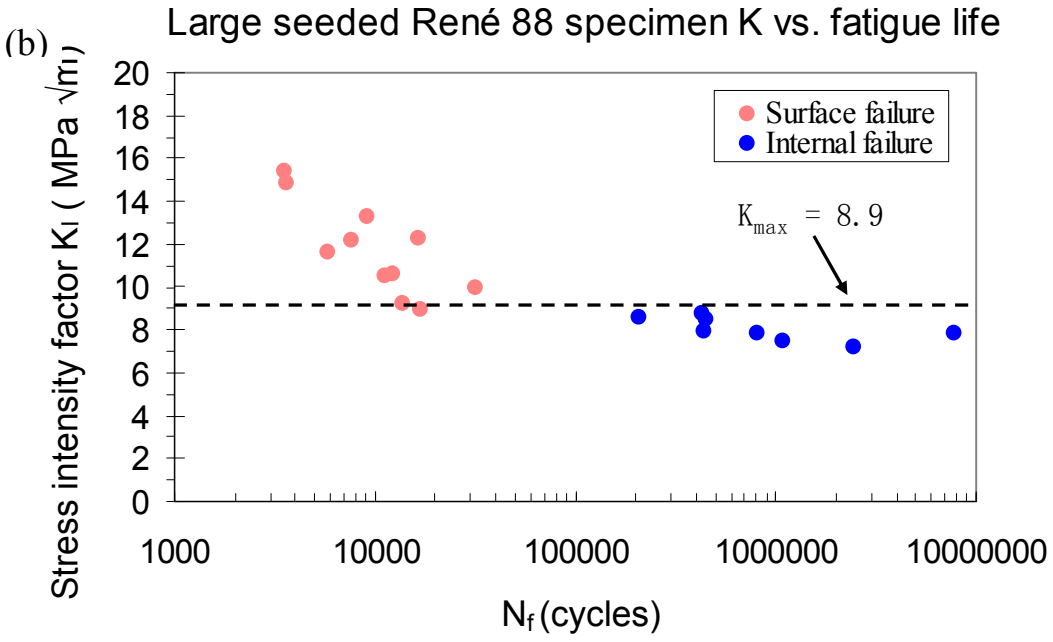

Figure 5.25 Relationship between stress intensity factor *K* at crack initiation site and the number of cycles to failure N_f: (a) Small seeded specimen and (b) Large seeded specimen

5.6 Binary Logistic Regression for Failures of Initiation Site

The relationship of stress amplitude to fatigue failure sites was studied using binary logistic regression. Specimens were considered either to have failed by surface-initiated failure or not, which is a binary response. Binary logistic regressions (BLR) assigned a value of one and internal-initiated failure is assigned a value of zero. To create employ three scales: logits, odds, and probability. Here, surface-initiated failure is a BLR for this type of response, a line is fitted so that all responses are between 0 and 1. The advantage of logistic regressions was, unlike linear regression which predicts the actual values of the response variables, logistic regression models the probability associated with each level of the variable by finding a linear relationship between predictor variables and a link function. Figure 5.26 presents the probability of surface-initiated failures as a function of stress amplitude, determined from the experimental data in Figure 5.6 and 5.7 by BLR. An interesting observation is the frequency of surface initiated failures, which increased with the stress. Also, researchers are often interested in the value of the explanatory variable that produces a 50:50 split. From Figure 5.26, the equal probabilities for surface-initiated and interior-initiated failures stress for seeded large specimen, seeded small specimen and unseeded small specimen are 670 MPa, 800, MPa and 1040 MPa, respectively. Similar dominance of surface-initiated failures at high cycle stress amplitudes can also be found in the data of high-strength steel [90] where limited fatigue duality, above the stress amplitude of 1200 MPa, was seen.

5.7 Evolution of Dual Fatigue Curves

Competing Modes in fatigue behavior refers to the presence of two distinct failure distributions on the S–N graph. One distribution is generally associated with fatigue

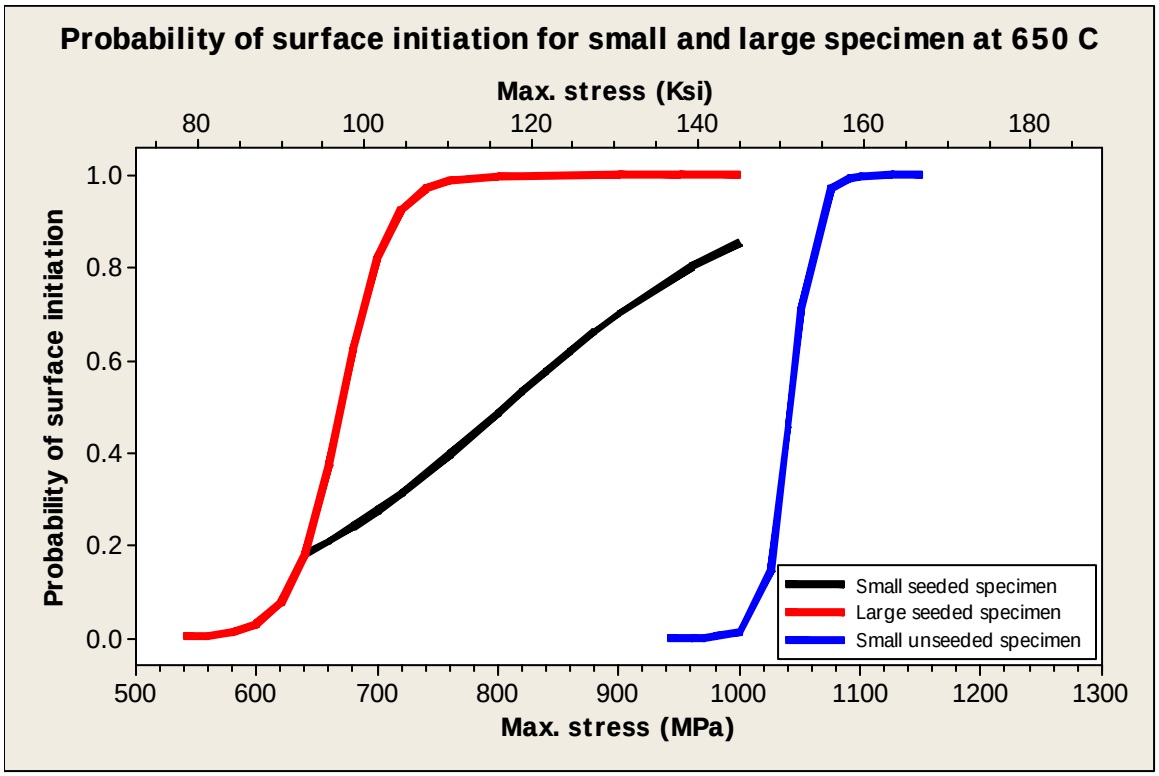

Figure 5.26 Binary regression results: Probability of surface crack initiation as a function of stress amplitudes

failure initiation from surface sites while the other involves failures nucleating from internal origins. Usually, surface initiations occur at higher stresses and shorter fatigue lives while the internal initiation is usually associated with lower stresses and longer lives. There is an overlap region at intermediate stresses where a mixture of failures occurs from initiations at both sites.

Fatigue data are expensive to generate and can be very time consuming, and hence, it is common to find S-N curves with not enough data points to discern the true trends. Hence, even though there may be internal fatigue initiations, the existence of competing mode behavior is not apparent and is not even considered. Wide variations in the results of fatigue experiments are attributed to the inherent scatter and no further

evaluation is performed and may not guarantee a faithful representation of the actual behavior. However, often upon the generation of additional data by large number of experiments, the occurrence of the two separate failure distributions can be realized.

Figure 5.27 illustrates a series of S-N plots of the seeded small specimen test results where there the data are plotted in the sequence with which they were plotted after a given number of tests were completed. The objective is to show that it takes a certain minimum of tests to reveal the dual fatigue curves.

It can be seen that the first 8 specimen tests do not have clear evidence of competing failures. It appears that at least a total number of 14 samples are needed, in this material, to reveal the two different fatigue modes as after illustrated in Figure 5.27(c). Similar results can also be found in section 2.6.2.

5.8 Extreme Value Statistics Analysis of Fatigue Failures

Figure 5.28 shows the plot of the reduced variate (the transformed variable that replaces cumulative distribution function) of $\sqrt{area}_{\max}$ versus $\sqrt{area}_{init}$ in the probability graph of extreme value for unseeded René 88DT. The minimum inclusion size, $\sqrt{area}_{\min}$, needed for inclusions responsible for fatigue failure was estimated by the intersection of the two trendlines corresponding to the inclusion size distributions at inspection area $\sqrt{area}_{\max}$ and inclusions at fatigue crack initiation sites $\sqrt{area}_{init}$. The 16.84 μm for Z_{crit} is the critical size of inclusion for unseeded René 88DT. Below which the fatigue fracture origins will not initiate from the inclusions but from specimen surface or internal microstructural inclusions. It is of interest to determine if the largest size of inclusions that would initiate a fatigue crack in a specimen can be predicted prior

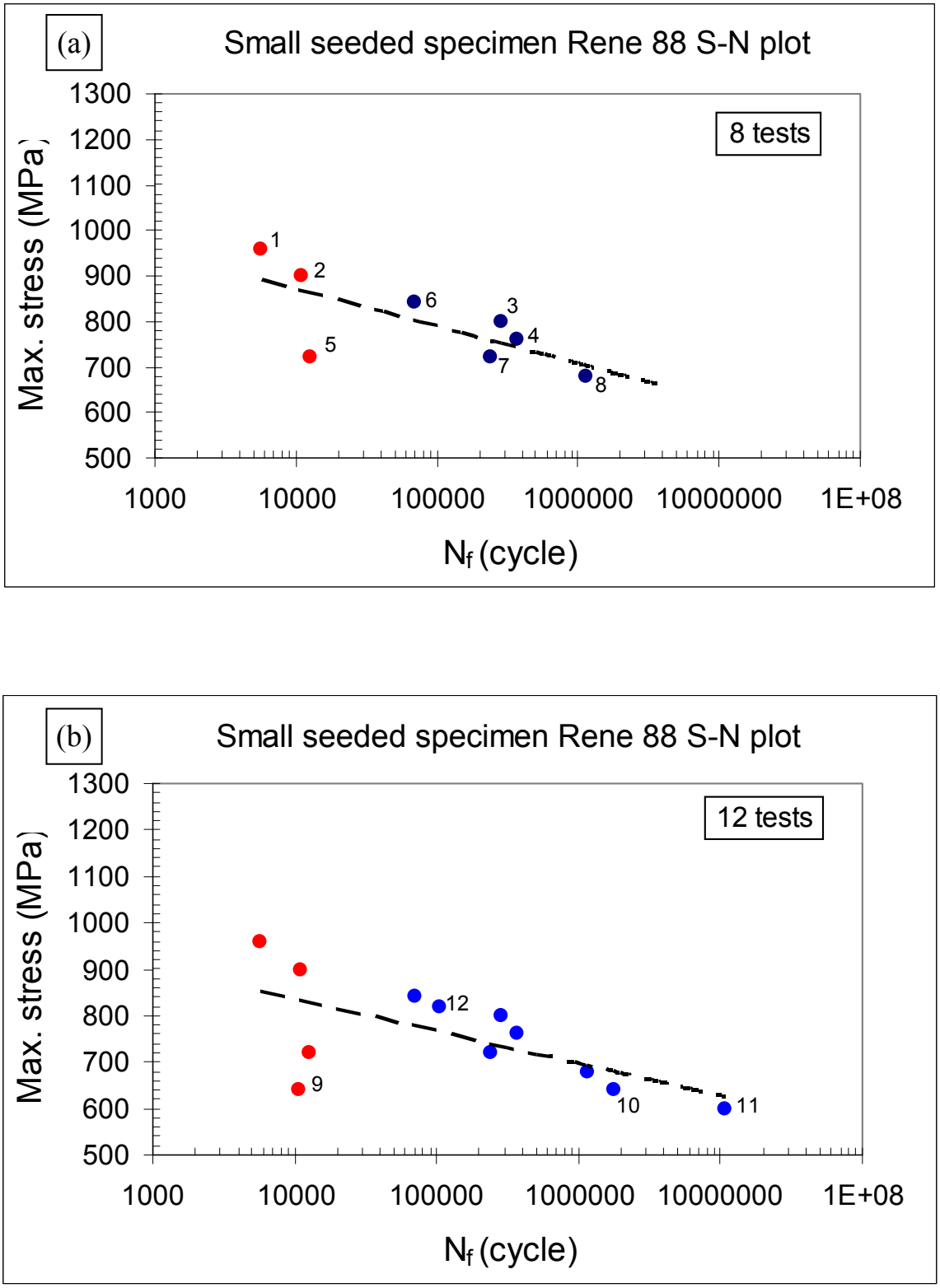

Figure 5.27 Evolution of S-N plot for seeded small specimen fatigue tested after (a) 8 tests (b) 12 tests (c) 14 tests (d) 22 tests. The numbers next to data points are the test sequence number.

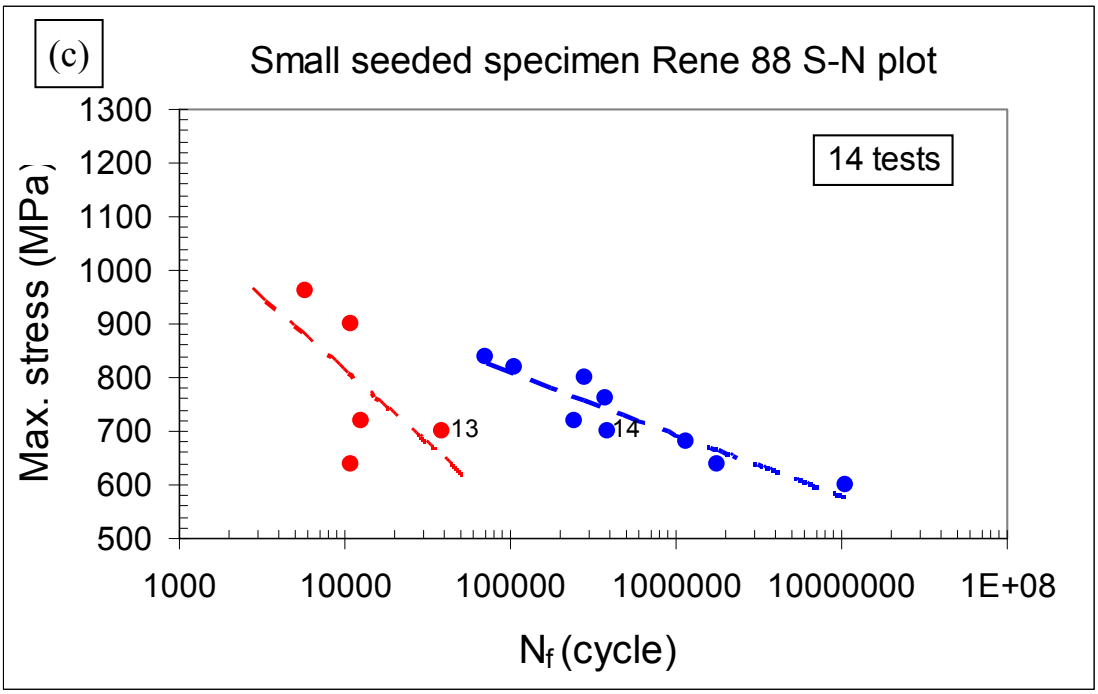

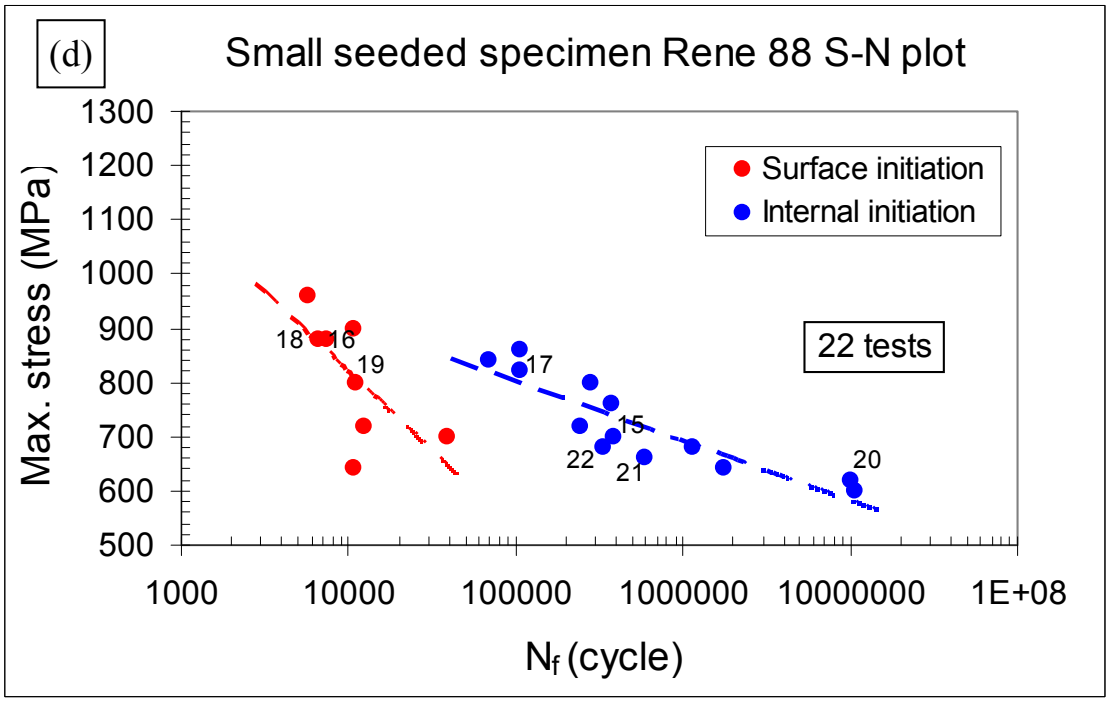

Figure 5.27 Continued.

to testing. For this purpose the inclusion size distribution as observed in metallographic specimens were evaluated against the actual size distribution of inclusion observed at fatigue failure sites in the specimens test.

Figure 5.28 shows the plot of the cumulative probability of extreme size distribution of inclusions found at the fatigue crack initiation sites together with the extreme-size distribution of inclusions. To plot the extreme-sized inclusions that were metallographically observed, a total of 385 frames of area 2.48 mm by 1.81 mm were examined. The largest size of the inclusion observed in each frames was collected. All the largest inclusion sizes were plotted as a function of $\sqrt{area}$ of that inclusion. A total of 385 inclusions were then plotted in the figure. The largest inclusion size determined in metallographic analysis was 38 μm. The fracture surfaces of the fatigue specimens,

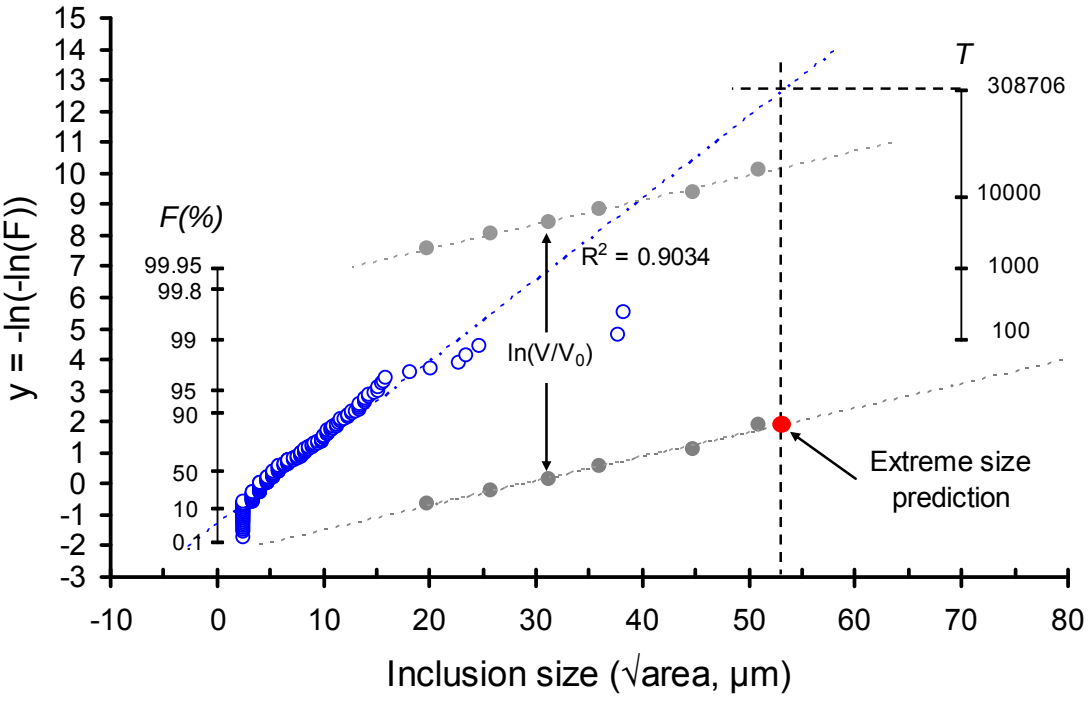

Figure 5.28 Statistics of extremes graph for unseeded René 88DT

however, revealed much larger inclusions. The method proposed by Murakami [89] was used in the transformation of the examined area into a volume by attributing a certain thickness to a 2-dimentional area. For example, if the inclusions contained in a single examined area S_0, and a thickness h are added to S_0, the 3-dimentional examined domain is created. The examined volume for each picture taken from optical microscope is then defined by $V_0 = h \times S_0$. The mean value of the $\sqrt{area}_{\max,j}$ of the inclusions examined is taken empirically as an appropriate value of the thickness h. The return period, T, can be calculated from specimen volume (V) by using the formula $T = V/V_0$. The significance of the return period is that it represents the cumulative volume of "examination" with respect to the volume of fatigue specimens. From the return period, the corresponding predicted value of the largest inclusion, $\sqrt{area}_{\max}$, can then be predicted.

The extreme size of the inclusion ($\sqrt{area}_{\max}$) predicted by the Murakami method is 52.7 μm for 16 test specimen volume. This agreed well with the largest size of 50.9 μm found from the fatigue tests fracture origin in fatigue tests.

Figure 5.29 shows the plot of extreme-sized inclusion from metallographic sections in seeded René 88 material. The plot clearly shows the presence of bilinear distribution of inclusions. This is to the case of unseeded René 88DT material where the inclusion distribution plot shows a nearly linear characteristic as illustrated in Figure 5.28. Inclusions of size range >18 μm were assumed to be relevant to fatigue crack initiation. For the seeded material, the 18 μm inclusion sizes or larger were considered in determining the extreme-size distribution for crack initiation. Then, the probability plot of inclusions at the fatigue crack initiation sites can be transformed base as:

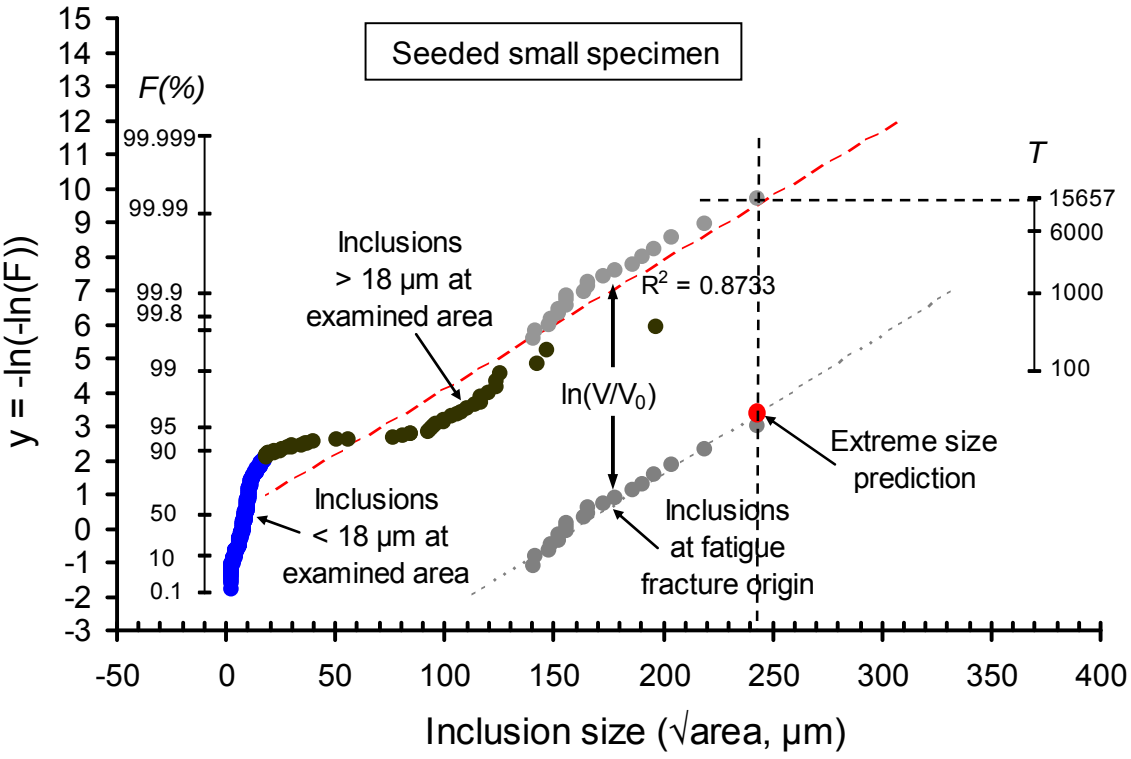

Figure 5.29 Statistics of extremes graph seeded René 88 small specimen

The reduce variate $y = -\ln[-\ln(F)]$ where F is the cumulative probability function.

The probability that j will be exceeded is $P_j = 1 - F$, A return period is the average time within which a given inclusion size will be exceeded just once. The return period T is by definition the reciprocal of P. Therefore,

$$T = 1 - \frac{1}{F} \Rightarrow F = 1 - \frac{1}{T} \tag{5.3}$$

$$y = -\ln\left[-\ln\left(1 - \frac{1}{T}\right)\right] = -\ln\left[-\ln\left(\frac{T-1}{T}\right)\right] \tag{5.4}$$

and $$-\ln\left(\frac{T-1}{T}\right)=\ln\left(\frac{T}{T-1}\right)=\ln\left(1+\frac{1}{T-1}\right) \tag{5.5}$$

Since $\ln(1+x)=\sum_{n=1}^{\infty}\frac{(-1)^{n+1}}{n}x^{n}=x-\frac{x^2}{2}+\frac{x^3}{3}-.....$ (Taylor series) (5.6)

If x is large, $\ln(1+x)=x$, then equation become

$$-\ln\left(\frac{T-1}{T}\right)=\ln\left(\frac{T}{T-1}\right)=\ln\left(1+\frac{1}{T-1}\right)=\frac{1}{T-1} \tag{5.7}$$

$$-\ln\left(\frac{1}{T-1}\right)=\ln(T-1)\approx\ln T \tag{5.8}$$

$$T=\left(\frac{V+V_0}{V_0}\right) \tag{5.9}$$

and when $V >> V_0$, $T=\frac{V}{V_0}$ (5.10)

$$\ln T=\ln\left(\frac{V}{V_0}\right) \tag{5.11}$$

Based on the above analysis one can use $\ln T=\ln\left(\frac{V}{V_0}\right)$ to transform the crack-initiating inclusions size distribution found at the fracture origin to correlate with the metallographically examined extre-size distribution.

The R^2 values of the linear trendlines for $\sqrt{area_{max}}$ at examined area and transformed inclusions at fatigue crack initiation sites was 0.87 and 0.85 for seeded small and large specimen, respectively. The extreme size of the inclusion ($\sqrt{area_{max}}$) expected to exist after testing 20 seeded small specimen volumes is 245 µm. This prediction compares very well with the 243 µm size found in the fatigue fracture origin in small test specimens. For the seeded large specimen, 19 pieces were tested and largest inclusion size found in the fracture origin was 231 µm. This also compares with the predicted size of 247 µm. Therefore, the predicted extreme sizes of the inclusions ($\sqrt{area_{max}}$) values agreed well with the sizes at the fracture origin of fatigue tested seeded small and large specimens (Figure 5.29, 5.30).

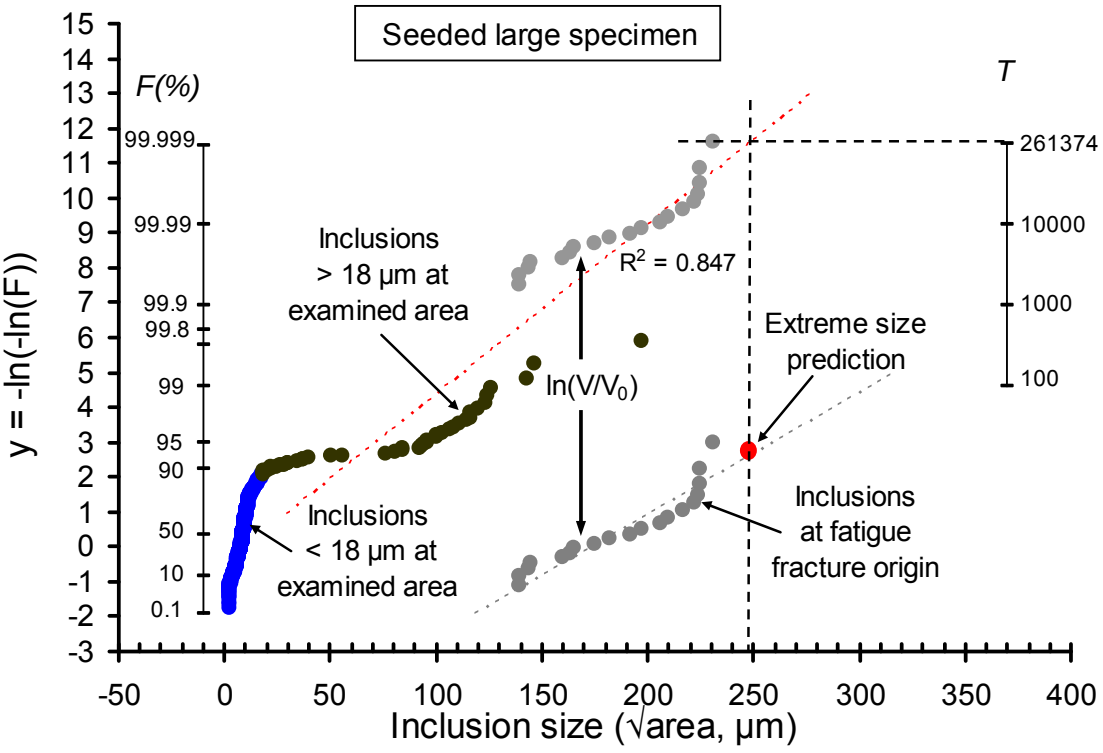

Figure 5.30 Statistics of extremes graph seeded René 88 large specimen

5.9 Size Effect

Real structures, which are larger in size than the specimens of the laboratory fatigue tests, can have considerably lower fatigue strengths. This behavior is called the size effect on fatigue. Engineering handbooks often present this effect in the form of the design curves that have been determined by the fatigue testing of specimens with the same geometry but different sizes. Kuguel [91] proposed a size effect relation, where the fatigue limit of structures is related to the highly stressed volumes:

$$\frac{\sigma_1}{\sigma_2} = \left[\frac{V_1}{V_2}\right]^{-0.034} \tag{5.7}$$

where σ_1 and σ_2 are the fatigue limits, V_1 and V_2 are the material volumes stressed to more than 95% of the maximum stress. Basically there are two reasons for the size effect (Murakami [89]):

- Differences in the stress distribution for the different sizes, and
- Statistical scatter of strength and microstructure at the critical part under cyclic loading.

Differences in the stress distribution for the different sizes are basically similar to the notch effect. The stress concentration factor, K_t, for two geometrically similar specimens with different sizes, under the same nominal stress is the same and the values of the maximum elastic stresses at the notch tips of both specimens are also the same, but the stress gradient is smaller for the larger specimen, and accordingly the critical condition for the larger specimen is more severe than that for the smaller specimen.

Statistical scatter of strength and microstructure at the critical part under cyclic

loading is very important. When the defects, e.g., the nonmetallic inclusions initiate fatigue cracks, in a volume of material subjected to the same cyclic stress, the fatigue failure occurs at the largest inclusion that is present in the volume. That is, fatigue fracture is a weakest link phenomenon. The fatigue strength is, thus, controlled by the extreme values of the population of inclusions. The size of the maximum inclusion in the population of inclusions can be estimated by the statistical methods such as statistics of extreme value method.

Results of our fatigue tests were evaluated to determine the size effect on fatigue. Life versus the applied stress amplitude for two different sizes of fatigue specimens, namely large and small specimens (gage straight section volume being 4633 mm^3 and 603 mm^3) are plotted in Figure 5.31a and Figure 5.31b, respectively. It is clearly seen that there is a size driven trend in the fatigue life of both seeded and unseeded specimens. Fatigue life is reduced slightly at large specimens in unseeded material. In seeded material, there seems to be no effect of test volume on surface initiation, but seeded large specimens have slightly reduced fatigue life in internal initiated failures. For the seeded specimen, as the gage volume decreases, fatigue life under the same applied stress also decreases. This can be explained in the following way: the probability of having inclusions of a given size in a smaller volume is less than the probability of having a similar inclusion in a larger volume. Since fatigue cracks initiate at the surface or inclusions, small specimens have a smaller surface area and apparently contain fewer inclusions. The large unseeded specimens have a larger surface area exposed to the outside environment, when compared with the small unseeded specimens. Thus, the environmental effect would be more dominant in the large unseeded specimens. Our

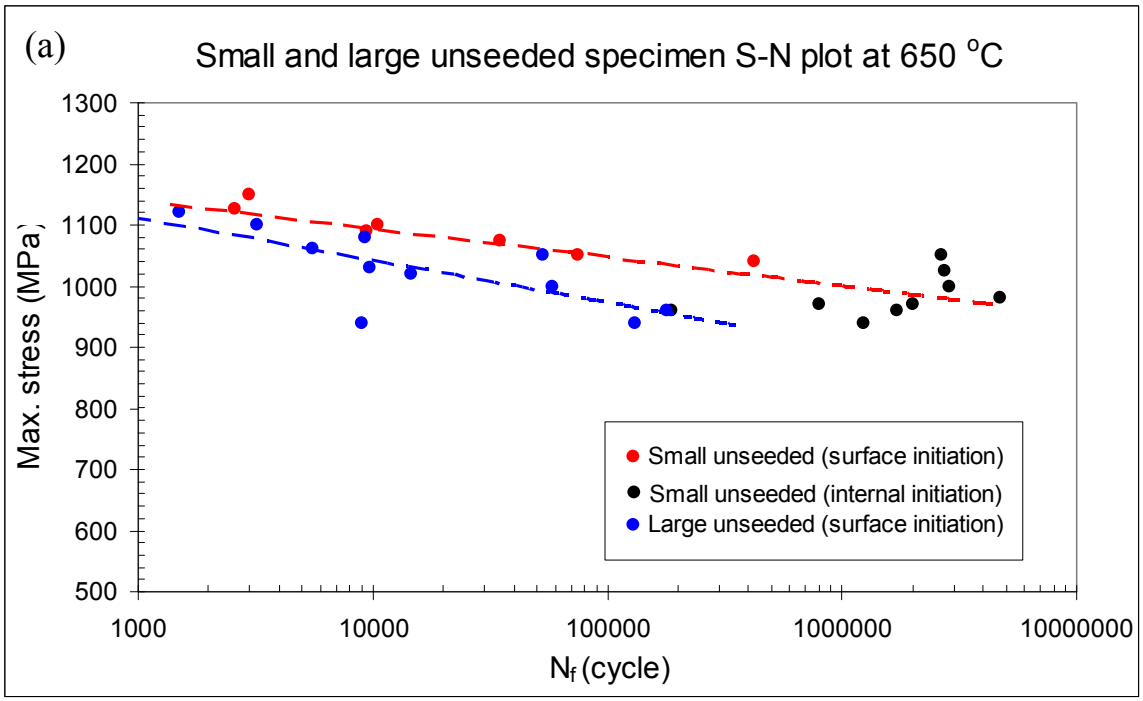

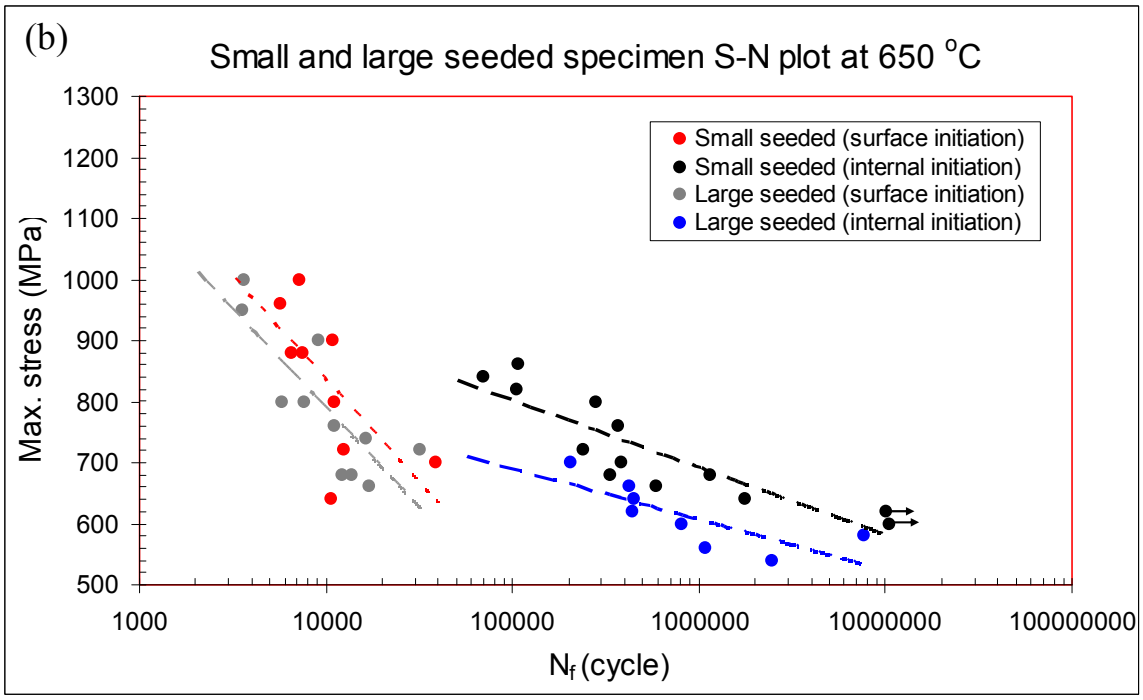

Figure 5.31 Size effect in fatigue test (a) Large and small unseeded specimen results (b) Large and small seeded specimen results.

results confirm that mechanical properties of René 88 DT are size dependent. For the seeded material, size effect is not so clear, and may be associated with microstructural instabilities and inclusions, rather than environmental effects.

CHAPTER 6

CONCLUSIONS

1. Both surface and internal crack initiation mechanisms were observed in both seeded and unseeded specimens. Results show clearly that competing mechanisms govern the fatigue crack initiation and fracture. Internal crack initiation is dominant at low stress amplitudes and high cycles. Surface fatigue crack initiation occurs at high stress amplitudes and low cycles.
2. Although two overlapping regimes of life, or duality, were not seen, distinct surface and internal crack initiation regimes were found in the S-N behavior of small unseeded René 88DT and were separated at about 10^5 cycles.
3. The fatigue data of seeded material showed two separate S-N curves, for surface and internal initiations. A clear duality or duplex is seen. It has been clearly established that defect content is needed to create dual S-N curves.
4. There was a difference in the duality behavior between small and large fatigue specimens in seeded material. In the fatigue life of seeded René 88 material, competing and two separate S-N curves were found in small test volume, where as in large test volume, the regions were separated by a "step" in S-N curve.
5. The difference in duality between small and large specimens seems to arise as a result of defect size. This was confined by stress intensity factor versus fatigue life curves determined based on Murakami's stress intensity factor solution.

Although the duality or duplex behavior was absent in this data, separated internal versus surface failure domains were seen.

6. For the unseeded material, cracks initiating from the surface of the fatigue specimens seemed to originate as a crack formed along grain boundaries of a few grains (intergranular regions), while cracks initiating in the subsurface of the fatigue specimens seemed to have started at an inclusion particle or cluster of inclusion particles.
7. All failures in small or large specimens of seeded material occurred due to cracks initiating from the seeded inclusions.
8. In the fatigue life of unseeded René 88 DT is reduced with increase in specimen test volume.
9. For seeded material with small and large specimen sizes, it was found that there is no direct relationship between the inclusion size and fatigue life. However, a correlation in terms of K_{max} was helpful to understand the duality of fatigue curves.
10. The extreme size of the unseeded inclusion ($\sqrt{area}_{max}$) predicted by Murakami method is 52.7 μm for 16 tested specimen volumes. This agreed well with the largest size of 50.9 μm found from the fatigue tests fracture origin in unseeded small specimen fatigue tests.
11. Based on extreme value statistics, the extreme size of the seeded inclusion ($\sqrt{area}_{max}$) expected to exist after testing 20 seeded small specimen volumes is 245 μm. This prediction compares very well with the 243 μm size found in the fatigue fracture origin in small test specimens. For the seeded large specimen, 19

pieces were tested and largest inclusion size found in the fracture origin was 231 μm. This also compares with the predicted size of 247 μm. Therefore, the predicted extreme sizes of the inclusions ($\sqrt{area}_{\max}$) values agreed well with the sizes at the fracture origin of fatigue tested seeded small and large specimens.

APPENDIX A

SMALL UNSEEDED SPECIMEN FATIGUE

TEST FRACTURE SURFACE IMAGES

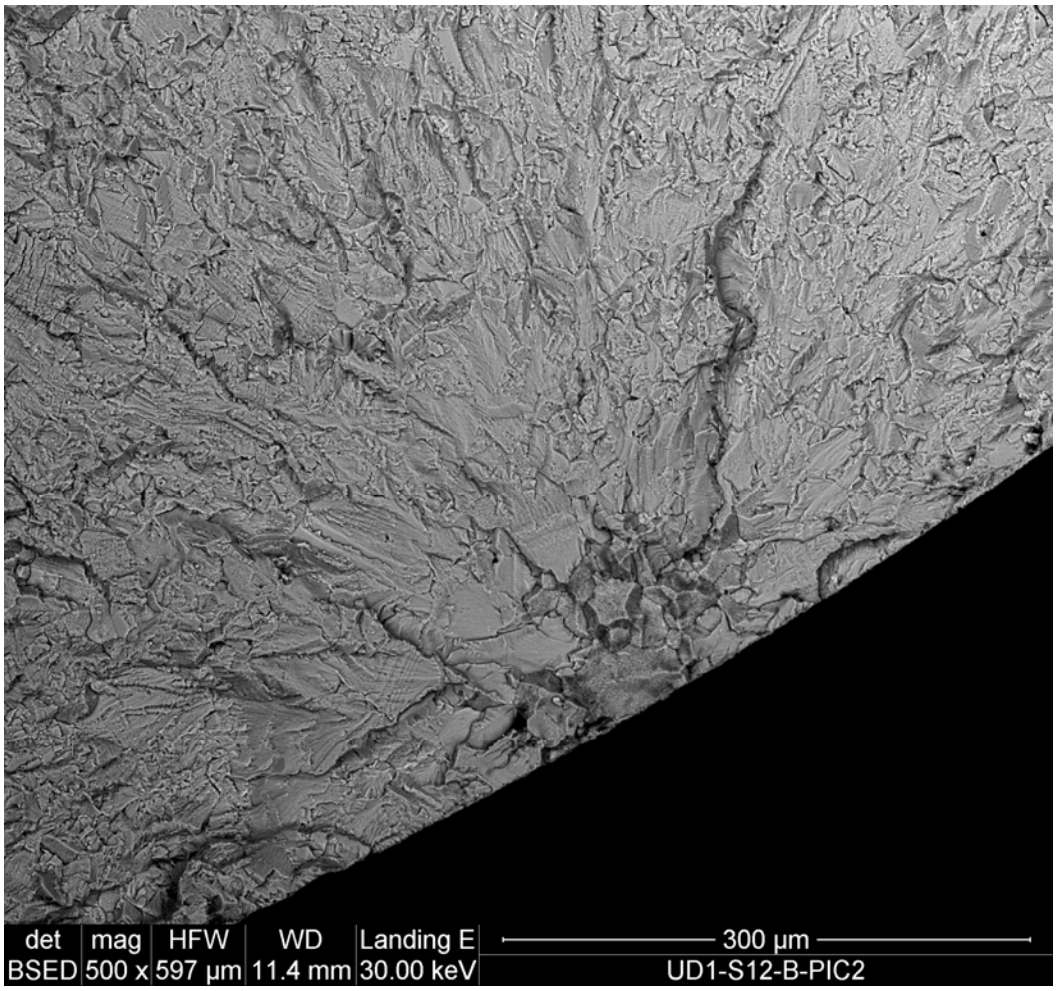

Figure A.1. Failure from surface faceted intergranular fracture in specimen UD1-S12 tested at 1050 MPa giving a life of 74762 cycles.

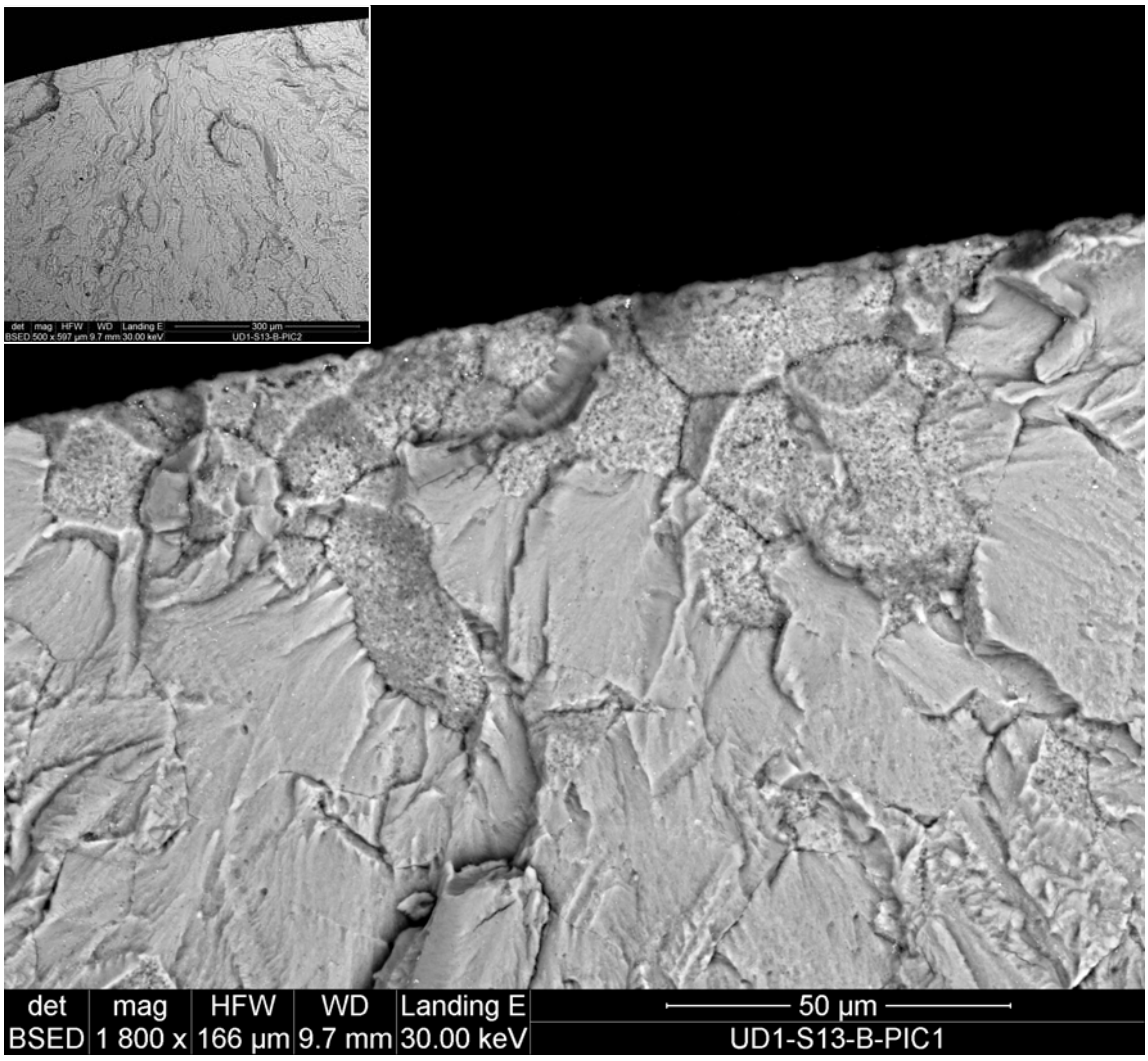

Figure A.2. Failure from surface faceted intergranular fracturein specimen UD1-S13 tested at 1100 MPa giving a life of 10575 cycles. The inset shows a lower magnification SEM image of the initiation site.

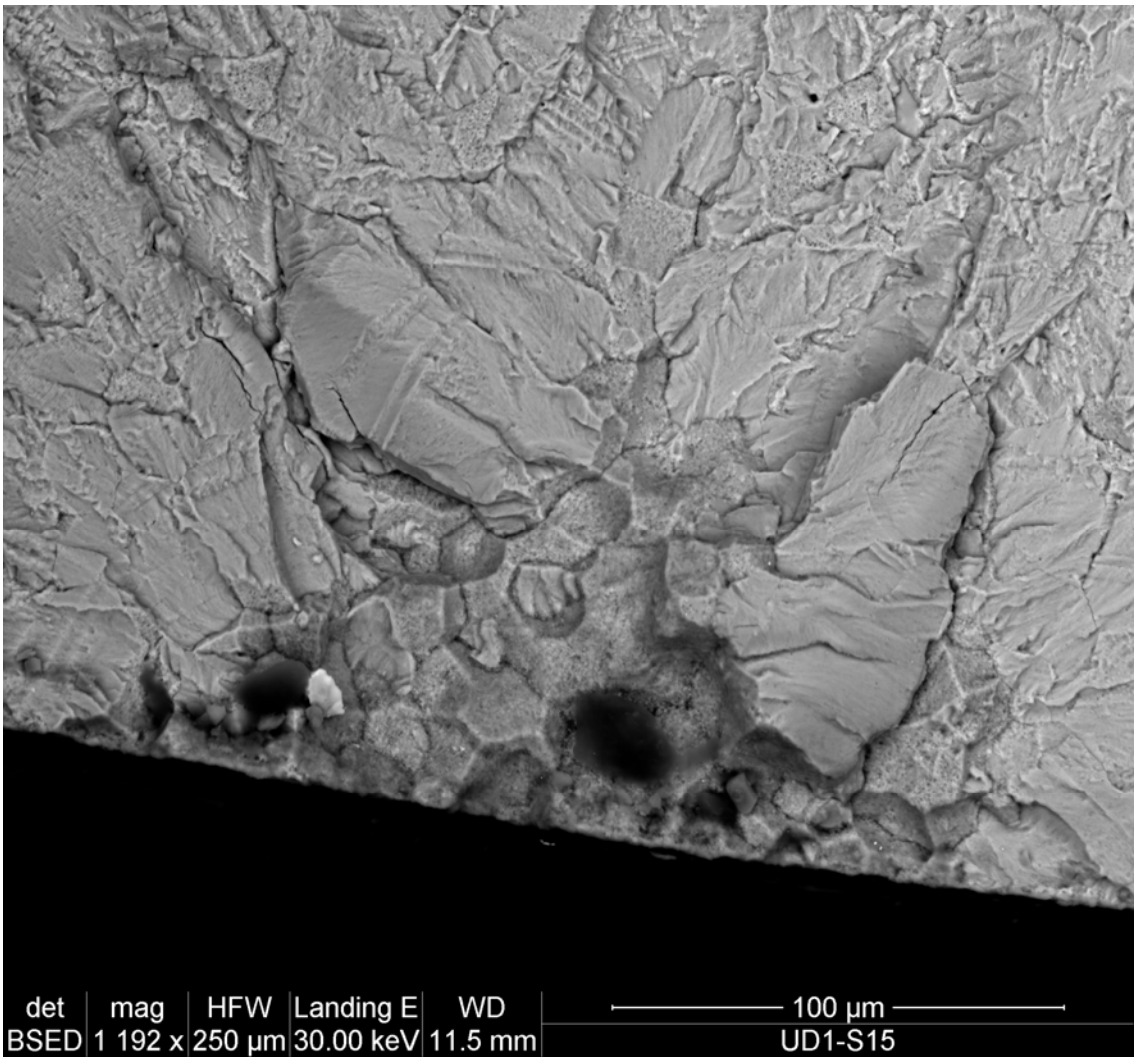

Figure A.3. Failure from surface faceted intergranular fracture in specimen UD1-S15 tested at 1075 MPa giving a life of 34796 cycles.

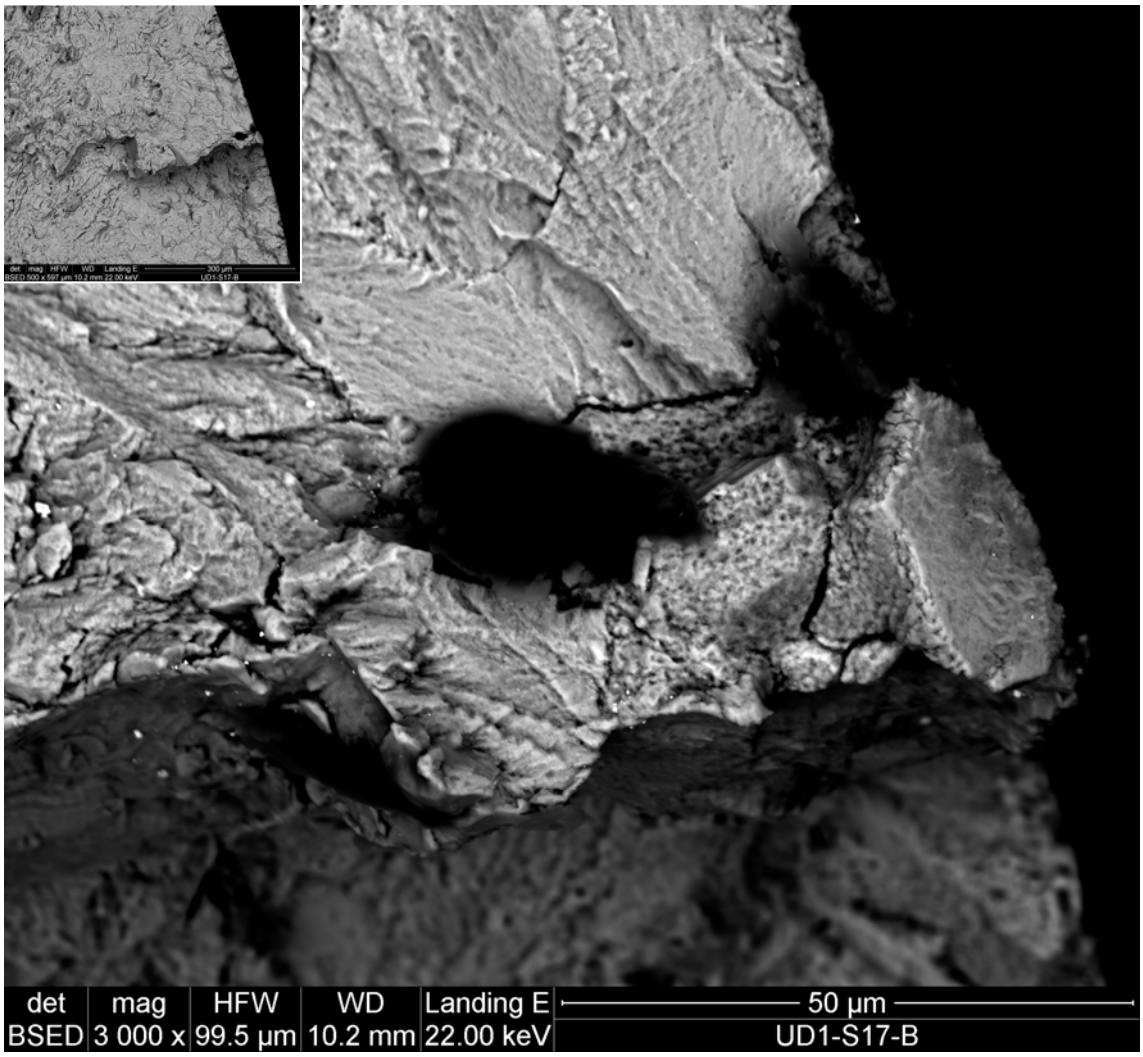

Figure A.4. Failure from surface faceted intergranular fracture in specimen UD1-S17 tested at 1150 MPa giving a life of 2997 cycles. The inset shows a lower magnification SEM image of the initiation site.

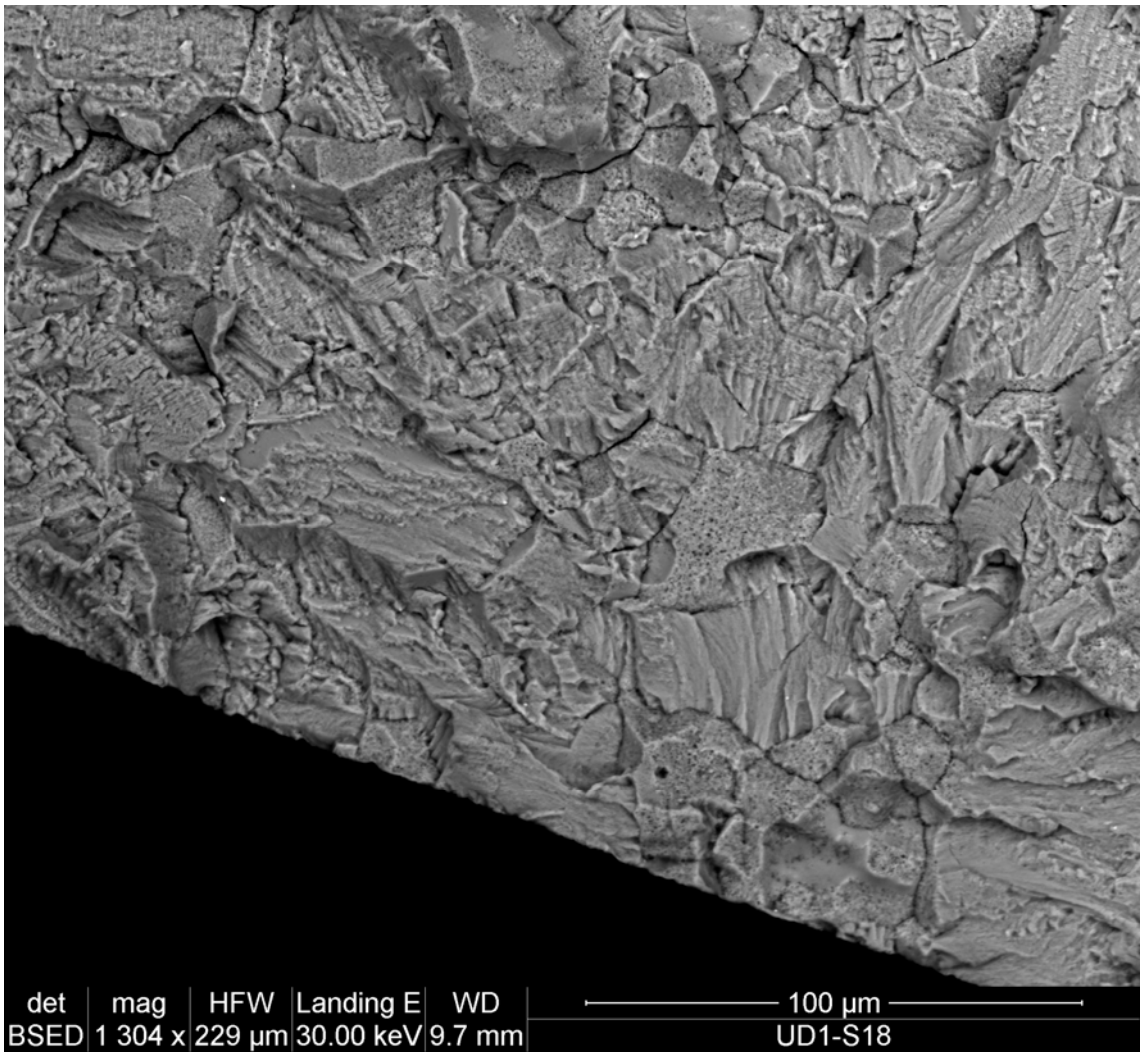

Figure A.5. Failure from surface faceted intergranular fracture in specimen UD1-S18 tested at 1125 MPa giving a life of 2576 cycles.

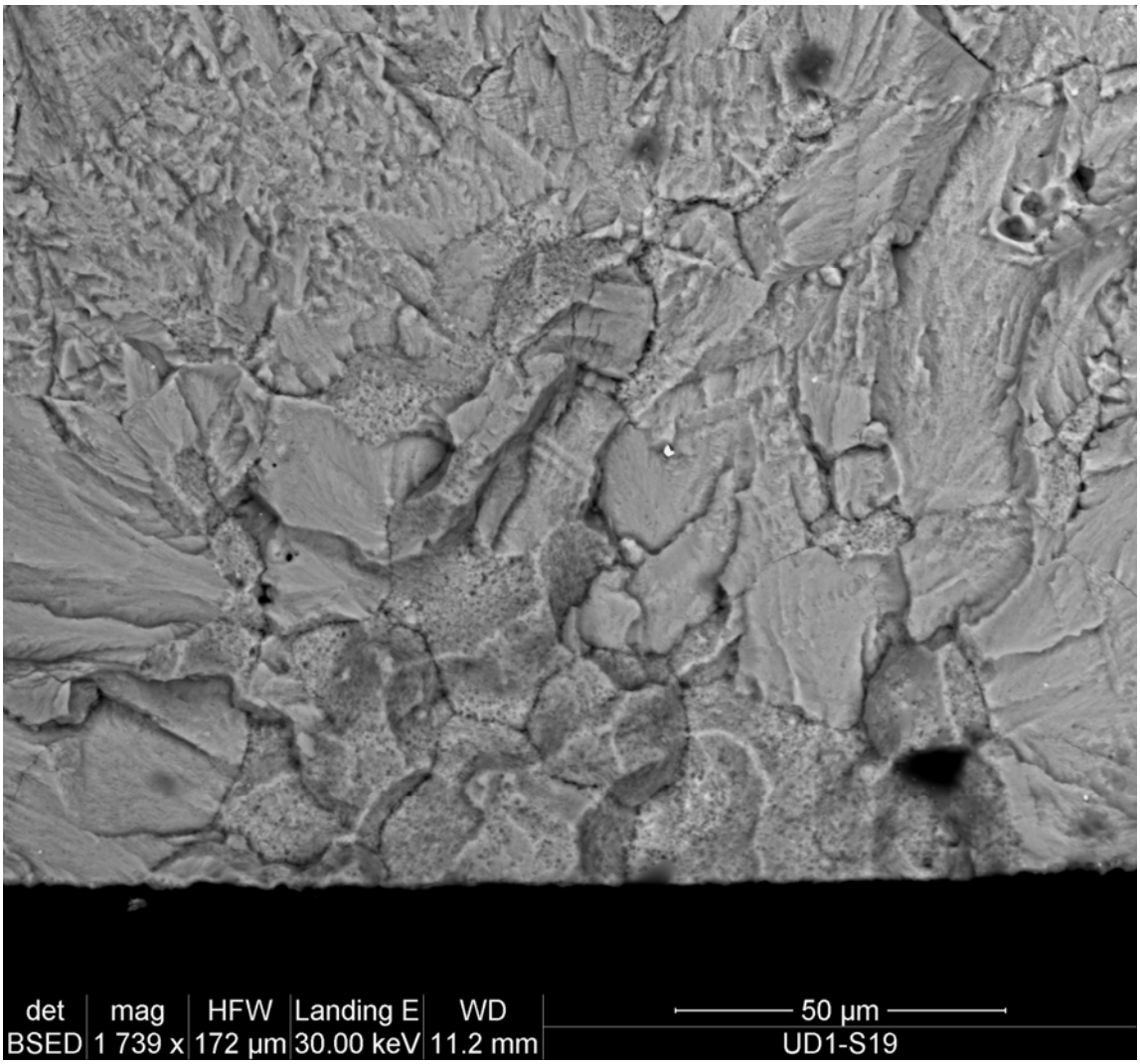

Figure A.6. Failure from surface faceted intergranular fracture in specimen UD1-S19 tested at 1090 MPa giving a life of 9397 cycles.

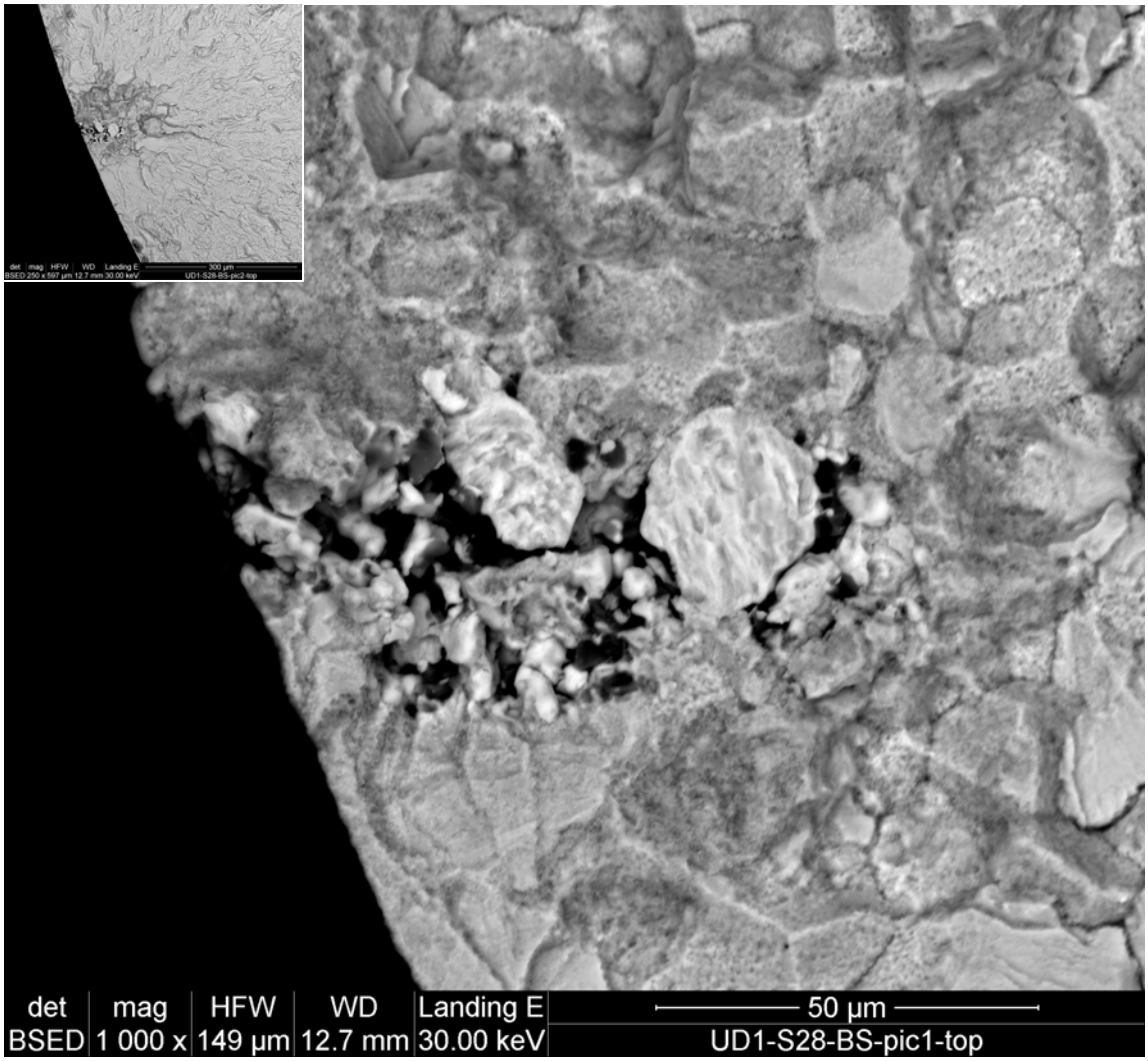

Figure A.7. Surface W particle failure in specimen UD1-S28 tested at 1040 MPa giving a life of 423320 cycles. The inset shows a lower magnification SEM image of the initiation site.

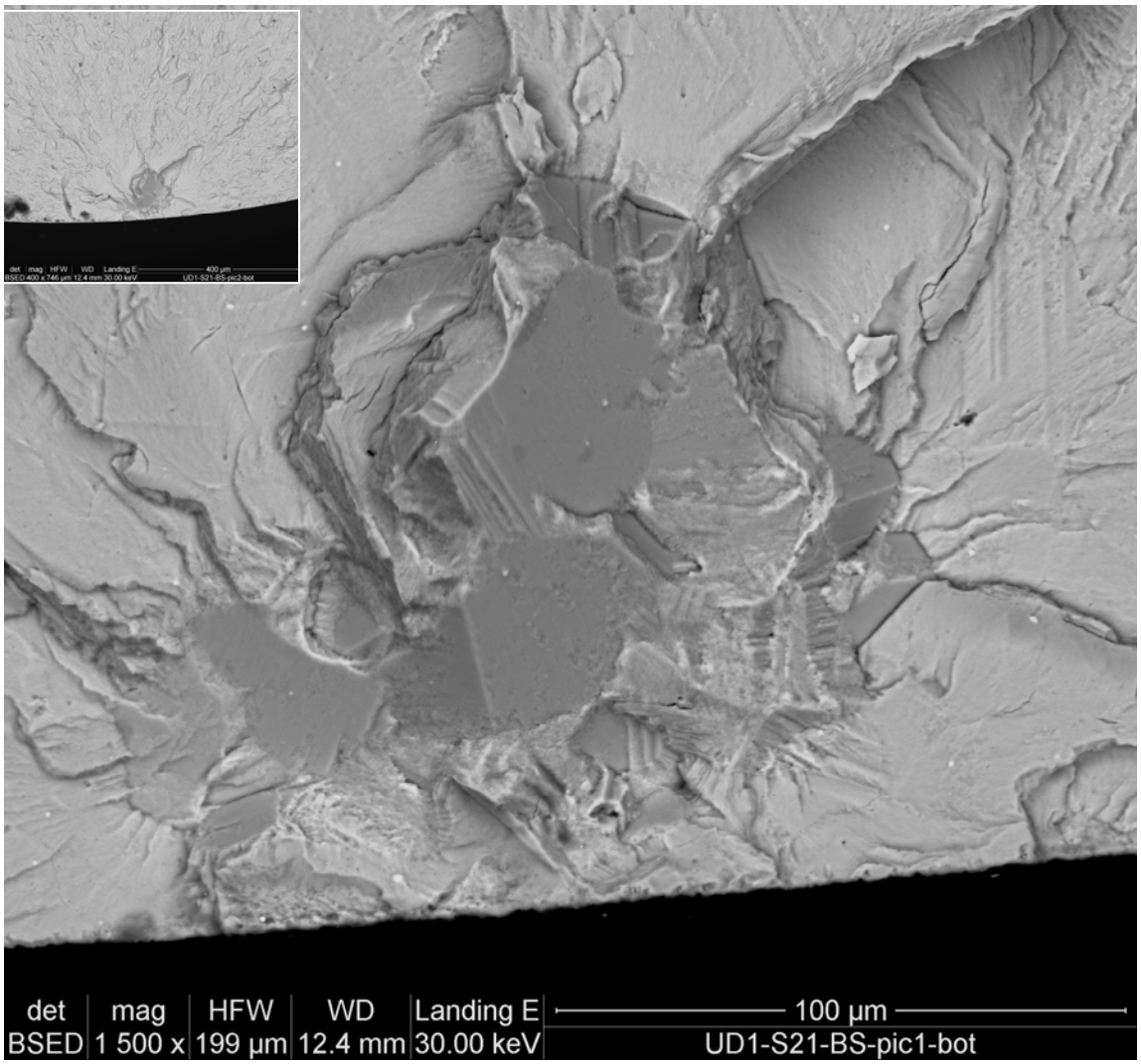

Figure A.8. Internal grain facet fracture in specimen UD1-S21 tested at 980 MPa giving a life of 4725134 cycles. The inset shows a lower magnification SEM image of the initiation site.

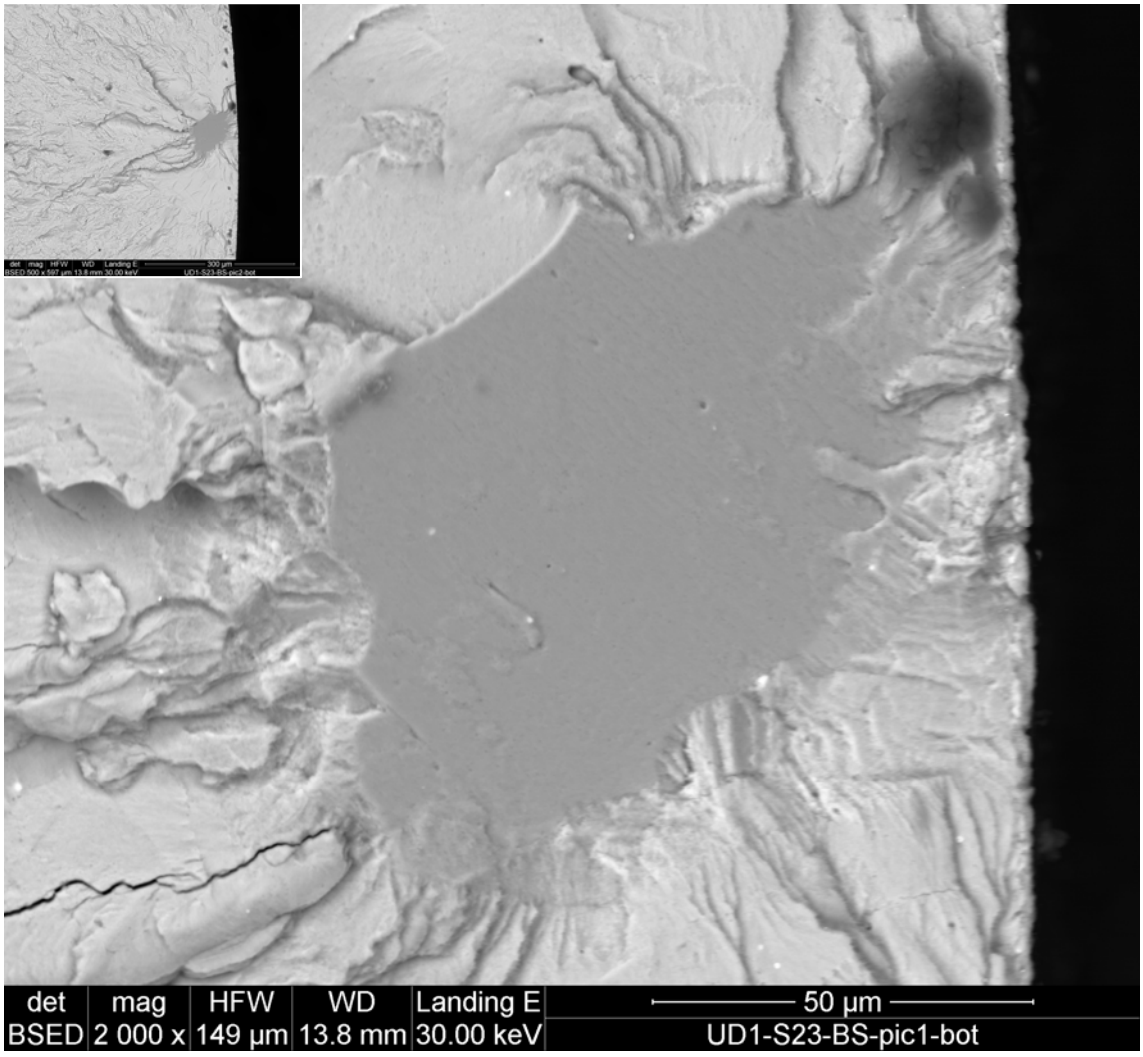

Figure A.9. Internal grain facet fracture in specimen UD1-S23 tested at 970 MPa giving a life of 2000946 cycles. The inset shows a lower magnification SEM image of the initiation site.

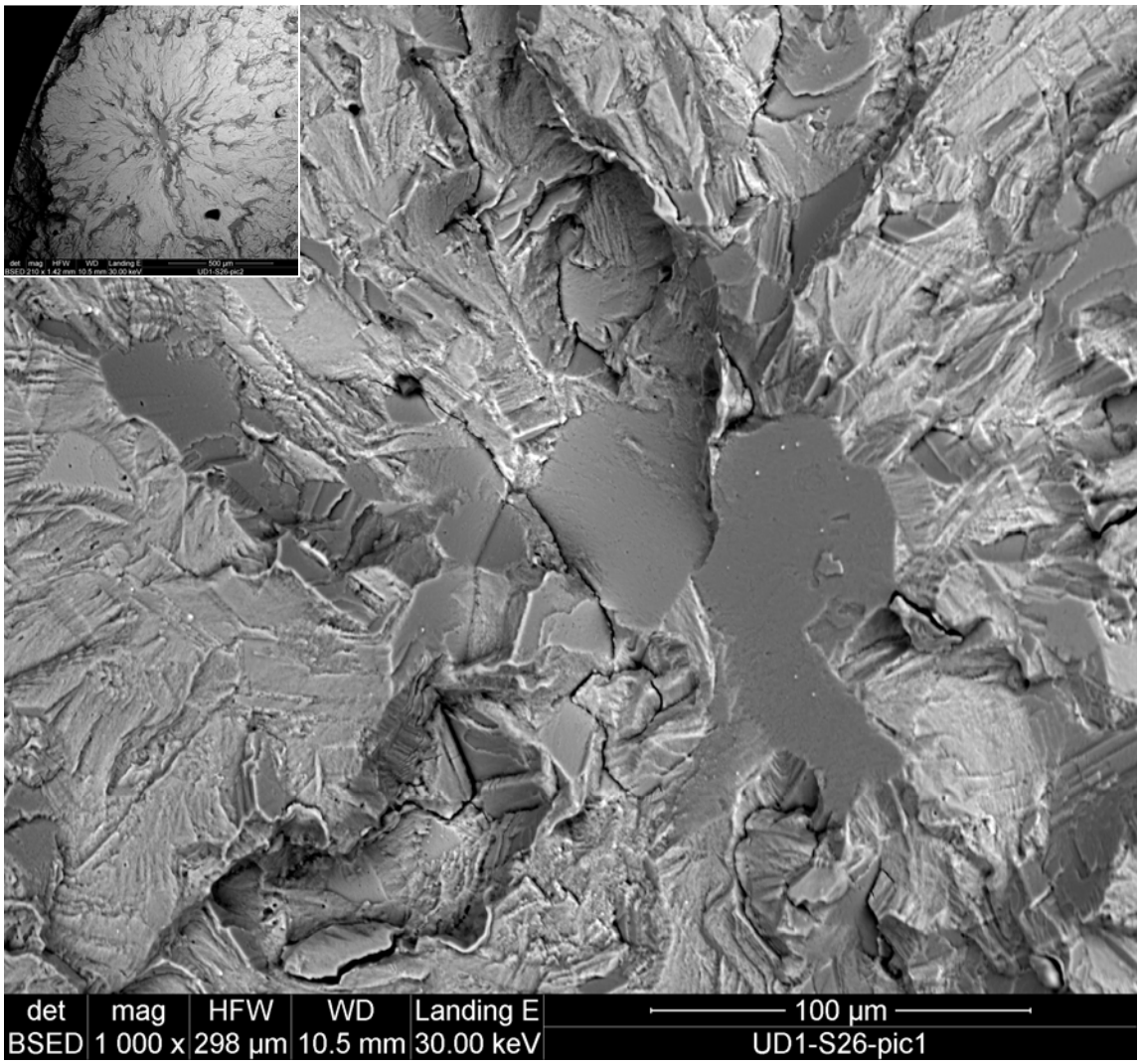

Figure A.10. Internal grain facet fracture in specimen UD1-S26 tested at 940 MPa giving a life of 1236583 cycles. The inset shows a lower magnification SEM image of the initiation site.

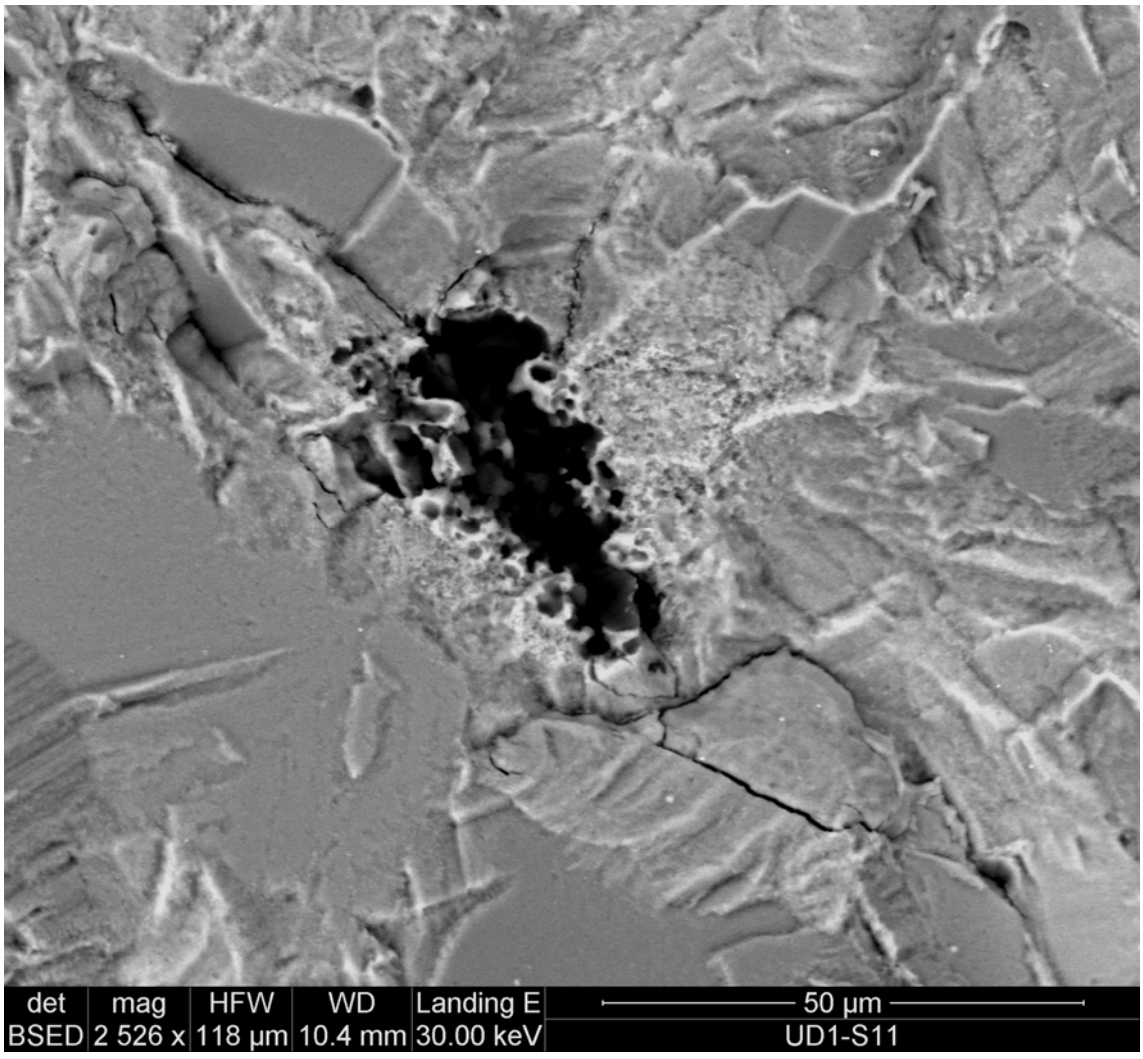

Figure A.11. Internal inclusion fracture in specimen UD1-S11 tested at 1000 MPa giving a life of 2864473 cycles.

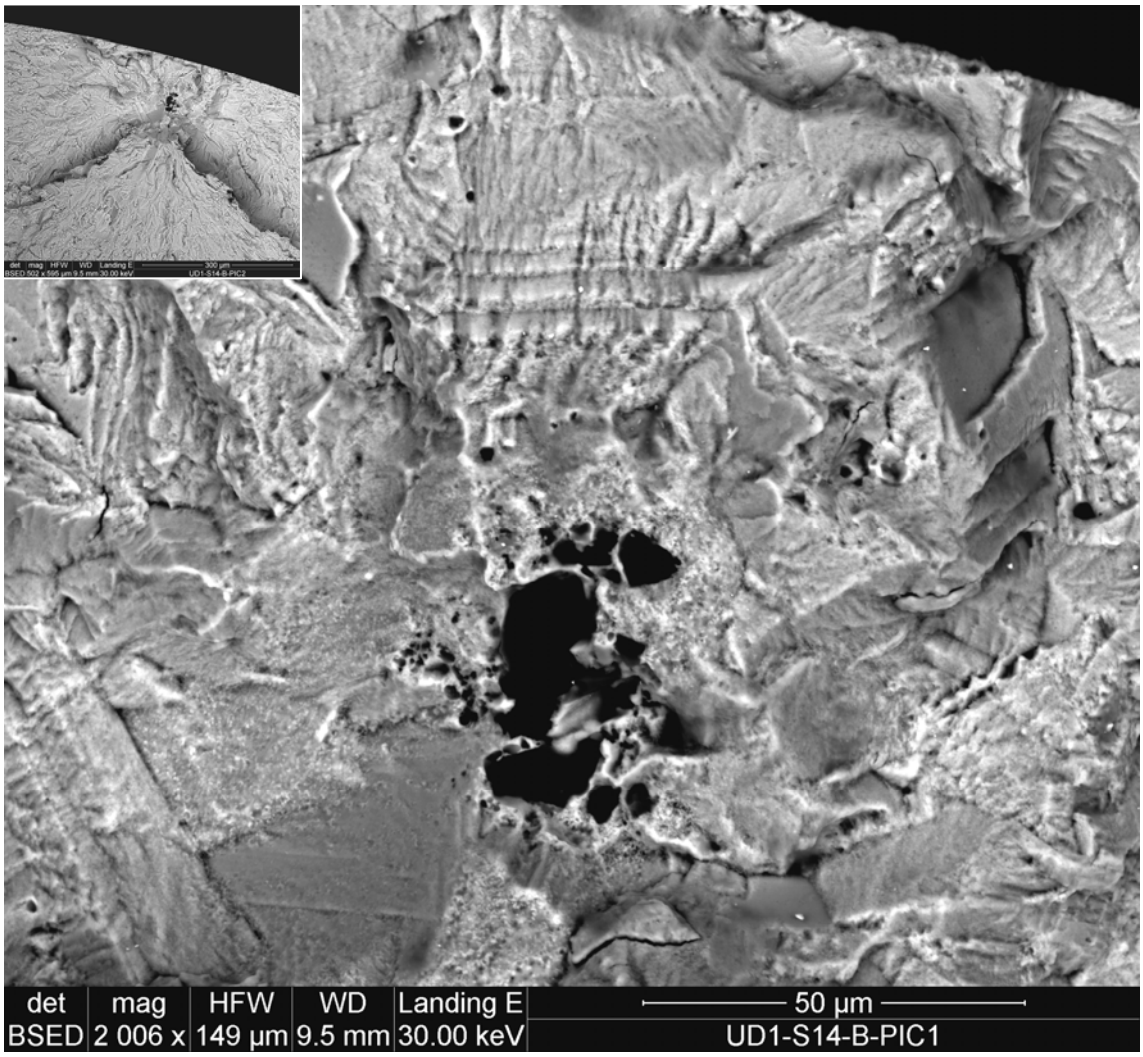

Figure A.12. Internal inclusion fracture in specimen UD1-S14 tested at 1050 MPa giving a life of 2643501 cycles. The inset shows a lower magnification SEM image of the initiation site.

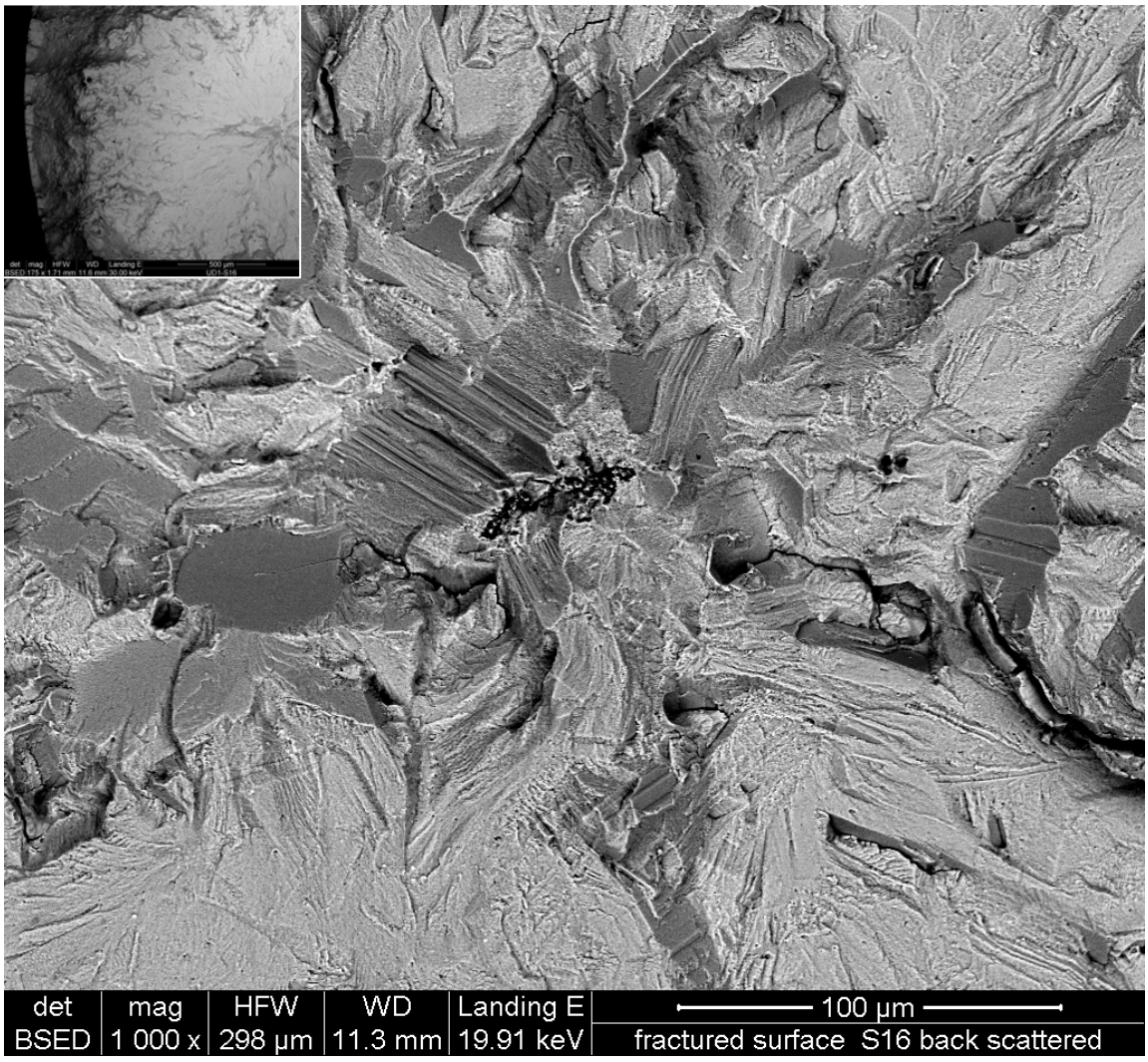

Figure A.13. Internal inclusion fracture in specimen UD1-S16 tested at 1025 MPa giving a life of 2735308 cycles. The inset shows a lower magnification SEM image of the initiation site.

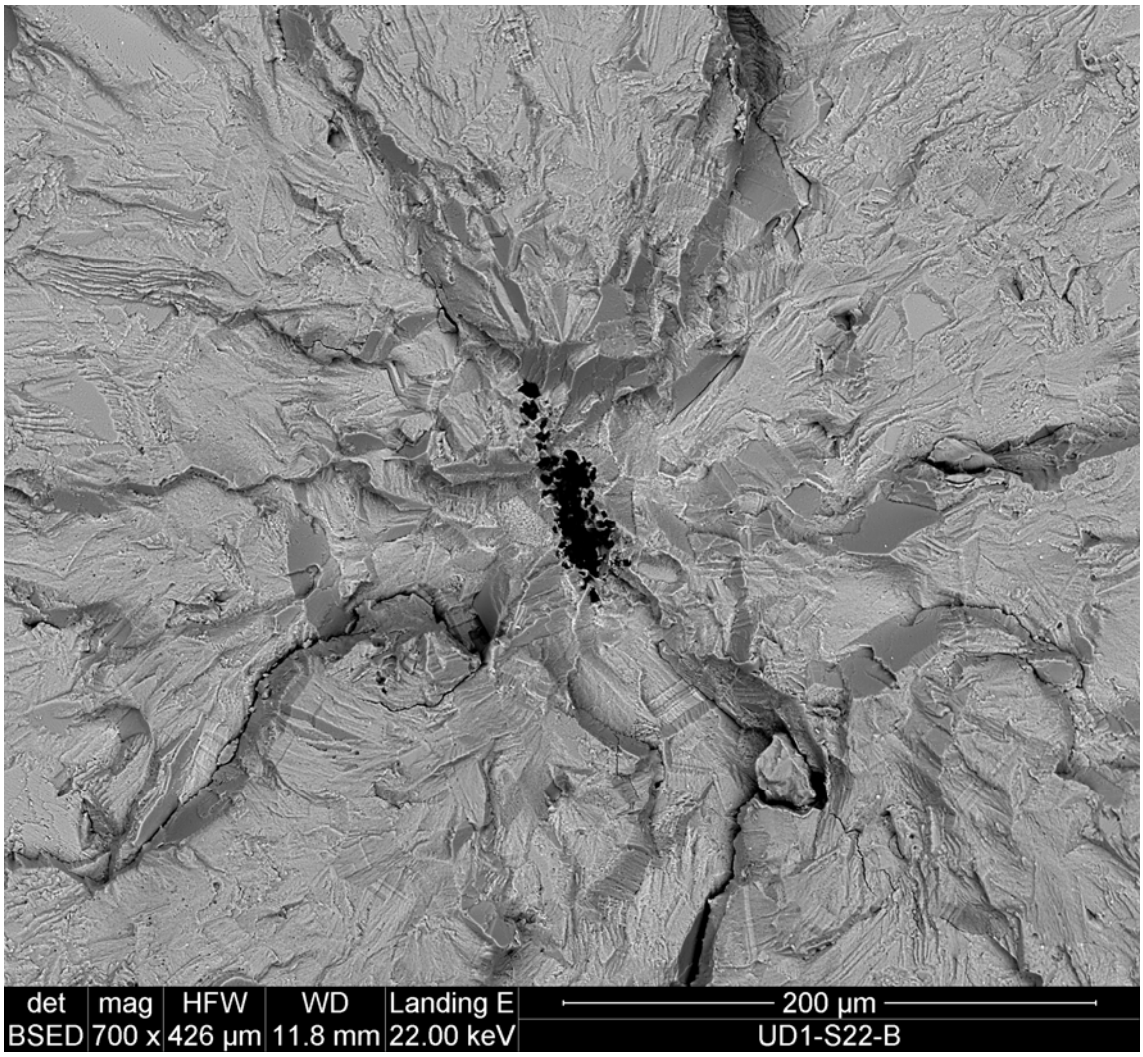

Figure A.14. Internal inclusion fracture in specimen UD1-S22 tested at 970 MPa giving a life of 801380 cycles.

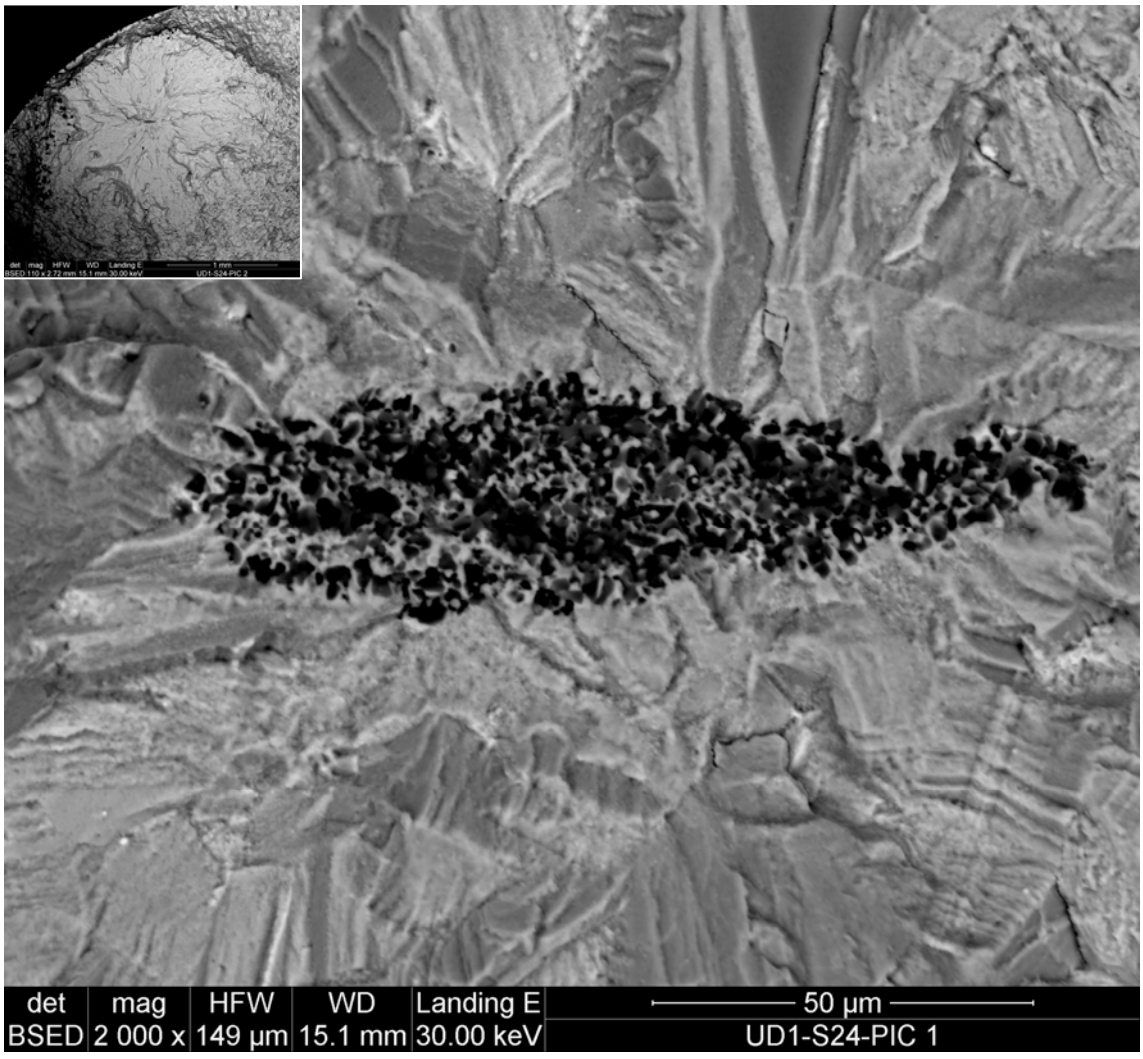

Figure A.15. Internal inclusion fracture in specimen UD1-S24 tested at 960 MPa giving a life of 187815 cycles. The inset shows a lower magnification SEM image of the initiation site.

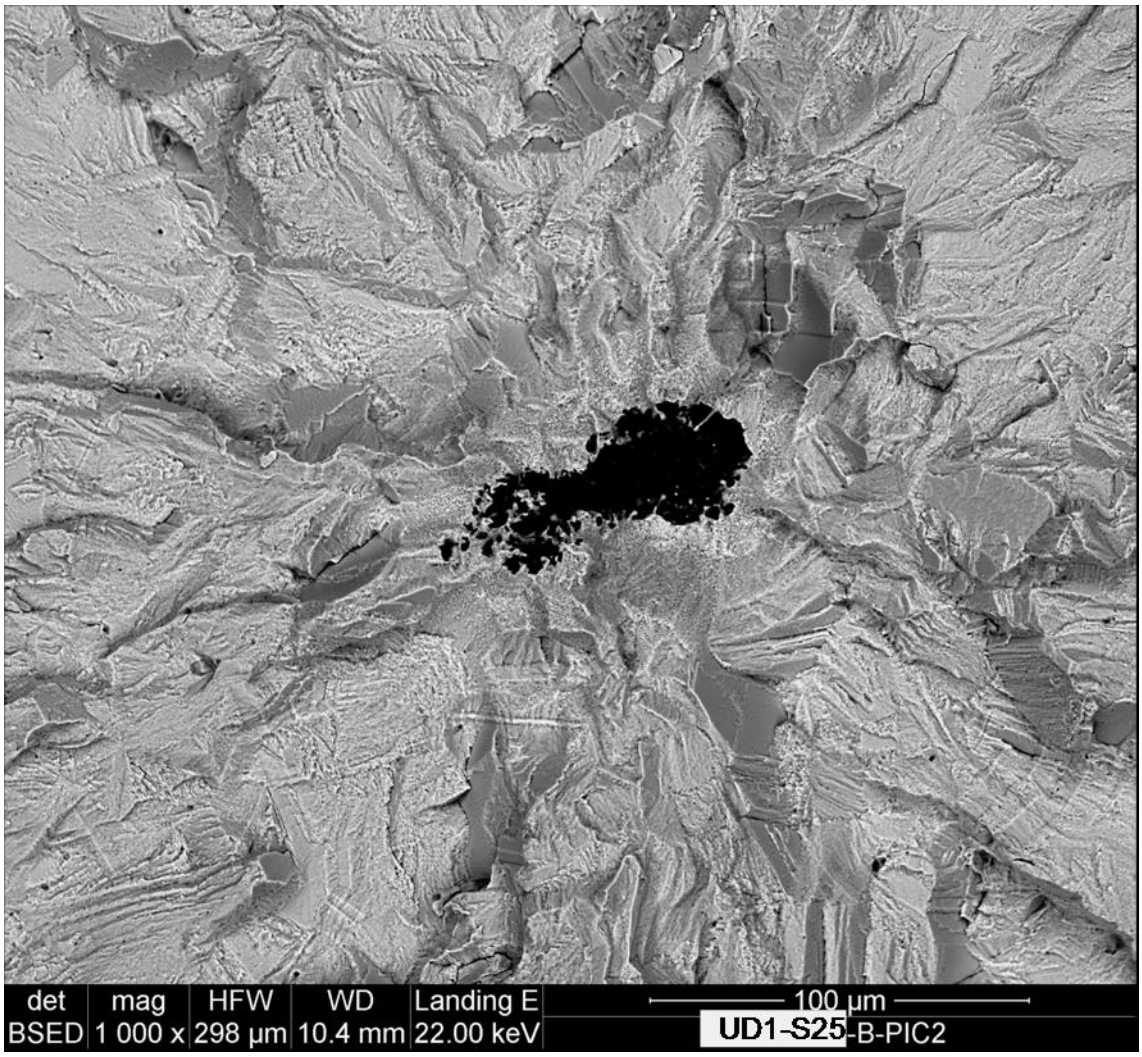

Figure A.16. Internal inclusion fracture in specimen UD1-S25 tested at 960 MPa giving a life of 1707944 cycles.

APPENDIX B

SMALL SEEDED SPECIMEN FATIGUE

TEST FRACTURE SURFACE IMAGES

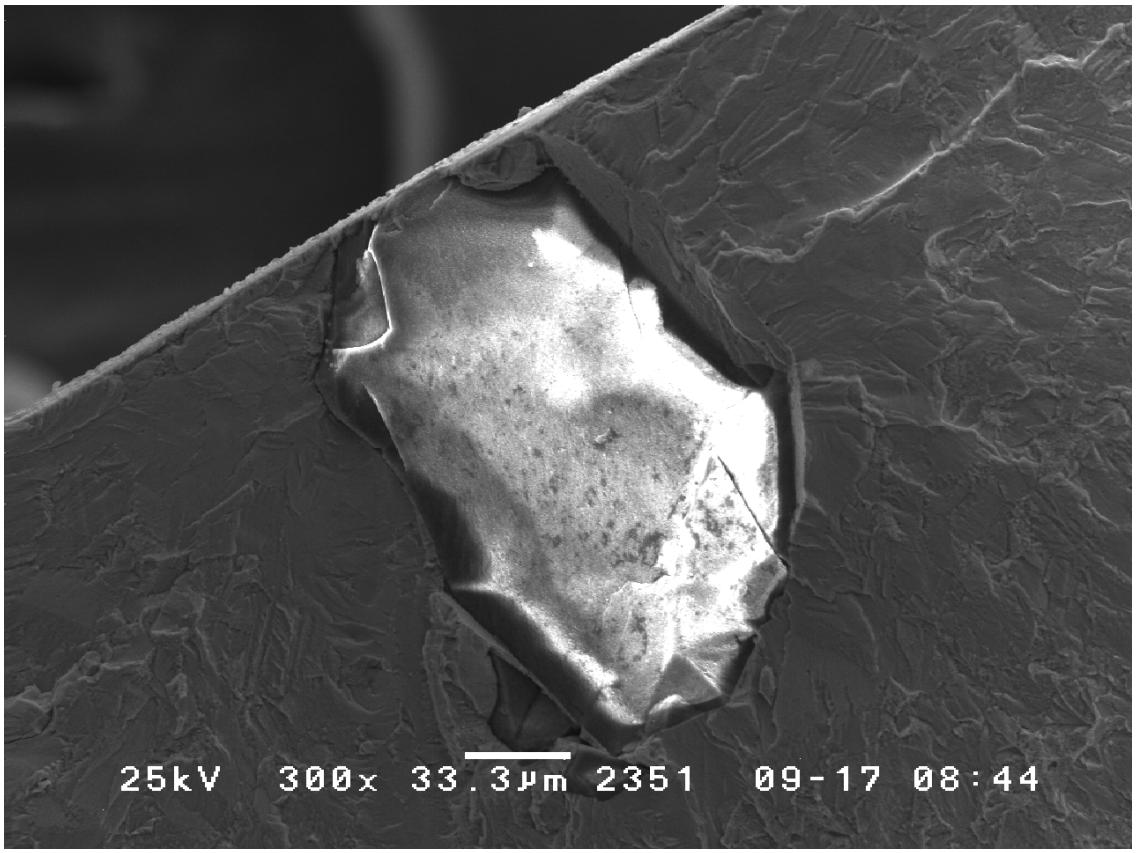

Figure B.1. Failure from surface-initiated seeded inclusion in specimen SD1-S1 tested at 900 MPa giving a life of 10921 cycles.

Figure B.2. Failure from surface-initiated seeded inclusion in specimen SD1-S2 tested at 1000 MPa giving a life of 7269 cycles.

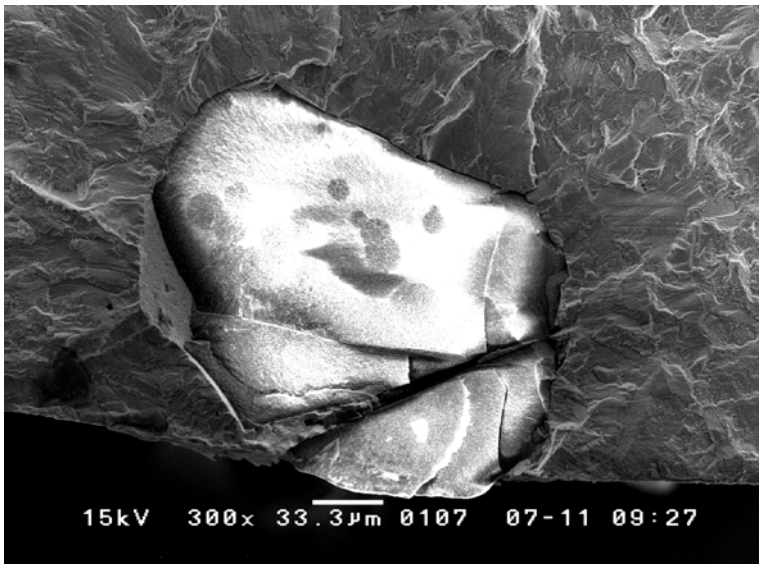

Figure B.3. Failure from surface-initiated seeded inclusion in specimen SD1-S5 tested at 960 MPa giving a life of 5715 cycles.

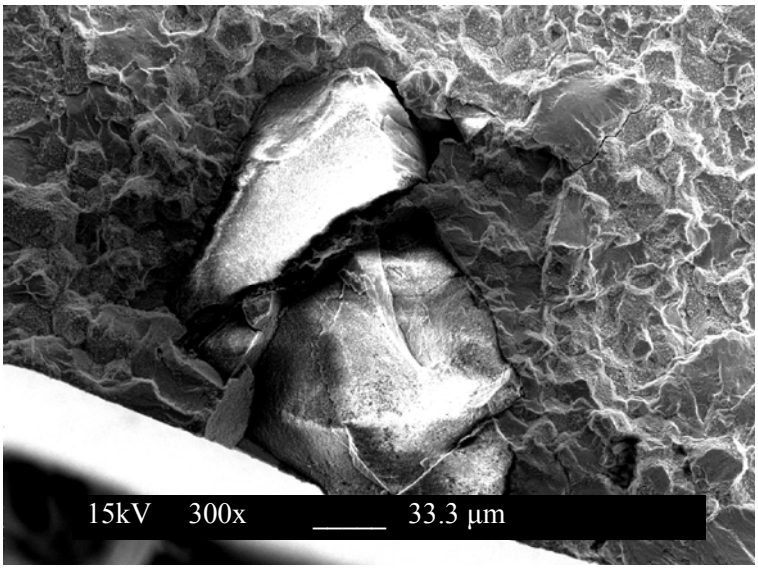

Figure B.4. Failure from surface-initiated seeded inclusion in specimen SD1-S8 tested at 720 MPa giving a life of 12551 cycles.

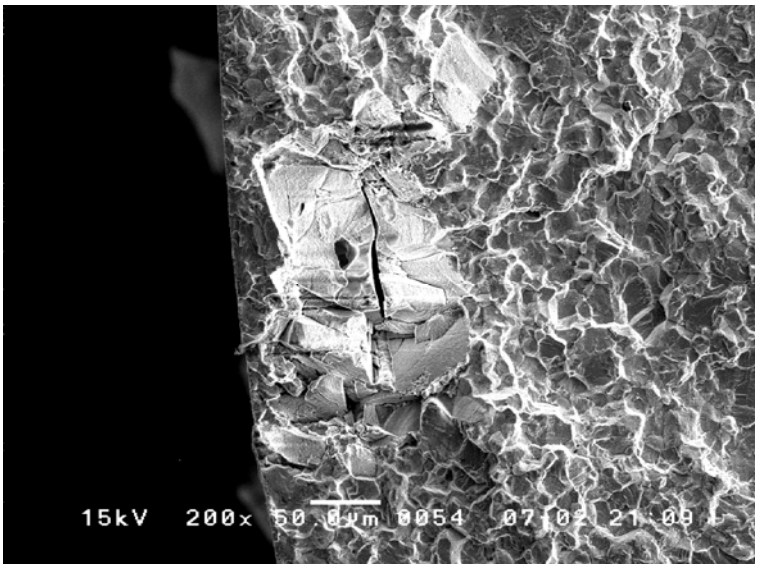

Figure B.5. Failure from surface-initiated seeded inclusion in specimen SD1-S12 tested at 640 MPa giving a life of 10789 cycles.

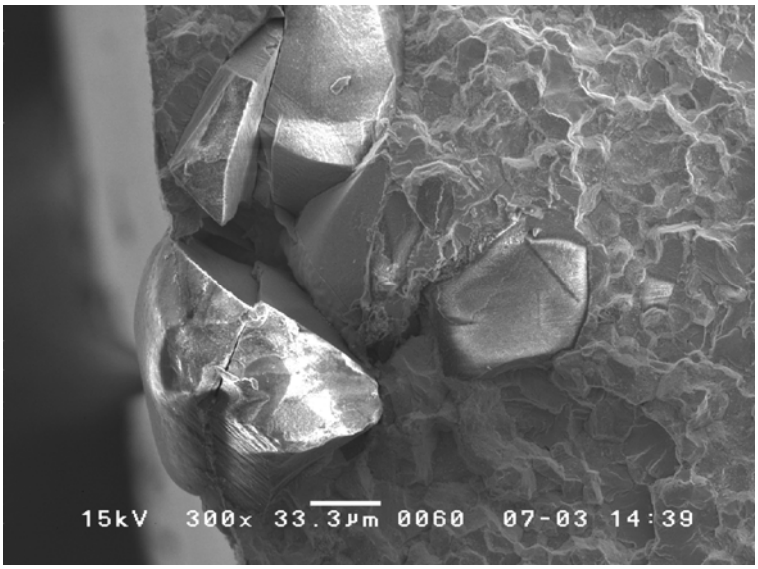

Figure B.6. Failure from surface-initiated seeded inclusion in specimen SD1-S16 tested at 700 MPa giving a life of 38818 cycles.

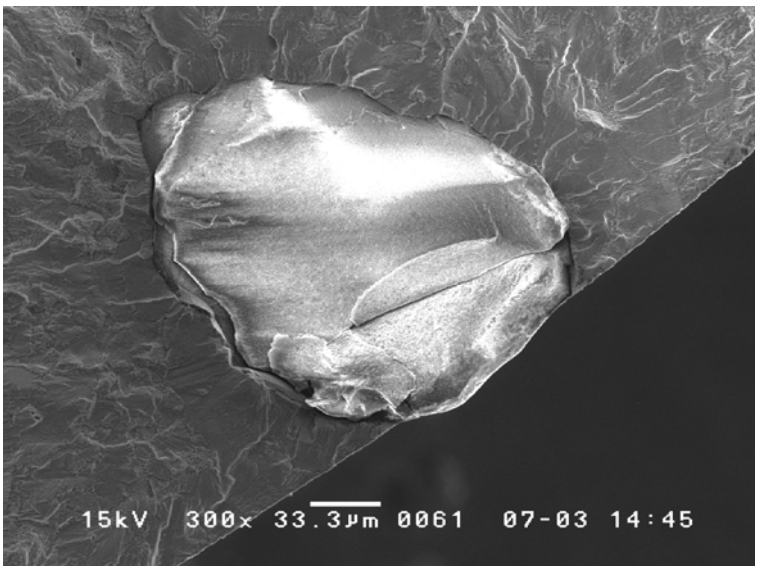

Figure B.7. Failure from surface-initiated seeded inclusion in specimen SD1-S19 tested at 880 MPa giving a life of 7501 cycles.

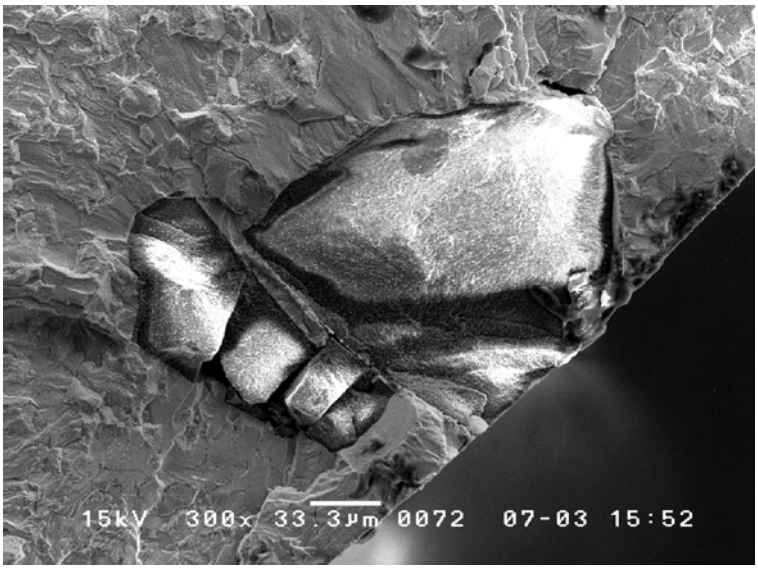

Figure B.8. Failure from surface-initiated seeded inclusion in specimen SD1-S22 tested at 880 MPa giving a life of 6553 cycles.

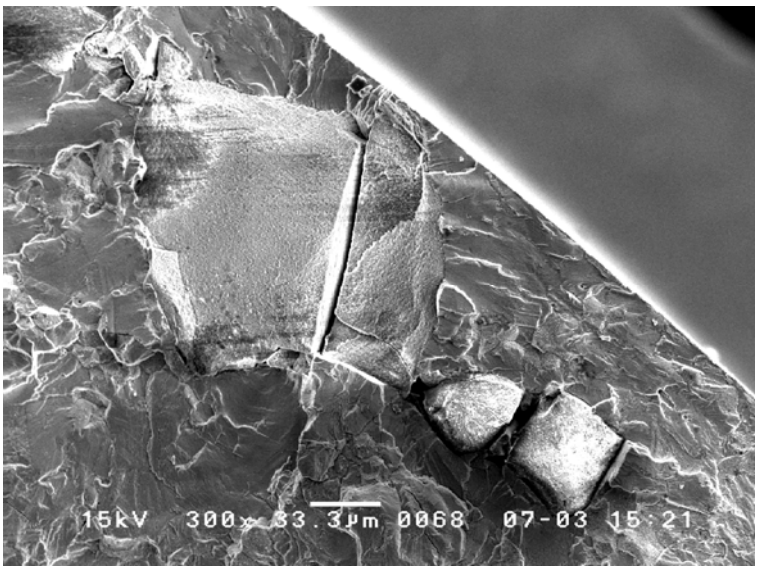

Figure B.9. Failure from surface-initiated seeded inclusion in specimen SD1-S24 tested at 800 MPa giving a life of 11162 cycles.

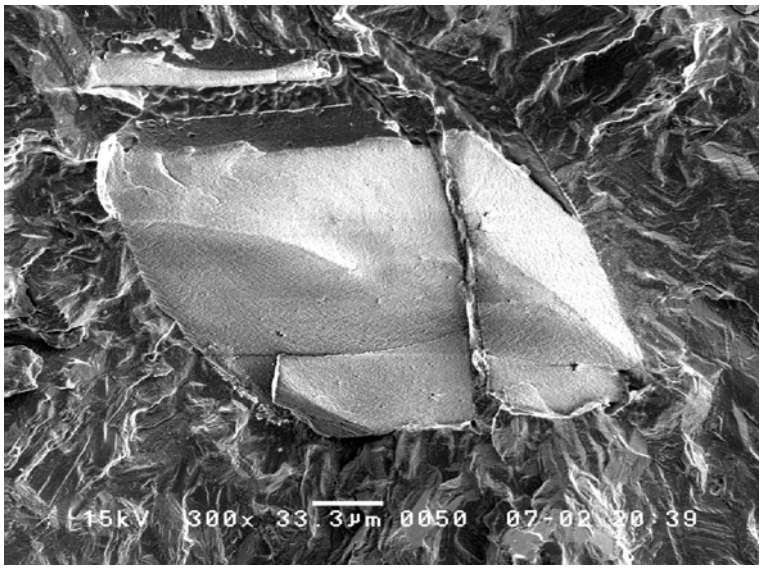

Figure B.10. Failure from internal-initiated seeded inclusion in specimen SD1-S6 tested at 800 MPa giving a life of 283304 cycles.

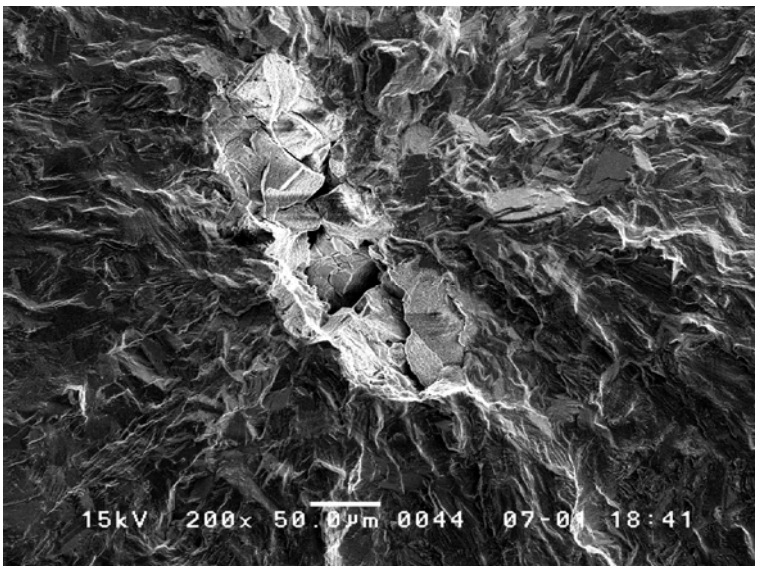

Figure B.11. Failure from internal-initiated seeded inclusion in specimen SD1-S7 tested at 760 MPa giving a life of 370468 cycles.

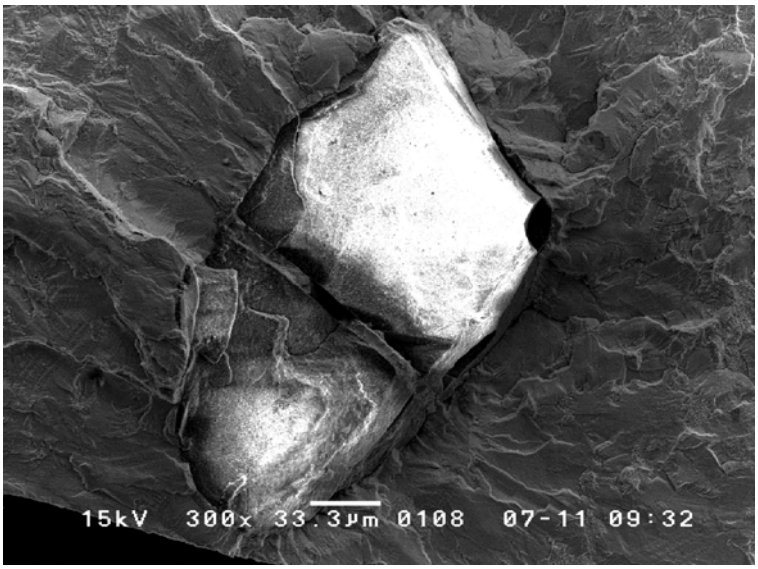

Figure B.12. Failure from internal-initiated seeded inclusion in specimen SD1-S9 tested at 840 MPa giving a life of 69989 cycles.

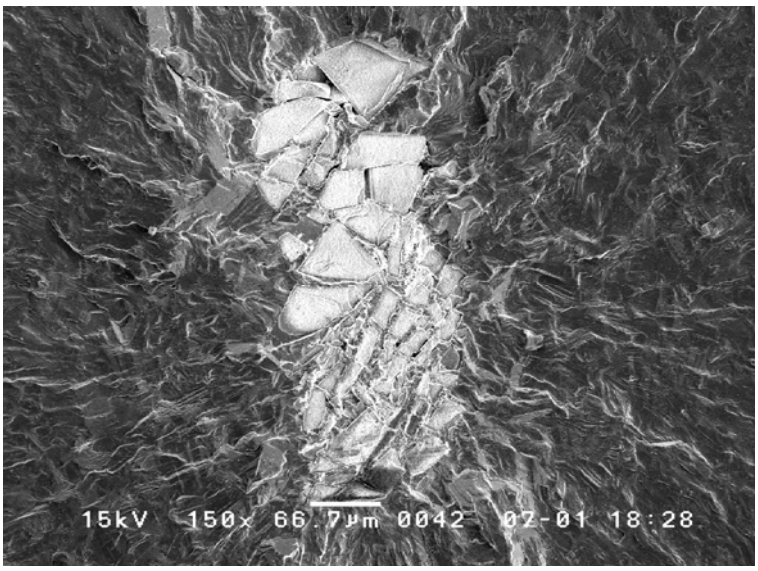

Figure B.13. Failure from internal-initiated seeded inclusion in specimen SD1-S10 tested at 720 MPa giving a life of 241320 cycles.

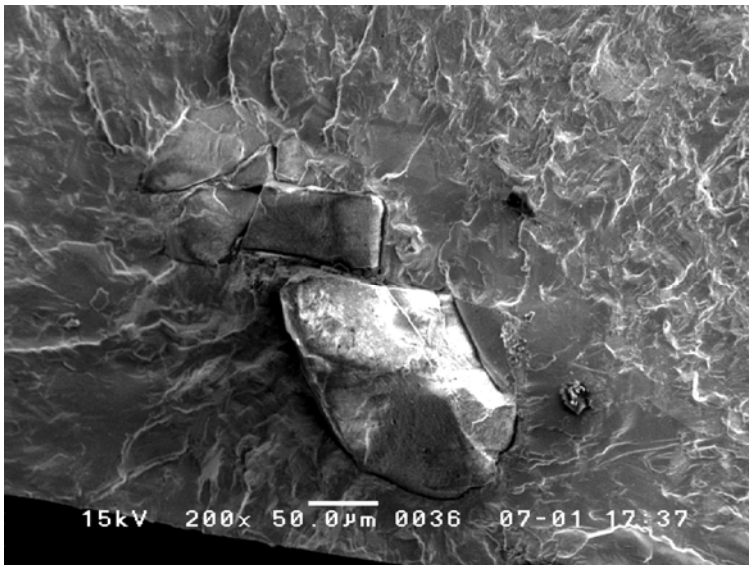

Figure B.14. Failure from internal-initiated seeded inclusion in specimen SD1-S11 tested at 680 MPa giving a life of 1153570 cycles.

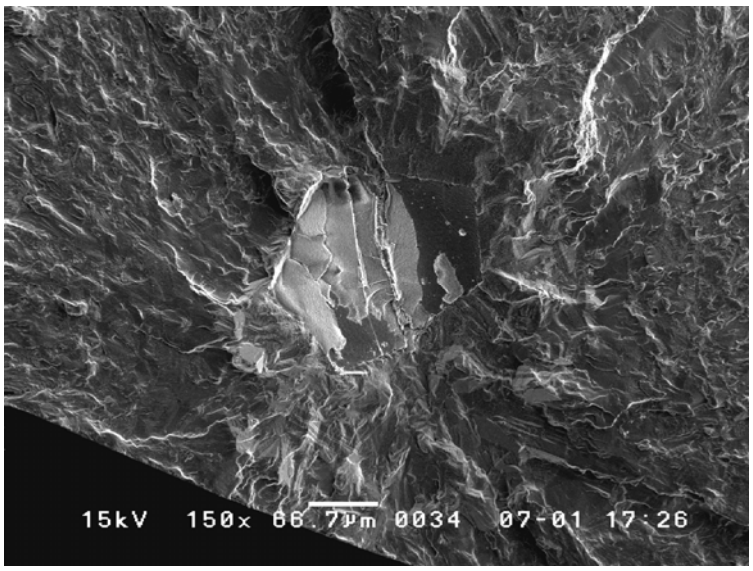

Figure B.15. Failure from internal-initiated seeded inclusion in specimen SD1-S13 tested at 640 MPa giving a life of 1771691 cycles.

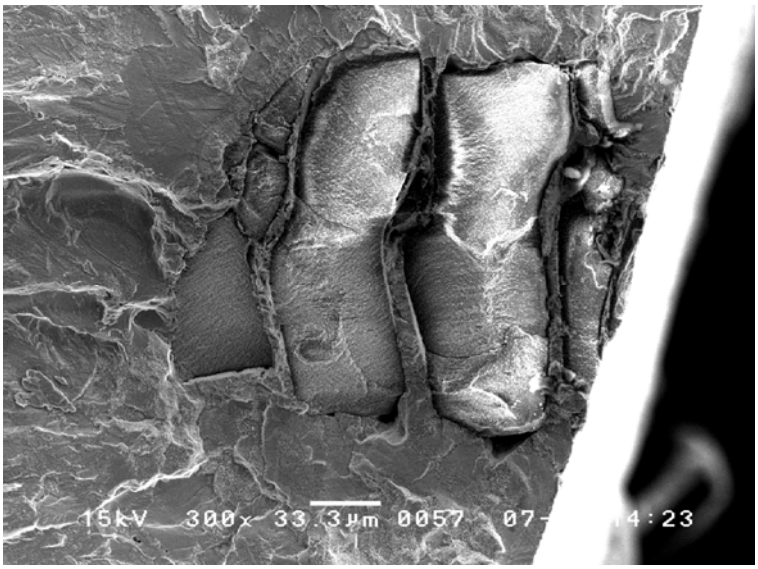

Figure B.16. Failure from internal-initiated seeded inclusion in specimen SD1-S15 tested at 820 MPa giving a life of 105277 cycles.

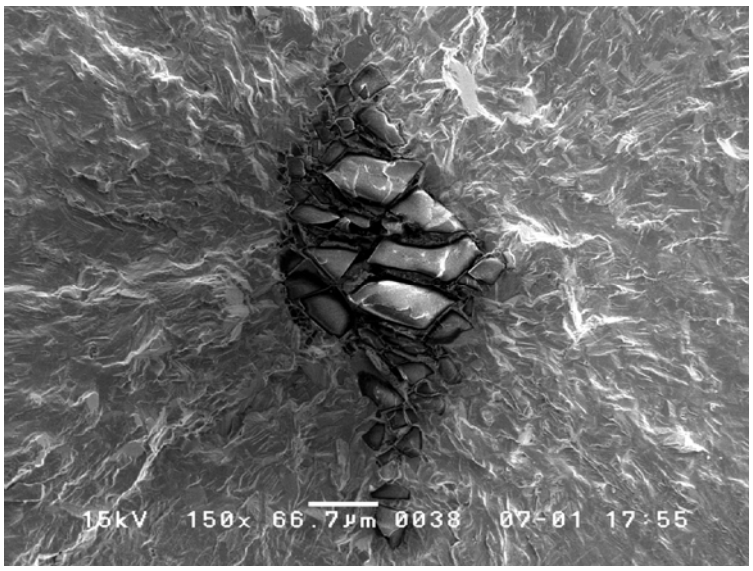

Figure B.17. Failure from internal-initiated seeded inclusion in specimen SD1-S18 tested at 700 MPa giving a life of 383225 cycles.

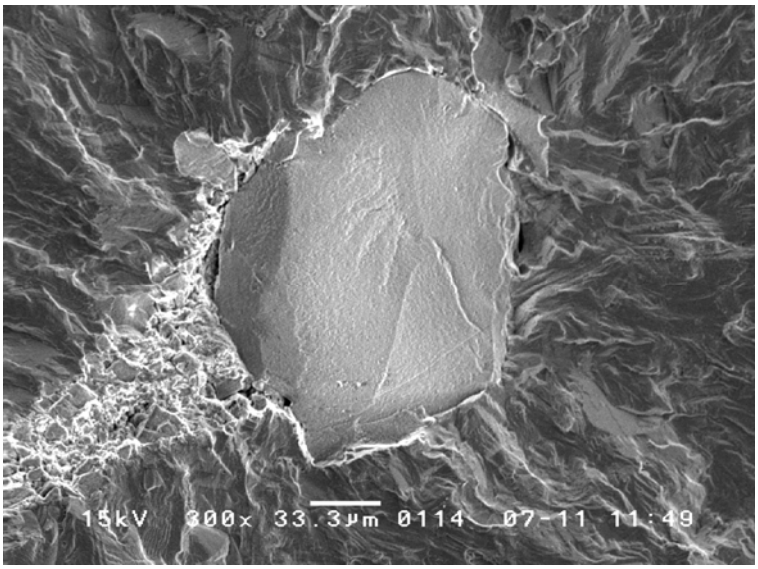

Figure B.18. Failure from internal-initiated seeded inclusion in specimen SD1-S20 tested at 860 MPa giving a life of 107446 cycles.

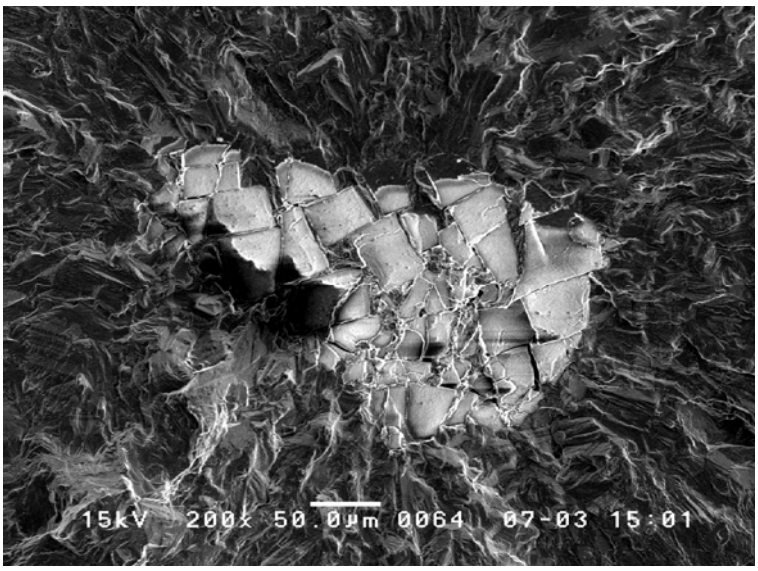

Figure B.19. Failure from internal-initiated seeded inclusion in specimen SD1-S25 tested at 680 MPa giving a life of 335557 cycles.

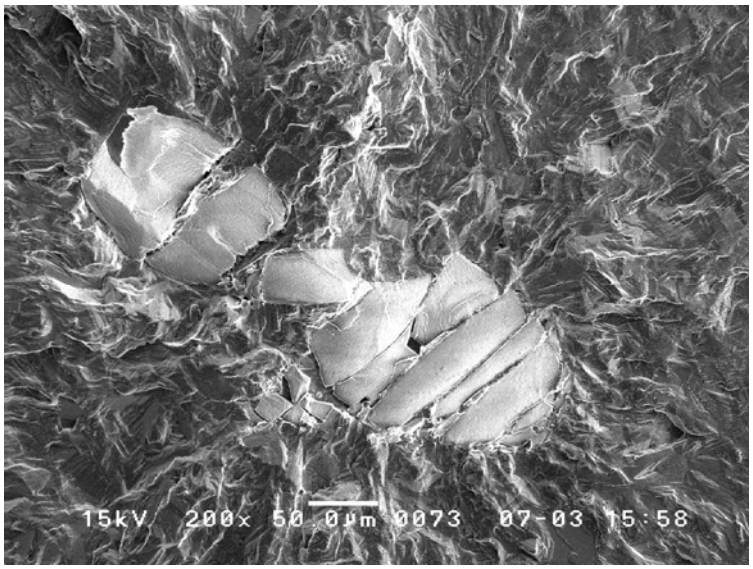

Figure B.20. Failure from internal-initiated seeded inclusion in specimen SD1-S27 tested at 660 MPa giving a life of 587750 cycles.

APPENDIX C

LARGE UNSEEDED SPECIMEN FATIGUE

TEST FRACTURE SURFACE IMAGES

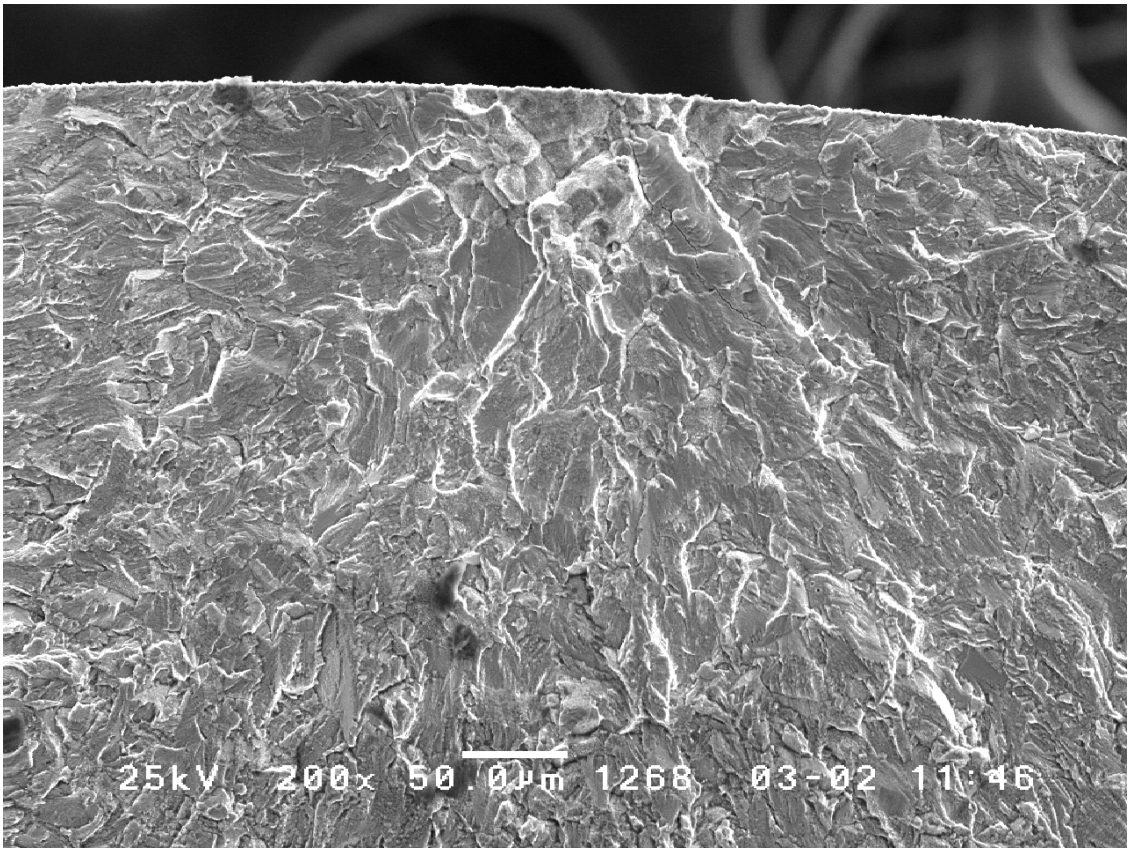

Figure C.1. Surface failure from faceted intergranular in specimen UD1-L6 tested at 1050 MPa giving a life of 53222 cycles.

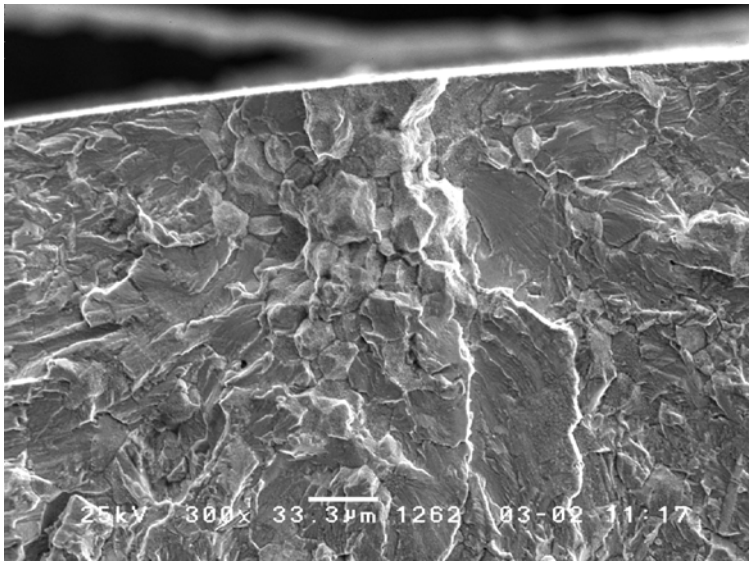

Figure C.2. Surface failure from faceted intergranular in specimen UD1-L8 tested at 1000 MPa giving life of 58751 cycles.

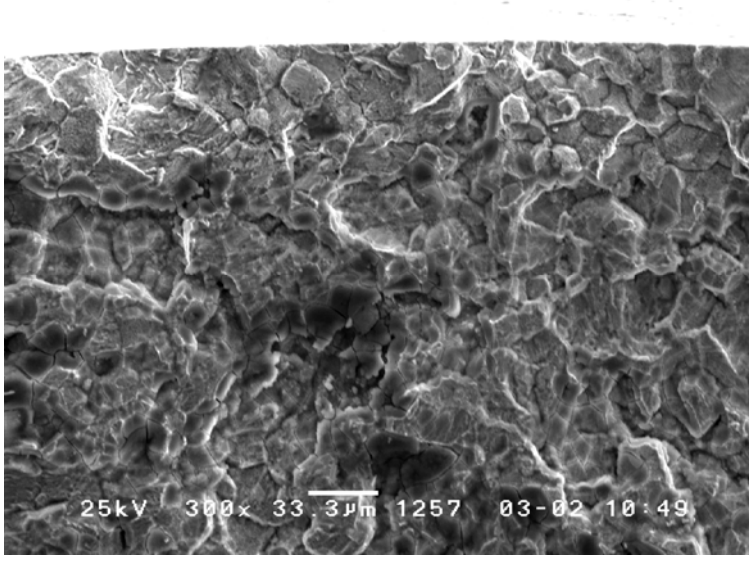

Figure C.3. Surface failure from faceted intergranular in specimen UD1-L10 tested at 940 MPa giving a life of 9063 cycles.

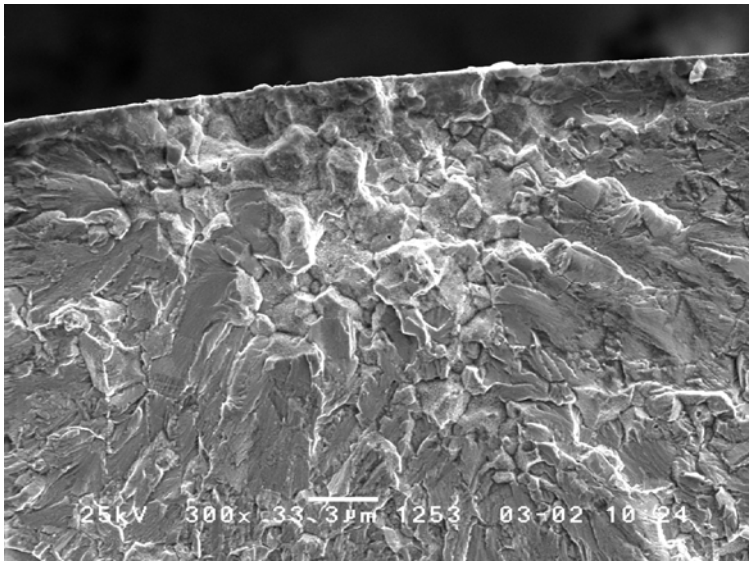

Figure C.4. Surface failure from faceted intergranular in specimen UD1-L11 tested at 960 MPa giving a life of 179325 cycles.

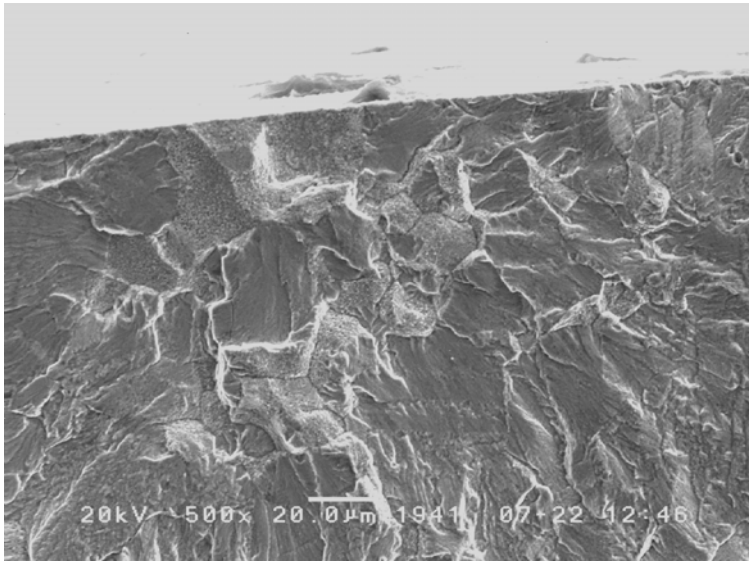

Figure C.5. Surface failure from faceted intergranular in specimen UD1-L14 tested at 1080 MPa giving a life of 9312 cycles.

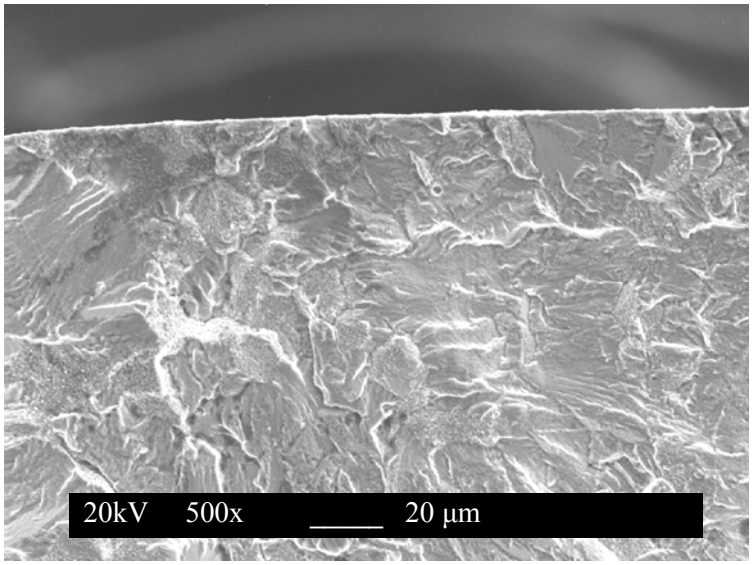

Figure C.6. Surface failure from faceted intergranular in specimen UD1-L15 tested at 1100 MPa giving a life of 3215 cycles.

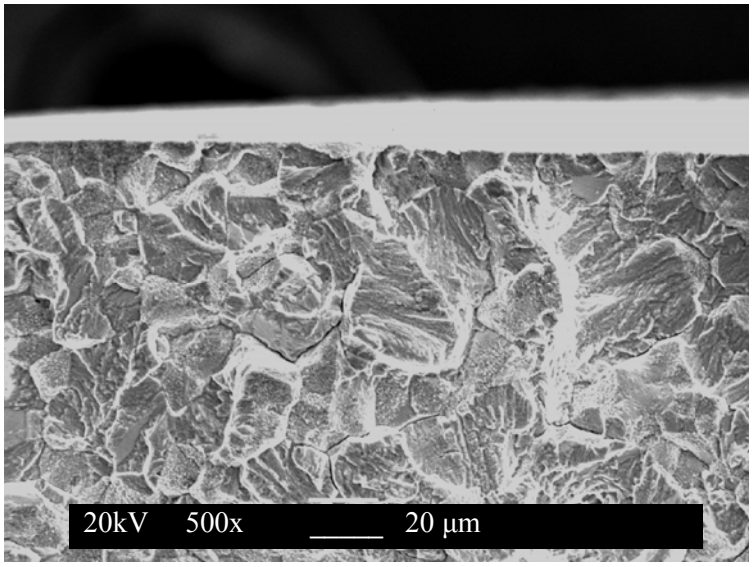

Figure C.7. Surface failure from faceted intergranular in specimen UD1-L16 tested at 1120 MPa giving a life of 1505 cycles.

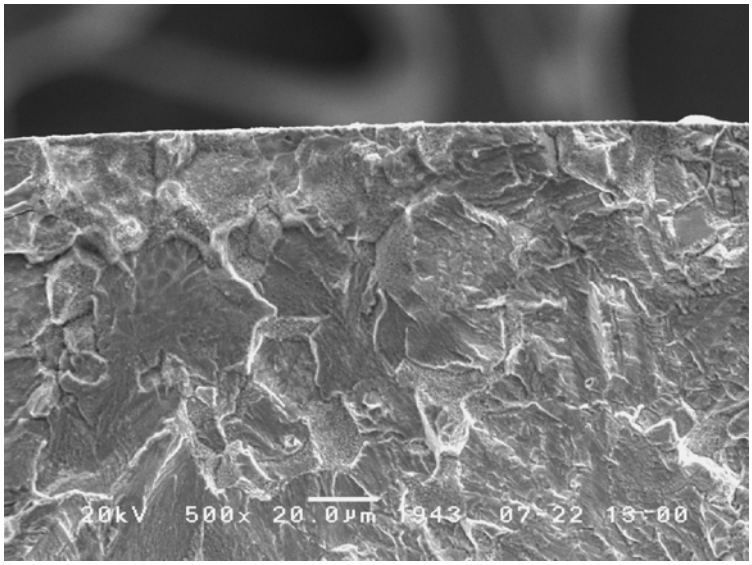

Figure C.8. Surface failure from faceted intergranular in specimen UD1-L18 tested at 1060 MPa giving a life of 5588 cycles.

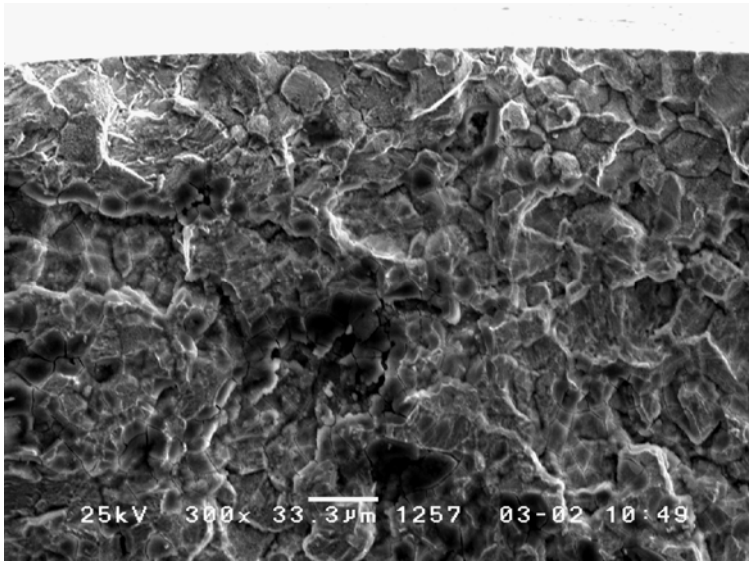

Figure C.9. Surface failure from faceted intergranular in specimen UD1-L19 tested at 1030 MPa giving a life of 9804 cycles.

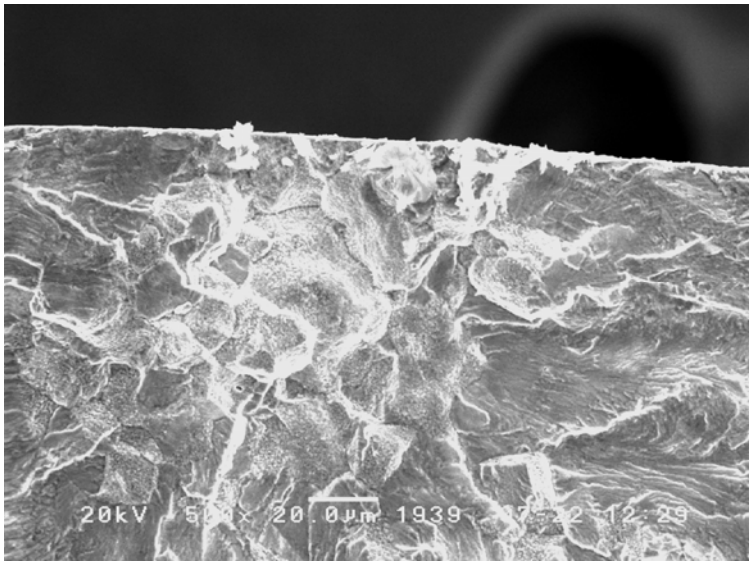

Figure C.10. Surface failure from faceted intergranular in specimen UD1-L20 tested at 1020 MPa giving a life of 14623 cycles.

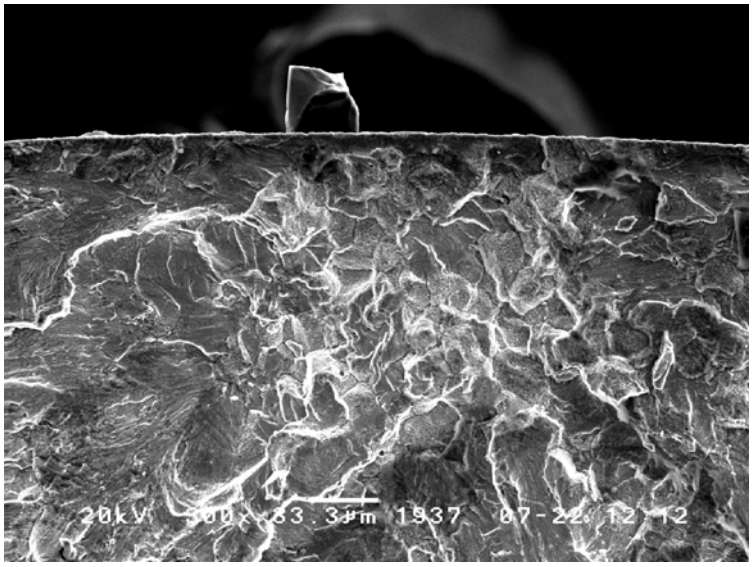

Figure C.11. Surface failure from faceted intergranular in specimen UD1-L22 tested at 940 MPa giving a life of 130893 cycles.

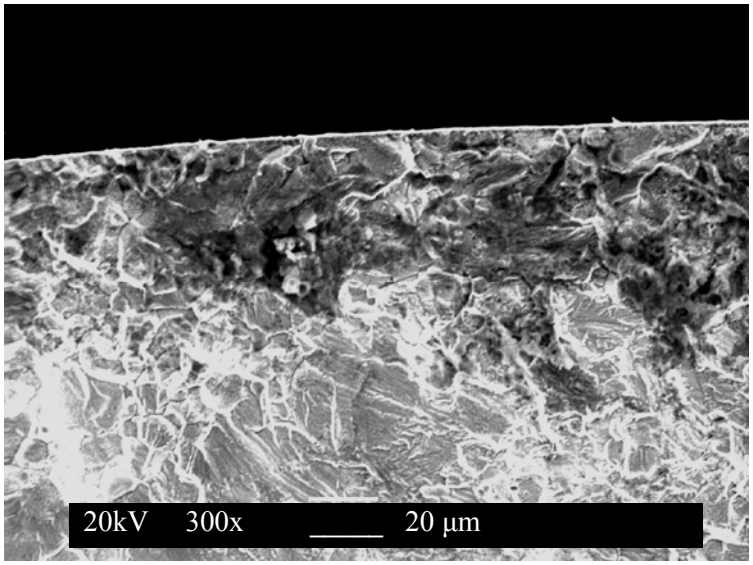

Figure C.12. Surface failure from faceted intergranular in specimen UD1-L26 tested at 920 MPa giving a life of 100217 cycles.

APPENDIX D

LARGE SEEDED SPECIMEN FATIGUE

TEST FRACTURE SURFACE IMAGES

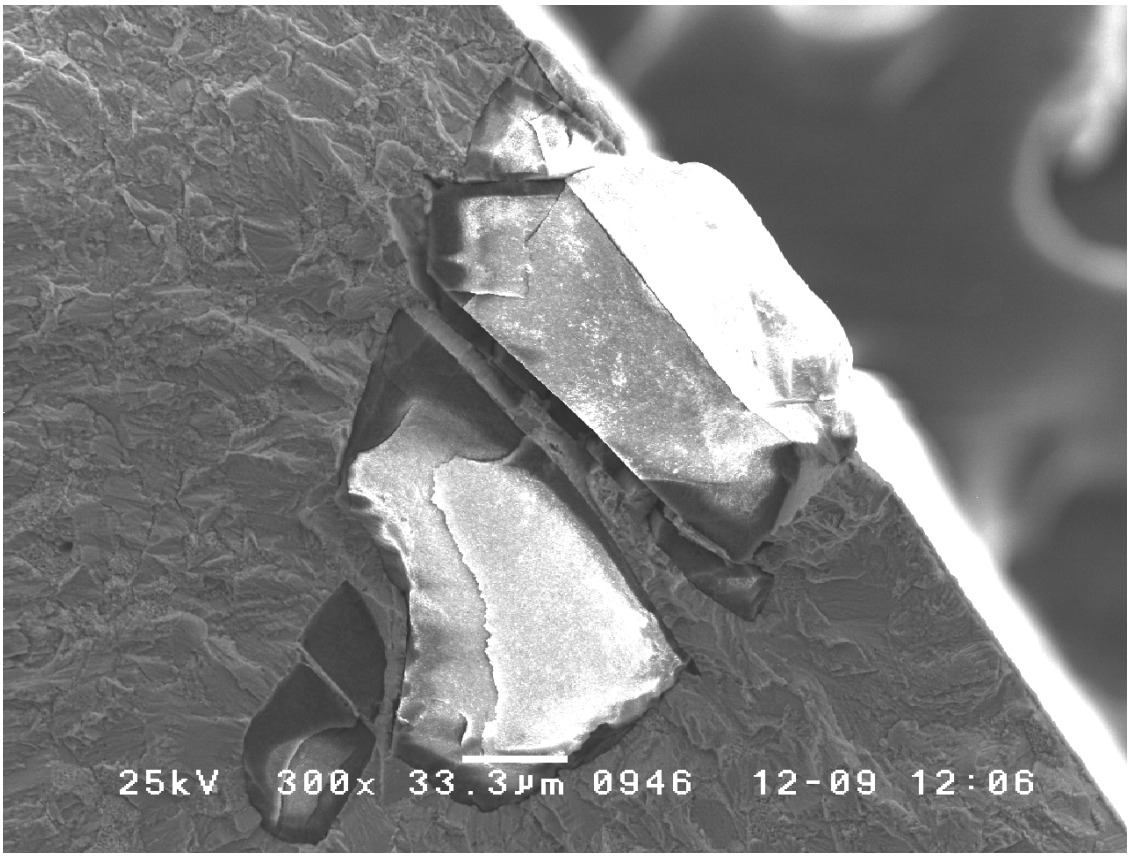

Figure D.1. Failure from surface-initiated seeded inclusion in specimen SD1-L1 tested at 1000 MPa giving a life of 3630 cycles.

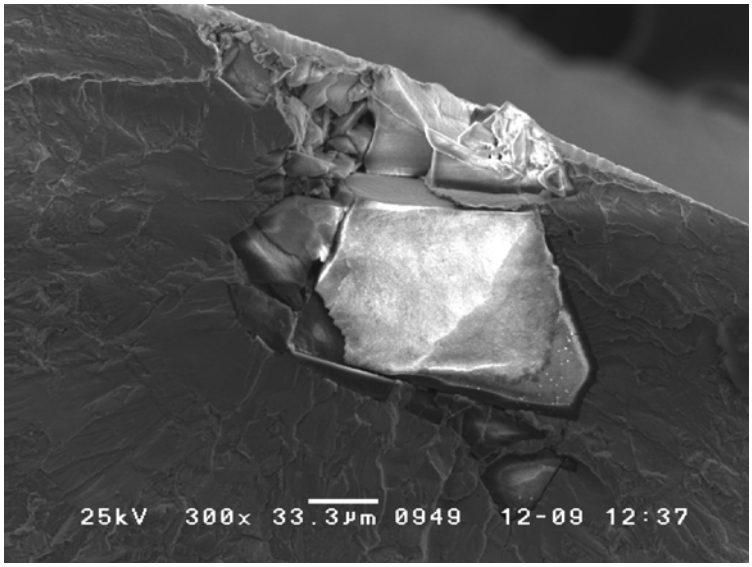

Figure D.2. Failure from surface-initiated seeded inclusion in specimen SD1-L2 tested at 900 MPa giving a life of 9217 cycles.

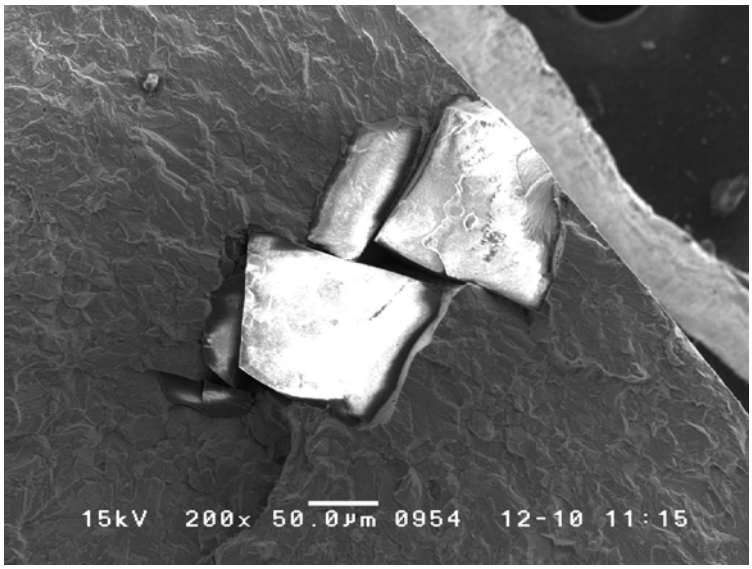

Figure D.3. Failure from surface-initiated seeded inclusion in specimen SD1-L3 tested at 950 MPa giving a life of 3560 cycles.

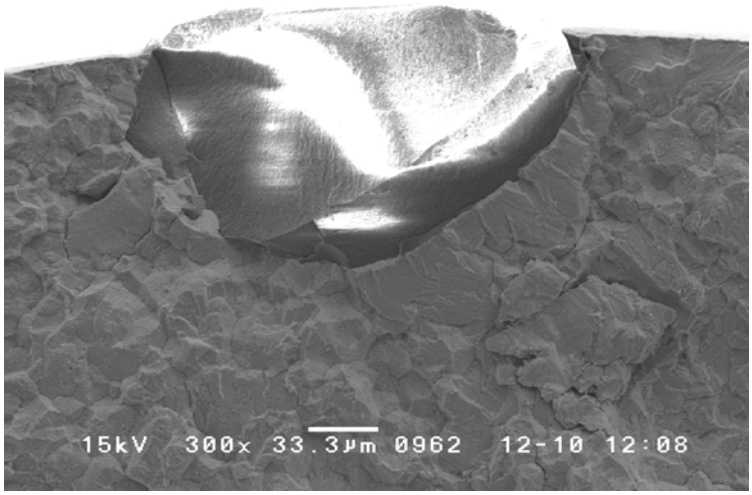

Figure D.4. Failure from surface-initiated seeded inclusion in specimen SD1-L6 tested at 760 MPa giving a life of 11170 cycles.

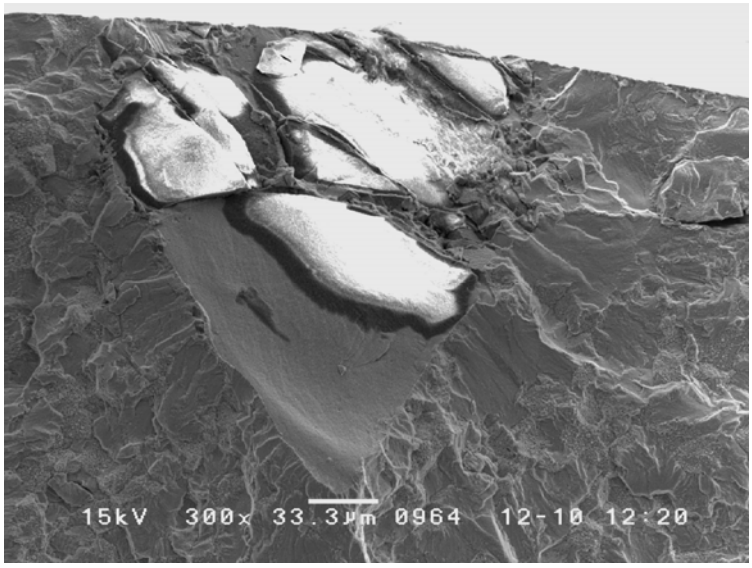

Figure D.5. Failure from surface-initiated seeded inclusion in specimen SD1-L7 tested at 800 MPa giving a life of 7685 cycles.

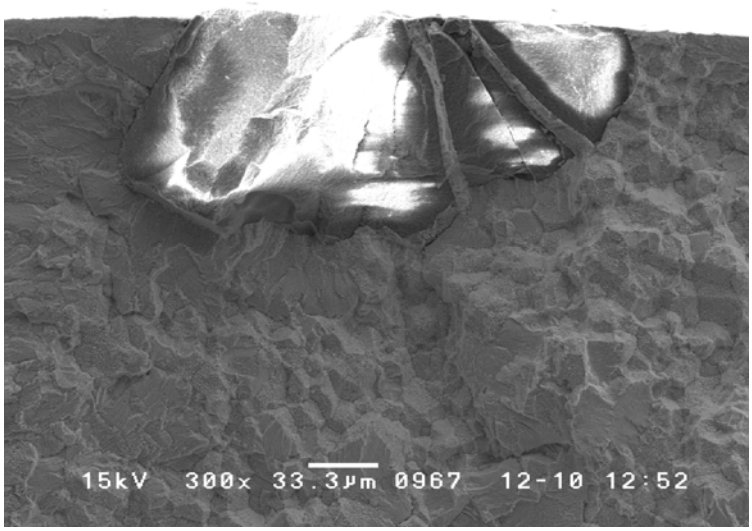

Figure D.6. Failure from surface-initiated seeded inclusion in specimen SD1-L8 tested at 720 MPa giving a life of 31992 cycles.

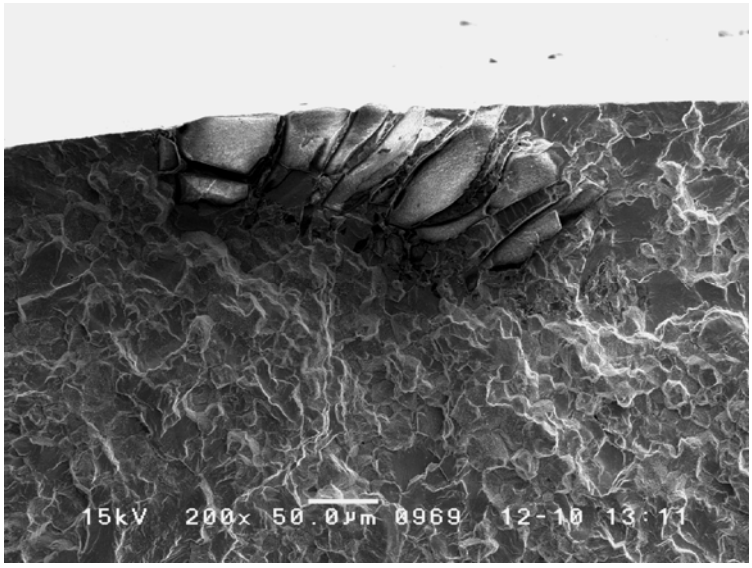

Figure D.7. Failure from surface-initiated seeded inclusion in specimen SD1-L9 tested at 680 MPa giving a life of 12222 cycles.

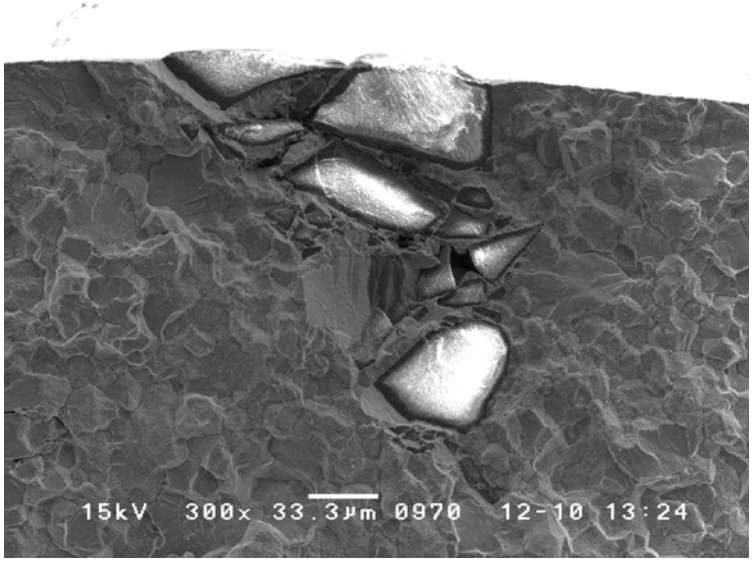

Figure D.8. Failure from surface-initiated seeded inclusion in specimen SD1-L10 tested at 660 MPa giving a life of 17016 cycles.

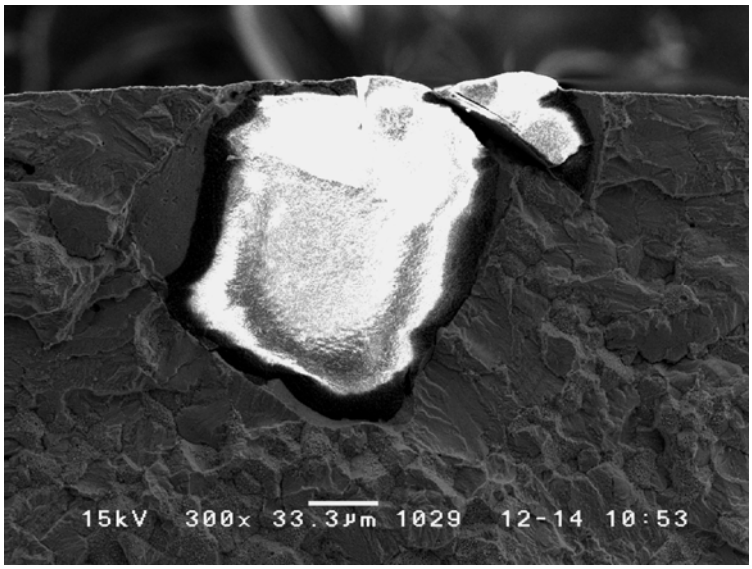

Figure D.9. Failure from surface-initiated seeded inclusion in specimen SD1-L14 tested at 800 MPa giving a life of 5853 cycles.

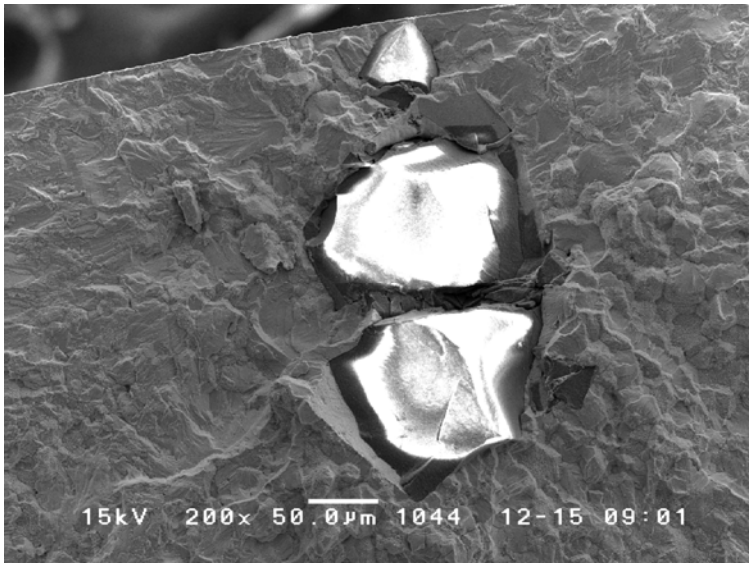

Figure D.10. Failure from surface-initiated seeded inclusion in specimen SD1-L17 tested at 740 MPa giving a life of 16362 cycles.

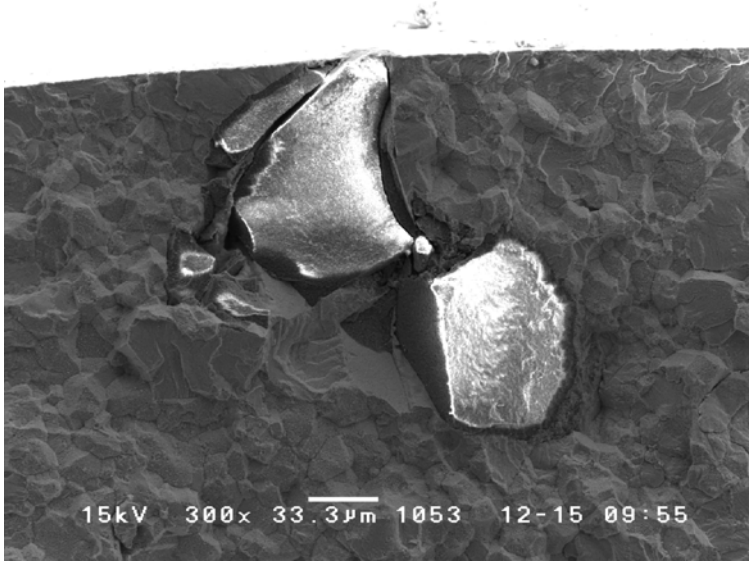

Figure D.11. Failure from surface-initiated seeded inclusion in specimen SD1-L19 tested at 680 MPa giving a life of 13899 cycles.

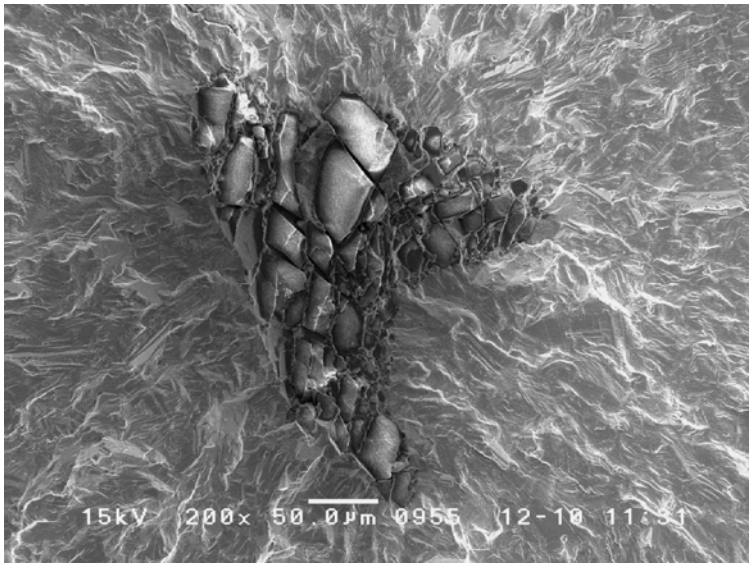

Figure D.12. Failure from internal-initiated seeded inclusion in specimen SD1-L5 tested at 700 MPa giving a life of 206911 cycles.

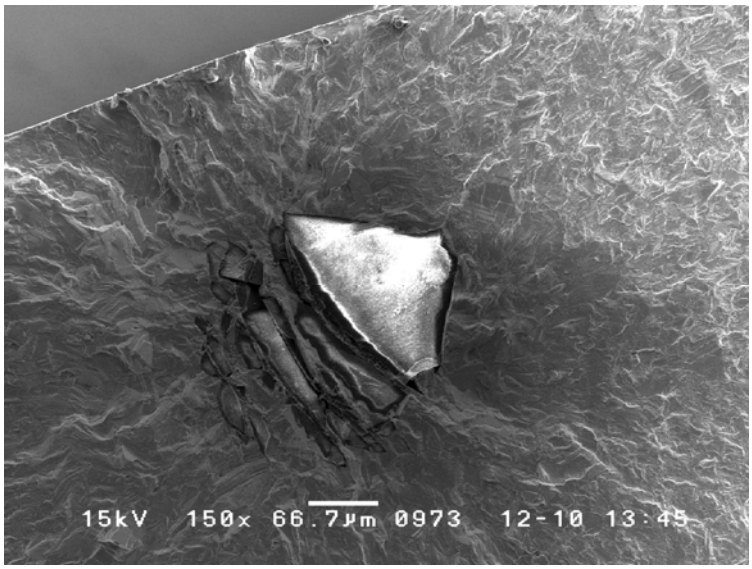

Figure D.13. Failure from internal-initiated seeded inclusion in specimen SD1-L11 tested at 620 MPa giving a life of 443568 cycles.

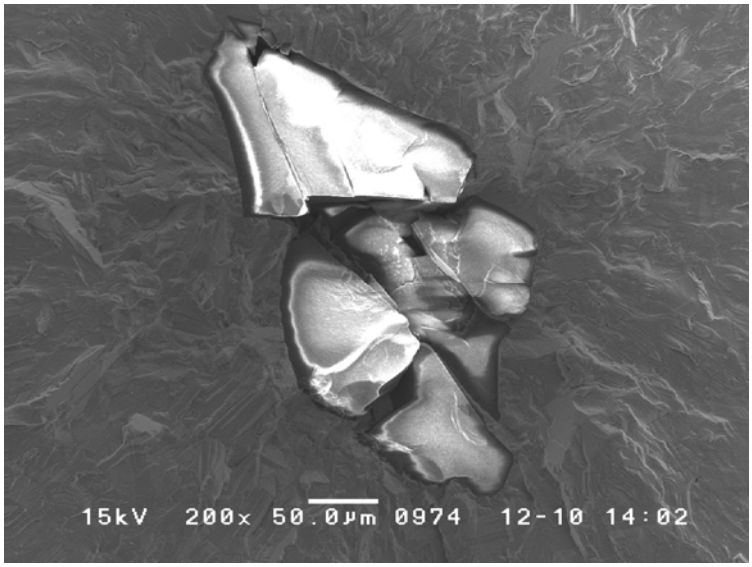

Figure D.14. Failure from internal-initiated seeded inclusion in specimen SD1-L12 tested at 600 MPa giving a life of 815993 cycles.

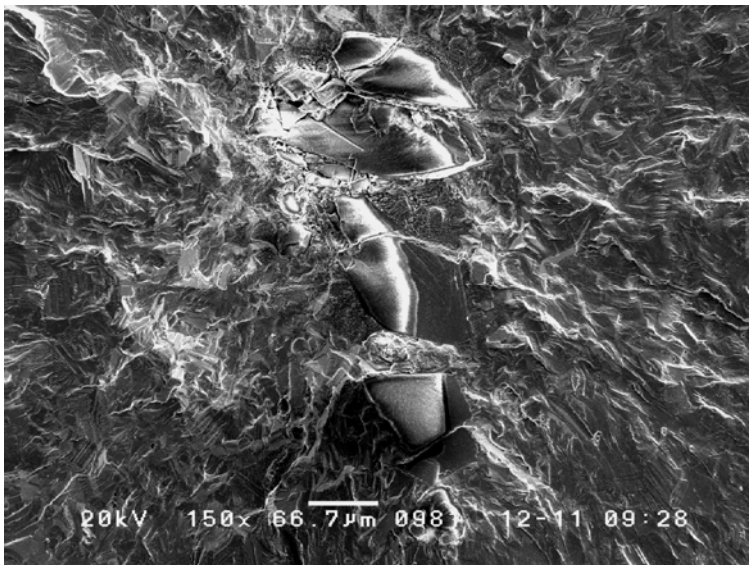

Figure D.15. Failure from internal-initiated seeded inclusion in specimen SD1-L13 tested at 580 MPa giving a life of 7717338 cycles.

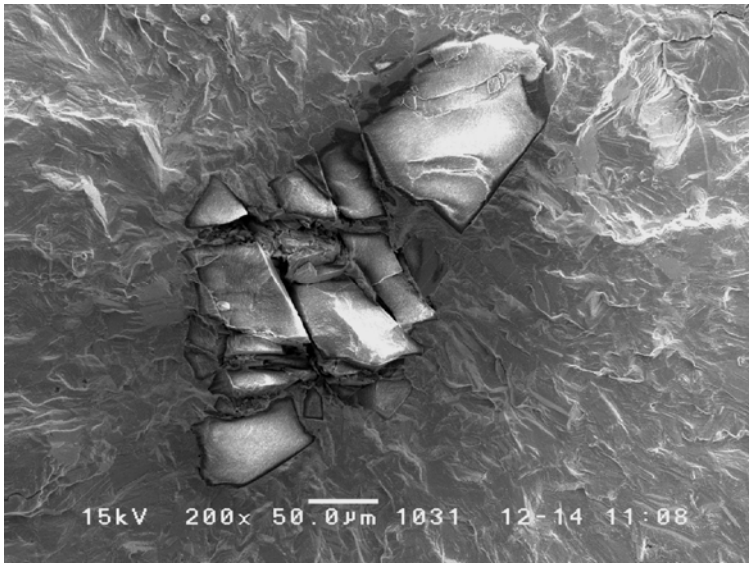

Figure D.16. Failure from internal-initiated seeded inclusion in specimen SD1-L15 tested at 560 MPa giving a life of 1091527 cycles.

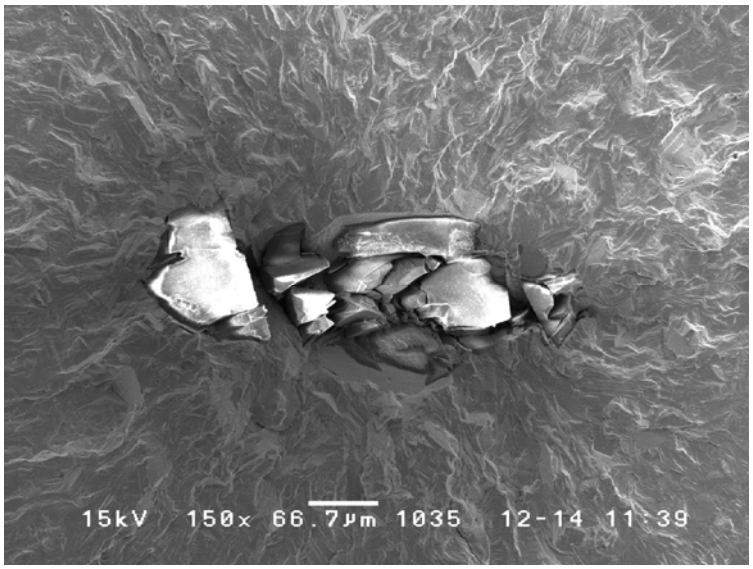

Figure D.17. Failure from internal-initiated seeded inclusion in specimen SD1-L16 tested at 660 MPa giving a life of 427949 cycles.

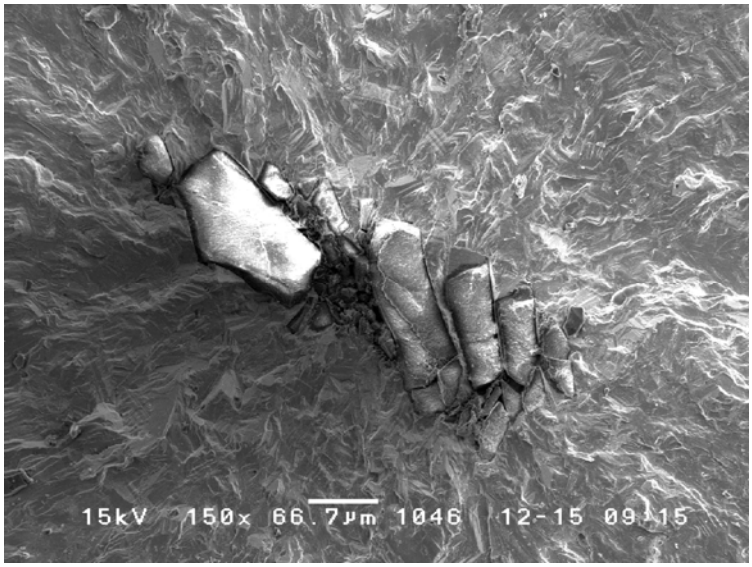

Figure D.18. Failure from internal-initiated seeded inclusion in specimen SD1-L18 tested at 640 MPa giving a life of 453361 cycles.

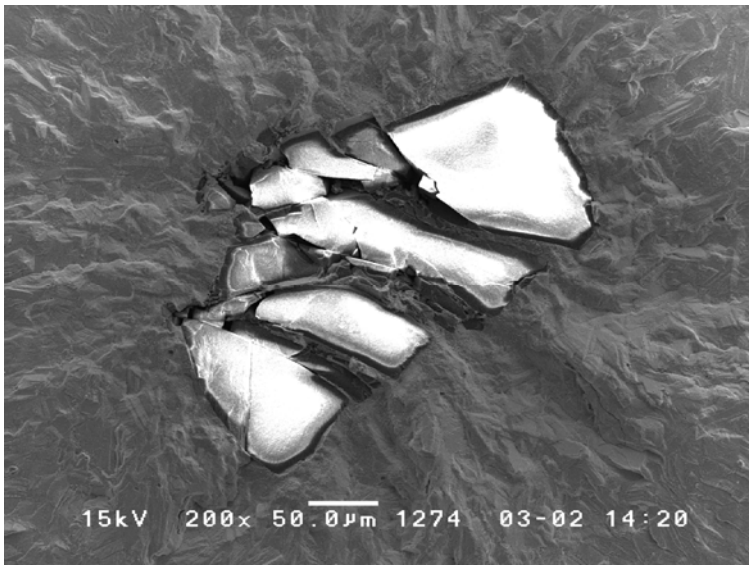

Figure D.19. Failure from internal-initiated seeded inclusion in specimen SD1-L27 tested at 540 MPa giving a life of 2483622 cycles

.

REFERENCES

1. O. Umezawa and K. Nagai: *ISIJ Intl*, 1997, vol. 37, pp. 1170-79.

2. A. Atrens, W. Hoffelner, T. W. Duerig, and J. E. Allison: *Scr. Metall.*, 1983, vol. 17, pp. 601-06.

3. S. K. Jha and K. S. Ravi Chandran: *Scr. Mater*., 2003, vol. 48, pp. 1207-12.

4. K. Tokaji, K. Ohya, and H. Kariya: *Fatigue Fract. Engng. Mater. Struct*., 2000, vol. 23, pp. 759–66.

5. K. Shiozawa and L. Lu: *Fatigue Fract. Engng. Mater. Struct.,* 2002, vol. 25, pp. 813-22.

6. Q. Y. Wang, C. Bathias, N. Kawagoishi, and Q. Chen: *Int. J. Fatigue*, 2002, vol. 24, pp. 1269-74.

7. M. Nakajima, K. Tokaji, H. Itoga, and H. M. Ko: *Fatigue Fract. Engng. Mater. Struct.*, 2003, vol. 26, pp. 1113-18.

8. J. M. Finney: *J. Inst. Metals*, 1964, vol. 92, pp. 380-82.

9. K. S. Ravi Chandran: *Nat. Mater.*, 2005, vol. 4, pp. 303-08.

10. K. S. Ravi Chandran and S. K. Jha: *Acta Mater*., 2005, vol. 53, pp. 1867-81.

11. Y. Murakami, N. N. Yokoyama, and H. Nagata: *Fatigue Fract. Engng. Mater. Struct.*, 2002, vol. 25, pp. 735-46.

12. K. Tokaji, H. N. Ko, M. Nakajima, and H. Itoga: *Mater. Sci. Engng. A,* 2003, vol. 345, pp. 197-206.

13. G. T. Cashman: *J. Eng. Mater. Technol*., 2007, vol. 129(2), pp. 293-303.

14. C. E. Shamblen and D. R. Chang: *Metall. Trans. A,* 1985, vol. 16, pp. 775-84.

15. A. Pineau: *Proc. Conf. on High Temperature Materials for Power Engineering*. Liege, Belgium, 1990, p. 913.

16. S. K. Jha, J. M. Larsen, and A. H. Rosenberger: *Acta Mater.,* 2005, vol. 53, pp. 1293–304.

17. S. K. Jha, J. M. Larsen, A. H. Rosenberger, and G. A. Hartman: *Scr. Mater*., 2003, vol. 48, pp. 1637–42.

18. K. Tokaji, H. N. Ko, M. Nakajima, and H. Itoga: *Mater. Sci. Engng. A,* 2003, vol. 345, pp. 197-206.

19. K. Tokaji, S. Takafuji, K. Ohya, Y. Kato, and K. Mori: *J. Mater. Sci.,* 2003, vol. 38, pp. 1153-59.

20. S. K. Jha and K. S. Ravi Chandran: *The Minerals, Metals & Materials Society,* 1999, p. 149.

21. S. K. Jha and K. S. Ravi Chandran: *Scr. Mater.,* 2003, vol. 48, pp. 1207-12.

22. K. Tanaka and Y. Akiniwa: *Fatigue Fract. Engng. Mater. Struct.,* 2002, vol. 25, pp. 775-84.

23. K. Shiozawa and H. Matsushita: *Fatigue'96, Proceedings of International Fatigue Congress (ed. G. Lutjering and H. Nowak) Pergamon Press.,* 1996, p. 301.

24. J. M. Hyzak and I. M. Bernstein: *Metall. Trans. A*, 1982, vol. 13, pp. 45-52.

25. K. Tokaji, K. Ohya, and H. Kariya: *Fatigue Fract. Engng. Mater. Struct.,* 2000, vol. 23, pp. 759–66.

26. K. Kobayashi and K. Yamaguchi: *Mater. Trans.,* 2005, vol. 46, pp. 861-71.

27. V. I. Shabalin: *Soviet Physics-Doklady*, 1958, vol. 3, pp. 1022-24.

28. P. J. Laz and P. M. Hillberry: *Int. J. Fatigue,* 1998, vol. 20, pp. 263–70.

29. A. Mareti: *Int. J. Fatigue*, 2005, vol. 27, pp. 33–44.

30. J.A. Odegard and K. Pedersen: *SAE Technical Paper SAE-940811*, 1994, pp. 25-32.

31. Q. G. Wang, D. Apelian, and D. A. Lados: *J. Light Met.,* vol. 1(1), 2001, pp. 73-84

32. W. Weibull: *Trans. Roy. Inst. Tech.,* 1949, vol. 27, pp. 1-49.

33. G. M. Sinclair and T. J. Dolan: *Trans. ASME,* vol. 75, 1953, pp. 867-72.

34. H. Y. Agha, A. S. Beranger, R. Dillardon, and F. Hild: *Fatigue Fract. Engng. Mater. Struct.,* 1998, vol. 21, pp. 287-96.

35. J. Z. Yi, Y. X. Gao, P. D. Lee, H. M. Flower, and T. C. Lindley: *Metall. Mater. Trans. A,* 2003, vol. 34, pp. 1879-90.

36. J. C. Ting, V. Frederick, and F. V. Lawrence: *Fatigue Fract. Engng. Mater. Struct.,* 1993, vol. 16, pp. 631-47.

37. W. Weibull: *Fatigue Testing and Analysis of Results,* Pergamon Press, Oxford, UK. 1961.

38. F. Cicci: *UTLAS Technical Note No. 73, Institute for Aerospace Studies,* University of Toronto*,* CA*,* 1964, pp. 1-16.

39. R. C. Reed: *The Superalloys: Fundamentals and Applications,* Cambridge University Press, Cambridge, UK, 2006, p. 19.

40. J. K. Tien and T. Caulfield: *Superalloys, Supercomposites and Superceramics,* Academic Press, Boston, MA, 1989, pp. 3-6.

41. J. R. Davis: *Heat Resistant Materials,* ASM International, Materials Park, *OH,* 1997. pp. 121-130.

42. C. R. Brook: *Heat Treatment Structure and Properties of Nonferrous Alloys,* American Society of Metals, Metals Park, OH, 1982, pp. 236-37.

43. C. T. Sims, N. S. Stoloff, and W. C. Hagel: *Superalloys II,* John Wiley & Sons, New York, NY, 1987. pp. 16-21.

44. S. T Wlodek: *The Stability of Superalloys,* TMS Annual Meeting, Warrendale, PA 1999, pp. 3-40.

45. C. E. Shamblen and D. R. Chang: *Metall. Trans. B,* 1985, vol. 16, pp. 775-84.

46. J.M. Hyzak and I.M. Bernstein: *Metall. Trans. A,* 1982, vol. 13, pp. 33-52.

47. M. Gell and G.R. Leverant: *Fracture*. *Second International Conference on Fracture,* London, 1969.

48. D. R. Chang, D. D. Krueger, and R. A. Sprague: *Superalloy Powder Processing, Properties and Turbine Disk Applications, Superalloys. Fifth International Symposium,* Champion, PA, 1984.

49. D.A. Jablonski: *Mater. Sci. and Engng. A*, 1981, vol. 48, pp. 189-98.

50. R.V. Miner and L. Dreshfield: *Metall. Trans. A,* 1981, vol. 12, pp. 261-67.

51. E. S. Huron and P. G. Roth: *Superalloys,* 1996, *TMS,* Warrendale, PA, pp. 359-68.

52. L. Bartosiewicz, A. R. Krause, A. Spis, J. Raghavan and S. K. Putatunda: *J. of Mater. Engng. and Performance*, 1992, vol. 1, pp. 67-74.

53. V. Singh, M. Sundararaman, W. Chen, and R. P. Wahi: *Metall. Trans A.,* vol. 22, 1991, pp. 499–505.

54. K. Kobayashi, K. Yamaguchi, M. Hayakawa, and M. Kimura: *Acta Metall. Sinica*, 2004, vol. 17(4), pp. 345-49.

55. T. Denda, T. L. Bretz, and J. K. Tien: *Metall. Trans A.* 1992, vol. 23**,** pp. 519-26.

56. D. D. Krueger, S. D. Antolovich, and R. H. Van Strom: *Metall. Trans A.,* vol. 18**,** 1987, pp. 1431-49.

57. R. V. Miner and J. Gayda: *Int. J. of Fatigue*, 1984, vol. 6(3), pp. 189-93.

58. F. Alexandre, S. Deyberb, and A. Pineau: *Scr. Mater.,* 2004, vol. 50(1), pp. 25-30.

59. S. Floreen and R. H. Kane: *Acta Mater.*, vol. 45(2), pp. 663-74.

60. H. H. Smith and D. J. Michel: *Ductility and Toughness Considerations in Elevated Temperature Service*, *Metal Properties Council Report, MPC-8, ASME,* 1978, pp. 225-46.

61. D. Zheng and H. Ghonem: *Metall. Trans. A*, 1992, vol. 23, pp. 3169-71.

62. S.T. Wlodek, M. Kelly, and D.A. Alden: *Superalloys 1996, 8th International Symposium,* Champion, PA.

63. M. N. Menon and W. H. Reimann: *J. of Mater. Sci.,* 1975, vol. 10, pp. 1571-81.

64. M. J. Caton, S. K. Jha, A.H. Rosenberger, and J.M. Larsen: *Superalloys,* 2004, *TMS,* Warrendale, PA, pp. 305-12.

65. B. I. Verkin and N. M. Grinberg: *Mater. Sci. Engng.,* 1979, vol. 41, pp. 149-81.

66. L. F. Coffin: *Overview of Temperature and Environment Effect on Fatigue of Structural Metals, in Fatigue, Environment and Temperature Effects,* Plenum Press, New York, NY, 1983, pp. 1-40.

67. R. P. Gangloff: *Corrosion Fatigue Crack Propagation Proceedings, NACE-10, National Association of Corrosion Engineers*, Houston, Texas, 1990, pp. 55-109.

68. M. Marchionni, D. Ranucci, and E. Picco: *Proc. Conf. High Temperature Alloys for Gas Turbines,* Dordrecht, Holland, 1982, pp. 791-804.

69. K. C. Liu and C. M. Loring Jr: *J. of Nucl. Mater.,* 1984, vol.122, pp. 783-88.

70. D. Ranucci, D. Marchionni, E. Picco, F. Gherardi, and O. Caciorgna: *Proc. 6th Int. Conf. on Strength of Metals and Alloys,* Melbourne, Australia, vol. 2, 1983, pp. 927-32.

71. S. Esmaeili, C.C. Engler-Pinto, B. Ilschner, and F. Rézaï-Aria: *Scr. Mater.,* 1995, vol. 32(11), pp. 1777-81.

72. H.L. Bernstein and J. M. Allen: *Journal of Engineering for Gas Turbines and Power, Trans. ASME,* 1992, vol. 114(2), pp. 293-301.

73. G. T. Cashman: *Inter. J. of Fatigue*., 2009, vol. 32(3), pp. 492-96.

74. J. Gayda, T.P. Gabb, and R. V. Miner: *Low Cycle Fatigue, ASTM STP 942., ASTM,* Philadelphia*,* PA 1988, pp. 293-309.

75. W. Hoffelner: *Mater. Sci. Tech.,* 1987, vol. 3, pp. 65-77.

76. J. E. King: *Met. Sci.,* 1982, vol. 16, pp. 345-55.

77. J. E. King, R. A. Venables, and M. A. Hicks: *Advances in Fracture Research 3,* Pergamon Press, Oxford, UK, 1984, p. 2081.

78. J. Albrecht: *Mater. Sci. and Engng. A*, 1999, vol. 263, pp. 176-86.

79. A. Pineau: *Mechanical Behaviour of Materials at High Temperature. NATO ASI Series 15,* Kluwer Academic Pubishers, 1996, pp. 135-154.

80. B. S. Kang, G. Zhang, P. Liu, and M. Ellathur: *Fatigue and Fracture at Elevated Temperatures, ASME International Mechanical Engineering Congress and Exposition,* San Francisco, CA, 1995.

81. P. A. W. Lewis and G. S. Shedler: *Nav. Res. Logist. Quart.* 1979, vol. 26, pp. 403-13.

82. G. T. Cashman: *J. Eng. Mater. Tech.* 2007, vol. 129, 159-68.

83. S. Coles: *Introduction to Statistical Modeling of Extreme Values*, Springer*,* London, 2001.

84. S. Beretta and Y, Murakami: *Metall. Trans. B,* vol. 32(3), 2001, pp. 517-23.

85. E. S. Huron and P. G. Roth: *Superalloys,* 1996, *TMS,* Warrendale, PA, pp. 359-68.

86. GE Aviation, Proprietary information.

87. M. Kutz: *Mechanical Engineers' Handbook: Material and Mechanical Design*, vol. 1, Third Edition, John Wiley & Sons, Inc., New York, 2006. p. 942.

88. S. K. Jha, M. J. Caton, J. M. Larsen, A. H. Rosenberger, K. Li, and W. J. Porter: *The Minerals, Metals & Materials Society,* 2005, pp. 343-50.

89. Y. Murakami: *Metal Fatigue: Effects of Small Defects and Nonmetallic Inclusions*, Yokendo Ltd., Tokyo, 1993. pp. 110-122.

90. K. Shiozawa and L. Lu: *Fatigue Fract. Engng. Mater. Struct.* 2002, vol. 25, pp. 813-22.

91. R. Kuguel: *Proceedings of the American Society for Testing and Materials, ASTM,* vol. 61*,* 1961, pp. 732-748.